



HAL
open science

Direct laser writing of a new type of optical waveguides and components in silver containing glasses

Alain Abou Khalil

► **To cite this version:**

Alain Abou Khalil. Direct laser writing of a new type of optical waveguides and components in silver containing glasses. Biotechnology. Université de Bordeaux; Université Laval (Québec, Canada), 2018. English. NNT : 2018BORD0290 . tel-02275792

HAL Id: tel-02275792

<https://theses.hal.science/tel-02275792>

Submitted on 2 Sep 2019

HAL is a multi-disciplinary open access archive for the deposit and dissemination of scientific research documents, whether they are published or not. The documents may come from teaching and research institutions in France or abroad, or from public or private research centers.

L'archive ouverte pluridisciplinaire **HAL**, est destinée au dépôt et à la diffusion de documents scientifiques de niveau recherche, publiés ou non, émanant des établissements d'enseignement et de recherche français ou étrangers, des laboratoires publics ou privés.

THÈSE EN COTUTELLE PRÉSENTÉE

POUR OBTENIR LE GRADE DE

DOCTEUR DE

L'UNIVERSITÉ DE BORDEAUX

ET DE L'UNIVERSITÉ LAVAL

ÉCOLE DOCTORALE DES SCIENCES PHYSIQUES ET DE L'INGÉNIEUR

SPECIALITÉ : LASERS, MATIÈRE ET NANOSCIENCES

Par Alain ABOU KHALIL

**Direct Laser Writing of a new type of optical waveguides
and components in silver containing glasses**

Sous la direction de Réal VALLÉE
et de Lionel CANIONI

Soutenue le 28 Novembre 2018

Membres de Jury :

M. POUHELLEC, Bertrand, Directeur de recherche CNRS, Université Paris-Sud	Président Rapporteur
M. EATON, Shane, Chercheur Permanent à istituto di Fotonica e Nanotecnologie	Rapporteur
M. MESSADDEQ, Younès, Professeur à l'Université Laval	Examineur
M. BELLEC, Mathieu, Chargé de recherche à l'Université Nice-Sophia Antipolis	Examineur
M. VALLÉE, Réal, Professeur à l'Université Laval	Examineur
M. CANIONI, Lionel, Professeur à l'Université de Bordeaux	Examineur
M. PETIT, Yannick, Maître de conférence à l'Université de Bordeaux	Invité

Résumé

L'interaction laser-matière a intéressé la communauté scientifique depuis la découverte du laser dans les années 1960. La recherche et le développement au cours des dernières années ont conduit à un nombre quasiment illimité d'applications industrielles et médicales basées sur le laser. Nettoyage laser, découpe, marquage, chirurgie des yeux au laser, ablation de tumeurs cancéreuses, imagerie médicale, le laser offre un outil polyvalent et non remplaçable dans les domaines industriels et médicaux. Plus spécifiquement, l'interaction laser-verre a été largement étudiée au cours des deux dernières décennies. Le processus de focalisation des lasers femtosecondes à l'intérieur des verres, afin de modifier leurs propriétés physico-chimiques, est appelé inscription laser directe. La technique d'inscription laser directe permet une structuration tri-dimensionnelle (3D) directe et rapide du verre, rendant possible la création de composants optiques 3D intégrés dans des matériaux transparents. Cette nouvelle technique présente de nombreux avantages par rapport à la lithographie, technique traditionnellement utilisée pour la création des composants optiques. La lithographie se limite à la structuration bi-dimensionnelle (2D) des matériaux et nécessite de nombreuses étapes, ce qui rend l'inscription laser directe hautement compatible pour le transfert de procédés de fabrication industrielle. De nombreuses applications pourraient être basées sur la technique d'inscription laser directe, telles que la création de capteurs miniaturisés et/ou de composants photoniques dans des puces de verre. En effet, par exemple, la technique d'inscription laser directe dans les verres a conduit à la création de Modular Photonics, une entreprise basée en Australie qui vend des micro-puces à base de verre manufacturées par la technique d'inscription laser directe pour des applications de sélection de mode, plus spécifiquement pour des besoins astronomiques. Toutefois, il reste pertinent de mener une recherche permettant de développer la compréhension et la maîtrise de nouveaux processus lors de l'interaction laser-matière, ce qui constitue le fondement de cette thèse.

Cette thèse a ainsi été réalisée grâce à une collaboration entre l'Université de Bordeaux (France) et l'Université Laval à Québec (Canada), dans le cadre du Laboratoire International Appliqué (LIA) LUMAQ (Lumière Matière Aquitaine Québec). Plus précisément, elle a été réalisée entre trois laboratoires, le Centre des lasers intenses et ses applications (CELIA) et l'Institut de chimie de la matière condensée de Bordeaux (ICMCB) de l'Université de Bordeaux et le Centre d'Optique, Photonique et Laser (COPL) à l'Université Laval, Québec, Canada. Elle consistait à consacrer près de la moitié du temps de la thèse dans chaque

université tout en travaillant sur le même projet, qui est la continuité des recherches menées dans le groupe « Short Pulse Lasers : Applications et Matériaux » (SLAM) de Lionel Canioni et le groupe « Chimie et Photonique des Matériaux Oxyde de Fluorescence », sous la direction de Thierry Cardinal à l'ICMCB. Les recherches précédentes étaient basées sur l'optimisation et la maîtrise de la synthèse des verres oxydes à base de phosphate de zinc contenant de l'argent, ainsi que sur la recherche et la compréhension des différents processus exotiques de l'interaction laser-verre après l'inscription laser directe. Ces recherches ont abouti à la création de l'entreprise « Argolight », une spin-off spécialisée dans la vente de lames de verre structurées au laser permettant l'étalonnage de fluorescence des microscopes. En outre, la NASA a utilisé un des produits d'Argolight pour équiper le microscope de fluorescence de la Station spatiale internationale pour le SpaceX SPX CRS 11 - Falcon 9.

Les travaux antérieurs du groupe sur les verres de phosphate de zinc contenant de l'argent ont permis d'une part de formuler et développer des verres innovants de qualité optique, et d'autre part d'induire par laser un riche éventail de propriétés induites par irradiation laser femtoseconde. En effet, de tels verres phosphate à l'argent sont des verres spéciaux et exotiques, en comparaison aux verres standards généralement utilisés par la communauté scientifique ou l'industrie manufacturière laser, pour réaliser l'inscription laser directe. L'incorporation d'ions d'argent à l'intérieur de la matrice de verre permet des réponses exotiques du verre après l'inscription laser directe, telles que : la création de très forts contrastes de fluorescence à partir de la synthèse de nouvelles espèces moléculaires de type agrégats ; l'exaltation localisée en 3D des propriétés optiques non linéaires de génération de troisième harmonique et aussi la création directe et pionnière de génération de second harmonique effective ; la fabrication localisée d'un milieu effectif verre/métal suite à la précipitation de nanoparticules métalliques d'argent à réponse plasmonique de surface. Dans ce contexte, ce projet de thèse ambitionne d'aller au-delà des avancées obtenues sur la création locale de propriétés optiques, en visant la création de nouvelles propriétés, et surtout le développement de fonctionnalités optiques. Ainsi, ce projet de thèse porte sur la création et la fonctionnalisation de nouveaux types de guides et composants optiques basés sur la photochimie de l'argent activée par irradiation laser. En particulier, le projet prévoit de créer de nouveaux types de guides d'ondes ainsi que des composants optiques intégrés, dont les propriétés ne sont pas accessibles à partir des verres standards.

Ce manuscrit de thèse est divisé en quatre chapitres. Le premier chapitre parle du fond du verre, du laser et de l'interaction laser-verre en général tandis que le deuxième chapitre concerne plus spécifiquement l'écriture laser directe dans les verres à l'argent qui présente une réponse originale.

Elle induit la création des agrégats d'argent fluorescents Ag_m^{x+} autour du voxel d'interaction. Leur distribution spatiale est dictée par la géométrie du faisceau laser gaussien au foyer de l'interaction. Ces espèces Ag_m^{x+} sont responsables d'un nouveau type de changement d'indice de réfraction (Δn) compatible avec les applications de guidage optique. Ce nouveau type de Δn diffère totalement du *type I* bien connu. En effet, il prend son origine dans la création d'agrégats d'argent photo-induits autour du voxel d'interaction. Ce type de Δn , basé sur de nouvelles espèces chimiques, implique de nouvelles liaisons chimiques avec des nuages d'électrons plus polarisables que ceux des ions argent, Ag^+ , initialement présents dans le verre, ce qui donne accès à un changement d'indice de réfraction local permanent, indépendamment de toute modification de la matrice de verre elle-même, c'est-à-dire une modification extrinsèque à la matrice vitreuse. Le Δn photo-induit augmente en fonction des paramètres d'irradiation et atteint une valeur maximale d'environ 8×10^{-3} . Des guides d'ondes multimodes et monomodes ont été créés à l'intérieur des verres à l'argent. Les guides multimode (MM) et monomodes (SM) ont été réalisés à partir de la photochimie induite de l'argent : un guide d'onde multimode (MM) dans les longueurs d'onde visible et infrarouge présentait des dimensions transverses typiques de $\sim 4 \times 15 \mu m^2$ avec un $\Delta n = 4.5 \times 10^{-3}$; un guide d'onde monomode (SM) à la longueur d'onde $\lambda = 630 \text{ nm}$ présentait des dimensions de $3 \times 6 \mu m^2$, $\Delta n = 2.5 \times 10^{-3}$ et des pertes de propagation dont la borne supérieure a été estimée à plus 1.2 dB/cm. Le profil de mode de guide d'onde SM est un mode guidé par chacun des deux plans des agrégats d'argent agissant comme un supermode. La simulation des profils de mode, conjointement à des études de microscopie corrélative, nous a permis de montrer une correspondance significative avec les modes expérimentaux d'une part, et d'autre part de confirmer que le Δn est vraiment basé sur la création des agrégats d'argent dans les verres d'argent. Après cela, un séparateur 50%-50% de faisceau de géométrie Y et un coupleur 50%-50% ont été écrits pour une longueur d'onde $\lambda = 630 \text{ nm}$, ouvrant la porte à la réalisation de composants optiques 3D intégrés et de circuits photoniques intégrés. Finalement, le processus de guidage d'onde a été démontré dans des fibres en forme de ruban contenant de l'argent en inscrivant un guide d'onde de 1,4 cm de long. Ces résultats offrent des opportunités uniques pour des applications telles que la détection fibrée, le filtrage, et/ou la photonique totalement intégrée.

Le troisième chapitre concerne une étude comparative entre le *type I* et le nouveau *type A* dans les verres contenant de l'argent.

En effet, l'inscription laser directe d'un changement d'indice de *type I* a été également réalisée, à la fois dans un verre au phosphate de zinc à l'argent et sans argent. Un Δn négatif de *type I* peut être observé pour le verre contenant de l'argent, par rapport à un Δn également de *type I* toujours positif dans un verre ne contenant pas d'argent, ce qui est probablement lié à la différence du rapport O/P dans la formulation de ces deux verres, ce qui a été déjà signalé par d'autres groupes de recherche. En revanche, dans les verres contenant de l'argent, en modifiant les paramètres et le régime du laser, il est possible de déclencher de façon sélective deux types de modifications différents, soit le *type A*, soit le *type I*. La modification d'indice de *type I* se produit dans le régime thermique avec une fluence laser élevée en utilisant un laser à taux de répétition de 250 kHz comparé à un régime athermique pour une modification de *type A* utilisant une faible fluence laser avec un laser à haut taux de répétition (9.8 MHz). Une comparaison de morphologie entre deux guides d'onde monomodes associé à chaque type montre la présence d'une grande zone affectée thermiquement pour une modification de *type I* et l'absence d'une telle zone pour le *type A*. Les dimensions globales des guides d'onde sont respectivement de $24 \mu\text{m} \times 38 \mu\text{m}$ et $3 \mu\text{m} \times 6 \mu\text{m}$. Cependant, les dimensions des profils de mode guidés sont similaires pour les deux types. En effet, dans le cas du *type I*, la zone de guidage est d'environ $4 \mu\text{m} \times 5 \mu\text{m}$ et présente un profil de mode circulaire (dû à l'utilisation des lentilles cylindriques dans but d'avoir un profil circulaire du faisceau laser) comparé à un modèle elliptique pour le *type A* ($3 \mu\text{m} \times 5.5 \mu\text{m}$). De plus, le Δn de *type I* peut passer de positif à négatif en fonction des paramètres d'irradiation, tandis que la modification du *type A* est toujours positive. Ainsi, nous introduisons un nouveau type de modification/changement d'indice de réfraction que nous appelons *type A* (inspiré du nom latin de l'argent, Argentum). Ce nouveau type est basé sur la création des agrégats d'argent qui prend lieu dans le régime de faible énergie d'impulsion, bien avant le régime de modification de *type I*. Ce nouveau type présente de nombreux avantages par rapport au *type I* qui sont rapportés dans ce travail : un Δn toujours positif pour différents paramètres laser, de plus petites dimensions, ainsi que la capacité unique d'écrire directement des guides d'onde rasants à la surface du verre, ceci en prenant avantage du régime énergétique à faible impulsion pour le *type A*. De tels guides de surface en *type A* sont donc prometteurs pour de futures applications de détection et la réalisation de capteurs.

Le quatrième chapitre présente un des avantages des guides de *type A* qui est l'inscription des guides d'ondes proche de la surface ainsi que la création d'un capteur d'indice de réfraction pionnière.

En prenant avantage du régime énergétique à faible impulsion pour créer le *type A* par rapport au *type I*, des guides d'ondes rasants à proximité de la surface ont été écrits dans un verre de phosphate de zinc à l'argent sans processus supplémentaires, ce qui constitue une première. Aucune attaque chimique, ni utilisation d'un verre renforcé, ni méthode de compensation ne sont nécessaires pour obtenir des guides d'ondes de *type A* proches de la surface en vue d'applications de détection. Non seulement des guides d'onde proches de la surface sont réalisables avec les guides d'ondes de *type A*, mais une écriture directe sur la surface du verre est également possible. Sur la base des guides d'ondes très proches de la surface (typiquement à 1 μm), un capteur d'indice de réfraction a été créé dans un bloc de verre de 1 cm. Ceci a permis de montrer pour la première fois, avec un guide intégré dans un échantillon monolithique, l'existence de deux résonances en terme d'énergie transportée dans le guide, donnant ainsi accès à une double zone de détection d'indice de réfraction du milieu environnant le verre, l'une pour des indices inférieurs à l'indice effectif du guide d'ondes et l'autre pour des indices égaux ou supérieurs. Une augmentation de 50% de la transmission et une diminution de 66% ont été observées, pour une gouttelette d'huile de 4 mm ayant un indice de 1.602 et 1.604 respectivement autour de l'indice du guide. Pour les guides d'ondes plus loin de la surface, une seule résonance est observée, correspondant à la chute de transmission lorsque l'indice de l'huile est égal ou légèrement supérieur à l'indice du guide d'ondes. Pour expliquer cette nouvelle phénoménologie de capteurs d'indice, un nouveau modèle théorique est proposé prenant en compte la forme du mode guidé, sa distance à la surface et le couplage évanescent entre le verre et le milieu extérieur, ainsi que le coefficient de réflexion de Fresnel. Ainsi, le nouveau modèle développé est le premier modèle à simuler l'augmentation de la transmission avant l'indice du guide d'onde. Enfin, un capteur d'indice de réfraction très sensible dans la gamme de $1 \rightarrow 1.632$ présentant une chute de transmission de 80% (7dB) pour une longueur d'interaction de 5 mm est fabriqué dans un bloc de verre de 1 cm contenant de l'argent. Ces résultats sont prometteurs pour toute application de détection de surface à partir de verres à l'argent dont l'indice de réfraction peut dès lors être ajusté en amont, en vue de la gamme réfractive visée.

Abstract

Direct Laser Writing (DLW) has been an exponentially growing research field during the last two decades, by providing an efficient and robust way to directly fabricate three dimensional (3D) structures in transparent materials such as glasses using femtosecond laser pulses. It exhibits many advantages over the lithography technique, which is mostly limited to two dimensional (2D) structuring and involves many fabrication steps. This competitive aspect makes the DLW technique suitable for future technological transfer to advanced industrial manufacturing. Generally, DLW in glasses induces physical changes such as permanent local refractive index modifications that have been classified under three distinct types: (Type I, Type II & Type III). In silver containing glasses with embedded silver ions Ag^+ , DLW induces the creation of fluorescent silver clusters $Ag_m x^+$ at the vicinity of the interaction voxel. In this work, we present a new type of refractive index change, called type A occurring in the low pulse energy regime that is based on the creation of the photo-induced silver clusters allowing the creation of new linear and nonlinear optical waveguides in silver containing glasses. Various waveguides, a 50-50 Y beam splitter, as well as optical couplers, were written based on type A modification inside bulk glasses and further characterized. In addition, a comparative study between type A and type I waveguides is presented, showing that finely tuning the laser parameters allows the creation of either type A or type I modifications inside silver containing glasses. Finally, based on type A near-surface waveguides, a highly sensitive refractive index sensor is created in a 1 cm glass chip, which could exhibit a pioneer demonstration of double sensing refractive ranges. The waveguiding properties observed and reported in the bulk of such silver containing glasses were transposed to ribbon shaped fibers of the same material. Those results pave the way towards the fabrication of 3D integrated circuits and fiber sensors with original fluorescent, nonlinear and plasmonic properties that are not accessible using the standard type I modification.

Table of contents

Résumé	ii
Abstract	viii
Table of contents	x
List of tables	xii
List of figures	xiv
List of Abbreviations	xliv
Acknowledgment	xlvi
General Introduction	1
Chapter I General background on glass and laser-matter interaction ...	7
I.1. Introduction	7
I.2. Glass	8
I.2.1. Glass history	8
I.2.2. Definition of glass	8
I.2.3. Glass formation	12
I.2.4. Glass making	15
I.2.5. Introduction to fiber optics	16
I.3. The laser	17
I.3.1. Definition of laser	18
I.3.2. Gaussian beam	21
I.3.3. Laser-material interaction	24
I.3.4. Effects of laser parameters	29
I.4. Conclusion	36
Chapter II Direct laser writing of a new type of waveguide in silver containing glasses	39
II.1. Introduction	39
II.2. Principle of DLW and Δn classification	40
II.2.1. Type I modification origins	42
II.3. State of the art:	43
II.3.1. Waveguides	43
II.3.2. Depressed cladding waveguides	49
II.3.3. Couplers:	51
II.3.4. Beam splitters	56
II.3.5. Waveguide Bragg grating (WBG)	57
II.3.6. Waveguide lasers	59
II.3.7. Photonic lantern	60
II.3.8. Study of phosphate glasses	61
II.4. Silver containing zinc phosphate glasses	63
II.4.1. Optical properties	64
II.4.2. Laser-silver containing glasses interaction	66
II.4.3. Writing window in silver containing glasses	71
II.4.4. Review of previous works on silver containing glasses	72
II.5. Experimental setup: Glass and laser used	74
II.5.1. Glass synthesis and fiber drawing	74
II.5.2. Silver containing zinc phosphate glass fibers	75
II.5.3. Laser setup:	79
II.5.4. Mode profile setup:	80
II.5.5. Confocal Microscope:	81
II.5.6. Measuring Δn : SID4Bio Phasics	81

II.6. Results	84
II.6.1. Structures' morphology	84
II.6.2. Δn vs laser parameters	86
II.6.3. Waveguiding	95
II.6.4. Optical components	110
II.6.5. Waveguides in Ribbon Fibers.....	115
II.7. Conclusion	118
Chapter III Comparative study between the type A and the type I refractive index changes	122
III.1. Introduction	122
III.2. Type I modification in phosphate – zinc phosphate glasses	124
III.3. Experimental methods	124
III.3.1. Glasses	124
III.3.2. Laser setup.....	125
III.4. Results	126
III.4.1. Type I modification in silver containing and non-containing zinc phosphate glasses	126
III.4.2. Structure morphology	133
III.4.3. Refractive index and mode profiles	135
III.4.4. Flipping Δn	138
III.4.5. Advantages of type A.....	144
III.5. Conclusion	146
Chapter IV Direct laser writing of rising near-surface waveguides in silver containing glasses with no additional processing	150
IV.1. Introduction	150
IV.2. Evanescent wave theory	152
IV.3. Evanescent wave based sensors	154
IV.3.1. Refractive index sensors	155
IV.4. Experimental methods	166
IV.4.1. Glass.....	166
IV.4.2. Laser setup	166
IV.5. Results	167
IV.5.1. Writing near surface waveguides	167
IV.5.2. RI sensor	176
IV.6. Conclusion	182
General Conclusion	184
Perspectives	186
Appendix	192
References	202

List of tables

Table II-1: Table summarizing the theoretical molar composition and the properties of the different zinc phosphate glasses used in this work. Taken from [135].----- 63

Table II-2: Different silver (Ag) species identified following DLW in silver containing glasses as reported in [139]. ----- 67

Table III-1: Table summarizing the different laser parameters for both lasers used in this chapter. ----- 126

Table III-2: Table summarizing the comparison between *type I* and *type A* modification ----- 145

List of figures

Figure I.1: The atomic arrangement of a A_2O_3 lattice of a (a) crystal (b) glass. The crystal exhibits atomic order compared to the disorder exhibited by the glass compound [5]. 9

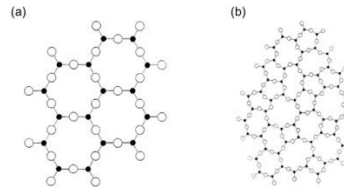


Figure I.2: Volume variation as a function of the temperature while cooling a liquid to form a crystal or a glass. Adapted from [1].10

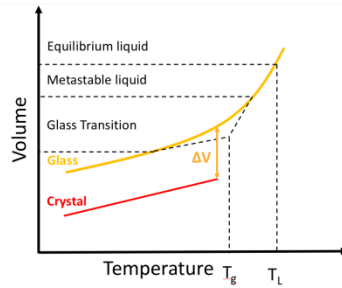


Figure I.3 The configurational entropy as a function of the temperature of the cooling process of an equilibrium liquid. The glass transition freezes the entropy and avoids a thermodynamic catastrophe. This is known as the Kauzmann paradox. Taken from [1].....11

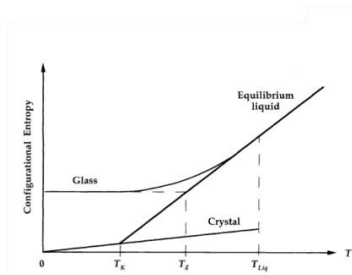


Figure I.4 Possible Differential Scanning Calorimetry (DSC) curve of a cooled liquid. T_g is the glass transition temperature, T_x the temperature of formation of the first crystal, and T_c the crystallisation temperature. The DSC curve taken from [11]. ..12

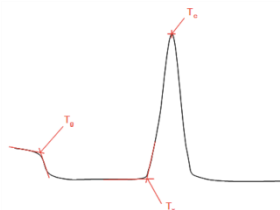


Figure I.5 : Schematic presentation of an incident light on a glass sample. I_0 is the incident light, I_R the reflected light, I_A the light absorbed, I_T the transmitted light and I_S the scattered light.....14

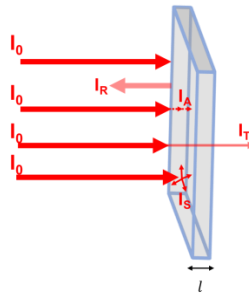


Figure I.6: Absorption spectrum of a Silica glass in the visible and near infrared region. A high transmission is shown in the visible range.....15

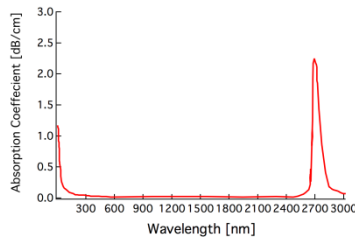


Figure I.7: Schematic representation of the melting-quenching process.....16

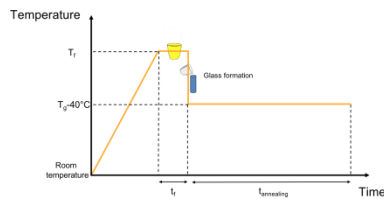


Figure I.8: Schematic presentation of a cylindrical optic fiber with inner core and outer cladding17



Figure I.9: Schematic presentation of a pulsed laser oscillator.....19

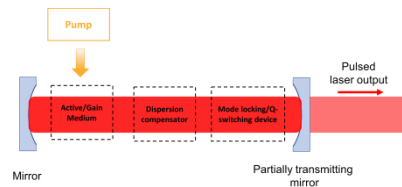


Figure I.10: Schematic presentation of a laser beam (input beam) amplified using an external amplifier. Taken from [29].20

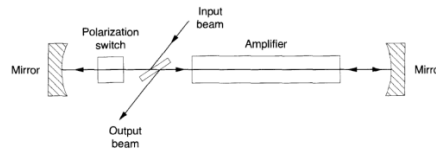


Figure I.11: Intensity profile distribution of a Gaussian beam as function of r22

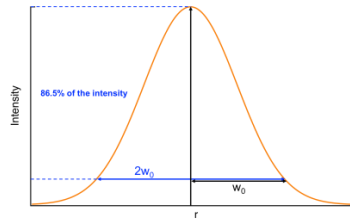


Figure I.12: Schematic presentation of a propagating Gaussian beam.23

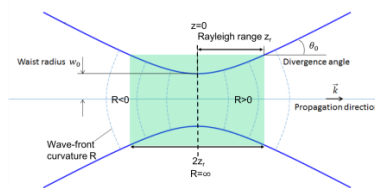


Figure I.13: Schematic presentation of the multi-photon absorption process. In this case, an electron in the valence band absorbs 3 photons to pass to the conduction band.24

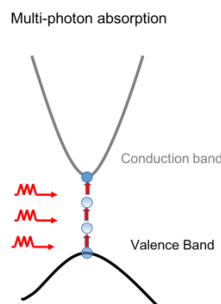


Figure I.14: Schematic presentation of the photo-ionization processes during laser-glass interaction. (a) Multi-photon ionization (MPI): An electron absorbs two or more photons to be promoted in the conduction band (b) Tunneling ionization where the electron passes through a barrier to be promoted the conduction band (c) Avalanche ionization where an electron in the conduction band absorbs two or more photons, then collides and promotes an electron from valence band to the conduction band. Inspired from [34, 35].25

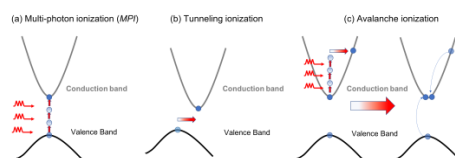


Figure I.15: (a) Scanning electron microscopy image of a track damage obtained by focusing femtosecond pulses inside fused silica (b) Numerical simulation electron density (c) Computed intensity counterplots. The comparison between experiment and simulations shows a good match of the morphology. Figure taken from [43]..27

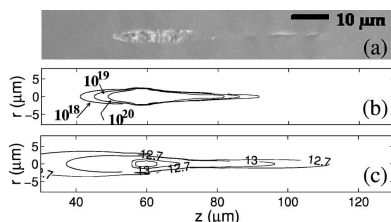


Figure I.16: Timeline of physical phenomena involved during laser-matter interaction. Inspired from [33].28

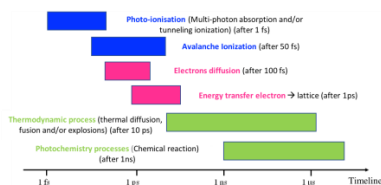


Figure I.17: Schematic presentation of the temporal evolution of the power of a (a) continuous laser (b) pulsed laser.30

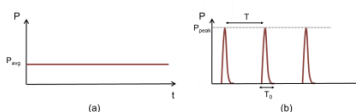


Figure I.18: Numerical simulations of the heat accumulation process inside glass following laser irradiation for different repetition rates, 100kHz, 500kHz and 1MHz. A heat accumulation process starts taking place at the 500kHz repetition rate [48].32

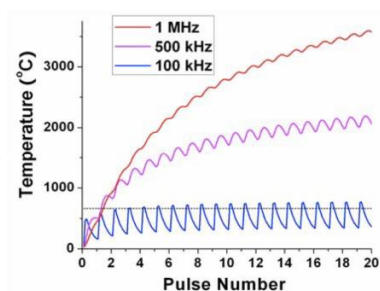


Figure I.19: Comparison between athermal and thermal regimes. For the athermal regime, low repetition rate laser, the pulses are well spaced in time so that the temperature does not have time to build up in the material. However for the thermal regime, high repetition rate laser, the pulses are close in time and the temperature builds up.33

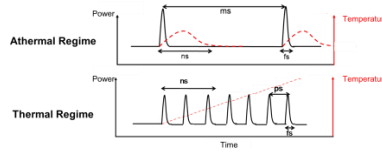


Figure I.20: Modification threshold dependence as a function of the numerical aperture of the microscope objective used in borosilicate glass [54].35

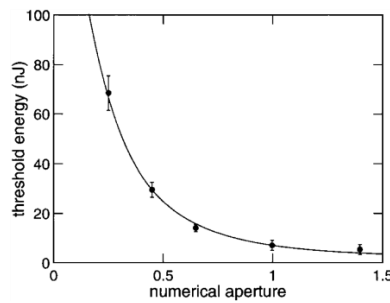


Figure II.1: Schematic presentation of the Direct Laser Writing (DLW) process.....40

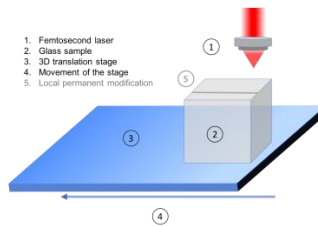


Figure II.2: Map of the modification thresholds in fused silica for the four regions/three types of modification as a function of the pulse energy and the numerical aperture. Adapted from [64].41

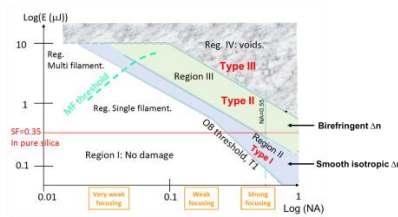


Figure II.3: The refractive index changes/modification classified as function of the irradiance. Pictures for every type of modification, waveguides, nanogratings and voids.....42

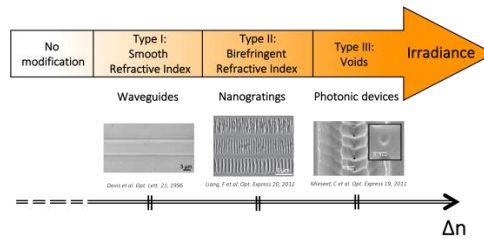


Figure II.4: Schematic of guided and unguided rays in a planar dielectric waveguide. The rays exhibiting a propagation angle θ lower than $\theta_c = \cos^{-1}(n_2/n_1)$ are only guided. Taken from [99].45

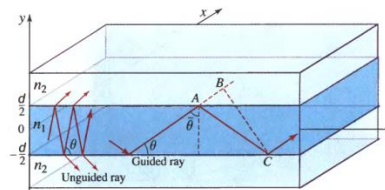


Figure II.5: Graphical solution of (II-2) to determine propagation angles θ of the mode of a planar dielectric waveguide. (a) The right side (RHS) and left side (LHS) of the equation are plotted as a function of $\sin\theta$. The intersection points marked by filled circles determines the propagation angles θ . On the other hand, each intersection of the \tan function (LHS) corresponds to a mode. In this example, the waveguide can support up to 9 modes. Taken from [99]. (b) RHS (orange dashed line) and LHS (black full line) of (II-2) is plotted for a planar waveguide exhibiting a single mode aspect with $\Delta n = 2 \times 10^{-3}$, dimensions of $5 \mu\text{m}$ at a wavelength of 630 nm47

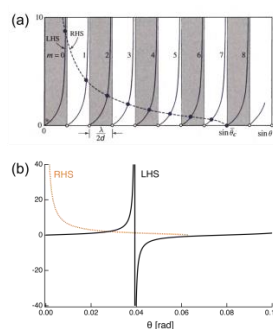


Figure II.6: Schematic presentation of the way light rays propagate inside a multimode step-index optical fiber. Taken from [99].48

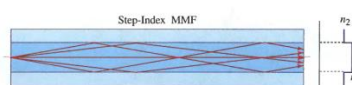


Figure II.7: The acceptance angle θ_a of an optical fiber. The rays within the acceptance cone are guided inside the fiber by total internal reflection. The numerical aperture is given by: $NA = \sin\theta_a$. Taken from [99].....49



Figure II.8: (a) Top View phase contrast image of a type I waveguide written in silver containing zinc phosphate glass under white light illumination (b) Optical Path Difference (OPD) profile associated to the waveguide. A negative OPD is observed.50

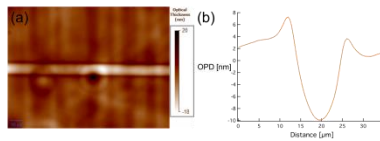


Figure II.9: Transverse view of a depressed cladding waveguide (DCW) (a) composed of 54 DCW distributed over 2 rings (b) composed of 212 DCW distributed over 4 rings. Taken from [101]51

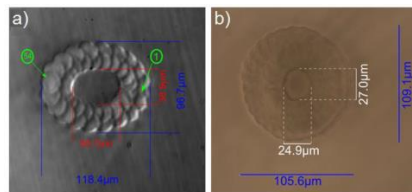


Figure II.10: Schematic presentation of two close waveguides interacting along a distance "L" and separated by a distance "d". The power is coupled between them.52

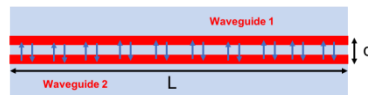


Figure II.11: Horizontal (squares) and Vertical (triangles) polarization transmission of laser written directional couplers as a function of the interaction length. First, the effect of the polarization is so slight, however when increasing the interaction distance, a bigger shift occurs indicating that the coupling effect could be altered based on the injected light polarization. Taken from [108].....54

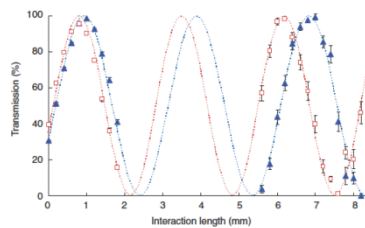


Figure II.17: Schematic presentation of the PointbyPoint (PbP) process of writing a Waveguide Bragg Grating (WBG) as well as a bright field image of the top view of the WBG. Taken from [101].....58

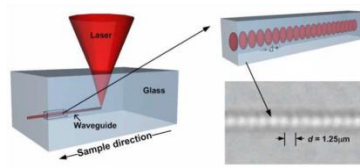


Figure II.18: (a) Top view of the Waveguide Bragg Grating (WBG). The waveguide is indicated by the black lines (b) Reflection spectrum of the written WBG (upper curve) compared to the transmission of a normal waveguide (lower curve). Taken from [115].....59

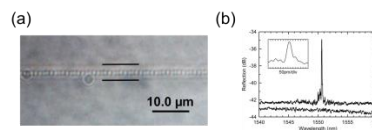


Figure II.19: Sketch of a photonic lantern (PL) starting by a multimode rectangular waveguide separating into several single mode waveguides. Taken from [125]. ...60

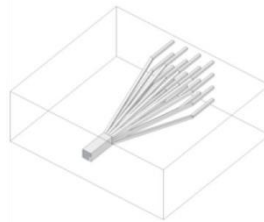


Figure II.20: Side view bright field photos of the (a) 4x4 single mode waveguides (b) rectangular multimode waveguide. Output mode images of (c) the 4x4 single mode waveguides following the injection in the rectangular multimode waveguide (d) rectangular waveguide mode following the injection of light in the 4x4 single mode array waveguides. Taken from [125].....61

Figure II.21: Absorption coefficient as a function of the wavelength for zinc phosphate glass and silver containing zinc phosphate glasses with different silver concentrations. The silver containing glasses exhibit a higher absorption band and are shifted to higher wavelengths compared to non-containing zinc phosphate glass. Adapted from [11].....65

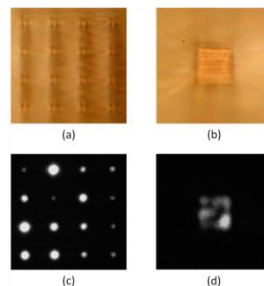


Figure II.22: Absorption as a function of the wavelength for the PZnAg2 sample from UV to IR. A good transparency window is observed between 380 nm and 2700 nm.65

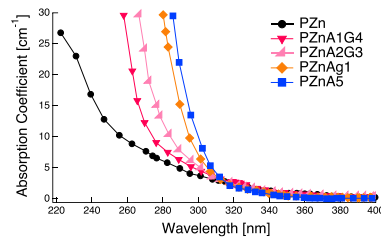


Figure II.23: Schematic presentation of the formation of silver clusters in silver containing glasses following laser irradiation.66

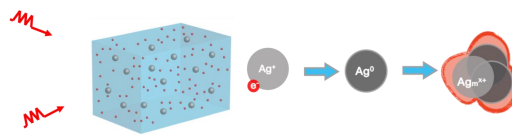


Figure II.24: Absorption (black) of the photo-induced silver clusters following laser irradiation exhibiting two main absorption bands around 290 and 345 nm. Fluorescence emission (orange) under blue light excitation at 405 nm.67

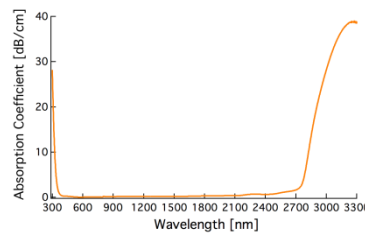


Figure II.25: (a) Sketch of the morphology of the structures following static direct laser writing (DLW) (b) confocal fluorescence images under UV excitation ($\lambda_{exc}=405nm$) of top view (xy) plane, ring shape (c) side view (xz) plane, two fluorescent lines in a pipe shape [136]. Schematic presentation of the writing process for (d) top view (xy) plane, photodissociation of the clusters in the middle (e) side view (xz) plane.68

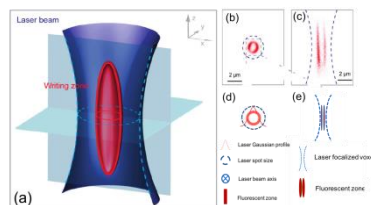


Figure II.26: Scheme of the formation of silver clusters during laser-glass interaction in silver containing glasses. Taken from [140].70

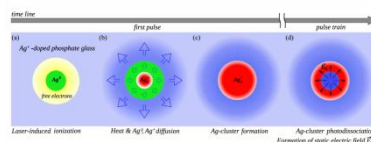


Figure II.27: (a) Fluorescence pattern of a written line under 405 nm excitation; (b) four-line of electric field induced second harmonic generation (EFISHG) under 1030 nm femtosecond laser excitation (c) superposition of the fluorescence and EFISHG correlated patterns under 405 nm and 1030 nm excitation. Taken from [143].....71

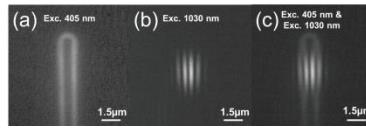


Figure II.28: Fluorescence intensity as a function of the laser irradiance and number of pulses for different laser repetition rates (a) 10MHz (b) 1MHz (c) 100kHz (d) 10kHz. Taken from [11].....72

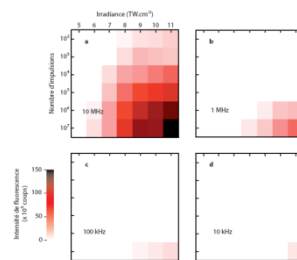


Figure II.29: Top view under white light illumination for different lines written using a 250 kHz laser emitting at 1030 nm with a fixed pulse energy of 0.26 µJ for three different speeds from the left to the right: 10 mm/s-5 mm/s-1 mm/s. To be compared with figure 4 in [148].74

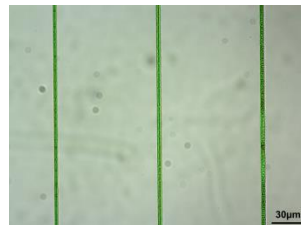


Figure II.30: Zinc phosphate glass under UV excitation (a) non-containing (PZG-4N) and silver containing (PZG-2N2A) preforms. PZG-2N2A only exhibiting fluorescence emission; (b) fibers and a leftover of a preform. Taken from [149]. .76

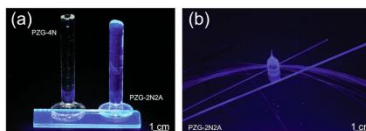


Figure II.31: Comparison between bulk glass and fiber fluorescence emission properties ($\lambda_{exc}=245\text{nm}$). A good match is found indicating that the drawing process preserved the glass properties. Taken from [149].....77

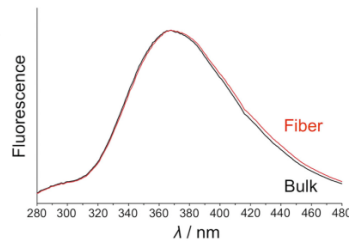


Figure II.32: (a) Thermal drawing of ribbon fibers. Preform, bottom-neck preform and drawn fibers under UV excitation ($\lambda_{exc}=245\text{nm}$). (b) Sketch, longitudinal and side view of the drawn ribbon fiber. A flat surface with a rectangular side view is obtained. Taken from [149].78

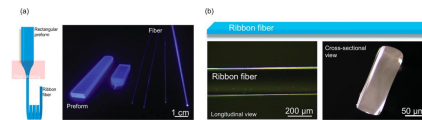


Figure II.33: Top view of the ribbon fiber (a) under white illumination before DLW (b) under UV excitation ($\lambda_{exc}=405\text{ nm}$) following DLW. The fluorescence of the written structures could be observed. (b) Fluorescence intensity broad band emission of the structures under UV excitation ($\lambda_{exc}=405\text{ nm}$). (c) Fluorescence of the written cartography and the corresponding differential transmission spectra. A higher absorption band is observed for a higher laser irradiance. Taken from [149].79

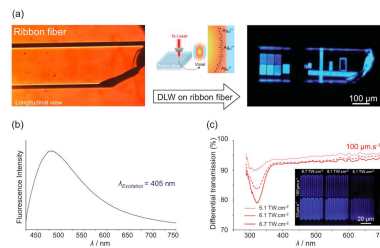


Figure II.34: Schematic of the laser setup used for direct laser writing.....80

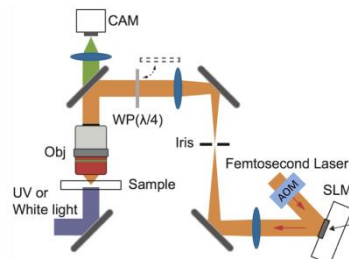


Figure II.35: Sketch of the SID4Bio wavefront sensor working principle. The incident beam is diffracted by the modified Hartmann Mask into four replicas making an interferogram on the sensor (CCD Camera) [155].82

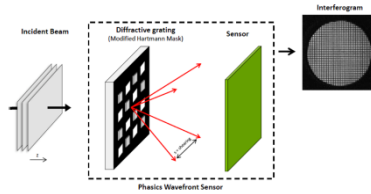


Figure II.36: Sketch of the light delayed by a refractive index object (n_2) with a specific thickness "e" different than the surrounding medium (n_1) leading to the construction of the phase image. The optical thickness i.e. optical path difference could be obtained [155].82

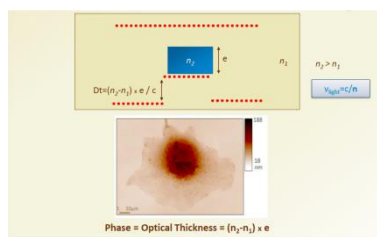


Figure II.37: The SID4Bio installed on a transmission microscope. The light is diffracted by the grating creating the interferogram on the CCD camera giving an output of an intensity and phase image [155].83

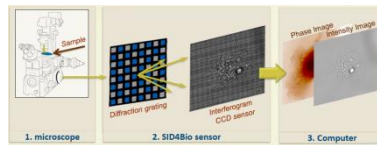


Figure II.38: (a) Schematic of the morphology of the structures following perpendicular translation to the laser beam propagation inside silver containing zinc phosphate glasses. Fluorescence confocal images of the (b.i) top view (xy) plane, and (c.i) side view (xz) plane. Schematic presentation of the writing process with (b.ii) top view and (c.ii) side view.85

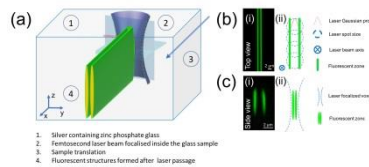


Figure II.39: (a) Fluorescence image ($\lambda_{ex}=480\text{nm}$, $\lambda_{em}=550\text{nm}$) of the written cartography. Writing irradiances are presented along the vertical axis while the number of pulses appears along the horizontal axis (b) Blowup of the phase image under white light illumination of the B2 structure (c) positive refractive index change (Δn) determined from the phase image of B2.....87

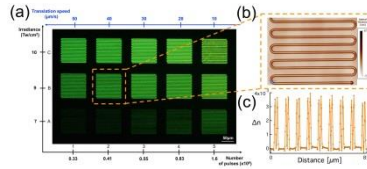


Figure II.40: (a) Phase image under white light illumination showing one line of phase shift; (b) Line profile obtained from the phase image revealing only one positive peak of optical path different in that case for the structures instead of two peaks; (c) left column: experimental silver cluster spatial distribution for a progressive scale of irradiances; right column: simulated distribution of the silver clusters. For (i) and (v) low laser irradiance is used and a full disk of fluorescence is observed, which is not the case for higher irradiances. Taken from [140]88

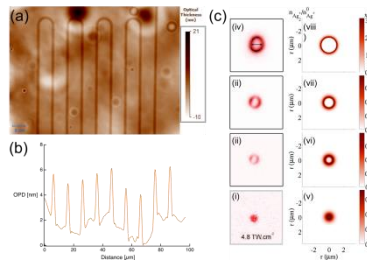


Figure II.41: Refractive index change variation (Δn) as a function of the number of pulses and laser irradiance. Δn increases as a function of the laser parameters. Laser repetition rate 9.8 MHz.89

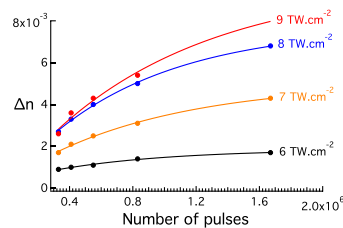


Figure II.42: Variation of the length of the structure along z as a function of the laser parameters, laser irradiance and writing speed. The dimensions increase as a function of the laser irradiance. Laser repetition rate 9.8 MHz. The shades correspond to the standard deviation of the values.90

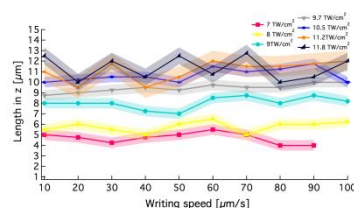


Figure II.43: Top view phase image of different lines separated by 1 μm in the z plane. The seventh line becomes blurry indicating that the optical system is limited to around 6 μm in depth.....91

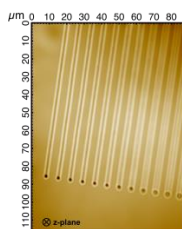


Figure II.44: Refractive index change (Δn) as a function of the number of pulses for two methods: (orange) using the compensation method (black) fixed method where the depth of the structure higher than 6 μm is considered as 6 μm . Both methods converge more or less to the same values. The black shades correspond to the standard deviation of the values.92

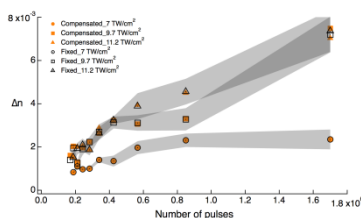


Figure II.45: (a) High Resolution Scanning Electron Microscopy (HRSEM) image of the top view of a ring shape structure formed by silver clusters; (b) Line profile extracted from the HRSEM photo indicating a bump on the edges; (c) Atomic Force Microscopy (AFM) profile indicating no bumps on the sides. The bumps observed in the HRSEM are due to a change in the chemical composition and not to topological changes. Taken from [136].....93

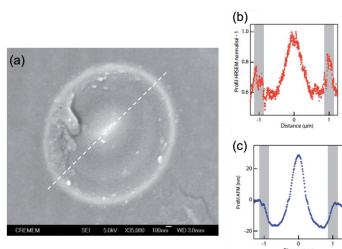


Figure II.46: (a) fluorescence; (b) HRSEM, top view of the photo-induced structures. The fluorescence spatial distribution is correlated to the HRSEM indicating that the silver clusters are responsible for the change in the chemical composition. The scale bar is 1 μm . Taken from [136].94

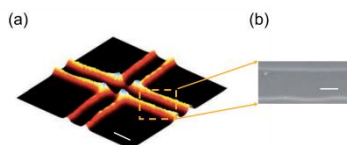


Figure II.47:(a) Silver clusters differential absorption spectrum as a function of the wavelength showing two main absorption bands near 290 nm and 350 nm; (b) Refractive index change (Δn) determined from the spectrum shown in (a) based on a Kramers-Kronig analysis, considering the filling factor of the silver clusters' spatial distribution. DLW parameters: $7\text{TW}/\text{cm}^2 - 40 \mu\text{m}/\text{s}$95

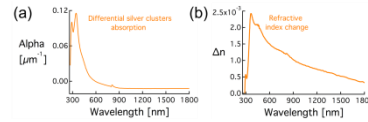


Figure II.48: (a) Schematic of the direct laser writing process and the laser injection; (b) Picture of the bulk sample under UV excitation ($\lambda_{\text{ex}}=405\text{nm}$) highlighting the fluorescence of the waveguide (indicated by the white arrow); (c) fluorescence image of the side view of the waveguide under UV excitation ($\lambda_{\text{ex}}=405\text{nm}$); (d) near-field guided mode profile following laser injection [149]. ..96

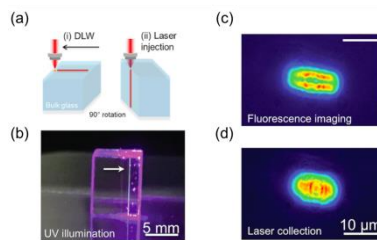


Figure II.49: Cross section view of fluorescence under UV side-excitation ($\lambda_{\text{exc}}=405\text{nm}$) of (a) WG1, (e) WG2. Superimposed near field mode profile and fluorescence features for (b) WG1, (f) WG2. Near field mode profile for a high order propagating mode of (c) WG1, (g) WG2. Simulated mode profile using LUMERICAL for (d) WG1, (h) WG2. DLW parameters for WG1: $8 \text{TW}/\text{cm}^2 - 10\mu\text{m}/\text{s}$. For WG2: $8\text{TW}/\text{cm}^2 - 20\mu\text{m}/\text{s}$98

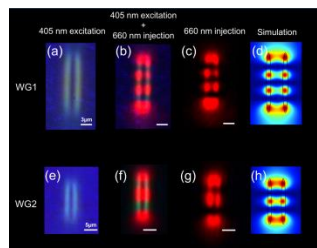


Figure II.50: Near field mode profile following laser injection at $1.55 \mu\text{m}$ (a) fundamental mode, (b) higher order mode. The waveguide presented a multimode aspect. DLW parameters: $8\text{TW}/\text{cm}^2 - 10 \mu\text{m}/\text{s}$99

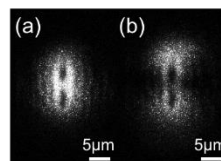


Figure II.51: (a) Fluorescence confocal image of the side view of the waveguide. (b) Normalized horizontal fluorescence profile averaged along the y axis. (c) Normalized vertical fluorescence profile averaged along the z axis. 100

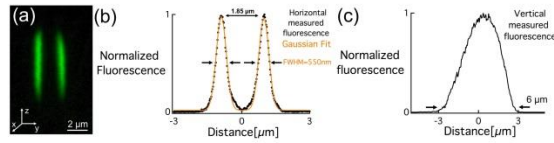


Figure II.52: (a) Phase image of the top view of the waveguide under white illumination (b) Refractive index change (Δn) profile obtained from the phase image. DLW parameters: $9 \text{ TW/cm}^2 - 60 \text{ } \mu\text{m/s}$ 101

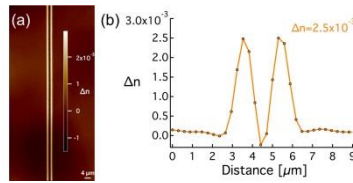


Figure II.53: Refractive index change (Δn) profile for different laser passages for an irradiance of 7 TW/cm^2 and a speed of writing of (a) $50 \text{ } \mu\text{m/s}$, (b) $30 \text{ } \mu\text{m/s}$, (c) $20 \text{ } \mu\text{m/s}$. A negative Δn dip appears for lower writing speeds and for many laser passages. 102

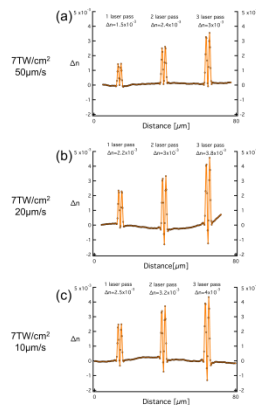


Figure II.54: Superposition of the silver cluster fluorescence spatial distribution (black), normalized topology after chemical etching (red) and silver ions concentration distribution (blue). Taken from [141]. 103

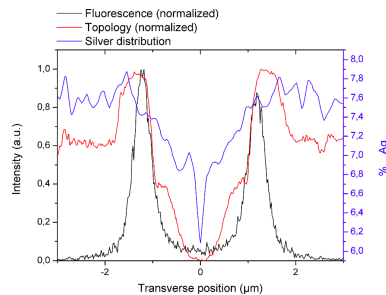


Figure II.55: The variation of the refractive index of the non-containing and silver containing zinc phosphate glasses as function of the silver concentration incorporated in the glass matrix. The higher the concentration of silver the higher the refractive index of the glass is (from bottom to top). Data from [135].104

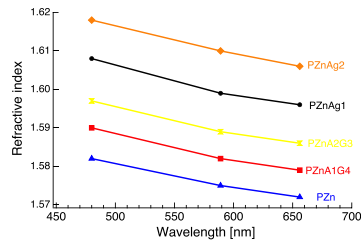


Figure II.56: (a) Experimental: (a.i) Near field mode profile after injecting a 630 nm laser, (a.ii) normalized horizontal mode profile intensity averaged along the z axis, and (a.iii) normalized vertical mode profile intensity averaged along the y axis. (b) Simulations: (b.i) simulated mode profile (to compare with Figure II.56.a.i), (b.ii) normalized horizontal intensity mode profile averaged along the z axis (to compare with Figure II.56.a.ii), and (b.iii) normalized vertical mode profile intensity averaged along the y axis.105

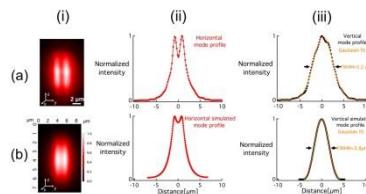


Figure II.57: Schematic model of the simulated waveguides using Lumerical Mode solutions software. The waveguides are simulated as two parallel ellipsoids with thickness "e", with a length "z" and separated by a distance "d". The color scale corresponds to the refractive index change. In this case, the glass refractive index change is 1.6 while the waveguide is 1.608 corresponding to a refractive index change (Δn) of 8×10^{-3}106

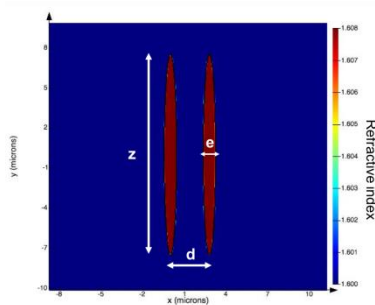


Figure II.58: Spatial superposition of the measured refractive index profile (Δn) (black), simulated near-field mode profile (blue) and experimental near-field mode profile (red). A good match is observed between the simulated and experimental modes and the Δn distribution..... 107

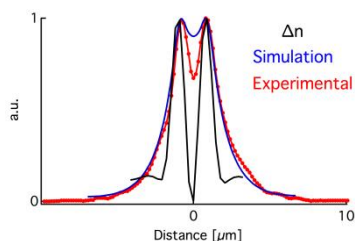


Figure II.59: Variation of the minimum Δn required to trigger the multimode aspect as a function of the thickness of the structures. Blue vertical line indicates the thickness measured by confocal microscope and used during simulations ($\sim 500\text{nm}$) while the red line indicates the HRSEM measurement ($\sim 100\text{nm}$) performed earlier in our group [139]. 108

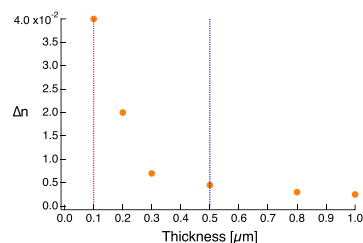


Figure II.60: Fundamental near-field mode profile of a (a) multimode (MM) waveguide, (b) single mode (SM) waveguide. (c) Near-field mode profiles of the MM and SM waveguides. DLW parameters for SM: $9\text{TW}/\text{cm}^2 - 60\mu\text{m}/\text{s}$, for MM: $10.5\text{TW}/\text{cm}^2 - 20\mu\text{m}/\text{s}$ 110

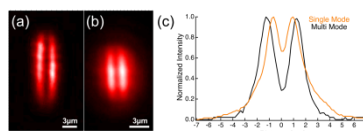


Figure II.61: (a) Sketch of the Y-beam splitter dividing the input light into two equal outputs (top view), (b) top view fluorescence image of the Y-junction ($\lambda_{\text{ex}}=480\text{nm}$, $\lambda_{\text{em}}=550\text{nm}$), (c) output modes of the beam splitter (d) normalized intensity profile of the output modes indicating an almost equal splitting of light between both outputs. DLW parameters: $9\text{TW}/\text{cm}^2 - 60\mu\text{m}/\text{s}$ 111

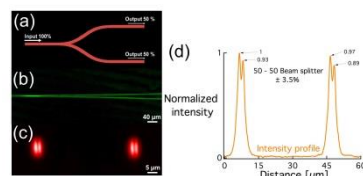


Figure II.62: Sketch of the S-bend 112

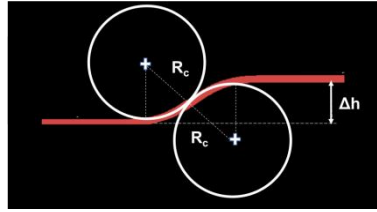


Figure II.63: Normalized transmission of the S-bend waveguides as a function of the radius curvature R_c and the separation distance Δh . Reversed injection data corresponds to backward injection in the S-bend waveguides. DLW parameters: $9.3\text{TW}/\text{cm}^2 - 40\mu\text{m}/\text{s}$ 113

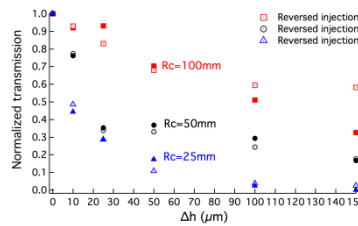


Figure II.64: Sketch of the coupler consisting of straight and S-bend waveguides. 113

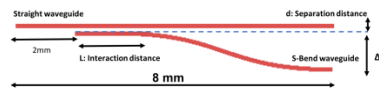


Figure II.65: Simulated and experimental normalized coupled power as a function of the separation distance between the two waveguides. DLW parameters: $9.3\text{TW}/\text{cm}^2 - 40\mu\text{m}/\text{s}$ 114

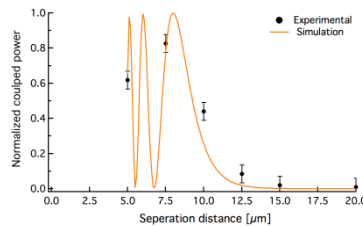


Figure II.66: (a) Near-field mode profiles of the output of the coupler; (b) normalized intensity of the mode profiles indicating the creation of a 50-50 coupler. DLW parameters: $10.8\text{TW}/\text{cm}^2 - 40\mu\text{m}/\text{s}$ 115

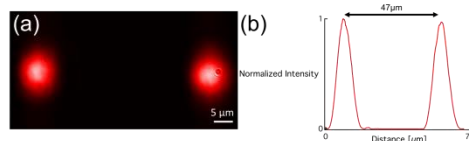


Figure II.67: (a) Cross-section view of the ribbon fiber with the guided mode in the middle; (b) blowup of the near-field mode profile; (c) horizontal mode profile; (d) vertical mode profile. The mode profile is similar to the mode profile in bulk glasses as shown in Figure II.56. DLW parameters: $10\text{TW}/\text{cm}^2 - 25\mu\text{m}/\text{s}$ 116

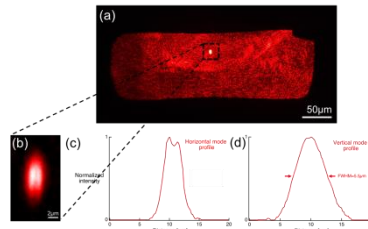


Figure III.1: Schematic presentation of the laser setup used for writing *type I* waveguides..... 126

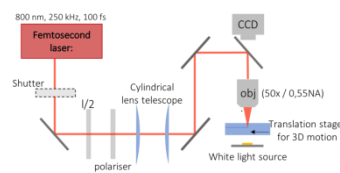


Figure III.2: Optical Path Difference (OPD) of the waveguide written in (orange) silver containing zinc phosphate glass (PZnAg2) and (black) non-containing silver zinc phosphate glass (PZn). 127

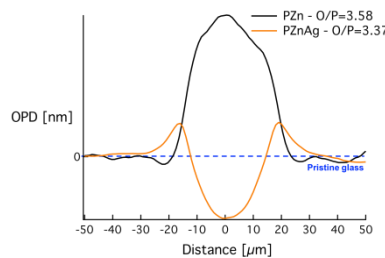


Figure III.3: Various optical path difference (OPD) profiles as a function of (a) writing speed (b) pulse energy. The Δn flips from negative to positive when increasing the pulse energy or decreasing the writing speed. 129

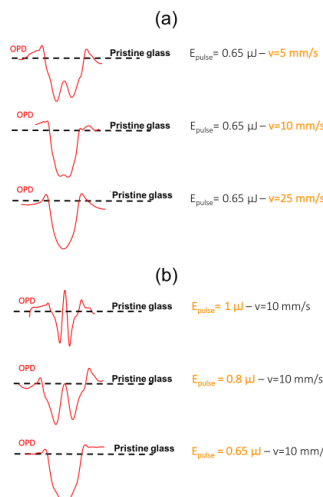


Figure III.4: Optical path difference (OPD) profiles of *type I* modification in non-containing silver zinc phosphate glass as a function of the laser parameters. The Δn is always positive. 131

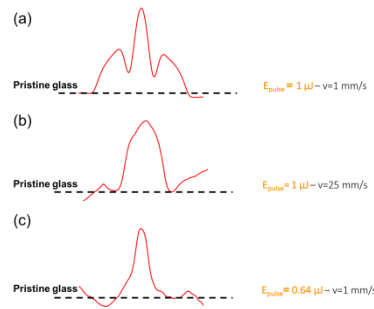


Figure III.5: Optical Path Difference (OPD) of the waveguide written in the same conditions ($E_p=1\mu\text{J}$ - $v=1\text{mm/s}$) in (orange) silver containing zinc phosphate glass (PZnAg2) and (black) non-containing silver zinc phosphate glass (PZn)..... 133

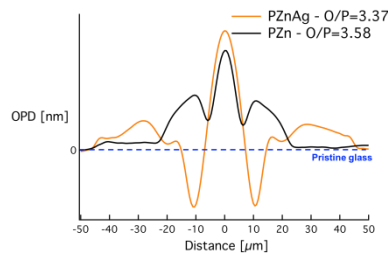


Figure III.6: Top view white light illumination (a.i) for *type I* waveguide, (b.i) for typical *type A* waveguide. Top view fluorescence (a.ii) for *type I* waveguide, (b.ii) for typical *type A* waveguide. Side view white light illumination (a.iii) for *type I* waveguide, (b.iii) for typical *type A* waveguide. Side view fluorescence image of (a.iv) for *type I* waveguide, (b.iv) for typical *type A* waveguide. 135

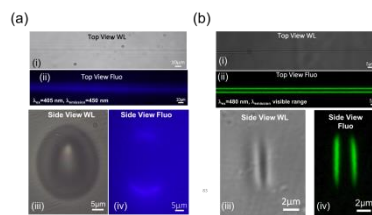


Figure III.7 Top view phase image of (a.i) *type I* waveguide, (b.i) *type A* waveguide. Refractive index profile of (a.ii) *type I* waveguide exhibiting one single positive Δn peak. Inset: side view of the *type I* waveguide under white light illumination. (b.ii) *Type A* waveguide exhibiting two positive Δn peaks. DLW conditions for *type I*: ($E_p=0.65\mu\text{J}$ - $v=5\text{mm/s}$ - $\tau_{rep}=250\text{ kHz}$ - $\text{NA}=0.55$ - $160\mu\text{m}$ below the surface), *type A* ($E_p=43\text{nJ}$ - $v=60\mu\text{m/s}$ - $\tau_{rep}=9.8\text{MHz}$ - $\text{NA}=0.75$ - $160\mu\text{m}$ below the surface). 136

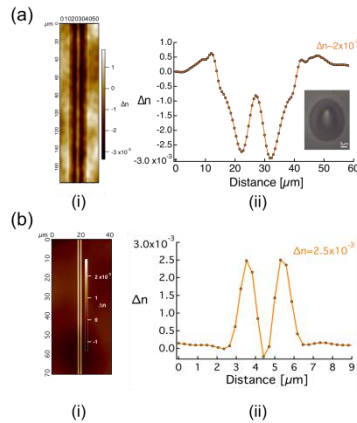


Figure III.8: Near-field mode profile following the injection of a 630nm laser for (a.i) *Type I* waveguide (b.i) *Type A* waveguide. Normalized horizontal intensity of (a.ii) *type I* waveguide (b.ii) *type A* waveguide. Normalized vertical intensity of (a.iii) *type I* waveguide (b.iii) *type A* waveguide. DLW conditions for *type I*: ($E_p=0.65\mu\text{J}$ - $v=5\text{mm/s}$ - $\tau_{rep}=250\text{ kHz}$ - $\text{NA}=0.55$ - $160\mu\text{m}$ below the surface), *Type A* ($E_p=43\text{nJ}$ - $v=60\mu\text{m/s}$ - $\tau_{rep}=9.8\text{MHz}$ - $\text{NA}=0.75$ - $160\mu\text{m}$ below the surface). 138

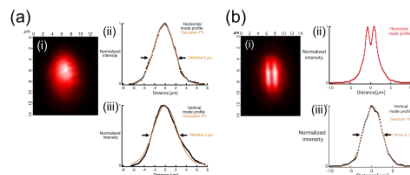


Figure III.9: Optical path difference (OPD) profiles as a function of (a) laser irradiance (b) writing speed. The *type A* Δn is always positive no matter what the laser conditions are. Pulse energies: $30\text{ nJ} \rightarrow 50\text{ nJ}$ 139

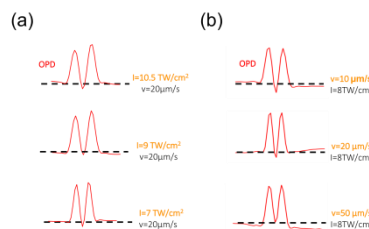


Figure III.10: Side view of a *type I* waveguide exhibiting negative Δn (a) under white light illumination; (b) fluorescence image under blue excitation and emission in the visible range; (c) guided mode profile following laser injection at 630 nm. The dashed lines indicates the location of the waveguide. A small portion of light is guided on the side of the waveguide. (d) Refractive index change profile of the waveguide exhibiting a negative one. DLW parameters: 0.65 μ J-25mm/s..... 141

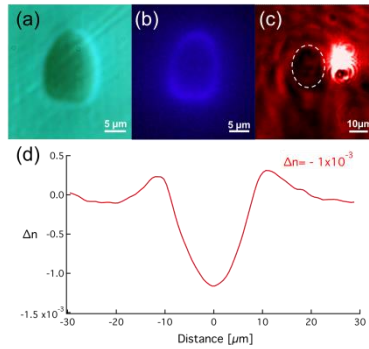


Figure III.11: Laser parameters for both lasers: (orange) T-pulse 200 which induces *type A* modification (blue) Ti:Sapphire which induces *type I* modification (a) laser fluence, (b) laser irradiance, (c) calculated laser dose deposited as a function of the writing speed. 143

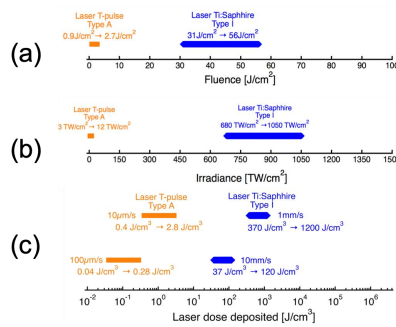


Figure III.12: Different types of modification classifications as a function of a progressive scale of the laser fluence. The introduction of the new *type A* modification sits below the standard well known *type I* modification. 144



Figure IV.1: Simulations of the confinement factor Γ as a function of the V parameter of the fiber for an LP_{01} mode. The confinement of the mode increases as the V parameter increases. 153

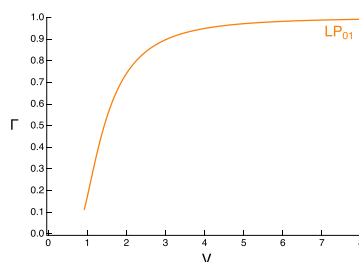


Figure IV.2: Schematic presentation of an evanescent wave based sensor. 154

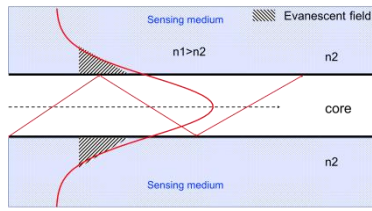


Figure IV.3: Schematic presentation of the sensor. Taken from [182]. 155

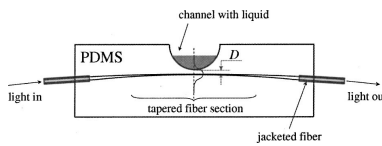


Figure IV.4: Variation of the optical transmission for different refractive index liquids for taper thickness of (1) $\sim 1.6 \mu\text{m}$ (2) $\sim 700 \text{ nm}$. Taken from [182]. 156

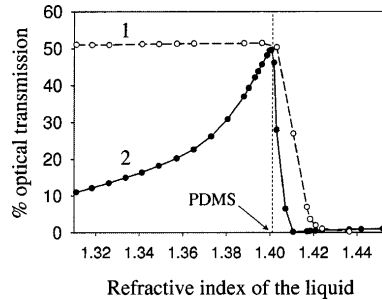


Figure IV.5: (a) Transverse cut of the plastic fiber. (b) Top view of the polished section. (c) Side view of the polished section. Due to the mismatch between the refractive index liquids and the fiber core, part of the beam is lost (2) by refraction in the sensing zone (3) guided by internal reflection. Taken from [183]. 156

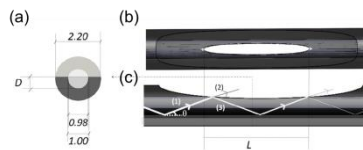


Figure IV.6: Experimental and theoretical normalized transmission output as a function of the refractive index liquids. Taken from [183]. 159

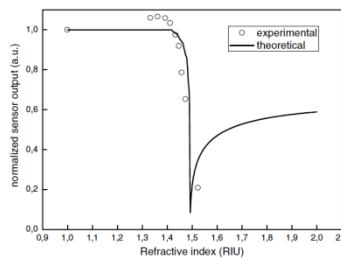


Figure IV.7: Schematic presentation of the refractive index (RI) sensor. Inset: Sketch of the optical rays in the sensing region. The refracted light represented in a dashed line only occurs when the RI of the liquid is higher than the RI of the cladding. Taken from [169].

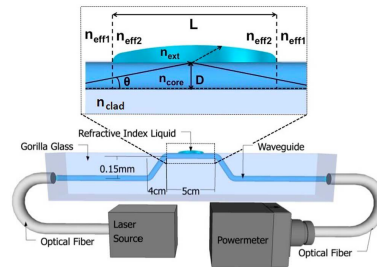


Figure IV.8: Experimental and simulated normalized transmitted powers as a function of the refractive index of the liquids. The previous model of Bilro et al [183] is represented with a dashed line. Inset: Comparison between Lapointe’s model [169] and Bilro’s model [183]. Taken from [169].

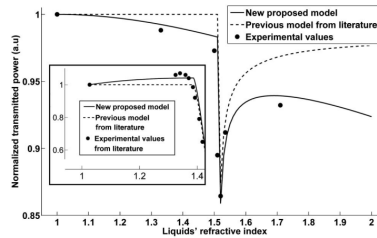


Figure IV.9: Side view of (a) (b) the near-surface waveguides written in soda lime glass. (d) Gorilla glass. (c) 25µm below the surface. Near field mode profiles of the waveguides in Gorilla glass. (e)(f) 25µm below the surface. (g)(h) Near-surface waveguide. Taken from [71].

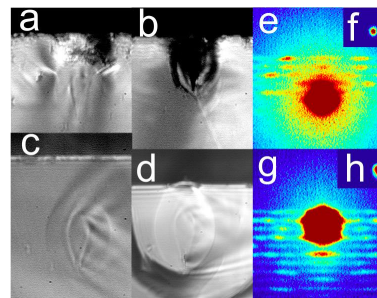


Figure IV.10: Side view of the near surface waveguides using the compensation method compared to waveguides written ~150 µm below the surface without the glass cover in (a) fused silica (b) Eagle. Taken from [91].

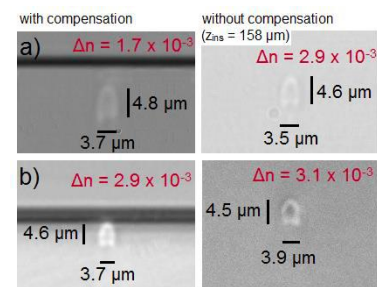


Figure IV.11: (a) Side view of near-surface waveguide using the compensation method and the guided mode profile following laser injection at $\lambda=488$ nm. (b) Fluorescence emission of an aqueous fluorescein solution excited by the evanescent wave of the light guided ($\lambda=488$ nm) in the near-surface waveguide observed through a band pass filter 528/38 (top view) (c) Dark field image of a linear periodic assembly of AG@SiO₂@FITC nanowires (top view) (d) Fluorescence emission of AG@SiO₂@FITC nanowires (top view). Taken from [197].....166

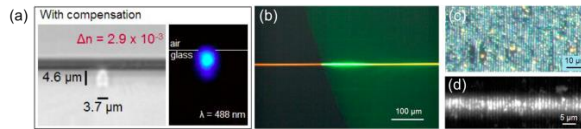


Figure IV.12: Sketch of the rising near-surface waveguide.....168



Figure IV.13: Side view under white light illumination of (a) 32 μm straight waveguide (b)(c)(d) rising near-surface waveguides. (e) Top view under white light illumination of a portion of a near-surface waveguide. Smooth modifications where no ablations or mini explosions were observed. DLW parameters: 28 nJ – 50 μm/s.169

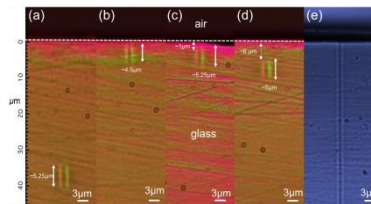


Figure IV.14: (a) Side view of the rising near-surface waveguide NWG1 under white light illumination. (b) Near-field mode profile following the injection of a 660 nm laser. (c) Sketch of the simulation of the waveguide where ~ 1 μm of the waveguide is simulated outside the glass. (d) Simulated mode profile based on the simulations shown in (c). A good match between experimental and simulated modes showing that the mode is confined more towards the glass due to the glass-air interface. 170

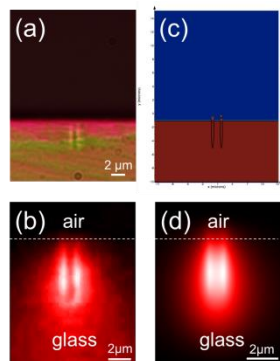


Figure IV.15: (a) Side view of a rising near-surface waveguide under white light illumination. (b) Near-field mode profile following the injection of a 660 nm laser. (c) Sketch of the simulation of the waveguide 2 μm away from the surface. (d) Simulated mode profile based on the simulations shown in (c). A good match between experimental and simulated modes showing that the mode is not affected.
 172

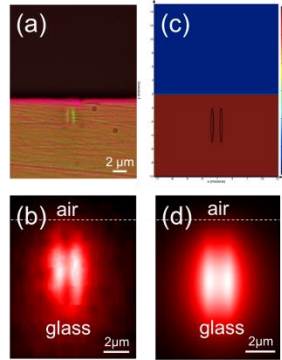


Figure IV.16: (a) Top view phase image of a portion of a waveguide neighboring the surface waveguides exhibiting smooth type A modification. (b) Δn profile extracted from the phase image showing two positive peaks of $\sim 2.4 \times 10^{-3}$. DLW parameters: 28 nJ – 50 $\mu\text{m}/\text{s}$.
 173

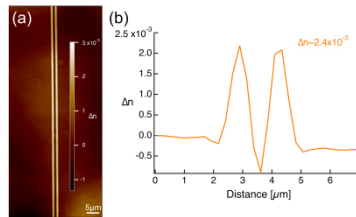


Figure IV.17: Normalized transmission for all written waveguides following the deposition of a ~ 4 mm droplet of 1.604 Cargile oil. No interaction was observed after 7 μm spacing between the waveguide and the surface. Inset: Near-field mode profile of the most sensitive waveguide at ~ 2 μm below the surface. DLW parameters: 28 nJ – 50 $\mu\text{m}/\text{s}$.
 175

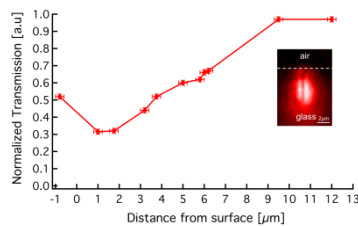


Figure IV.18: Normalized transmission as a function of the size of the droplet of a 1.604 Cargille oil for two waveguides with different distances from the glass surface. The larger the droplet the higher the losses in transmission. 176

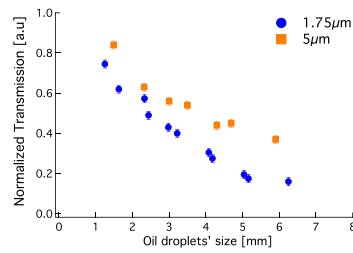


Figure IV.19: Normalized transmission as a function of different refractive index (RI) Cargille oils deposited on the glass surface for four different waveguides at different depths from the surface. DLW parameters: 28 nJ – 50 μm/s. 178

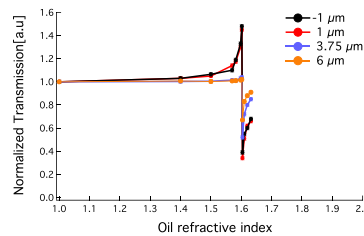


Figure IV.20: Experimental (full line) and simulations (dashed lines) for two different near surface waveguides at different distances from the surface. A good match between the experiment and the simulations. 180

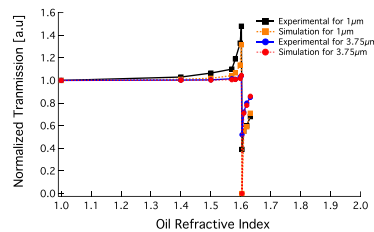
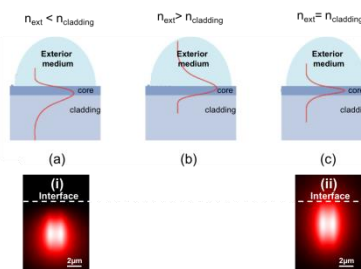


Figure IV.21: Sketch of the evanescent wave/mode profile inside a near-surface waveguide for a refractive index (RI). (a) Lower than the cladding/glass; (b) higher than the cladding/glass; (c) equal to the cladding/glass. Inspired from [200]. Simulated mode profile for a (a.i) glass-air interface; (c.ii) glass-oil interface with a refractive index of oil matching the glass $n_{ext} \sim n_{glass}$ 181



List of Abbreviations

DLW	Direct Laser Writing
CELIA	CENtre des Lasers Intenses et ses Applications
ICMCB	Institut de chimie de la matière condensée à Bordeaux
COPL	Centre d'optique, photonique et laser
SLAM	Short Laser Pulses: Applications & Materials
NPs	Nanoparticles
DSC	Differential Scanning Calorimetry
IR	InfraRed
TIR	Total Internal Reflection
VI	Visible
UV	Ultra-Violet
NIR	Near InfraRed
MPI	Multi Photon Ionization
NA	Numerical Aperture
3D	Three Dimensions
2D	Two Dimensions
Δn	Refractive Index Change
SLM	Spatial Light Modulator
DWC	Depressed Waveguide Cladding
WG	Waveguide
WBG	Waveguide Bragg Grating
PbP	Point by Point
WGL	Waveguide Laser
DFB	Distributed Feedback
PL	Photonic Lantern
MM	Multimode
SM	Single Mode
AOM	Acousto-Optic Modulator
OPD	Optical Path Difference
QWLSI	Quadri-Wave Lateral Shearing Interferometry
DHM	Digital Holographic Microscopy
TIE	Transport Of Intensity
HRSEM	High Resolution Scanning Electron Microscopy
AFM	Atomic Force Microscopy
FWHM	Full Width Half Maximum
EFISHG	Electric Field Induced Second Harmonic Generation
LPG	Long Period Grating
FBG	Fiber Bragg Grating
RI	Refractive Index
WL	White Light

Fall Down 7 times ... Get up 8

Acknowledgment

This PhD has been completed between two labs in two different countries, France and Canada. These labs collaborating together under the umbrella of the Laboratoire International Associé (LIA) LUMAQ (Lumière Matière Aquitaine Québec). I would like to thank the directors of LUMAQ Thierry Cardinal and Younès Messaddeq as well as of the Centre des Lasers Intenses et ses Applications (CELIA), Philippe Balcou and Eric Mevel and the director of the Centre d'Optique, Photonique et Laser, Réal Vallée for accepting me as a member of their great labs.

I would like to thank also, Dr. Bertrand Poumellec, Dr. Shane Eaton, Prof Younès Messaddeq and Dr. Mathieu Bellec for accepting to take part in my PhD jury. It was an honor for me.

To my PhD supervisors, Prof. Lionel Canioni, Prof. Réal Vallée and Dr. Yannick Petit, special thanks for choosing me for this PhD. Thank you for your support, understanding and help during the most difficult time of the PhD. Prof. Lionel Canioni, you were a real mentor during my PhD and also my personal life. I really appreciated all the discussions we had, related or not related to the PhD project. Thank you for the huge amount of trust you put in me. I also enjoyed travelling to several conferences with you. I am grateful for your contribution in teaching me new things and introducing me to the scientific community. Prof. Réal Vallée, I have always admired your way of engaging me in lab meetings so I could give more, work more and get better results. Yes, you are a picky person in science but I love that because I think it is a good quality for a scientist and it made me a better scientist. It was a pleasure to work for you, in your lab. Dr. Yannick Petit thank you for your friendly reception and the friendly environment you created during the course of the PhD. Thank you for following all of my work and for your constructive, critical remarks and observations. I learned a lot from you.

I also wish to thank all my colleagues in the SLAM group and COPL. Thank you all for your help and the good times we spent together. Being a part of the SLAM group is like being a part of a family and I really liked this atmosphere. Thank you to the SLAM (ex) colleagues/friends, EungJang Lee, Marie Vangheluwe, Brice Mutelet, Allu Amarnath Reddy, Arthur Le Camus, Sophie Rouzet, Délphine Syvilay, Wendwesen Gebremichael (Wendey), Laura Loi, Inka Mannek-Honninger and Bruno Bousquet. Thank you all for the great atmosphere we had in the lab and outside the

lab. Also thank you to Arnaud Royon for the interesting discussions about the PhD project. Thank you to my colleagues at ICMCB: Jean-Charles Desmoulin, Alexander Fargues, Sylvain Danto, Téa Skopak and Thierry Cardinal. Thank you to Jean-Charles Desmoulin and Sylvain Danto for providing glass samples, otherwise my project would not have been possible. Thank you for enduring my special demands! Téa Skopak, thank you for the discussions we had and for the time we spent talking. Special thanks and appreciation to Thierry Cardinal for all the financial support for my travels to Canada. Thanks also to my (ex) colleagues in COPL for the warm welcome and friendly environment: Mathieu Boivin, Cheikou Ba, Souleymane Toubou Bah, Frédéric Jobin, Frédéric Maes, JC Gauthier, Laurent Dusablon, Simon Duval, Yigit Ozan Aydin, Clément Frayssinous and Feng Liang. Thank you to Denis Boudreau, Alex Grégoire, Victor Azzi for the help and letting me use their equipment. Thank you also to Yannick Ledemi and Sandra Messadeq for the help. I would like to thank also Tigran Galstian for accepting me to assist him in his lab course. It gave me a great experience. Special thanks to Marc D'Auteuil, Stéphane Gagnon, David Hélie, Martin Blouin, Vincent Fortin and Diane Déziel. Marc, thank you for all you help in mounting my setups and finding the tools. I really appreciated the volleyball discussions we used to have. Stéphane, Stéphane... I asked you a lot of difficult and tricky tasks to do with my glasses during my PhD so thank you a lot for your help. Without your help and skills, it would have been nearly impossible for me to do it by my own. David and Diane, thank you a lot for the help provided for me before my arrival and to facilitate my arrival. Moreover, your friendly welcome is amazing and really appreciated. David thank you for the Québécois cultural introduction during the sugar shack. Martin Bernier, thank you for the warm welcome and the reputation you gave me at COPL (don't ask about it). It was really a pleasure to get to know you in Rochester and dance, to interact with you in and outside the lab (on my farewell party). Thank you! Julien, it was a pleasure playing volleyball with you, I really enjoyed it. Now the two brothers I had at COPL, JP Bérubé and Jérôme Lapointe. Guys!!! It was really a pleasure to work with you and go out together for beer and pool. Jay (Jérôme), I will miss having a beer with you buddy, working late together at night and our paths crossing late in the lab. JP, thank you for answering all my emails almost every day for almost 2 years, following my daily work, giving advice and helping me with my work. Thank you for enduring my persisting character and correcting my papers/abstracts. I hope you are not bored now that I am not around anymore.

Also thank you to Céline, Sophie, Sonia, Cinthia, Michelle, Caroline and Carole from both universities for all the administrative help that you provided.

Of course, I would like to thank my funding sponsors, the French National Research Agency (ANR), "Investments for the Future" Idex program for the mobility grant, LAPHIA for funding the contract extension. From the Canadian side, I would like to thank the Natural Sciences and Engineering Research Council of Canada (NSERC) (CG101779), Canada Foundation for Innovation (CFI) (GF072345), and Fonds de Recherche du Québec-Nature et Technologies (FQRNT) (FT097991, CO201310) for their funding and for the equipment bought and used during this project.

On a personal note, I would like to dedicate this PhD to my parents. I would like to thank my friends from France and Canada who supported and helped me during this PhD: Christelle, Georges, Jean-Baptiste, Clément, Linh, Diaa. To the close friends, Vittorio, Jack and Georges thank you. Vittorio, I will miss our trips together man. Arthur Bagramyan: Thank you for having me as your friend and being like family in Québec. We had awesome memories together. And Joyce, it was a pleasure meeting you from the first day I arrived to the lab and I am lucky to have you as a friend. That's enough for you. A person who stood by me, he calls himself "the sun", thank you very much. You helped a lot. I appreciate it.

General Introduction

Laser-matter interaction has challenged the scientific communities since the discovery of the laser in the 1960s. Research and development through the past years led to almost a limitless number of industrial and medical laser-based applications. Ranging from laser cleaning, cutting, welding, marking to laser-eye surgery, ablating cancer tumours, medical imaging, the laser provides a versatile and non-replaceable tool in both the industrial and medical fields. More specifically, laser-glass interaction has been extensively studied during the last two decades. The process of focusing femtosecond lasers inside glasses in order to change the physical-chemical properties of the glass is called Direct Laser Writing (DLW). DLW technique provides fast direct three-dimensional (3D) structuration of the glass allowing the creation of 3D optical components embedded inside transparent materials. It exhibits many advantages compared to the lithography technique which is limited to the two-dimensional (2D) structuring of materials and involve many steps, making DLW highly compatible with industrial manufacturing. Many applications could be based on the DLW technique such as the creation of miniaturized sensors and/or photonic components on glass chips. Indeed, for example, the DLW technique in glasses has led to the creation of Modular Photonics a company based in Australia selling glass based micro-chips processed by the DLW technique used for mode-selective applications, more specifically for astronomical needs.

This PhD was performed in a joint collaboration between University of Bordeaux, France and Université Laval in Québec, Canada in the framework of the Laboratoire International Associé (LIA) LUMAQ (Lumière Matière Aquitaine Québec). More specifically, it was carried out between three labs: Centre des Lasers Intenses et ses Applications (CELIA) and Institute of Chemistry of the Condensed Matter of Bordeaux (ICMCB) at University of Bordeaux, France and Centre d'Optique, Photonique et Laser (COPL) at Université Laval, Québec, Canada. It consisted in spending almost half the time of the PhD at each university while working on the same project which is a continuity of research activities conducted in the "Shortpulse Lasers: Applications and Materials" (SLAM) research group of my supervisor Lionel Canioni and the group "Chimie et photonique des matériaux oxide de fluore", supervised by Thierry Cardinal at ICMCB. Previous work was based on optimizing and mastering the silver containing zinc phosphate glasses synthesis, investigating and understanding the exotic laser-glass process following DLW. Those activities led to the creation of "Argolight", a spin-off company selling laser

structured glass slides allowing the fluorescence calibration of microscopes. Furthermore, NASA used one of Argolight's products to equip the International Space Station microscope for the SpaceX SPX CRS 11 – Falcon 9.

While the previous works of the group on silver containing zinc phosphate glasses were mostly based on the investigation of the laser-glass response, this PhD project aims at creating and functionalizing of new type of optical components based on the creation of fluorescent silver clusters. In fact, silver containing zinc phosphate glasses are special and exotic glasses compared to the standard glasses used for DLW by the scientific community. The incorporation of silver ions inside the glass matrix allows exotic responses from the glass following DLW i.e. creation of silver clusters exhibiting properties such as fluorescence, nonlinearity and plasmon resonance. In particular, the project intends to create new types of optical components with properties that were not accessible in previous standard glasses.

The first part of the project explains the standard laser-glass interaction that is mainly known by the scientific community as well as the state of the art of some optical components manufactured in glasses. Next, the exotic response of silver containing glasses following DLW is presented in detail with a theoretical model. The creation of a new type of waveguides and optical components in silver containing glasses are presented in detail. The second part consists in functionalizing the new type of waveguides and the creation of a refractive index sensor inside silver containing glasses.

More specifically, the first chapter of the project consists in introducing the glass and laser and presenting their history. The main laser-glass interaction processes are also explained in this chapter.

The second chapter is the main part of this manuscript. It takes into account the different types of modifications induced in glasses following DLW as well as a review of some previous works. Then, silver containing zinc phosphate glasses are introduced as well as the exotic laser-glass interaction they produce. Finally, the design, fabrication and characterization of optical components are presented in this chapter.

The third chapter consists of a comparison between the standard *type I* modification and the new *type A* modification reported in this manuscript. The

comparison takes into consideration the morphology, the refractive index changes and the near-field guided mode profile.

The fourth and last chapter consists in introducing the writing of near-surface waveguides that do not require any additional process as well as a presentation of a pioneer refractive index sensor exhibiting the advantages of *type A* modification.

Table of contents:

I. General background on glass and laser-matter interaction	7
I.1 Introduction	7
I.2 Glass	8
I.2.1 Glass history	8
I.2.2 Definition of glass	8
I.2.2.a Glass transition.....	9
I.2.2.b Thermodynamic aspect.....	10
I.2.3 Glass formation	12
I.2.3.a Optical properties: Transparency window	13
I.2.4 Glass making.....	15
I.2.4.a Lab technique.....	15
I.2.5 Introduction to fiber optics	16
I.3 The laser	17
I.3.1 Definition of laser.....	18
I.3.2 Gaussian beam	21
I.3.3 Laser-material interaction.....	24
I.3.3.a Non-linear absorption mechanisms in glasses	24
I.3.3.b Time scale	28
I.3.4 Effects of laser parameters	29
I.4 Conclusion	36

Chapter I

General background on glass and laser-matter interaction

I.1. Introduction

Laser-matter interaction is a broad research area with loosely defined boundaries. The laser is used to interact with different types of matter going from biological tissues, up to metals, dielectrics, plastics. It has become an essential tool in medical and industrial fields. In order to develop such effective and robust industrial tools, the study of the laser-matter process is prerequisite. The understanding of the effect of the laser on the matter and the physical-chemical phenomena that occur during this interaction is mandatory. Every material interacts with the laser irradiation in a specific way from the other. In this chapter, we will start by presenting glass material used in this work by walking through its history, the definition, the fabrication process and some other properties while the second part will introduce the history of the laser and its functionality.

Finally, the last part highlights the interaction between femtosecond lasers and glasses. This interaction highly depends on the type of laser used as well as on the glass properties. The different physical phenomena that occur following the interaction of femtosecond lasers with glasses will be presented in detail in order to understand the core of the laser-glass interaction.

I.2. Glass

I.2.1. Glass history

The oldest records of glass making are some clay tablets dating from around 650 BC. They were not completely understandable as no dictionaries exist explaining the technical terms used back then (inspired from [1]). However, the oldest documented glass making record was around 1673-1676 by Ravenscroft. Then in AD 1612, Antonio Neri's book "L'arte Vetraria", appeared. It was the most influential one compared to other books. But still, this book contained recipes more than science due to the limited developments in chemistry. At that time, glass makers did not have the quality control on their powder materials. They probably depended on the taste of their powders given that sodium and potassium salts have different tastes as do carbonate chloride, sulphate and nitrate for example. Moreover, one should not forget the problems they had with furnaces. How to build one, how to maintain high temperature, how to control it and measure it. Nowadays, many industrial glass companies exist such as Corning, Saint-Gobain, Pilkington, Asahi Glass Co, etc. and they master the art of glass making.

I.2.2. Definition of glass

Many definitions have been proposed by scientists over the last two decades. In 1990, Elliot suggests that glasses are materials that do not present a long distance of atom periodicity like crystals and are an amorphous solid exhibiting a glass transition [2]. Zarzycki said that a glass is a non-crystalline solid exhibiting the phenomena of glass transition [1]. The glass is a solid presenting a structure of a liquid, non-crystalline solid or simply amorphous solid taking into consideration the atom disorder based on X-ray diffraction [3]. Finally, Shelby in 1997 said that the glass is an amorphous solid with the absence of atomic order at long distance while exhibiting a glass transition zone. Every material, inorganic, organic or metal formed by any technique presenting a glass transition is a glass [4]. So eventually, we can describe the glass as a super cooled liquid in a metastable condition exhibiting a glass transition region with atomic disorder. Compared to the atomic structure of crystals (Figure I.1.a), glass exhibits a non-organized atomic structure (Figure I.1.b). Nowadays, we have many categories of glasses: oxide glasses, metallic glasses, fluorinated glasses, chalcogenide glasses and organic glasses. In this project, we will be working on oxide glasses, more specifically zinc phosphate glasses.

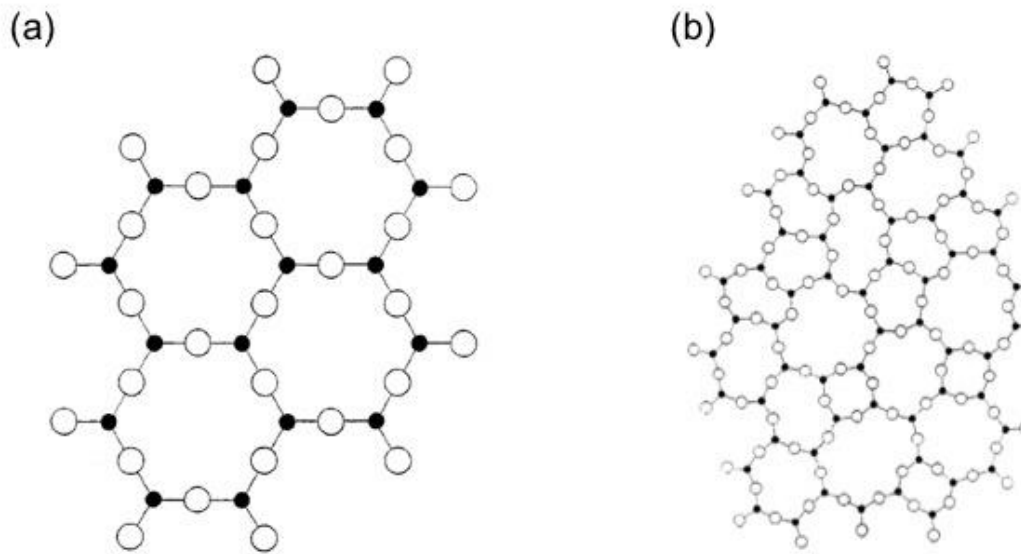


Figure I.1: The atomic arrangement of a Al_2O_3 lattice of a (a) crystal (b) glass. The crystal exhibits atomic order compared to the disorder exhibited by the glass compound [5].

I.2.2.a. Glass transition

Earlier in this manuscript, the glass was defined as an amorphous solid exhibiting a glass transition phase. So, what is a glass transition phase? When a liquid is cooled below the melting temperature (T_L) it enters the state of metastable liquid. Below T_L , two options are possible: The cooled liquid could form a crystal or it could form a glass. If the thermodynamic barrier to nucleation occurs, the volume of the system sustains a drastic discontinuity of the volume ΔV and a crystal is formed as shown in Figure I.2. However, in the case of absence of nucleation, the liquid remains in a metastable equilibrium below T_L with the same thermal contraction coefficient, without drastic change of the system's volume. At a lower temperature than T_L , the atomic mobility decreases and the atoms end up by being trapped in fixed positions. This occurs over a range of a temperature called the glass transition region and then the glass starts to form. Generally, the glass transition temperature (T_g) is the intersection of the extrapolated lines from the glass and metastable liquid ranges Figure I.2.

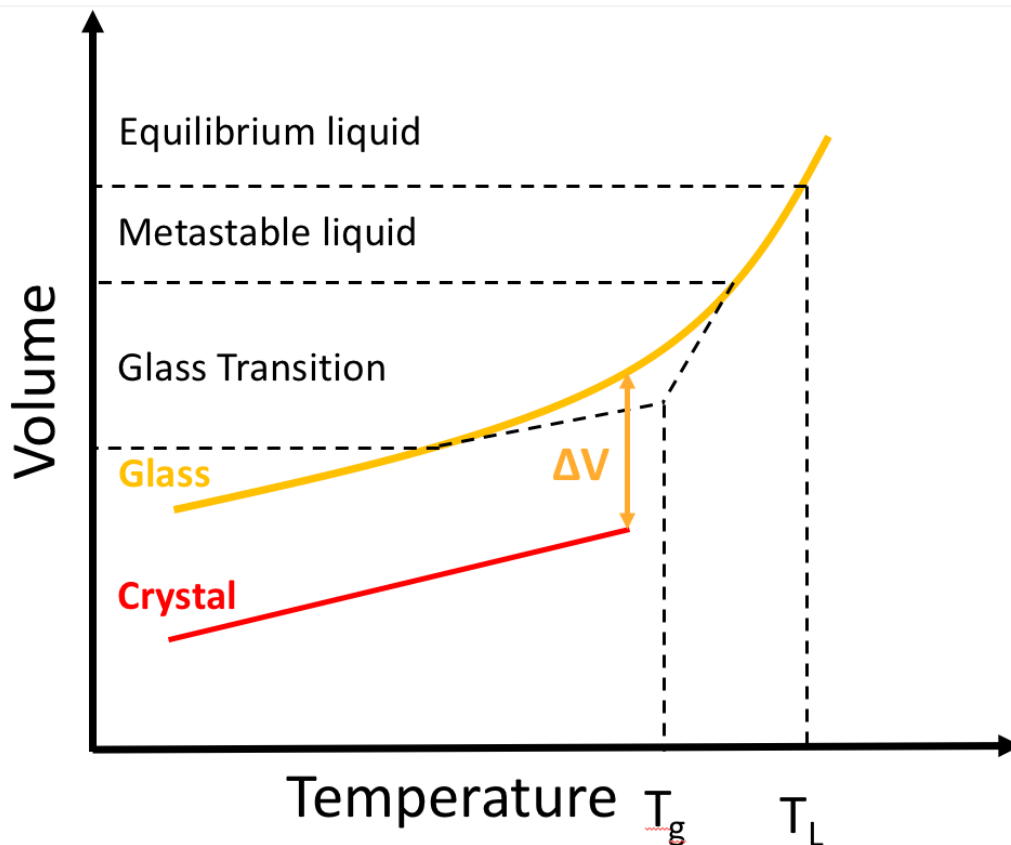


Figure I.2: Volume variation as a function of the temperature while cooling a liquid to form a crystal or a glass. Adapted from [1].

I.2.2.b. Thermodynamic aspect

Is the glass transition a phase transition? In order to answer this question, we will look into the thermodynamic aspects of the glass formation and the Kauzmann paradox [1]. But first let us introduce the entropy notion. The entropy (S) defines the disorder in the system. For instance, as mentioned before in section I.2.2, the crystal exhibits an organized atomic structure on a large scale, therefore the disorder is minimum implying a low entropy. However, for the glass, the atomic disorder is much greater, therefore we have a higher entropy than the crystal.

Let's consider again a hot liquid being cooled down to form a glass or a crystal. Kauzmann in 1948, noted that the configuration entropy of an equilibrium liquid decreases as a function of the temperature that if extrapolated below the temperature T_K , it would fall below the crystal entropy (Figure I.3). That was not acceptable given that it does not fit with the third law of thermodynamics which states that the entropy of a crystal must be null at a temperature of 0K ($S=0 \rightarrow$

$T=0K$). This disturbing phenomenon is stopped by a coincidental intervention of the kinetic phenomenon, the glass transition. The entropy freezes at a characteristic value of the equilibrium liquid at T_g as shown in Figure I.3. Moreover, the interval between T_k and T_g is generally quite small. The glass exhibits an entropy at 0K which is not the case for the crystal (Figure I.3). This is the Kauzmann paradox.

Grest and Cohen in 1981 tried to explain the glass transition as a first order phase transition [6], Gibbs and Dimarzio in 1958 suggested a second order phase transition [7] when Stillinger in 1988 proposed that no phase transition was happening [8]. Eventually, Stillinger was right. The glass transition is not a phase transition at all. It does not fulfil the Ehrenfest criteria for first or second order phase transition [9], contrary to the crystal where the cooling process of a liquid to form a crystal is considered as a phase transition from liquid to solid state.

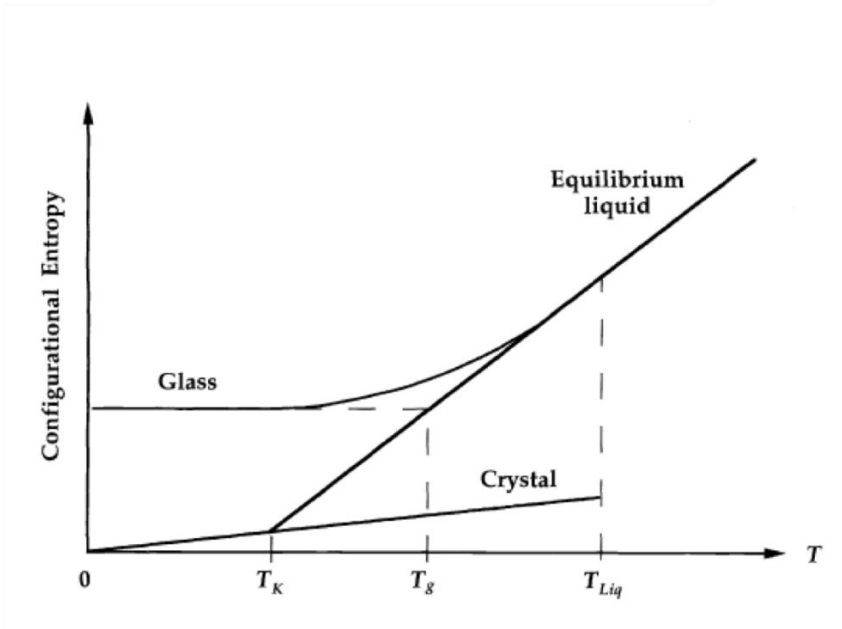


Figure I.3 The configurational entropy as a function of the temperature of the cooling process of an equilibrium liquid. The glass transition freezes the entropy and avoids a thermodynamic catastrophe. This is known as the Kauzmann paradox. Taken from [1]

Given that the glass transition is characterized by a change in the heat capacity ΔC_p , it could be experimentally detected using the Differential Scanning Calorimetry (DSC). Comparing to another reference sample, the DSC output curve allows us to see the glass transition i.e. the differential heat capacity therefore detecting the glass transition temperature T_g . A DSC curve is shown in Figure I.4. The T_g can be

detected when the step change in heat capacity attains half the value of the total step change [10] (Figure I.4). Moreover, the DSC curve allows the detection of the temperature where the crystallisation effect starts at T_x and the peak of crystallisation at T_c . One should note that the T_g highly depends on the glass composition and its viscosity in the liquid state. Finally, in order to correctly measure T_g we should start by cooling the equilibrium state i.e. cooling the liquid [10].

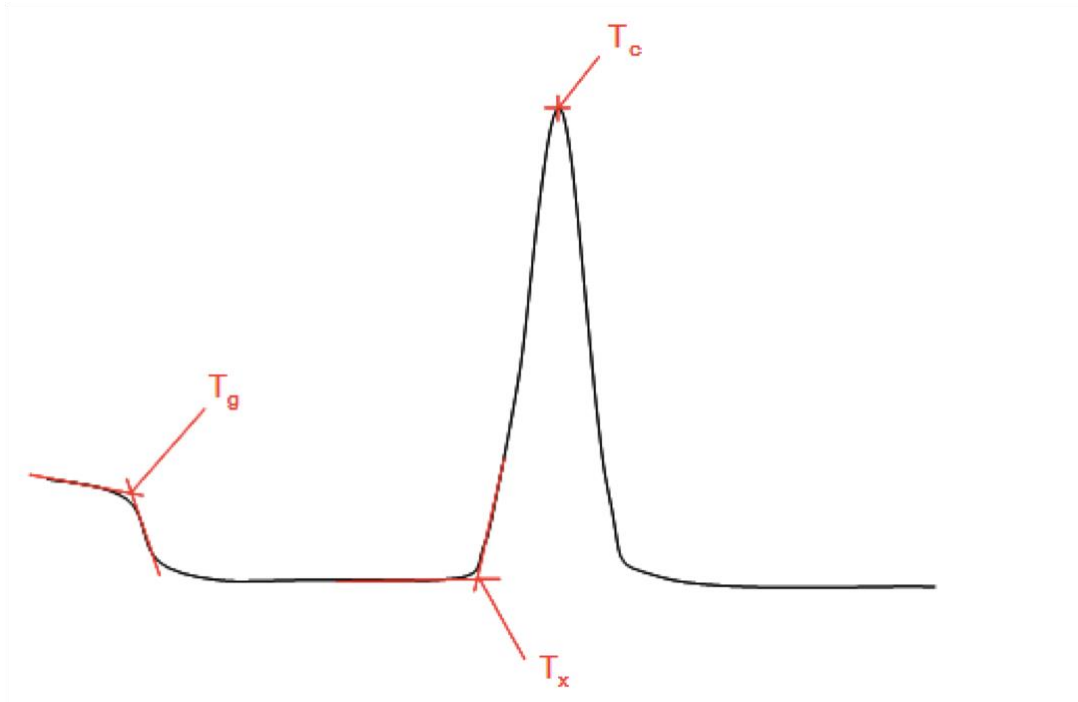


Figure I.4 Possible Differential Scanning Calorimetry (DSC) curve of a cooled liquid. T_g is the glass transition temperature, T_x the temperature of formation of the first crystal, and T_c the crystallisation temperature. The DSC curve taken from [11].

I.2.3. Glass formation

After chemistry and physical chemistry were developed over the years, scientists started proposing criteria and formulas about glass formation instead of recipes based on tasting their powders to form glass. More specifically, in 1926 scientists proposed criteria for glass formation that may be applicable in some cases. This subject will not be discussed in detail in this manuscript. If readers are interested in this part, they may refer to the following readings [5, 12-15].

We will be interested only in oxide glasses since the glasses used in this work are oxide ones. In order to form a glass, scientists have classified the oxide glasses in three categories. Glass formers, modifiers and intermediates [5, 14].

Glassformers constitute the bone of the glass i.e. the main lattice and can usually form a glass with ordinary lab techniques (melt-quenching). Examples are Ba₂O₃, SiO₂, GeO₂, P₂O₅, As₂O₅ etc. Normally these types of glasses exhibit a high melting temperature. Therefore glass modifiers are added in order to lower it. *Modifiers* do not form glass under normal conditions and are usually added to the glass to weaken the glass [14]. Examples of glass modifiers are Na₂O, CaO or K₂O. *Intermediates* usually play a role between glassformers and modifiers. However, they cannot make a glass by themselves. Examples of intermediate glass constituents are: Al₂O₃, ZnO, Ga₂O₃, TiO₂.

I.2.3.a. Optical properties: Transparency window

The optical properties of a glass depend on the elements forming this glass, in other words the cations and ions used to form the glass. The optical transparency for glasses is directly linked to the absorption of the glass for different wavelengths (this part inspired by [1]). Let's consider an incident light passing through a bulk glass. A quantity of light will be reflected, scattered, absorbed and the rest will be transmitted (Figure I.5). The coefficient of absorption is given by the Lambert-beer law as:

$$I = I_0 e^{(-\alpha l)} \quad (I-1)$$

where I is the light transmitted, I_0 the initial incident light, α is the absorption coefficient while l is the length of the sample as shown in Figure I.5. So, from (I-1) we can express the absorption coefficient as:

$$\alpha = -\frac{1}{l} \ln\left(\frac{I}{I_0}\right) \quad (I-2)$$

Based on the transmission of the glass, the absorption coefficient could be calculated using (I-2). It is recommended to represent the absorption of the glass using the absorption coefficient in cm⁻¹ or dB/cm and not the transmission percentage. This gives more quantitative data about the transmission of the glass.

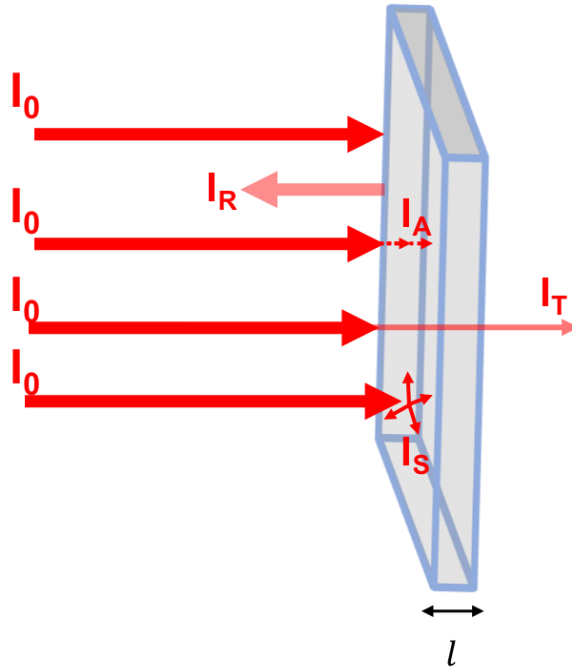


Figure I.5 : Schematic presentation of an incident light on a glass sample. I_0 is the incident light, I_R the reflected light, I_A the light absorbed, I_T the transmitted light and I_S the scattered light.

The reflected light of one facet of a glass is known as the Fresnel reflection. The percentage of reflected light depends on the refractive index change of the material. For example, silver containing zinc phosphate glass used in this work with a refractive index change of $n \sim 1.6$, Fresnel reflection is calculated to be around 5% using the following formula:

$$R = \left(\frac{n_1 - n_2}{n_1 + n_2} \right)^2 \quad (\text{I-3})$$

where n_2 in this case is the glass refractive index and n_1 is equal to 1 which is the refractive index of the air.

As mentioned before, the transparency window of the glass depends on its composition and the choice of glass network former and modifier molecules. Generally, standard oxide glasses exhibit a high transmission in the visible range and NIR but high absorption in the UV (Figure I.6). However, other type of glasses can exhibit a high transmission in the Infrared (IR) region and low transmission in the VIS such as chalcogenide [16]. Generally, the absorption in the UV range is linked to electronic transitions due to the absorption of an electron in the valence

band to be promoted in the conduction band. However, the absorption in the IR is linked to the molecular vibrations at this wavelength and the phonon energy [9].

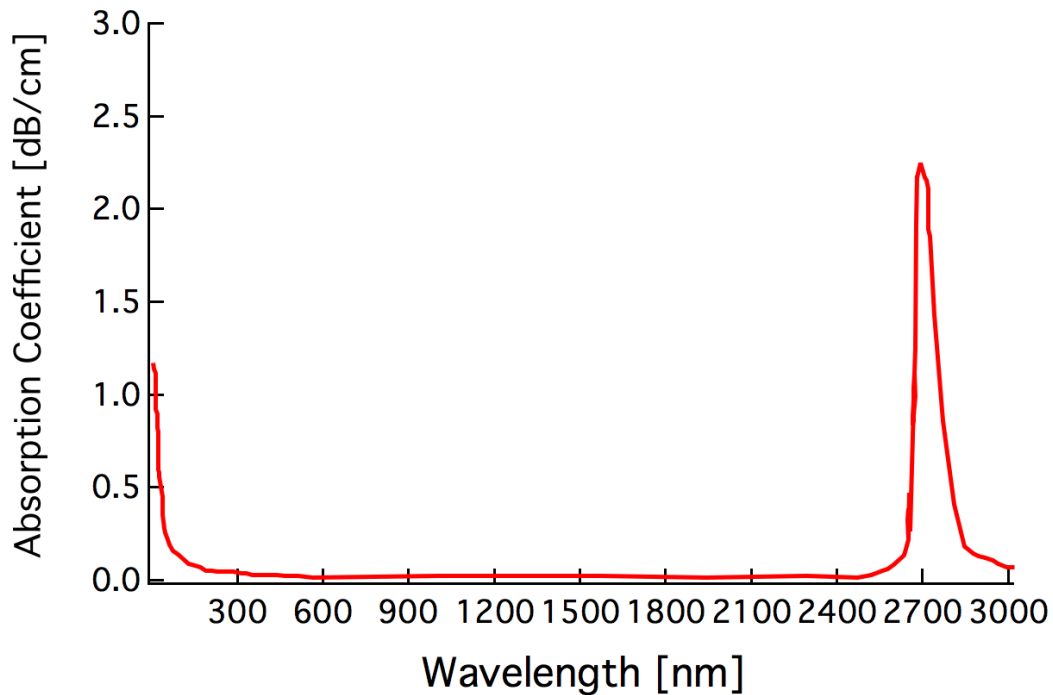


Figure I.6: Absorption spectrum of a Silica glass in the visible and near infrared region. A high transmission is shown in the visible range.

I.2.4. Glass making

Making glasses could be performed by many techniques. It could be formed from plasma (evaporation), from liquid (quenching technique, sol-gel) or from solids (decomposition) [9]. In this framework, we will be interested in the melt-quenching technique which is used to form the glass. Two methods of melt-quenching techniques exist. The first one is the float glass which is an industrial technique used for the creation of large quantities of glass (which is not going to be presented herein) and the lab technique which is more of a “homemade” technique.

I.2.4.a. Lab technique

The lab technique used at ICMCB to make silver containing glasses is the melt-quenching technique shown in Figure I.7. It starts by choosing and weighing the corresponding mix of powders to form the glass. Then the powders are placed in a platinum crucible where they will be heated up to the melting temperature T_L (1200°C) in a furnace during 12h. At that temperature, the mixed powders will be

transformed into melted liquid (Figure I.7). Then the crucible is removed from the furnace and quenched rapidly to form glass and to avoid any crystallisation process. When rapidly quenching the liquid, the atoms do not have time to get into order and crystallize. One should note that the quenching method is performed manually; therefore the cooling process of the glass is not the same. It differs from one batch to another, from person to person. Eventually, one should note that the glass properties may differ from one glass batch to another. Afterwards, the glass is annealed at $40\text{ }^{\circ}\text{C}$ below the glass transition T_g for at least 4h to relax the accumulated mechanical constraints. Finally, after the annealing process the glass is removed from the furnace and allowed to rest at room temperature waiting to be cut and polished.

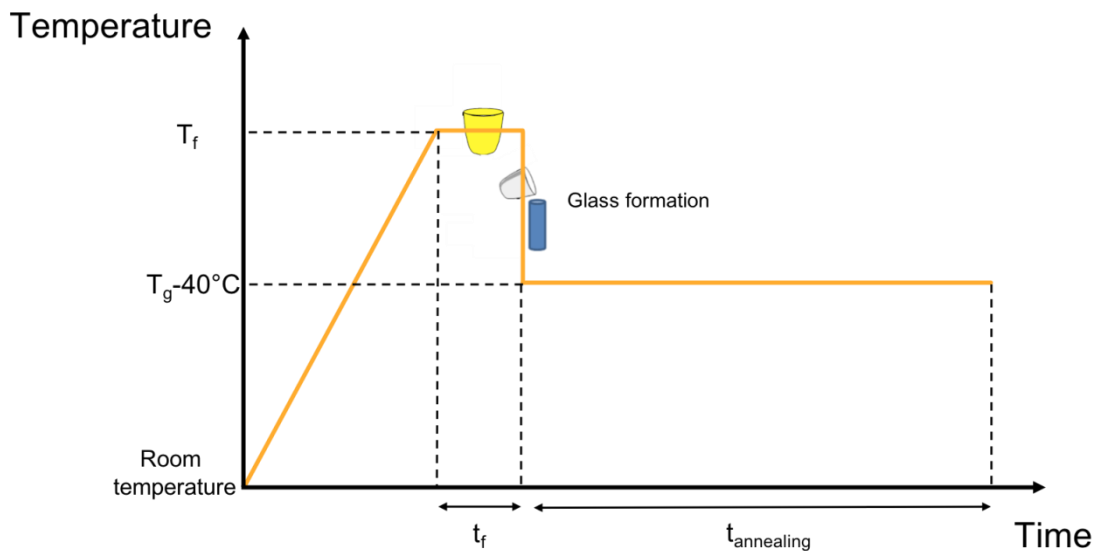


Figure I.7: Schematic representation of the melting-quenching process.

I.2.5. Introduction to fiber optics

The previous part consisted in talking about the fabrication of bulk glasses. In this part, we will introduce fiber optics. Bulk glasses can be shaped into fibers forming a thin glass wire that we call an optical fiber where light can propagate inside based on Total Internal Reflection (TIR). Optical fiber is generally formed in a cylindrical shape and made with low loss material such as fused silica glass. It has a centre core in which light is guided because of TIR, and is embedded in an outer cladding of slightly lower refractive index as shown in Figure I.8. Fiber optics is responsible for most of our communication systems and internet. Thousands of kilometers of

optical fiber exist underwater in the world in order to connect the world together using the internet. Optical fiber exhibits many advantages for light/information transportation. It exhibits lower signal attenuation and higher band pass compared to electric wires. This waveguiding process in fiber optics will be discussed furthermore in Chapter II at section II.3.1.a as well as the DLW process in ribbon shaped silver containing fibers in section II.6.5.

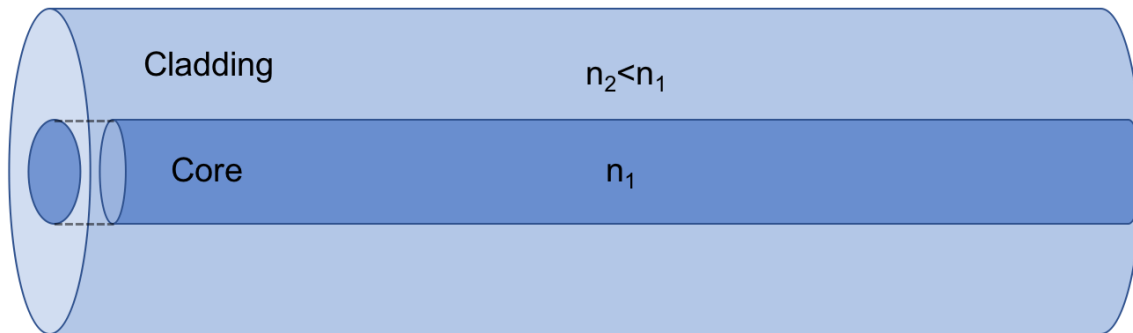


Figure I.8: Schematic presentation of a cylindrical optic fiber with inner core and outer cladding

I.3. The laser

In the 1960s, the laser was invented and characterized as a solution in search of a problem [17]. Scientists did not imagine the range of applications they could have access to using a laser. Nowadays lasers are everywhere. In our daily life, we use products that are related to the laser. The internet connection, networking, data storage and many other applications are accessible thanks to lasers. Laser presents a versatile number of applications for spectroscopy, interferometry, communications, and in the medical and industrial fields. Some examples of the use of lasers in the medical sector are in odontology, dermatology, gynaecology and ophthalmology. In industrial applications, lasers are used for processing materials, cleaning, welding, cutting and drilling. The wings of airplanes are drilled by lasers, bottles of perfume are marked by laser and even fruit is now being marked by laser. Recently in 2016, a laser interferometry system was used to detect gravitational waves and the first observation ever of a binary black hole merger [18]. In short, laser applications in the medical and industrial fields are somewhat unlimited. Research is extending the boundaries of potential applications.

Specifically for this project, the laser is used for writing photonic components inside glasses.

We can clearly see that the invention of the laser was a great achievement during the twentieth century (inspired by [17]). It all started with the discovery of the process of stimulated emission in which a beam of radiation passing through a gain medium can generate identical photons to those of the incident beam as reported by Albert Einstein in 1917. The first amplification based on the simulated emission was not achieved till 1954 by the research team of Charles Townes at Columbia University [19]. They managed to build a microwave amplifier based on stimulated emission radiation that they called "maser". That was the beginning of the laser. The "maser" was developed into an "optical maser" operating in the visible (Vis) and infra-red (IR) regions in 1958 [20] by the same research group. Then, the race was on to demonstrate a working laser and Theodor Maiman of Hughes Laboratories won it in May 1960 [21]. He managed to get a pulsed laser emitting in the red wavelength out of a ruby crystal pumped by a flash-tube. Later on, in 1961 a continuous gas laser was demonstrated by Bell Labs by Javan, Bennet and Herriott. That laser operated in the near infra-red (NIR) wavelength at $1.15\mu\text{m}$ [22]. Following these two discoveries, the number of lasers increased significantly. Many types of lasers were created operating at different wavelengths, different powers, different mode regimes. Currently, a huge number of lasers exist, going from solid state [21], dye [23], semi-conductor [24], gas [25], fibre [26] , free-electron [27] to X-ray lasers [28] that can operate in continuous and pulsed modes.

I.3.1. Definition of laser

LASER stands for "Light Amplification by Stimulated Emission of Radiation". It is based on the stimulated emission process introduced by Einstein in 1917. Basically, a laser is composed of a pump source, active/gain medium and a cavity as shown in Figure I.9. The amplification process of light takes place inside the laser cavity, more specifically in the gain medium. It is achieved by a stimulated emission process from an atomic or molecular system with transitions in an inverted population (i.e. the upper energy level is more populated than the lower).

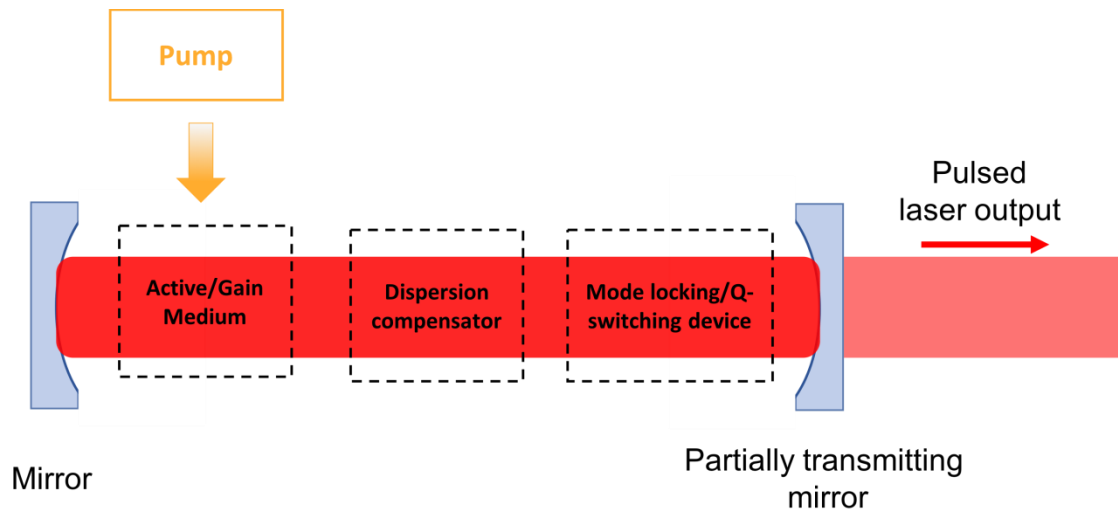


Figure I.9: Schematic presentation of a pulsed laser oscillator.

Generally, the laser is characterized by its wavelength emission, average power, operating mode (continuous or pulsed), repetition rate and pulse duration (in case of pulsed laser). A continuous laser could be transformed into a pulsed one using two techniques: Q-Switching (using saturable absorbers, electric-optic shutters,...) allowing pulses in the nanosecond range or Mode locking (using SESAMs, acousto-optic switches, ...) allowing shorter laser pulses in the pico to femtosecond range [29]. As shown in Figure I.9, in order to have a femtosecond laser, the insertion of a Mode locking device is a must as well as compensating for the cavity dispersion due to the presence of a large band active medium. For more information and details the reader is referred to the following reference [29]. Then, to have higher laser energies that are sufficient for applications demanding it such as direct laser writing, the laser presented in Figure I.9 for example could be amplified using an external amplifier as shown in Figure I.10.

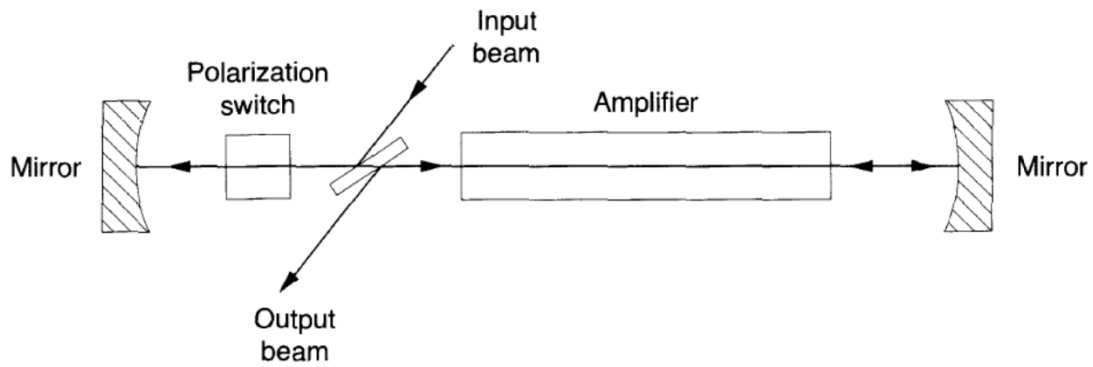


Figure I.10: Schematic presentation of a laser beam (input beam) amplified using an external amplifier. Taken from [29].

During this project, the lasers used for direct laser writing are mode locked lasers. The wavelength emission is determined by the gain medium i.e. the atomic/molecular transitions between the atomic levels. Lasers could operate in wavelengths going from X-ray [28] to the IR regions [30].

Maxwell's wave equations, predicting the propagation of transversely oscillating electromagnetic waves, were the first indication of the true nature of light. Therefore, laser light propagation is defined by the Maxwell Equations published in 1864 (inspired from [31]). Considering the use of lasers in this project, the equations herein represent the propagation of light in a dielectric medium, in this case glasses.

$$\nabla \cdot \mathbf{E} = -\frac{1}{\epsilon_0} \nabla \cdot \mathbf{P} \quad (\text{I-4})$$

$$\nabla \cdot \mathbf{H} = 0 \quad (\text{I-5})$$

$$\nabla \times \mathbf{H} = \epsilon_0 \frac{d\mathbf{E}}{dt} + \frac{d\mathbf{P}}{dt} + \mathbf{J} \quad (\text{I-6})$$

$$\nabla \times \mathbf{E} = -\mu_0 \frac{d\mathbf{H}}{dt} \quad (\text{I-7})$$

Using the Maxwell equations above, the general wave equation of the electric field E could be obtained:

$$\nabla \times (\nabla \times E) + \frac{1}{c^2} \frac{d^2 E}{dt^2} = -\mu_0 \frac{d^2 P}{dt^2} - \mu_0 \frac{dJ}{dt} \quad (I-8)$$

where P is the polarization

J current density

H vector quantity of the magnetic flux

ϵ_0 permittivity in the vacuum

μ_0 permeability of the vacuum

The right side of the equation is called the source terms. The first term is related to the polarization changes while the second term is related to the conduction charges that are applicable in metallic materials. Given that in this work we are using glasses, the second term will not be taken into consideration; therefore the general wave equation becomes:

$$\nabla \times (\nabla \times E) + \frac{1}{c^2} \frac{d^2 E}{dt^2} = -\mu_0 \frac{d^2 P}{dt^2} \quad (I-9)$$

I.3.2. Gaussian beam

As mentioned before, the laser amplification process occurs generally inside the laser cavity between two mirrors. The propagation of light back and forth between the two mirrors implies a Gaussian intensity profile for the propagating mode in the cavity which is the TEM_{00} (without getting into details). The mode maintains the same shape everywhere inside the laser cavity (between the two mirrors) and beyond the cavity (output of the laser) unless an optical element is introduced that distorts or changes the Gaussian profile. Generally, most of the output laser modes are TEM_{00} Gaussian modes which is the case also in this work.

Let's now consider a Gaussian beam propagating along the z -axis as shown in Figure I.11. It is characterized by the intensity profile, the beam waist, Rayleigh range, the depth of focus, the beam divergence and the beam wave front curvature.

The intensity distribution of a simple Gaussian beam is given by:

$$I = I_0 e^{-2r^2/w_0^2} \quad (\text{I-10})$$

where I_0 is the maximum intensity and w_0 is the beam waist inside of which 86.5% of the energy is concentrated as shown in Figure I.11.

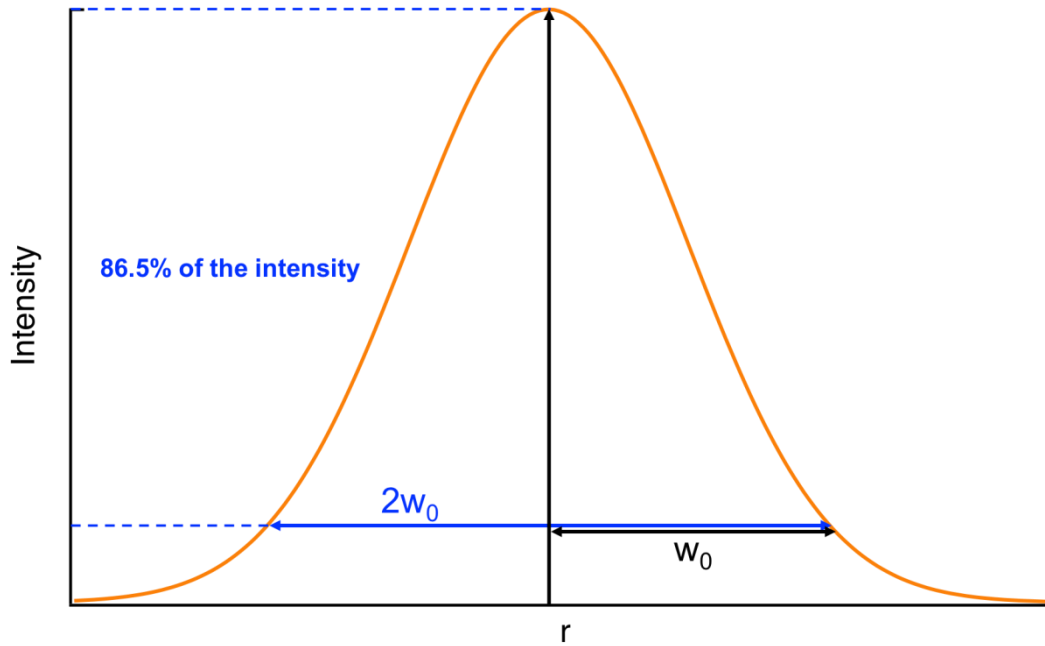


Figure I.11: Intensity profile distribution of a Gaussian beam as function of r .

Beam waist at a distance $\pm z$ from w_0 :

$$w(z) = w_0 \left[1 + \left(\frac{\lambda z}{\pi w_0^2} \right)^2 \right]^{1/2} \quad (\text{I-11})$$

$$\text{Rayleigh Range: } z_R = \frac{\pi w_0^2}{\lambda} \quad (\text{I-12})$$

$$\text{Depth of focus: } b = 2z_R = 2 \frac{\pi w_0^2}{\lambda} \quad (\text{I-13})$$

$$\text{Beam divergence: } \theta_0 = \frac{\lambda}{\pi w_0} \quad (\text{I-14})$$

$$\text{Wave front curvature at } z \text{ position: } R(z) = z \left[1 + \left(\frac{\pi w_0^2}{\lambda z} \right)^2 \right] \quad (\text{I-15})$$

Where w_0 is the beam waist, λ is the wavelength of the beam and z the position along the propagating z axis.

Following propagation, the width of the Gaussian beam decreases ($R < 0$) until it reaches its minimum waist size w_0 ($z=0$) at the wave front curvature $R=\infty$ (Figure I.12). Afterwards, the beam expands and diverges ($R > 0$) as a cone of half-angle θ_0 . The beam is considered to be parallel to the propagation axis on a length of $2z_r$ that is called depth of focus or the confocal parameter (Figure I.12) corresponding to the double of the Rayleigh length. One should note that the tighter we focus the beam the faster it diverges. We can conclude that the major beam intensity is restrained in a voxel corresponding more or less to the depth of focus of the beam. Therefore, the morphology of the interaction zone is dictated by the laser's Gaussian shape. Generally, the laser beam quality is defined by the factor $M^2 \geq 1$. In this work, the laser beams exhibit a quality factor $M^2 \sim 1.1$. The beam quality factor M^2 defines the beam illumination pattern as well as the laser propagation and transformation properties. It also indicates how the laser output beam is close to the fundamental Gaussian beam mode. The larger the value of M^2 the lower the beam quality is. For more information about the M^2 the reader is referred to the following references [29, 32]. However, in some experiments cylindrical lenses were installed in order to change the beam shape at the focus plane i.e. change the morphology of the modified region. This part will be more detailed in section III.3.2.b. Also, beam shaping is possible using a Spatial Light Modulator (SLM) which is not used during this work for beam shaping.

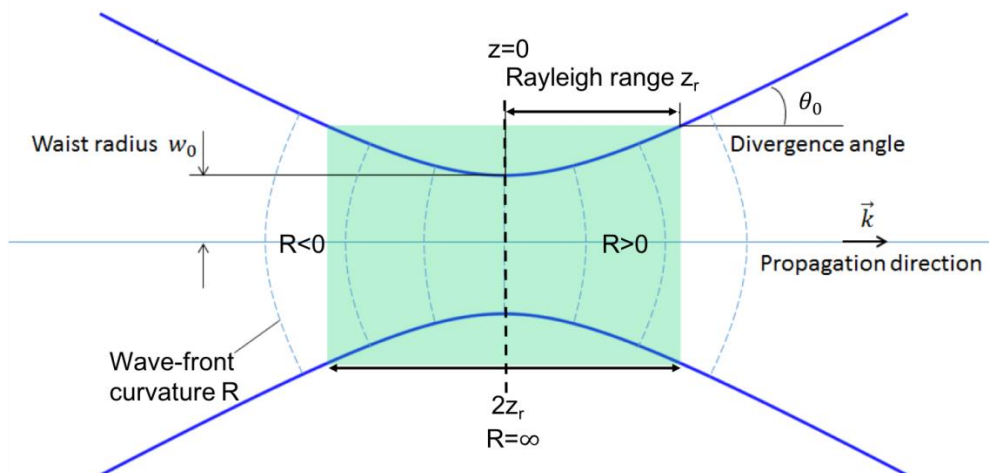


Figure I.12: Schematic presentation of a propagating Gaussian beam.

I.3.3. Laser-material interaction

Laser-matter interaction could be realized using a CW or a pulsed laser. In this framework, it is realized using pulsed femtosecond lasers. In dielectric materials such as glasses, a non-linear absorption process is present when the light intensity is sufficient to generate one. Femtosecond lasers provide a high intensity of light in a short time which triggers the non-linear effects. The photons are absorbed by the atoms forming the glass matrix and then, if the energy is sufficient, the electrons are able to pass from the valence band to the conduction band. Therefore we have photoionization. More specifically, the electrons gain enough kinetic energy to move freely in the glass matrix. The process is shown in Figure I.13 for dielectric materials. The energy absorbed by the electrons should be higher than the band gap E_g between the valence and the conduction band. In dielectric materials, the E_g is generally higher than the energy of one photon; therefore, in order for the electrons to pass to the conduction band, the non-linear absorption process is a must. Moreover, the non-linear absorption process confines the deposited energy in a 3D interaction voxel allowing the creation of sub-micrometre structures [33].

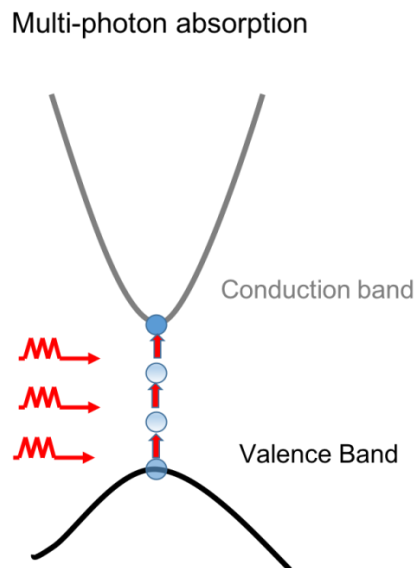


Figure I.13: Schematic presentation of the multi-photon absorption process. In this case, an electron in the valence band absorbs 3 photons to pass to the conduction band.

I.3.3.a. Non-linear absorption mechanisms in glasses

Generally, the laser average intensity used exceeds the ionization threshold of the glass and the matter is photo-ionized. Three dominating non-linear excitation

processes in dielectric materials mainly occur: *Multi-photon ionization (MPI)*, *tunnelling ionization* and *avalanche ionization*. The first two processes are considered as direct photo-ionization of the medium. Avalanche ionization is an indirect process given that the electrons are promoted to the conduction band due to the collision between free electrons accelerated by the electric field. The three processes are presented in Figure I.14.

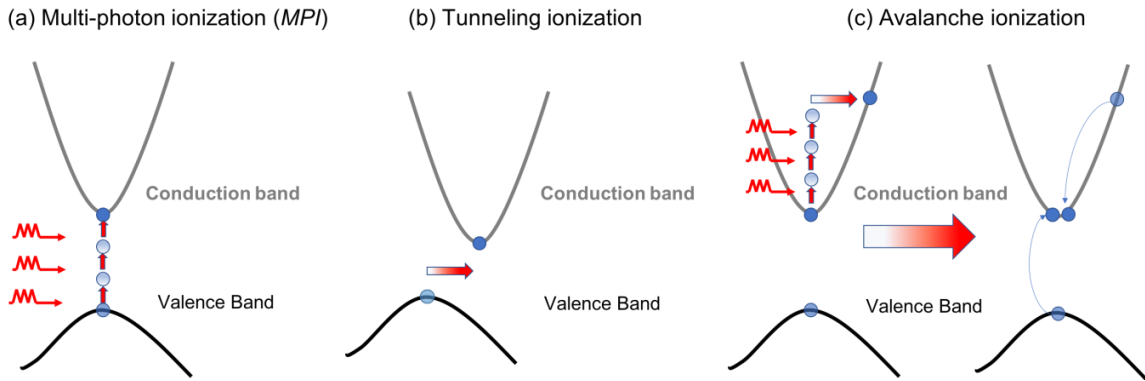


Figure I.14: Schematic presentation of the photo-ionization processes during laser-glass interaction. (a) Multi-photon ionization (MPI): An electron absorbs two or more photons to be promoted in the conduction band (b) Tunneling ionization where the electron passes through a barrier to be promoted the conduction band (c) Avalanche ionization where an electron in the conduction band absorbs two or more photons, then collides and promotes an electron from valence band to the conduction band. Inspired from [34, 35].

Multi-Photon Ionization (MPI) refers to the absorption process of the energy of two or more photons by an electron in the valence band to pass to the conduction band. This photoionization rate highly depends on laser intensity. The multiphoton ionization rate is given by [34, 36, 37]:

$$P(I) = \sigma_k I^k \quad (\text{I-16})$$

where σ_k is the multiphoton absorption coefficient for absorption of k photons and I is the laser intensity. In order to have photoionization, a minimum number k of photons is required to satisfy the relation $k\hbar\omega \geq E_g$. Therefore, the total energy absorbed is related to the number of photons. In the case of silver containing zinc phosphate glasses that are used in this work, the band gap is between 4.5 eV and 4.8 eV depending on the concentration of silver ions inside the glass [11]. When using a 1030 nm laser which exhibits a photon energy of 1.2 eV, a four-photon absorption process is required in order to achieve ionization.

Tunneling ionization refers to an electron passing through a short barrier and becoming free. The electric field generated by the laser intensity eliminates the Coulomb potential wells that bind a valence electron to its atom. When the field is very strong, the Coulomb potential well is eliminated and the electron passes through the short barrier and becomes free [36] as shown in Figure I.14.a This type of nonlinear process prevails for strong laser fields and low laser frequency (high λ). However, it could simultaneously occur with the Multi-Photon Ionization process in other cases. Keldysh proposed a parameter to express the transition between the two processes known as the Keldysh parameter [38]:

$$\gamma = \frac{w}{e} \left[\frac{m c n \epsilon_0 E_g}{I} \right]^{1/2} \quad (\text{I-17})$$

where w is the laser frequency, c velocity of light, n refractive index change of the medium, ϵ_0 permittivity in the vacuum, E_g band gap, m and e reduced mass and charge of the electron and I the laser intensity. When the Keldysh parameter is higher than 1 ($\gamma > 1$), the *MPI* dominates the process while when it is lower ($\gamma < 1$), the *tunneling ionization* dominates. However, when it is around 1 ($\gamma \sim 1$), the intermediate regime [39], we have a mix of both *MPI* and *tunneling ionizations*. In our framework, γ is estimated to be higher than 1 ($\gamma \sim 1.3$) which puts us in the *MPI* process regime.

Avalanche ionization refers to a two-step process. A free electron in the conduction band absorbs photons until its energy exceeds the E_g of the material. An electron with higher energy than the band gap $E > E_g$ can collide and excite another electron in the valence band to the conduction band as shown in Figure I.14.b. This process will continue as long as the pulse is increasing the number of free electrons in the focal volume [36].

- **Plasma generation**

The three previously mentioned non-linear effects contribute to ionize the material resulting in the creation of high density electronic plasma in the vicinity of the focal volume. This is due to the high density of electrons generated. The electron density distribution could be described by the following equation [35]:

$$\frac{dn_e}{dt} = W_{PI} + \alpha_c I n_e (1 + \sum_{j=1}^{k-1} \beta_j I_j) \quad (I-18)$$

where α_c is the avalanche ionization coefficient, n_e electron density and β_j the cold avalanche which was not introduced in this manuscript. If readers are interested in further details, they are referred to [40-42]. The first term of the left part of the equation indicates the contribution of the photo-ionization process while the second term is linked to the avalanche ionization effect. The creation of plasma could be linked to both processes or only to photo-ionization [43]. The morphology and the type of modifications in the material following laser-matter interaction are directly linked to the electron density distribution in the plasma. In fact, the threshold of modification is associated to a certain value of the electron density and the deposited energy is proportional to the electron density. In other words, the electron density distribution in the material i.e. the shape of the plasma dictates the morphology of the modified region. This was proved by Couairon et al. They compared the morphology of a modified region in fused silica glass with the numerical simulation of electron density distribution and they found a significant match [43] as shown in Figure I.15.

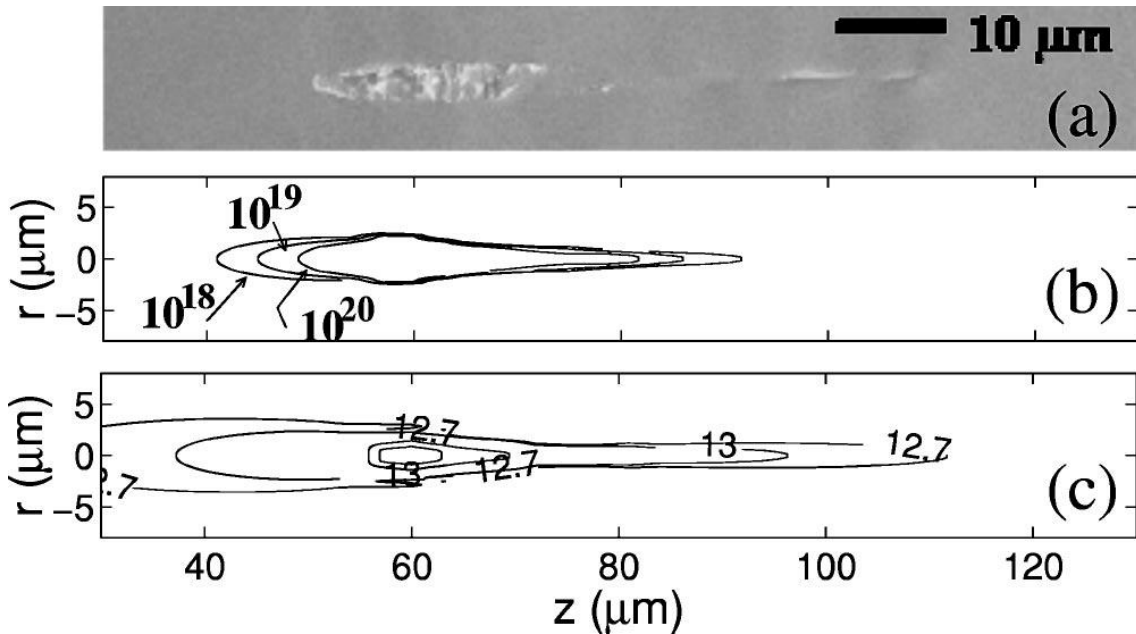


Figure I.15: (a) Scanning electron microscopy image of a track damage obtained by focusing femtosecond pulses inside fused silica (b) Numerical simulation electron density (c) Computed intensity counterplots. The comparison between experiment and simulations shows a good match of the morphology. Figure taken from [43].

I.3.3.b. Time scale

Laser-matter interaction has been widely used and studied during the last two decades. The comprehension of the ongoing physical processes and their timeline characteristics is important. Although it depends on the properties of the materials and the irradiation regime, the community agrees that during the interaction of a single femtosecond laser pulse with matter some of the following events occur as shown in Figure I.16. Firstly, the laser energy is absorbed by the material and creates photoelectrons. These photoelectrons then transfer their kinetic energy to the lattice. Finally, heat diffusion occurs by melting, fusion or exploding the material depending on the threshold modification of the material. The latter process induces a local modification of the glass and will be discussed in detail in Chapter II section II.2. For photochemical reactions, an great number of pulses needs to be accumulated in order to drive the diffusion of chemical species inside the temperature gradient [44]. That is what is required in silver containing glasses as we are going to see during this work. In summary, the laser is absorbed then modification of the structural network occurs and finally a permanent change in the physical proprieties of the material/glass takes place.

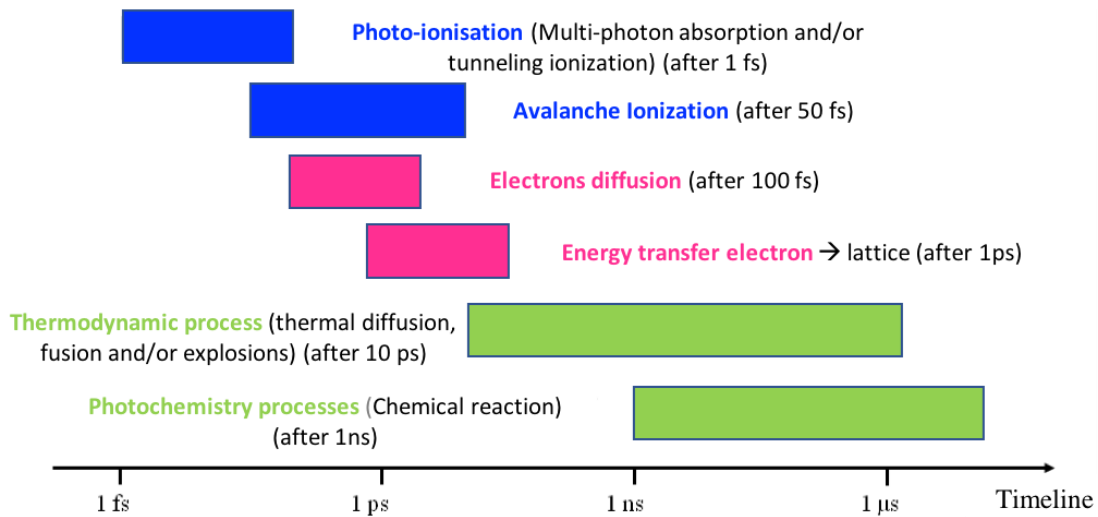


Figure I.16: Timeline of physical phenomena involved during laser-matter interaction. Inspired from [33].

I.3.4. Effects of laser parameters

Laser-matter interaction is a two-way process. The interaction response depends on the matter used i.e. glass, metals, soft tissues, etc. as well as the laser parameters. In this framework, we are working on glasses, changing one laser parameter could sometimes make a lot of difference as we are going to see in this part.

- **Wavelength:**

The laser wavelength is an important parameter in laser-glass interaction. If the glass exhibits a band gap in the UV, in order to have a non-linear process, a green laser for instance or Infra-Red (IR) laser must be used. However, a laser operating in the UV could be used but the interaction with the glass will be a linear one. Therefore, the non-linear processes are not present. Moreover, the wavelength used can define the number of photons absorbed to defy the glass band gap. For the same glass, using different wavelengths can generate two-photon absorption or four-photon absorption for example. If a glass exhibiting a band gap of 4.6 eV when irradiated using a 1030 nm laser, a four-photon absorption process occurs; however using a 515 nm implies a two-photon absorption process. For instance, Hernandez-Rueda et al. investigated the influence of the laser wavelength on the written waveguides in fused silica [45] by using lasers from the UV to the IR range. It was concluded that using shorter wavelengths leads to smaller written features, lower thresholds and narrower energy range for waveguide fabrication [45].

- **Repetition rate, heat accumulation and laser writing regimes**

As mentioned before, a laser can operate in continuous mode (CW) or in pulsed mode. When the laser is operating in continuous mode, it has no repetition rate because it is emitting light all the time, non-stop as shown in Figure I.17.a However, a pulsed laser emits pulses spaced by a certain time depending on its repetition rate (Figure I.17.b). The pulses exhibit a pulse duration T_0 and are separated by a period of T which is determined by the laser repetition rate $\tau = 1/T$. The number of pulses per second is determined by the laser repetition rate. For example if a laser is operating at $\tau=250$ kHz, it delivers 250 000 pulses per second. During this work, femtosecond lasers are used exhibiting short pulses of hundreds of femtoseconds which is equivalent to 10^{-15} s as we are going to see in the following chapters.

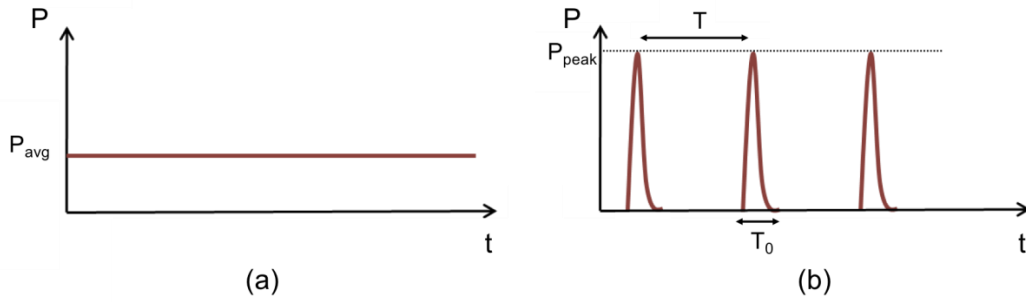


Figure I.17: Schematic presentation of the temporal evolution of the power of a (a) continuous laser (b) pulsed laser.

When using a CW laser, the material does not have time to cool down. However, when using a pulsed laser, depending on the repetition rate as well as the thermal properties of the material, thermal relaxation is possible and the material could have time to cool down. The heating process following the interaction of femtosecond lasers with glasses has been studied by many research groups. First it was proposed by *Schaffer et al.* in 2003 in zinc doped borosilicate glass (Corning 0211) where the radius of the structures was observed to increase as the number of the pulses increases [46]. Over many number of pulses the glass heats and melts a larger volume than the focal volume. After the pulse train is switched off, the glass is cooled and resolidifies in a way different from the initial one. These observations were explained and modeled by the authors as a thermal melting mechanism [46]. The latter work was confirmed and enhanced by *Eaton et al.* in 2005 and *Zhang et al.* in 2007. Both *Eaton and Zhang* studied the heat accumulation effects with variable repetition rates. They also found that the radius of the structures produced increased as a function of the repetition rate i.e. number of pulses in borosilicate glass [47]. What is more interesting in this work was the numerical model of cumulative heating that was proposed. A finite differential method was applied to laser conditions to investigate the physical processes [48]. The laser pulses were modeled as periodic heat sources appearing as delta functions in time since the electron heating and the electron-phonon coupling time ($<1\text{ps}$) is much shorter than the thermal diffusion time of the glass in this case ($>0.1\mu\text{s}$). The laser energy distribution was modeled as a spherical Gaussian mode:

$$E(r) = E_0 e^{(-r^2/w_0^2)} \quad (\text{I-19})$$

where r is the radial distance and w_0 is the 1/e radius at the focused laser beam waist. And the model was based on the radial component of the 3-D heat diffusion equation that was solved numerically:

$$\frac{\partial}{\partial r} \left(r^2 \frac{\partial T}{\partial r} \right) = \frac{r^2}{D} \frac{\partial T}{\partial t} \quad (\text{I-20})$$

where $T(r,t)$ is the temperature and D is the thermal diffusivity of the glass.

The results of the numerical model for different repetition rates are shown in Figure I.18. The horizontal black dashed line presents the annealing temperature of the glass used. This is the temperature where the glass melts and starts sustaining modifications. Three repetition rates were taken into consideration, 100kHz, 500kHz and 1MHz [48]. For the 100kHz repetition rate, we can observe that the glass temperature is increasing roughly above the annealing temperature after receiving the first pulse. However, afterwards the temperature decreases well below the annealing temperature before the next pulse arrives. The glass has sufficient time to cool down before the next pulse. The time between two pulses is lower than the thermal diffusion of the glass $T < D$. So on the one hand, we do not have a cumulative thermal effect or more specifically we have minimum heat accumulation.

On the other hand, for the 500kHz and 1MHz repetition rates, we clearly see that we have a cumulative effect of pulses i.e. cumulative thermal effect (heat accumulation). After the first pulse, the glass temperature increases above the annealing temperature and the second pulse arrives quickly so the glass does not have time to cool down and the temperature continues to build up. For the 1MHz, the thermal cumulative effect is more significant due to the fast repetition rate i.e. shorter time intervals between two consecutive pulses, the glass has no time to cool down before the following pulse. The time between two pulses is higher than the thermal diffusion of the glass $T > D$ which leads to thermal modification volumes much larger than the laser focus plane [47, 48].

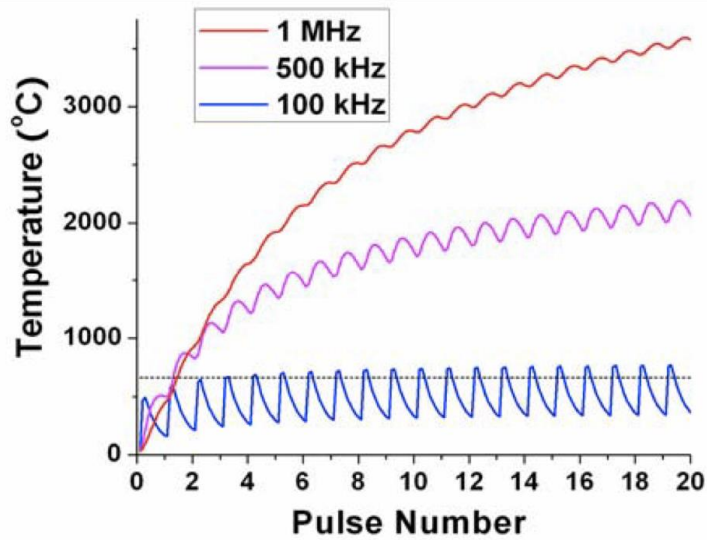


Figure I.18: Numerical simulations of the heat accumulation process inside glass following laser irradiation for different repetition rates, 100kHz, 500kHz and 1MHz. A heat accumulation process starts taking place at the 500kHz repetition rate [48].

Based on the heat accumulation effect in glasses, we can now introduce the writing regimes. Two known writing regimes exist: the athermal and thermal modification regimes [49]. The athermal regime is associated to the KHz repetition rate with pulse energy in the μJ range. The thermal regime is associated to the MHz repetition rate with pulse energy in the nJ regime. It is directly linked to the heat accumulation process. Figure I.19 represents the pulse shape, energy and the temperature as a function of time. For the athermal regime, the pulses are widely spaced so the glass has the time to cool down and the temperature does not build up ($T < D$) however for the thermal regime the pulses are narrow in time and the glass has no time to cool down, therefore the temperature builds up and thermal accumulation occurs ($T > D$).

As we are going to see in this work, more specifically in Chapter III the repetition rate does play a big role in the laser-glass interaction response.

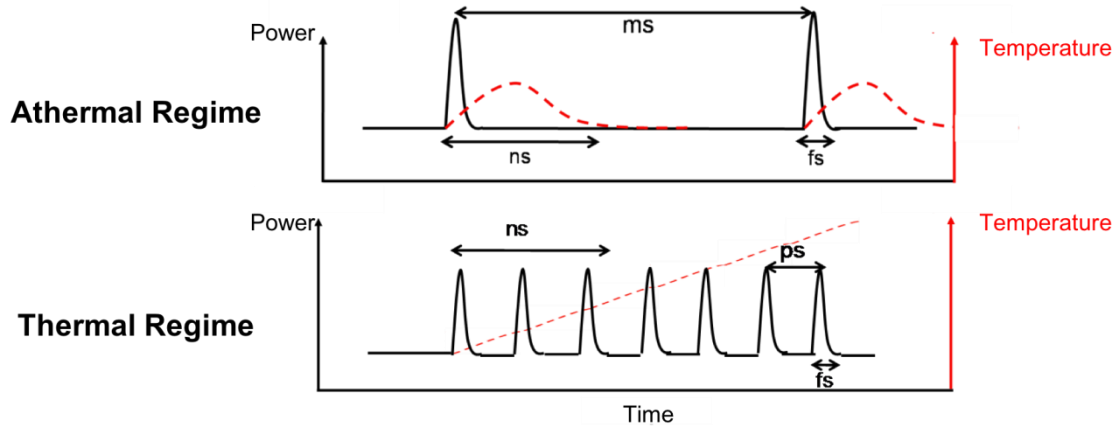


Figure I.19: Comparison between athermal and thermal regimes. For the athermal regime, low repetition rate laser, the pulses are well spaced in time so that the temperature does not have time to build up in the material. However for the thermal regime, high repetition rate laser, the pulses are close in time and the temperature builds up.

- **Polarisation:**

Laser polarisation during laser-glass interaction could sometimes affect the results. It has been reported by *Stalmashonak et al.* that reshaping metallic nanoparticles (NPs) into non-spherical ones depends on laser polarisation [50]. The *MPI* was found to be significantly higher for a linear polarization compared to a circular one in fused silica and sapphire as reported by *Temnov et al* [51]. Moreover, the polarization was found to strongly affect the creation of nanogratings in glasses, in which the nanogratings are only formed with linear polarization [52]. In the waveguides field, it has been reported by an Australian research team that using a circular polarisation increases the transmission i.e. decreases the propagation losses of photo-written waveguides [53].

- **Numerical Aperture**

The numerical aperture (NA) of the focusing objective determines the size of the beam at the focus plane, therefore determining the area of the irradiated zone. The beam waist at the focus plane for a $NA < 0.7$ is given by:

$$w_0 = 0.518 \frac{\lambda_0}{NA} \quad (I-21)$$

When for a high NA i.e. $NA > 0.7$, it is given by:

$$w_0 = 0.61 \frac{\lambda_0}{NA} \quad (I-22)$$

where λ_0 is the wavelength in the free space and NA the numerical aperture of the focusing objective. So, one can conclude, that using a higher NA objective i.e. focusing the beam tighter, leads to the creation of smaller structures and vice versa.

It was reported that increasing the NA of the focusing objective used drastically decreases the modification threshold in glasses [54, 55] as shown in Figure I.20. Therefore, when using a high NA, objective pulse energy of nJ can produce modifications in glasses. This is expected since it increases the laser irradiance interacting with the glass. The laser irradiance is defined by the quantity of power per surface area of the beam spot size. Having the same amount of power in a tighter surface area (smaller beam spot size) increases the irradiance/laser dose deposited in the glass. Taking into account (I-23), we can see that decreasing the beam waist increases the laser irradiance in the glass. In this work, we consider the laser irradiance to be:

$$I = \frac{P_{avg} \cdot T \cdot k}{(T_0 \cdot (\frac{\pi w_0^2}{2}))} \quad (I-23)$$

where P_{avg} is the laser average power after the objective, T the time between two pulses, k the Gaussian constant estimated to be 0.93 assuming that the pulse profile is a Gaussian one and not square, T_0 the pulse duration and w_0 the beam waist.

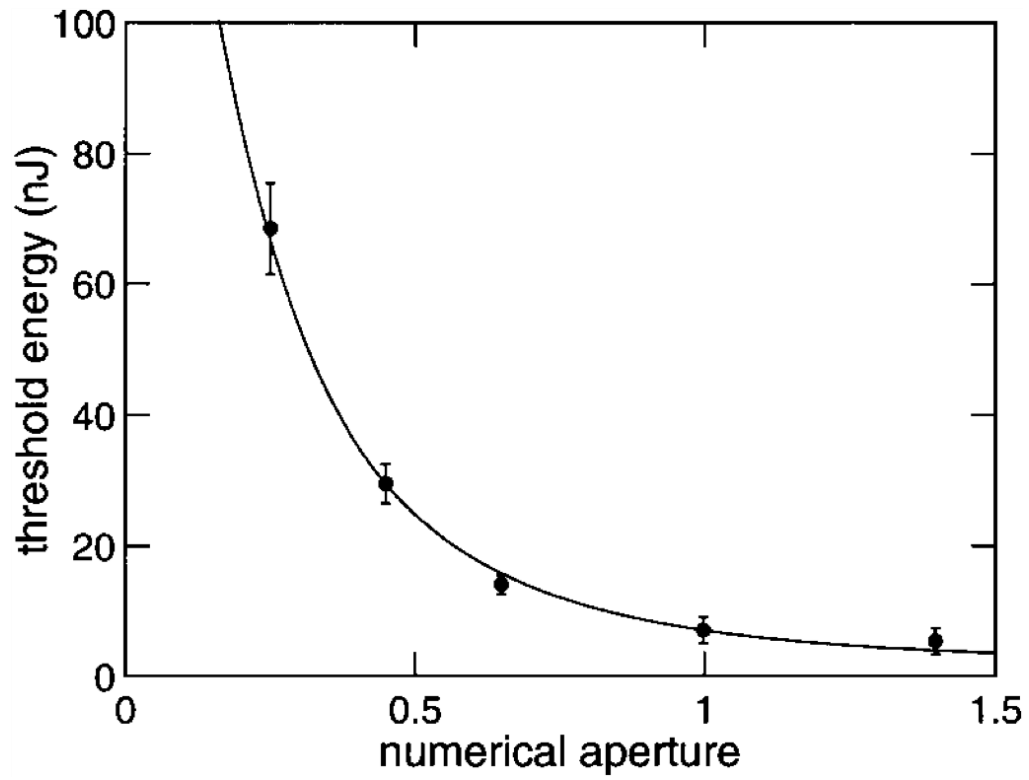


Figure I.20: Modification threshold dependence as a function of the numerical aperture of the microscope objective used in borosilicate glass [54].

I.4. Conclusion

This chapter covers the theoretical approach of laser-glass interaction in general. It starts by introducing the glass and its characterizations, the laser and eventually the process of femtosecond laser-glass phenomena.

We first start by introducing the history of glass that dates back to 650 BC, then by defining the glass itself as well as the glass transition phase. Even though in the beginning of time, forming glasses was based on some recipes, nowadays the glass industry is a vast one and glass is considered as an easy product to make. The ease of making it, the optical window transparency in different wavelengths and the fact that it could be shaped into fibers makes the glass a very attractive platform for photonic and sensing applications.

Secondly, the laser is introduced and more specifically the laser-glass interaction process. It is based on a non-linear process that allows the interaction of a laser with a transparent substrate glass. The different timeline of physical processes was presented following laser-glass interaction as well as the plasma generation around the interaction voxel. We saw different glass responses for different laser parameters, which highlights the effect of laser parameters in the interaction process. Finally, we defined two inscription regimes based on the heat accumulation process that were classified as athermal and thermal regimes.

The broad points regarding glass, lasers and basic laser-glass interactions were covered allowing to tackle the main theme of this work where we will be introducing in Chapter II: Direct laser writing of a new type of waveguide in silver containing glasses. Chapter III will present a comparative study between the *type I* and *type A* photo-induced refractive index change by femtosecond laser writing. Finally, Chapter IV the last chapter will address the direct laser writing of near-surface waveguides as well as the creation of a refractive index sensor.

Table of contents:

II. Direct laser writing of a new type of waveguide in silver containing glasses	39
II.1 Introduction.....	39
II.2 Principle of DLW and Δn classification	40
II.2.1 Type I modification origins	42
II.3 State of the art.....	43
II.3.1 Waveguides	43
II.3.1.a Theory of waveguiding	44
II.3.2 Depressed cladding waveguides	49
II.3.3 Couplers	51
II.3.4 Beam splitters	56
II.3.5 Waveguide Bragg grating	57
II.3.6 Waveguide lasers.....	59
II.3.7 Photonic lantern.....	60
II.3.8 Study of phosphate glasses	61
II.4 Silver containing zinc phosphate glasses	63
II.4.1 Optical properties.....	64
II.4.2 Laser-silver containing glasses interaction	66
II.4.2.a Physical processes associated to the formation of silver clusters ...	69
II.4.3 Writing window in silver containing glasses.....	71
II.4.4 Review on previous works on silver containing glasses	72
II.5 Experimental setup: Glass and laser used.....	74
II.5.1 Glass synthesis and fiber drawing.....	74
II.5.2 Silver containing zinc phosphate glass fibers	75
II.5.3 Laser setup	79
II.5.4 Mode profile setup.....	80
II.5.5 Confocal Microscope	81
II.5.6 Measuring Δn :SID4Bio Phasics.....	81
II.6 Results.....	84
II.6.1 Structure morphology.....	84
II.6.2 Δn vs laser parameters	86
II.6.3 Waveguiding	95
II.6.3 Multimode waveguiding	95
II.6.3.b Single mode waveguide	99

II.6.3.c Multimode – Single mode aspects	109
II.6.4 Optical components.....	110
II.6.4.a Y-Beam splitters	110
II.6.4.b Directional couplers.....	111
II.6.5 Waveguides in Ribbon fibers.....	115
II.7 Conclusion	118

Chapter II

Direct laser writing of a new type of waveguide in silver containing glasses

II.1. Introduction

In the past decades, laser-matter interaction has occupied the scientific community due to its wide range of applications. More specifically, direct laser writing (DLW) in transparent glasses has attracted the interest of many research groups. This simple technique allows to directly address 3D micro-structures inside transparent materials. It exhibits many advantages over lithography techniques which are limited to 2D structuring and involve multiple steps, making DLW highly compatible for faster material processing and for future technological transfer to advanced industrial manufacturing. DLW in glasses induces a local permanent refractive index change that could be used for the creation of waveguides as reported by *Davis et al* [56]. Generally, the creation of waveguides is based on the *type I* refractive index change as has been reported by many research groups [57-63].

In this chapter, we present the special response of the silver containing glasses with femtosecond laser pulses. Following laser irradiation, fluorescent silver clusters are created in the vicinity of the interaction voxel. Those silver clusters are responsible for a novel type of refractive index change (Δn) that is compatible with waveguiding applications. The morphology of the photo-induced structures, the Δn and the dimensions of the structures as a function of the laser irradiance were investigated. Multimode and single mode waveguides were written and characterized. A 50-50 Y-shaped beam splitter and a 50-50 directional coupler were written also paving the way toward 3D integrated circuits. Finally, the waveguiding process was demonstrated in silver containing ribbon fibers.

II.2. Principle of DLW and Δn classification

Direct laser writing (DLW) in glasses consists in focusing femtosecond laser pulses inside a transparent glass substrate using a microscope objective while moving the sample which is placed on a 3D translation stage as shown in Figure II.1. Following laser irradiation, the glass structure is changed resulting in a local permanent change (modification) of the refractive index. The latter change in the refractive index allows the fabrication of optical components and circuits embedded inside the glass.

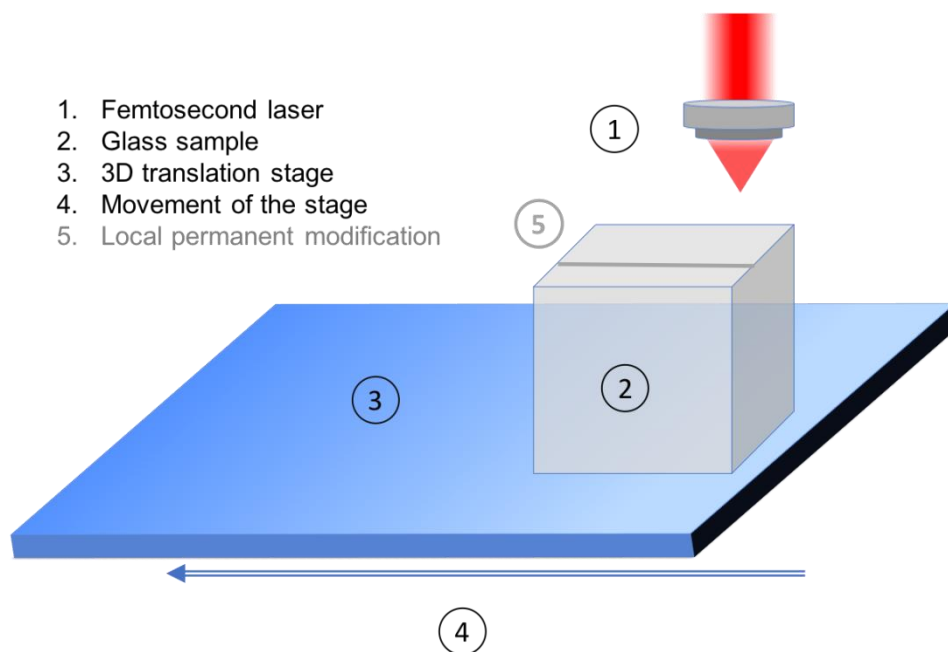


Figure II.1: Schematic presentation of the Direct Laser Writing (DLW) process.

This was first reported by Davis et al. in 1996, when focusing a femtosecond Ti-Sapphire laser operating at 810 nm in silica glass induced a local modification of the glass [56]. Normally, the refractive index change (Δn) results from the non-linear absorption of the femtosecond laser pulses as previously explained in section I.3.3.a. The Δn induced by laser-glass interaction are classified generally as three distinct types following an increasing pulse energy scale [64, 65]: *Type I*, *Type II* and *Type III* as shown in Figure II.2. Poumellec et al. mapped the modification process in pure silica glass for different pulse energies in four different regions. *Region I*: no modification, *Region II*: *Type I* modification with isotropic Δn , *Region III*: *Type II* modification with anisotropic Δn . *Region IV*: *type III* modification is

associated with formation of voids (Figure II.2) [64]. The following classification could extend to all glasses while changing the modification thresholds and the energy window for each region (region I, II, III or IV) depending on the glass bandgap and photosensitivity. Energy windows are defining the range of energy where each type of modification can be obtained.

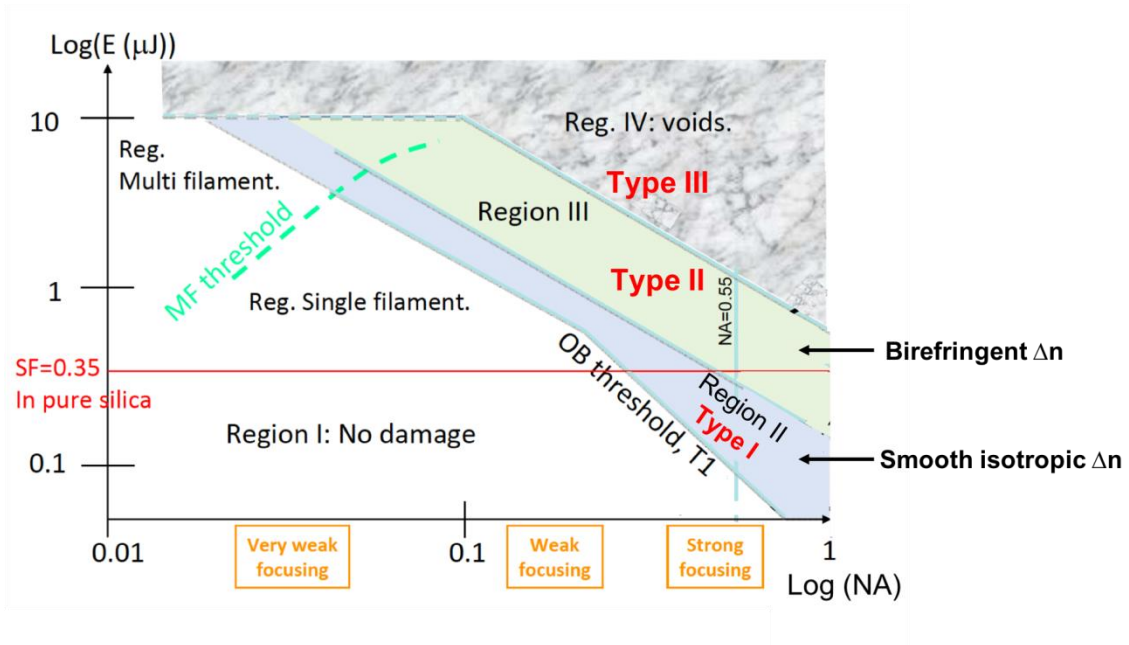


Figure II.2: Map of the modification thresholds in fused silica for the four regions/three types of modification as a function of the pulse energy and the numerical aperture. Adapted from [64].

Generally, *type I* modifications are smooth isotropic changes of the refractive index change allowing the formation of waveguides for optical circuit applications (Region II in Figure II.2) [62, 63, 66-71]. *Type II* modifications result from a birefringent change in the refractive index associated with nano-structuration of the glass and self-organized nano-gratings formation due to the production of local moderate plasma (Region III in Figure II.2) [72-74]. Further increasing the pulse energy, leads to *type III* modifications resulting in voids or disorganized damage features in the glass matrix, due to an excessive plasma production and subsequent Coulomb explosion which are generally detrimental to the fabrication of photonic devices (Region IV in Figure II.2). For this work, the three different modifications (*type I*, *type II* & *type III*) cited are taking into consideration mainly the creation of optical waveguides and it does not extend to the creation of Bragg gratings for instance. The three different types of Δn are shown in Figure II.3.

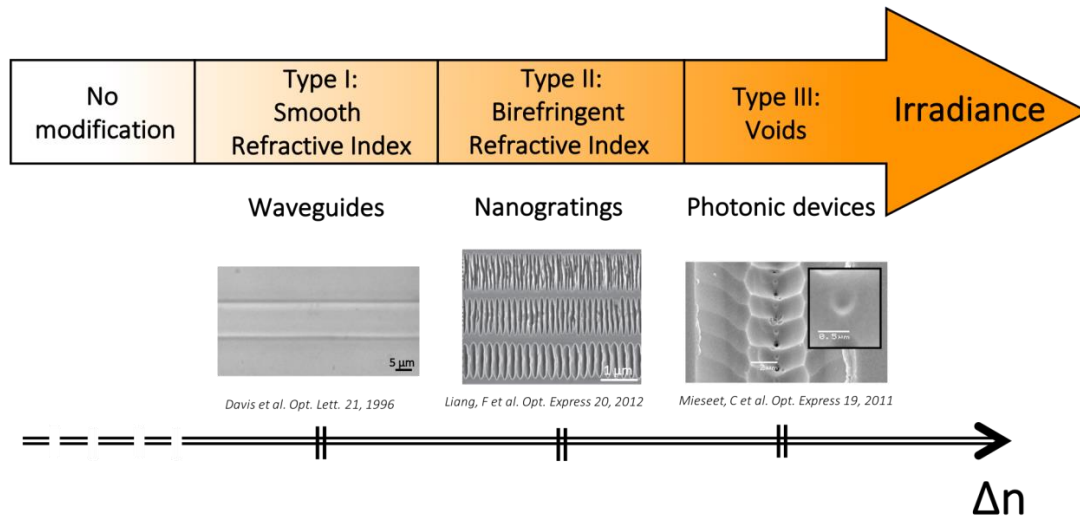


Figure II.3: The refractive index changes/modification classified as function of the irradiance. Pictures for every type of modification, waveguides, nanogratings and voids.

II.2.1. Type I modification origins

For the direct laser writing of photonic components such as waveguides, one is usually interested in *type I* modification due to the smooth nature of the index change associated with this type. Therefore, in this manuscript we will be interested generally in *type I* modification. Over all, *type I* refractive index change (Δn) is associated to the formation of color centers [60, 75, 76] and/or the change in the glass density [46, 77-79]. Color centers result from a defect in the glass lattice implying the absence of an atom from the place it would normally occupy in the glass lattice. The electrons are trapped in such defects, which lends a certain absorption band and color to the material. Thus, laser irradiation could create enough color centers that the Δn could be correlated to the Kramers-Kronig mechanism [60]. The formation of color centers has been observed in many glasses such as phosphate [76] and borosilicate [80]. Some groups have suggested that the presence of color centers produces a metastable change in the polarizability associated with a change in the molar refraction of the material [81]. The change in polarizability is caused by a variation in the concentration of ionic bonds that results from the capture of free electrons by defects in the network structure that occur during irradiation [82]. This change in polarizability may induce a decrease [76, 83] or increase [43] of the Δn mainly on the material in which it is induced. Generally, color centers are not stable and they disappear after thermal annealing.

However, the change in the glass density is due to the local heating of the glass and restructuration during the cooling process following laser passage. In the laser focal spot, due to the absorption of the laser energy, the glass is heated to a temperature higher than T_g , therefore it melts [77] and following the laser passage, it cools down at a different speed and process from the initial non-irradiated glass resulting in a change in the density of the material creating a change of Δn of the material. The Δn created could be positive or negative based on the material irradiated [62]. Several groups have noticed that the magnitude of the index variation is related to the cooling rates of the material, which confirms the link between the index change and the thermal processes that occur during laser irradiation [60]. Moreover, the change in the glass density i.e. the photo-induced Δn could also be related to the ion exchange following laser irradiation as observed by *Kanehira et al.* [84] and others [85]. Obviously, several parameters play an important role in the determination of the sign and the magnitude of the refractive index variation in the glass going from the laser parameters to the glass composition. This part will be more detailed in Chapter III

II.3. State of the art:

II.3.1. Waveguides

Over the past two decades, many research groups created waveguides inside glasses using the direct laser technique since the first demonstration by *Davis et al.* in 1996 [56]. The inscription of waveguides in glasses is the basic application that builds up for the creation of integrated optical circuits. Two different writing configurations are possible, longitudinal and transverse in which the sample is translated respectively along and perpendicularly to the beam propagation axis. The longitudinal writing configuration [62] results in intrinsically symmetric, round waveguides and their size is determined by the focal spot of the laser beam. However, their length is limited by the focal length of the focusing objective. Furthermore, the transverse writing provides much more versatility and flexibility in creating complex 3D geometries. The disadvantage could be producing a strong asymmetry in the waveguide cross section resulting sometimes in elliptical waveguides. Certain methods were introduced to overcome this problem. Some research groups use a slit placed before the microscope objective [63]. Others use cylindrical telescope lenses [86, 87] and some use a spatial light modulator (SLM) [69] to reduce the asymmetry and create circular waveguides.

Waveguides were written in fused silica glasses [45, 57, 68], phosphate glasses [61, 62, 76], Borosilicate glasses [48, 88], fluoride glasses [89], chalcogenide glasses [90, 91] and other glasses as well. Depending on the glass transmission windows, waveguides operating from the visible [61, 62, 89] to the IR [87, 92-94] (up to 3.85 μm) region were written using direct laser writing. Moreover, low loss waveguides in the order of 0.1 dB/cm (Borosilicate glasses, Fused silica glasses and chalcogenide glasses) [48, 66, 95] and even lower to 0.027dB/cm in Gorilla glass [71] were reported, paving the way for a bigger scale of material processing and optical/photonic circuits in needed cases as well as for industrial transfer. However, the lowest propagation losses of 0.027dB/cm [71] has not been reported/reproduced by any research team to date. One can say that the DLW losses could be comparable to silicon based ultra-low loss waveguides processed with lithography technique exhibiting losses of 0.0008dB/cm [96] and 0.026dB/cm [97] for example.

Finally, based on the creation of waveguides using DLW, many optical components were created like couplers, splitters, waveguide lasers etc. The following part will briefly discuss some of the significant work done over the past years based on waveguides written in glasses. But before, a small overview of the waveguiding theory is presented.

II.3.1.a. Theory of waveguiding

This part is inspired from [98, 99]. Let's consider a planar dielectric waveguide surrounded by a lower refractive index medium as shown in Figure II.4. The light propagates inside the waveguide by the Total Internal Reflection (TIR) principle. The inner part of the waveguide is called the core while the outer part is called the cladding. Light propagates inside the waveguide's core while making angles θ with the z axis (Figure II.4) following many multiple internal reflections (Figure II.4).

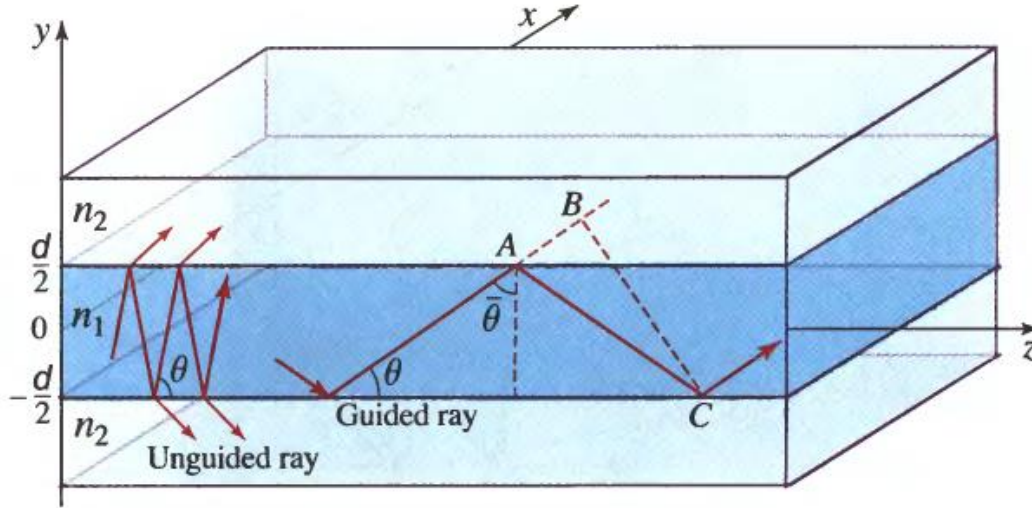


Figure II.4: Schematic of guided and unguided rays in a planar dielectric waveguide. The rays exhibiting a propagation angle θ lower than $\bar{\theta}_c = \cos^{-1}(n_2/n_1)$ are only guided. Taken from [99].

The rays exhibiting a propagation angle θ smaller than the critical angle given $\bar{\theta}_c$ by, $\bar{\theta}_c = \cos^{-1}(n_2/n_1)$ could be guided inside the waveguide. The light propagates inside the waveguide as a form of a mode that could be determined using the self-consistency condition. Modes are fields that maintain the same transverse spatial distribution and polarization all along the waveguide along the propagation axis. Assuming that a monochromatic light is propagating inside a planar waveguide with an angle θ smaller than the critical angle $\bar{\theta}_c$, we impose the self-consistency condition that a wave reproduces while propagating to determine the propagating modes. In one round trip, the different optical path distance that occurs is given by: $\overline{AC} - \overline{AB} = 2d\sin\theta$ while d is the waveguide width (Figure II.4). Every time the light bounces on the interface core-cladding a phase shift occurs presented by ϕ_r . For self-consistency, the phase shift between two waves should be zero or a multiple of 2π , therefore:

$$\frac{2\pi}{\lambda} 2d\sin\theta - 2\phi_r = 2\pi m \quad (\text{II-1})$$

The reflection phase ϕ_r is as a function of the propagation angle θ . It depends also on the polarization of the incident wave, TE (Transvers Electric) or TM (Transvers Magnetic). Let's consider a TE wave propagating inside the waveguide (the electric field is in the x direction) the self-consistency condition is given by:

$$\tan\left(\pi \frac{d}{\lambda} \sin\theta - m \frac{\pi}{2}\right) = \sqrt{\frac{\sin^2\theta_c}{\sin^2\theta}} - 1 \quad (\text{II-2})$$

The solution of (II-2) is a graphical one as shown in Figure II.5. The self-consistency condition allows to determine the number of propagating modes in a waveguide as well as the propagation angles for different modes (in case the waveguide is multimode). No more details are presented in this manuscript concerning that matter but if readers are interested, they are referred to chapter 8 of the following reference [99].

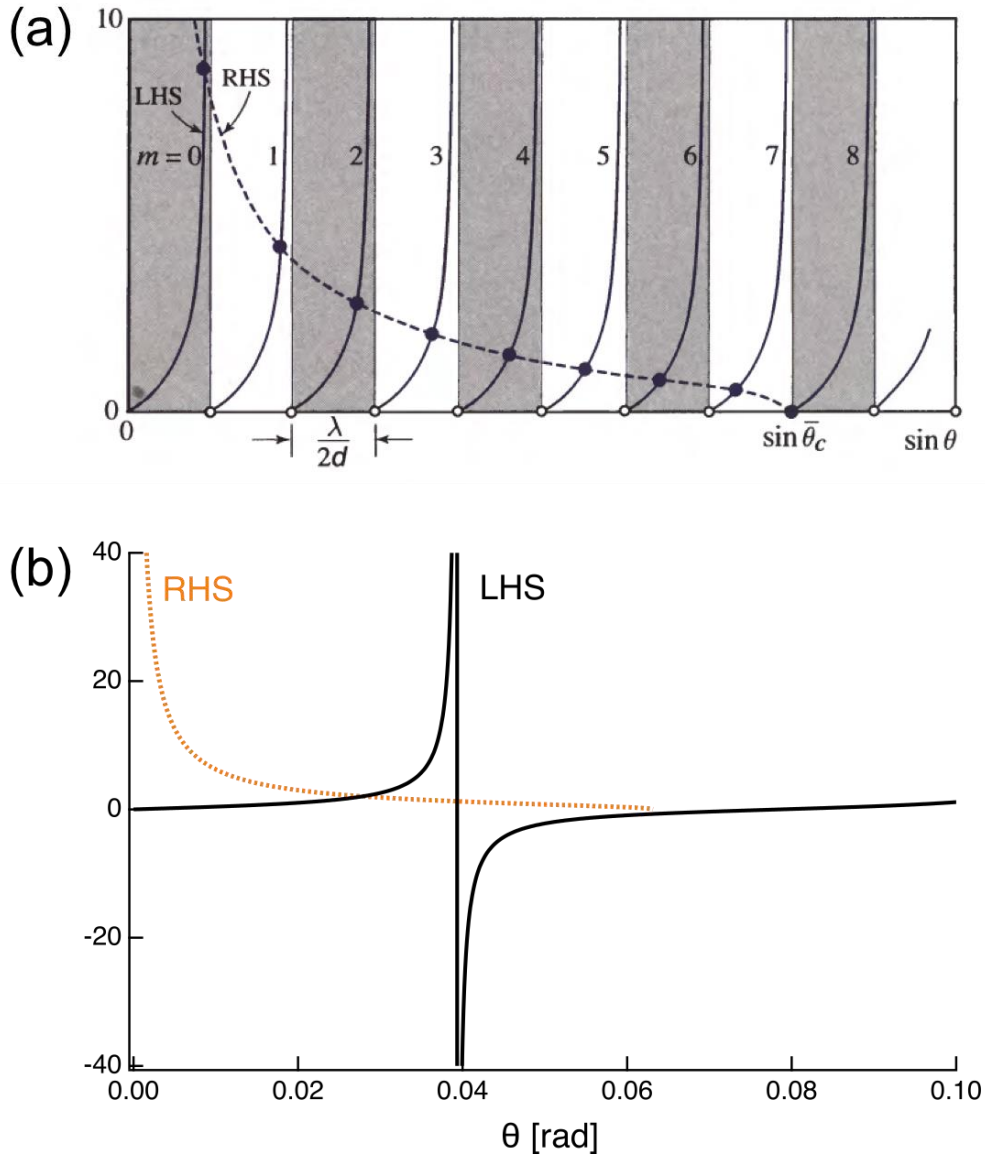


Figure II.5: Graphical solution of (II-2) to determine propagation angles θ of the mode of a planar dielectric waveguide. (a) The right side (RHS) and left side (LHS) of the equation are plotted as a function of $\sin \theta$. The intersection points marked by filled circles determine the propagation angles θ . On the other hand, each intersection of the tan function (LHS) corresponds to a mode. In this example, the waveguide can support up to 9 modes. Taken from [99]. (b) RHS (orange dashed line) and LHS (black full line) of (II-2) is plotted for a planar waveguide exhibiting a single mode aspect with $\Delta n = 2 \times 10^{-3}$, dimensions of $5 \mu\text{m}$ at a wavelength of 630nm .

The previous explanation was the case of a planar dielectric waveguide in 1 dimension (1D). However, an optical fiber is a 3D medium. Therefore cylindrical coordinates are to be taken into consideration to write the Helmholtz equation. In that case, the fiber is characterised by a Characteristic equation expressed using Bessel functions instead of a self-consistency equation. Also, the solution of the

characteristic equation could be a graphical one (similar to the self-consistency condition) allowing to determine the fiber parameters. This part will be briefly presented later in the manuscript (section II.3.3). For more details, the reader is invited to read chapter 9 of the following reference [99].

In a more general and simple way, the waveguiding process in fibers that are dielectric waveguides is based on total internal reflection (TIR) as shown in Figure II.6. The Δn between the core and the cladding is enough to confine light inside the core. The Δn could be a step-index or a gradient one. In this case, we are only considering the step-index case given that the photo-written waveguides almost exhibit a step index Δn between the pristine glass and the irradiated zone.

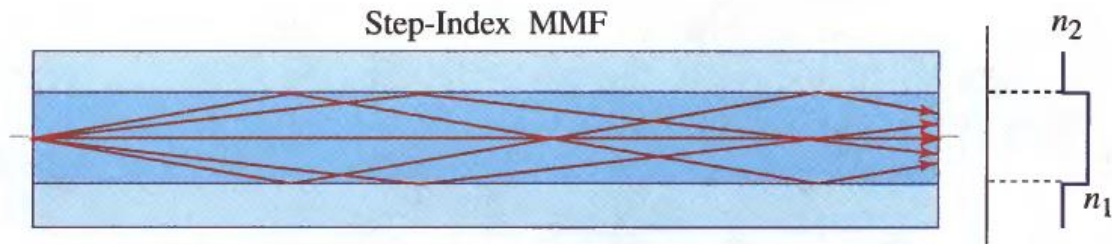


Figure II.6: Schematic presentation of the way light rays propagate inside a multimode step-index optical fiber. Taken from [99].

The photo-written waveguides could be considered as an optical fiber with an infinite cladding which is the glass. The Δn is given by:

$$\Delta n = \frac{n_1 - n_2}{n_1} \quad (\text{II-3})$$

An incident light beam into the fiber/waveguide could be guided if it makes an angle θ with the fiber axis that is smaller than $\bar{\theta}_c$ with $\bar{\theta}_c = \cos^{-1}(n_2/n_1)$. An acceptance angle θ_a is required so the light is guided with: $\theta_a = \sin^{-1}NA$ where NA is the numerical aperture of the fiber/waveguide as given by:

$$NA = \sqrt{n_1^2 - n_2^2} \quad (\text{II-4})$$

The acceptance angle/the numerical aperture determines the cone of acceptance of the fiber/waveguide as shown in Figure II.7. The guided rays inside the fiber exit while diverging according to the acceptance angle i.e. numerical aperture.

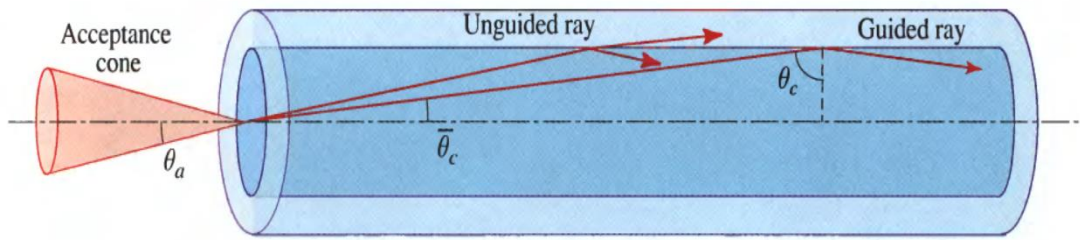


Figure II.7: The acceptance angle θ_a of an optical fiber. The rays within the acceptance cone are guided inside the fiber by total internal reflection. The numerical aperture is given by: $NA = \sin\theta_a$. Taken from [99].

For an optical fiber or perfectly circular waveguides, the parameter V allows to identify the number of modes propagating in the waveguide i.e. if the waveguide/fiber exhibit a single mode or a multimode aspect for a specific wavelength, it is given by:

$$V = 2\pi \frac{a}{\lambda} NA \quad (\text{II-5})$$

The parameter V depends mainly on the NA i.e. Δn and the dimension of the waveguide a , once the propagating wavelength is fixed. Single mode waveguides/fibers exist in the region where $V < 2.405$. Beyond that region, the waveguides/fibers represent a multimode aspect [98]. Many modes other than the fundamental mode could propagate. So, in order to control the V parameter in waveguides, one could change the photo-induced Δn and/or the dimensions of the waveguides. However, one should mention, that the photo-written waveguides are not always circular ones, especially in this project. They are elliptical. Still, one can approximate the V parameter using (II-5).

II.3.2. Depressed cladding waveguides

Actually, waveguides could be written in two ways: standard waveguides as mentioned in the previous section and depressed cladding waveguides (DCWs). Following laser-glass interaction a smooth Δn is produced (with the right parameters). However, the photo-induced Δn is not always a positive one. Sometimes it is a negative one [100] which complicates the creation of waveguides. Therefore, researchers have found a way to live with negative Δn and started creating depressed cladding waveguides.

For instance, in silver containing zinc phosphate glasses used in this project, using a 250 kHz repetition rate laser could induce a negative Δn as shown in Figure II.8. This part will be discussed more in detail in Chapter III

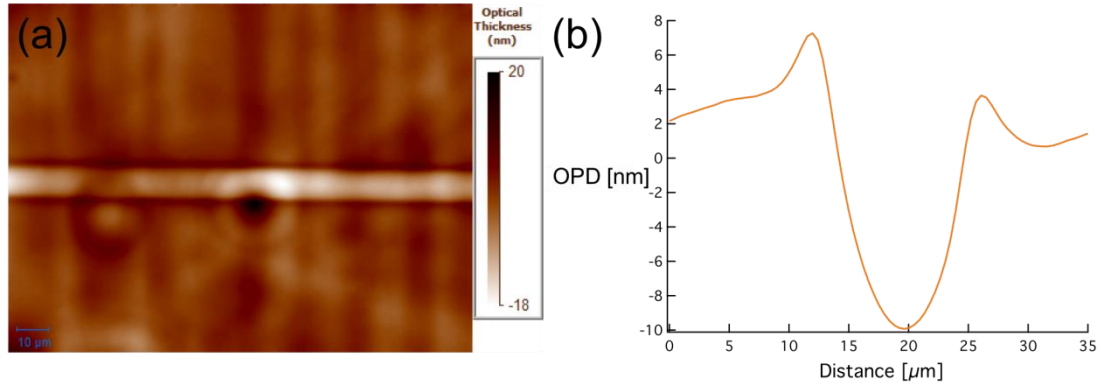


Figure II.8: (a) Top View phase contrast image of a type I waveguide written in silver containing zinc phosphate glass under white light illumination (b) Optical Path Difference (OPD) profile associated to the waveguide. A negative OPD is observed.

Another example of negative Δn is in ZBLAN glasses as reported by Bérubé [101]. A depressed waveguide cladding was made by writing a series of waveguides exhibiting a negative Δn in a ring shape as shown in Figure II.9. In that case, the guiding process takes place inside the non-irradiated zone where the refractive index is higher compared to the modified region. This process eventually requires more time and more processing to the glass in order to make a waveguide. This technique was also used by other researchers to make waveguides in phosphate glasses [102] and ZBLAN glasses also [103].

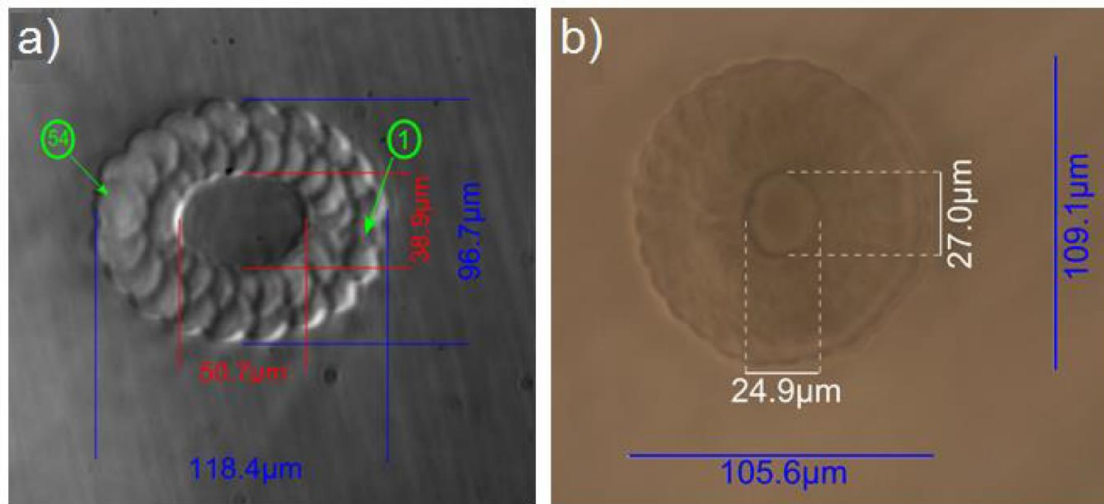


Figure II.9: Transverse view of a depressed cladding waveguide (DCW) (a) composed of 54 DCW distributed over 2 rings (b) composed of 212 DCW distributed over 4 rings. Taken from [101]

II.3.3. Couplers:

If two waveguides/fibers are close enough such as their evanescent fields overlap, light can be coupled from one to the other based on the evanescent field interaction. Light could be transferred between waveguides allowing to make optical couplers and switches. Based on coupled-mode theory [104] we can consider the coupling between two waveguides/optical fibers as one waveguide/fiber creating a perturbation for the second one [105]. The light injected in one waveguide/fiber is coupled to the other one. Generally, in order to have the best coupling effect, the two waveguides/fibers should be identical (same dimensions, same Δn) exhibiting the same propagation constant. Let's consider two identical parallel waveguides separated by a distance (center to center) "d" and with an interaction distance "L" as shown in Figure II.10.

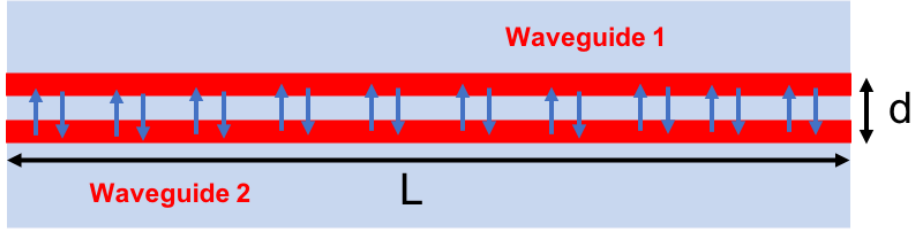


Figure II.10: Schematic presentation of two close waveguides interacting along a distance "L" and separated by a distance "d". The power is coupled between them.

The power could be partially or totally coupled from waveguide 1 (WG1) to waveguide 2 (WG2) depending on the separation distance "d" and interaction distance "L". The coupling is defined for circular cores by a coupling coefficient given by [106]:

$$C = \frac{(2\Delta n)^{1/2} u^2 K_0(wd/a)}{aV^3 K_1^2(w)} \quad (\text{II-6})$$

where u and w are the normalized transverse parameters in the core and in the cladding, respectively. They are related to the normalized frequency by the equation:

$$V^2 = u^2 + w^2 \quad (\text{II-7})$$

and $K_l(w)$ is the second order of Bessel function, l is the azimuthal parameter of the LP_{lm} propagating modes, a the radius of the fiber, d separation distance between the two waveguides. The parameter u could be found by a solution of the characteristic equation of an optical fiber. For more detail, the reader is invited to the following references [99, 105, 107].

The power coupled between two identical waveguides is given by:

$$P_{\text{Coupled}} = P_0 \sin^2(CL) \quad (\text{II-8})$$

where P_0 is the input power and L the interaction distance between the waveguides.

When considering two identical waveguides, which is generally the case, a total transfer of power could occur from one waveguide to another after a specific distance called beat length calculated based on the coupling coefficient:

$$z_B = \frac{\pi F}{C} \quad (\text{II-9})$$

Where F is given by:

$$F = \frac{1}{\sqrt{1 + \left(\frac{\Delta\beta}{2C}\right)^2}} \quad (\text{II-10})$$

with β as the propagation constant and C , the coupling coefficient given by (II-6). In this case, where the waveguides are identical, $F=1$ given that they exhibit the same propagation distance; therefore $\Delta\beta = 0$.

Generally, the coupling coefficient and the power exchange are dictated by the waveguides parameters only. However it was found that the polarization of the guided beam could affect the coupling coefficient over a long distance of interaction in directional couplers written using DLW technique, as reported by Crespi et al. [108] and shown in Figure II.11.

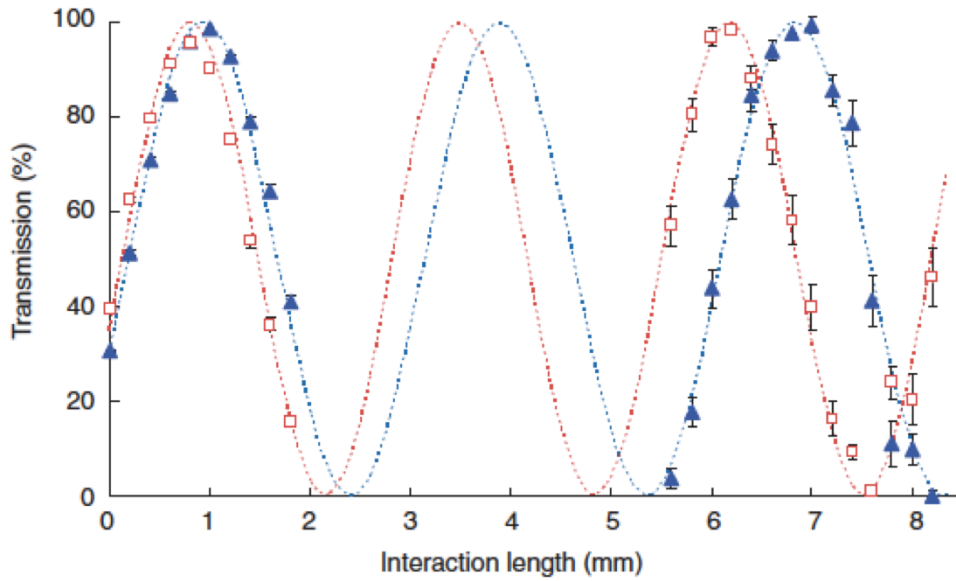


Figure II.11: Horizontal (squares) and Vertical (triangles) polarization transmission of laser written directional couplers as a function of the interaction length. First, the effect of the polarization is so slight, however when increasing the interaction distance, a bigger shift occurs indicating that the coupling effect could be altered based on the injected light polarization. Taken from [108].

If the reader is interested in more details about coupling he is referred to the following references [98, 104].

Directional couplers were inscribed inside glasses using direct laser writing. The first demonstration of directional couplers was in a borosilicate glass using a high repetition rate frequency doubled Ti:Sapphire oscillator [109]. It consisted of a 15 mm straight waveguide and a three-segment waveguide 3.5 μm away from the centre of the straight waveguide (Figure II.12). It had 5 cm radius arcs at the ends with a straight sector in the middle. The 9 mm long line in the middle was parallel to the straight waveguide providing a 9 mm interaction length between the two waveguides as shown in Figure II.12. The following coupler exhibited a coupling ratio of ~ 1.9 dB at 633 nm wavelength [109].

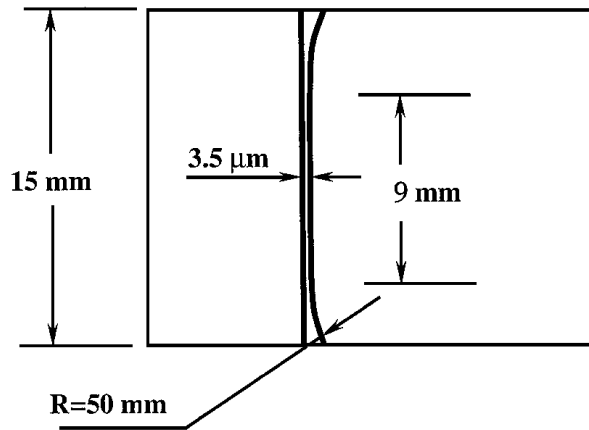


Figure II.12: Schematic presentation of the first demonstration of a directional coupler presented by Strelstov et al [109].

Eaton et al. demonstrated low-loss and efficient directional couplers operating in the telecom wavelengths using a 1 MHz repetition rate fiber laser [110]. A coupling ratio of $\sim 99\%$ as well as the creation of a 50-50 coupler were reported for telecom wavelengths between 1310 nm and 1550 nm. The couplers consisted of two symmetric double S-bend waveguides as shown in Figure II.13. For the 50/50 coupler the waveguides were separated by $17.5 \mu\text{m}$ while the interaction distance was 20.6 mm (Figure II.13).

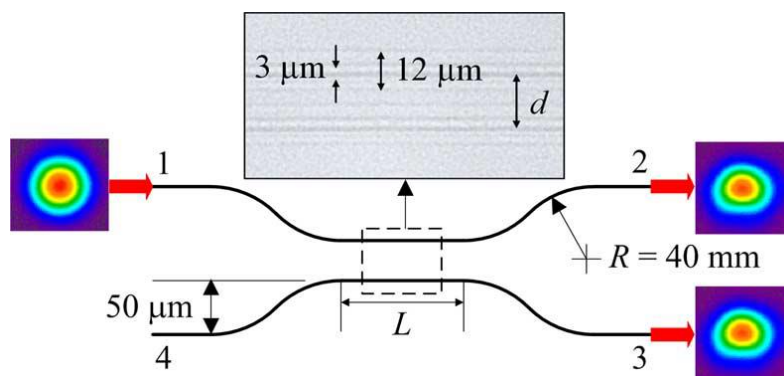


Figure II.13: Schematic presentation of a 50-50 directional coupler. The light is injected in one branch and 50% of the power is coupled into the other branch. Taken from [110].

The following reported couplers were written in the 2D planes, however, an interesting work reported by *Kowalewicz et al.*, exhibited a 3D, 3x3 directional coupler [111]. The design was three waveguides fabricated on the edges of an equilateral triangle as depicted Figure II.14.a. A 43%:28%:29% coupling ratio was reported at the output following 800 nm laser injection (Figure II.14.b). The coupler

was manufactured in soda-lime glass using a 5.85 MHz repetition rate Ti:sapphire oscillator [111].



Figure II.14: (a) Schematic presentation of the 3D coupler (b) Mode profiles of the output indicating that the light is coupled in the three branches with a ratio of 43%:28%:29%. Taken from [111].

II.3.4. Beam splitters

A beam splitter consists of an optical component splitting light in an adiabatic process into two or more branches while conserving the spatial mode distribution. One of the first beam/power splitters was reported in 1999 in fused silica using a low repetition rate 1kHz Ti:sapphire oscillator and longitudinal writing geometry. It was a Y-shaped beam splitter dividing the input light into two different outputs at a 514.5 nm wavelength [112].

An impressive demonstration of high quality low loss beam splitters has been reported in 2005 by *Liu et al.* [113]. A 1 to 8 optical waveguide beam splitter operating at 1.55μm was fabricated in fused silica using a 150kHz Ti:Sapphire laser. The total length of the component was 18 mm. It was composed out of 7Y junctions as shown in Figure II.15.a. The curvature radius was from 200.005 μm to 225.010 μm to minimize any bending losses. The input light was successfully split into eight output branches as shown in Figure II.15.b.

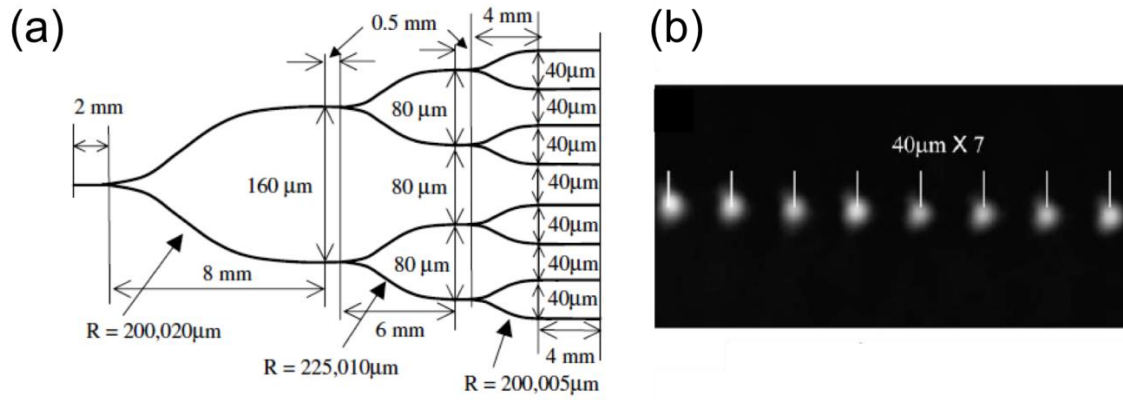


Figure II.15: (a) Schematic design of the 1 to 8 beam splitter with 7-Y junctions (b) Side view output of the far-field modes [113]

Another approach for 3D beam splitters by the group of S.Nolte where a 1x3 splitter (Figure II.16) was written inside fused silica operating at 1.05 μm wavelength using a 1 kHz Ti:sapphire laser [114].

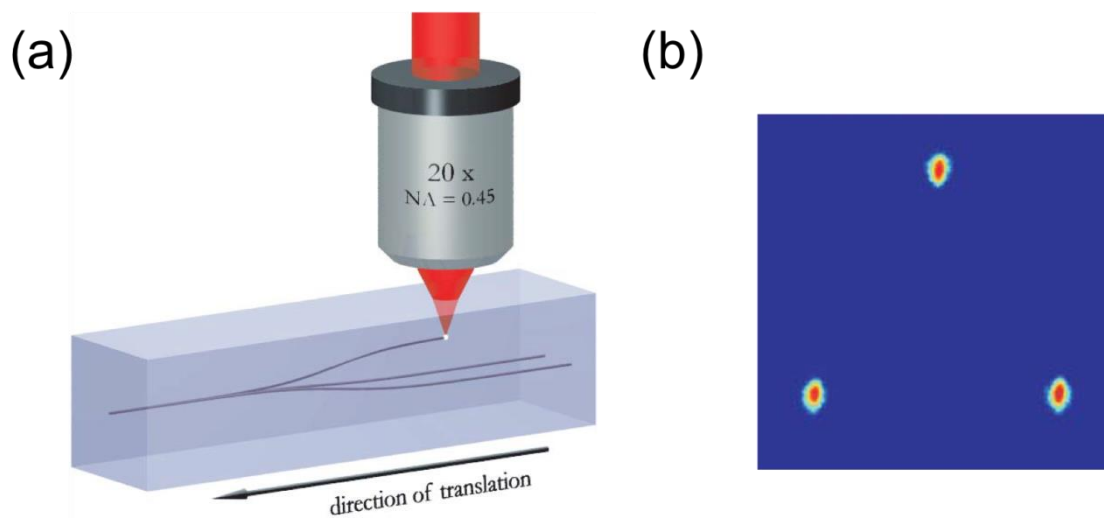


Figure II.16: (a) Schematic presentation of the laser writing of the 1x3 beam splitter (b) Side view output visualization of the divided modes [114].

II.3.5. Waveguide Bragg grating (WBG)

A waveguide Bragg grating (WBG) consists of a periodic perturbation of the effective refractive index of the light guided inside the bulk material. This perturbation is based on a modulation of Δn that reflects particular wavelengths of light, centered mainly at the Bragg wavelength while transmitting all the other

wavelengths. It acts as a filter or reflector of light. Two methods of fabricating WBG exist, the point by point (PbP) method and the modulated burst method.

The first demonstration of a WBG was in 2006 by Marshall et al [115] using the PbP method. It consists in modulating the Δn point by point by modulating the laser repetition rate and speed allowing to control the spatial separation between each pulse as schematically presented in Figure II.17.

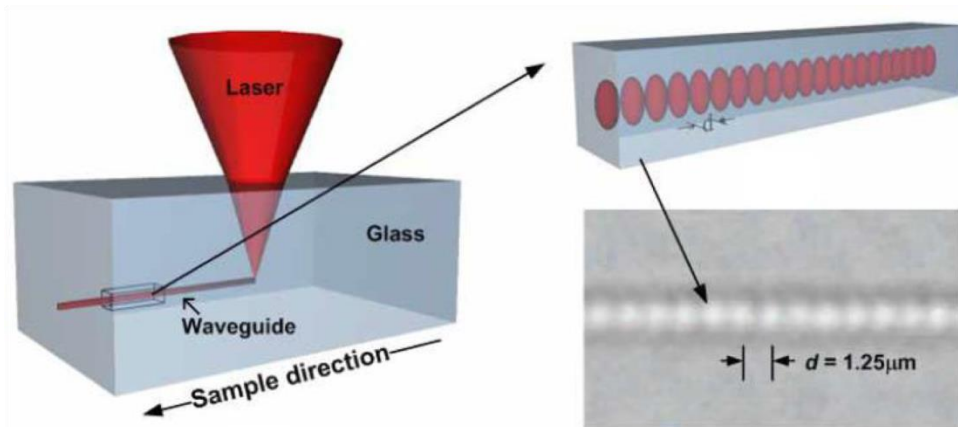


Figure II.17: Schematic presentation of the PointbyPoint (PbP) process of writing a Waveguide Bragg Grating (WBG) as well as a bright field image of the top view of the WBG. Taken from [101]

The waveguide was written before the grating structure and the WBG extended all over the waveguide length (Figure II.18.a). A Bragg reflection was observed at a 1550.63 nm wavelength, as shown in Figure II.18.b [115]. *Zhang et al.* demonstrated later on that WBGs could be fabricated using the PbP method with only one scan of laser writing [116].

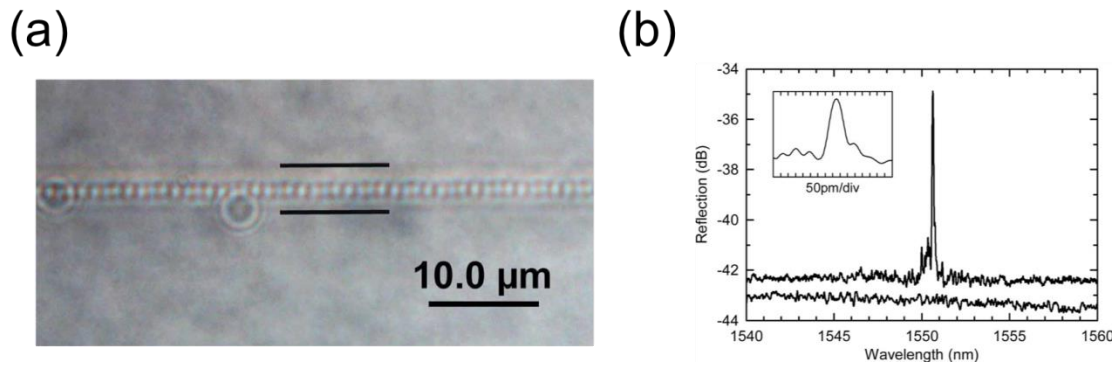


Figure II.18: (a) Top view of the Waveguide Bragg Grating (WBG). The waveguide is indicated by the black lines (b) Reflection spectrum of the written WBG (upper curve) compared to the transmission of a normal waveguide (lower curve). Taken from [115].

The second method is the modulated burst method where the laser source was modulated to generate a burst of laser pulses. The WBG is written with a one step process while modulating the Δn based on the modulation of the pulse energy. Many WBGs were created using this technique [117, 118]. Given that this project will not be taking into consideration WBG manufacturing, this part will be limited and if the reader is interested in more details, the following reference [118] is of interest.

II.3.6. Waveguide lasers

Waveguide lasers (WGL) are lasers based on the creation of waveguides in doped glasses by the direct laser writing process as reported by many research groups [119, 120]. The glasses were doped with rare earth elements like erbium Er or Ytterbium Yb while the waveguides were used as a gain medium and mainly external Bragg gratings to create the laser cavity. The first femtosecond laser written waveguide laser was manufactured in a Er:Yb doped phosphate glass (Kigre QX) in 2004 [119]. It consisted of a 20 mm active waveguide, optically pumped at 975 nm by two laser diodes and two external fiber Bragg gratings to create the laser cavity. A maximum output power of 1.7 mW was obtained at 1.533 μm wavelength. Furthermore, to improve the power stability, a preliminary result was obtained on the feasibility of a Distributed feedback (DFB) laser configuration by writing the Bragg gratings inside the glass substrate, in 2008 [120]. The glass was an Er:Yb doped phosphate glass (Kigre QX). A 20 mm long waveguide and a superposed Bragg grating were fabricated in a single step writing process. The laser device demonstrated operated at a 1537.627 nm wavelength and delivered a 0.36

mW maximum output under 710 mW incident pump power in a combined pumping scheme (980 and 976 nm pump wavelengths) [120]. The mentioned results were mainly in phosphate glasses, but WGL were also manufactured in other types of glasses such as silicate [121], chalcogenide [122] and fluoride glasses [123]. Since this project will not be taking into account the creation of WGL, this part will be limited to the information provided above. If the reader wants further information, the following reference [124] is of interest.

II.3.7. Photonic lantern

Direct laser writing in glasses led also to the formation of photonic lanterns (PL) which are used for instance for astronomy purposes. PLs consist in writing multiple waveguides forming one multimode (MM) rectangular waveguide that gets separated into several single mode (SM) waveguides on the exit facet of the glass, as schematically depicted in Figure II.19.

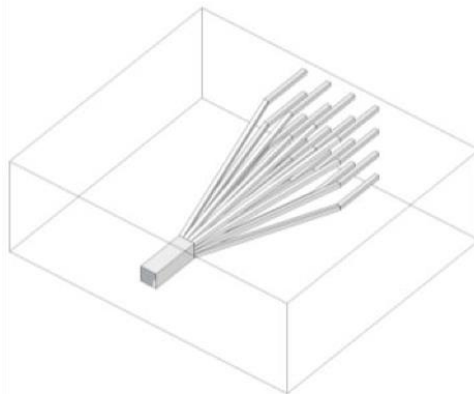


Figure II.19: Sketch of a photonic lantern (PL) starting by a multimode rectangular waveguide separating into several single mode waveguides. Taken from [125].

It acts as a mode converter from MM to SM. The first PL was created by *Thomson et al.* where 16 SM waveguides arranged in a two-dimensional (2D) 4x4 array, with an inter-spacing of 50 μ m were brought together at the opposite facet creating one MM waveguide in borosilicate glass (Corning Eagle) as shown in Figure II.20. As expected, the modes of MM fiber are split into an array of SM waveguides as shown in Figure II.20.c.

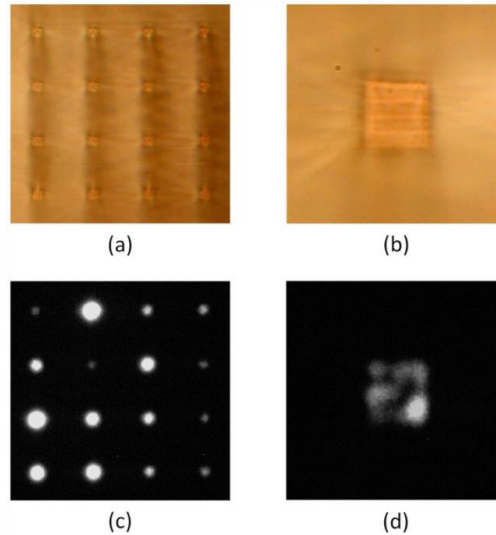


Figure II.20: Side view bright field photos of the (a) 4x4 single mode waveguides (b) rectangular multimode waveguide. Output mode images of (c) the 4x4 single mode waveguides following the injection in the rectangular multimode waveguide (d) rectangular waveguide mode following the injection of light in the 4x4 single mode array waveguides. Taken from [125].

Later on, the creation of PLs in Corning Eagle 2000 glass was demonstrated for astronomical uses operating at $1.55 \mu\text{m}$ wavelength [126]. Eventually, this work led to the creation of Modular Photonics a company selling glass based micro-chips (processed by direct laser writing) used for mode-selective applications [127].

This section has presented a general review of the optical components written in different types of glasses using the DLW technique. The following section will emphasize the DLW process in phosphate based glasses.

II.3.8. Study of phosphate glasses

Since the 1990s, a considerable amount of research has focussed on phosphate glasses. Phosphate glasses exhibit many advantages compared to silica glasses. Those advantages are represented by the capacity of the host matrix to accept a high quantity of rare earth and metals, in particular silver [128]. However, phosphate glasses have a low resistance to water corrosion, due to the pentavalence of the phosphorus atom. The introduction of an oxide modifier was necessary in order to reduce the corrosion of these glasses to water. In particular, the introduction of zinc oxide (ZnO) into phosphate glasses has been reported to greatly improve chemical stability [129], thus the reason for using zinc phosphate glasses. In the mid 1990s, a patent was registered by Corning for the first

invention of zinc phosphate glasses called zinc containing phosphate glasses [130]. Many experiments to create waveguides in zinc phosphate glasses were attempted in past years. Writing in the athermal regime while using kHz laser repetition rates and pulses in the microjoule (μJ) range allows structural change of the glass based on the nonlinear optical absorption where the matter has time to thermally relax between the laser pulses as explained in section I.3.4. A positive Δn could be generated in a controlled way allowing the direct fabrication of optical waveguides with low losses [63]. However, writing in the thermal regime while using a few MHz repetition laser and pulses in the nanojoule (nJ) range prevents the thermal relaxation of the glass between two consecutive laser pulses causing heat accumulation. Therefore, the glass behaves in another way compared to the athermal regime. Mainly the observed Δn is a negative one making the creation of optical waveguides more complicated in that case.

Many waveguides were inscribed in phosphate and zinc phosphate glasses. Single mode waveguides were written exhibiting a $\Delta n=3.5 \times 10^{-3}$ and propagation losses estimated to be 0.95dB/cm and 0.39dB/cm for 635 nm and 1550 nm respectively [63]. However, it was found that the glass response following laser irradiation highly depends on the glass composition as reported by Fletcher et al. [62]. Indeed, the O/P ratio is responsible for the sign of the Δn created inside the glasses [62, 100, 131, 132]. Many zinc phosphate glasses were fabricated and irradiated and only glasses exhibiting an O/P ratio of 3.25 exhibited positive Δn where the others glasses exhibited negative Δn [62, 100, 132]. Single mode waveguides at 660 nm where the ratio of O/P=3.25 was also written in zinc phosphate glasses exhibiting a $\Delta n=3 \times 10^{-4}$ [131]. Ferrer et al. also reported the laser writing of waveguides operating at 633 nm [133].

As mentioned before, one of the advantages of phosphate glasses is their capacity to be doped with high concentrations of rare earth and metals. Many research groups created waveguides inside such glasses aiming towards the creation of active waveguides. Active waveguides allow light amplification by being the gain medium in WGL integrated in glass chips. An optical gain at a wavelength of 1.5 μm inside Er:Yb doped waveguides was reported in 2002 by *Osellame et al.* for the first time in Er:Yb doped phosphate glass [59]. *Fletcher et al.* again demonstrated the effect of the O/P ratio on the sign of Δn created following direct laser writing but this time in Er:Yb doped zinc phosphate glasses. A waveguide exhibiting total losses of 4.3 ± 0.4 dB (including a coupling loss of 2.3 ± 0.2 dB, Fresnel losses of 0.360 ± 0.005 dB and the Er^{3+} absorption of 1.27 ± 0.1 dB at 660 nm $\rightarrow \sim 0.74$ dB/cm) and a $\Delta n=1 \times 10^{-3}$ was reported for a 5 mm waveguide following the injection of a 660 nm laser [132]. Later on, in 2008, *Osellame et al.* managed to make a

waveguide laser (WGL) inside Er:Yb phosphate glass (QX, Kigre Inc) exhibiting a $\Delta n=8 \times 10^{-3}$, 7 dB of gain, 0.4 dB/cm propagation losses in the C-band telecom wavelengths (1530-1565 nm) [134]. In 2012, Fletcher also reported 1dB/cm gain at 1534 nm in a waveguide written inside Er-Yb co-doped zinc phosphate glass with a $\Delta n=3 \times 10^{-3}$.

II.4. Silver containing zinc phosphate glasses

The glasses used in this project are silver containing zinc phosphate glasses exhibiting different silver concentrations. These glasses were developed and optimized during many years of research at ICMCB and the laser writing process took place in the SLAM group at CELIA. The detailed composition of the glasses is shown in Table II-1.

However, some experiments were conducted using Argolight glasses AG01 Argolight is a start-up company that was created by Arnaud Royon and Gauthier Papon who were working on the development and irradiation of silver containing zinc phosphate glasses at ICMCB and in the SLAM group. Currently, they sell microscope slides irradiated by femtosecond laser allowing the calibration of fluorescent microscopes in terms of resolution, fluorescence collection and spectral response.

Table II-1: Table summarizing the theoretical molar composition and the properties of the different zinc phosphate glasses used in this work. Taken from [135].

Sample	Name	[P] (%mol.)	[Zn] (%mol.)	[Ga] (%mol.)	[Ag] (%mol.)	T _g (±5°C)	O/P
PZnGa _{5.5}	PZn	56	38.5	5.5	0	435	3.58
PZnGa _{5.5} :Ag _{5.5}	PZnAg1	52.7	36.3	5.5	5.5	396	3.275
PZnGa _{5.4} :Ag ₈	PZnAg2	51.3	35.3	5.4	8	381	3.37

Based on the previous results on the zinc phosphate glasses as mentioned in the previous section II.3.8, the first silver containing zinc phosphate glass was a $40\text{P}_2\text{O}_5\text{-}55\text{ZnO}\text{-}5\text{Ag}_2\text{O}$ exhibiting an O/P ratio of 3.25. However, it was found that this composition was not stable for long terms and exhibited crystallization after around 65 months [11]. So, it was necessary to add an additional compound to stabilize the glass matrix. Therefore the choice fell on gallium oxide Ga_2O_3 , a glass former used in order to stabilize the glass matrix. Furthermore, one should mention that the introduction of ZnO and Ga_2O_3 did not interfere or modify the absorption bands of the glass. Both ZnO and Ga_2O_3 absorption bands neither overlap with the silver nor tend to promote the reduction of the silver ions inside the glass [11]. So, silver containing zinc phosphate glasses are zinc phosphate glasses where silver was introduced into the glass network in the form of silver ions Ag^+ .

II.4.1. Optical properties

To study the optical properties, the absorption spectrum in the UV range was monitored in non-containing silver glasses and silver containing glasses with different silver concentrations. The O/P ratio was roughly the same while the silver concentration was changed. The non-containing silver glass starts exhibiting an absorption around 230 nm, which is attributed to the presence of defects and impurities in small quantities in the glass [11]. However, for the silver containing glasses, the absorption band is remarkably higher and shifted towards the higher wavelengths i.e. lower energy levels. The higher the concentration of silver the more the absorption band is shifted as shown in Figure II.21. The following results imply that the incorporation of silver in the glass influences the absorption band of the glass by shifting it to higher wavelengths. This is a typical property of the silver ions integrated into the glass matrix. So, the bandgap of the glass is shifted to lower energy levels (higher wavelengths as shown in Figure II.21) implying that the silver ions enhance the photosensitivity of the glass.

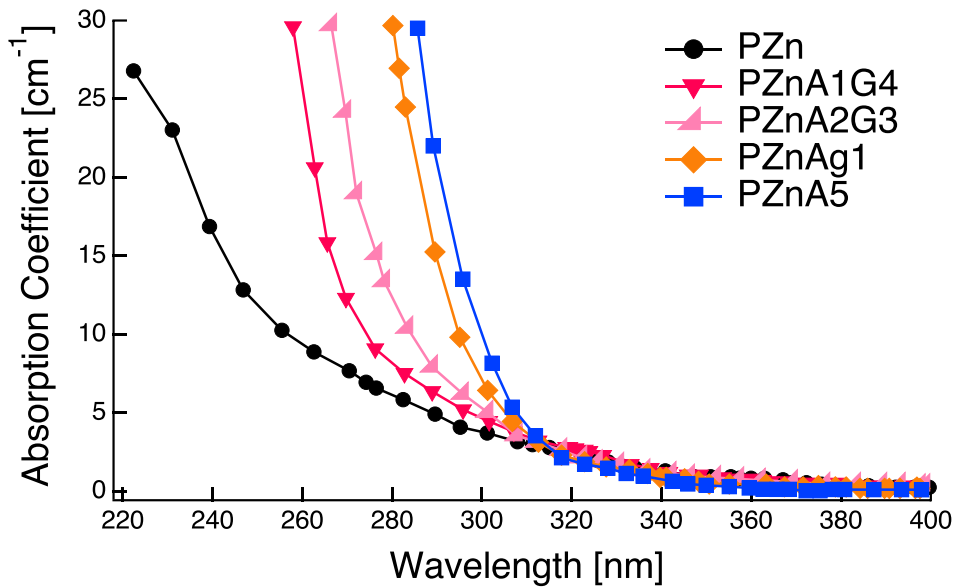


Figure II.21: Absorption coefficient as a function of the wavelength for zinc phosphate glass and silver containing zinc phosphate glasses with different silver concentrations. The silver containing glasses exhibit a higher absorption band and are shifted to higher wavelengths compared to non-containing zinc phosphate glass. Adapted from [11].

Overall, silver containing zinc phosphate glasses exhibit a good transparency window from the visible range to the mid IR as shown in Figure II.22 allowing applications in a good range of wavelengths.

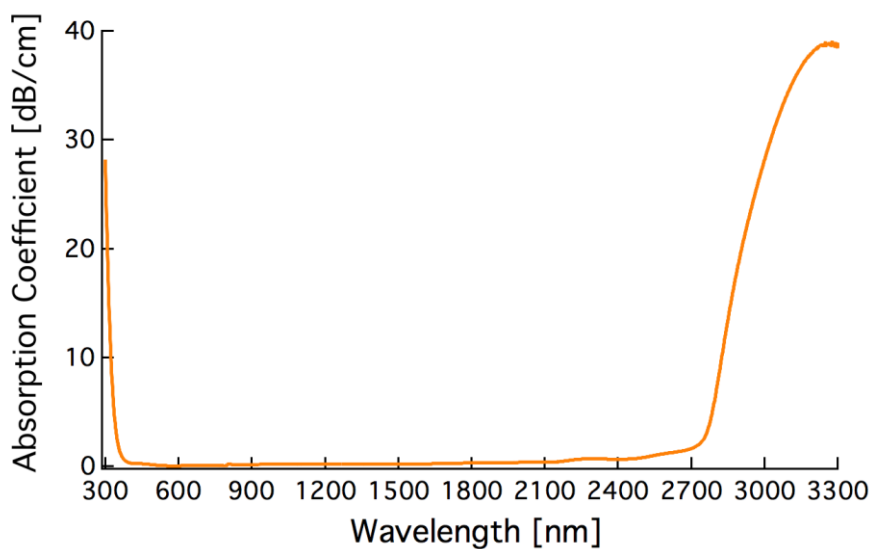


Figure II.22: Absorption as a function of the wavelength for the PZnAg2 sample from UV to IR. A good transparency window is observed between 380 nm and 2700 nm.

II.4.2. Laser-silver containing glasses interaction

The interaction between a laser and silver containing glasses exhibits an exotic response that totally differs from the standard laser-glass interaction in the literature. Following laser irradiation, photo-induced silver clusters Ag_m^{x+} are generated in the vicinity of the interaction voxel. This is based on a non-linear absorption mechanism, a pulse-to-pulse process by heat accumulation which results in the aggregation of silver atomic and ionic species. The formation of the photo-induced clusters could be explained by the following: after laser-glass interaction a reservoir of free-electrons is generated from the multiphoton process enabling the reduction of Ag^+ silver ions pre-existing in the glass into Ag^0 atomic states, which then aggregate with silver ions in order to form Ag^{2+} . Based on a chain reaction, larger silver clusters Ag_m^{x+} are formed from Ag^+ , Ag^0 and Ag^{2+} inside the glass matrix [44, 136], as schematically presented in Figure II.23. The transverse Gaussian beam profile induces the photo dissociation of the silver clusters in the centre region where the irradiance is higher [136].

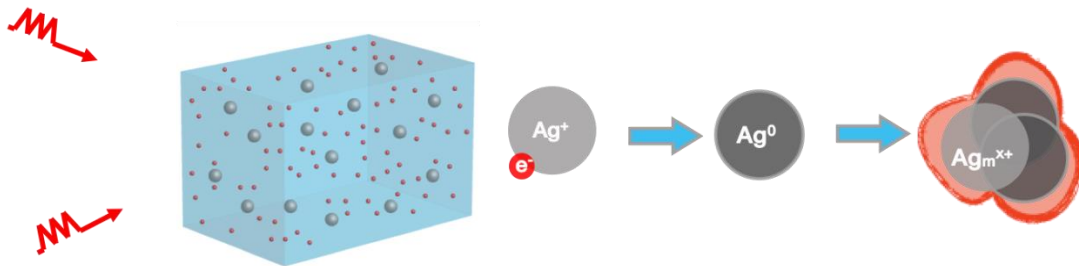


Figure II.23: Schematic presentation of the formation of silver clusters in silver containing glasses following laser irradiation.

The photo-induced silver clusters Ag_m^{x+} generally exhibit two main absorption bands around 290 nm and 345 nm [136-139] affiliated to the creation of $Ag_{\alpha}(1)$ and $Ag_{\alpha}(2)$ clusters respectively [139] resulting in a broad band fluorescence response under UV-Blue excitation as shown in Figure II.24. $Ag_{\alpha}(1)$ and $Ag_{\alpha}(2)$ could be the dominating clusters exhibiting the two dominating absorption bands. Also other types of clusters are generated following DLW that were identified in a previous report from our group [139] and presented in Table II-2.

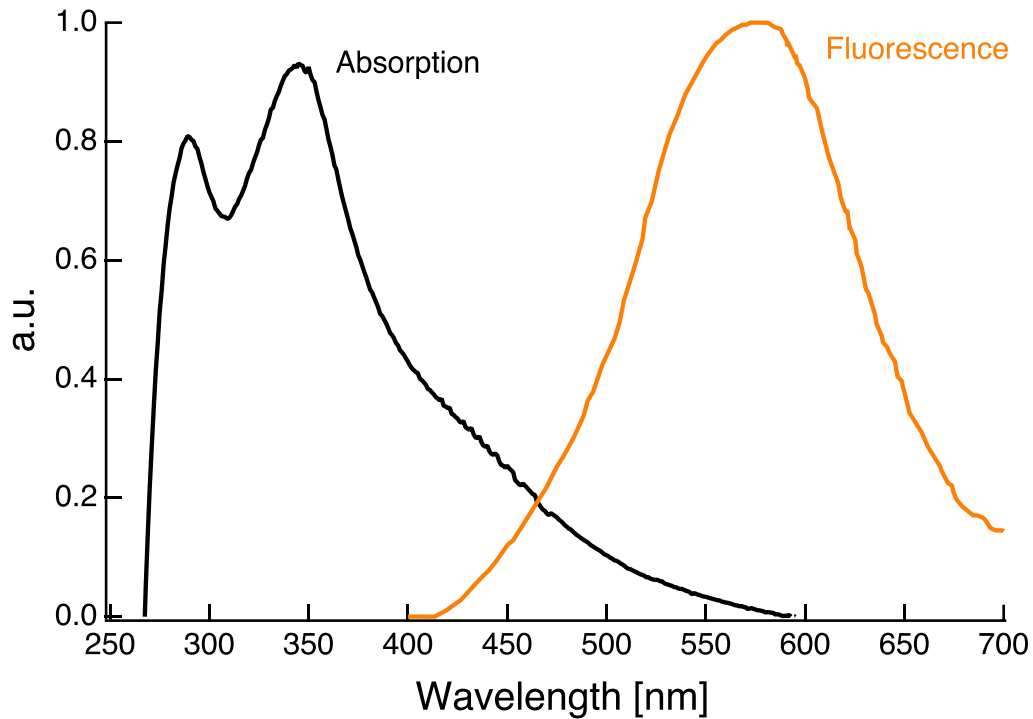


Figure II.24: Absorption (black) of the photo-induced silver clusters following laser irradiation exhibiting two main absorption bands around 290 and 345 nm. Fluorescence emission (orange) under blue light excitation at 405 nm.

Table II-2: Different silver (Ag) species identified following DLW in silver containing glasses as reported in [139].

Ag specie	Peak absorption [nm]
$Ag_{\alpha}(1)$	287 ± 2
Ag_2^+	302 ± 3
$Ag_{\alpha}(2)$	340 ± 2
Ag^0	387 ± 4
Ag_n	442 ± 1

Normally, the laser used for writing in such glasses is a high repetition laser, around 10 MHz emitting femtosecond pulses at 1030 nm wavelength. However, the glass is transparent at a wavelength of 1030 nm, as is shown in Figure II.22. Using a femtosecond laser induces non-linear effects i.e. four-photon absorption process in this case. This process was already explained in detail in section I.3.3.a. In addition to that, thanks to the non-linear process, structures below the diffraction

limit could be created inside silver containing glasses, as it has been reported earlier by our group [136].

Static direct laser writing of silver containing glasses, i.e. laser fixed and sample fixed, results in the creation of 3D fluorescent (due to the silver cluster formation) structures exhibiting dimensions below the diffraction limit [136]. In order to have a better idea of the morphology of such structures, they were visualized using a fluorescence confocal microscope to resolve the structures as shown in Figure II.25. The confocal fluorescence images of the top view of the structures reveal a ring shape of fluorescence [136]. The fluorescence is attributed to the distribution of silver clusters; therefore, the clusters are distributed around the interaction voxel. The ring shape is due to the photo dissociation of the silver clusters created in the middle thanks to the transversal Gaussian profile of the laser beam (Figure II.25.b-d). The side view photo exhibits two fluorescent lines arranged into a pipe shape corresponding more or less to the Rayleigh range (Figure II.25.c-e) [44]. Eventually, one can say that the structures' morphology is dictated by the laser beam profile.

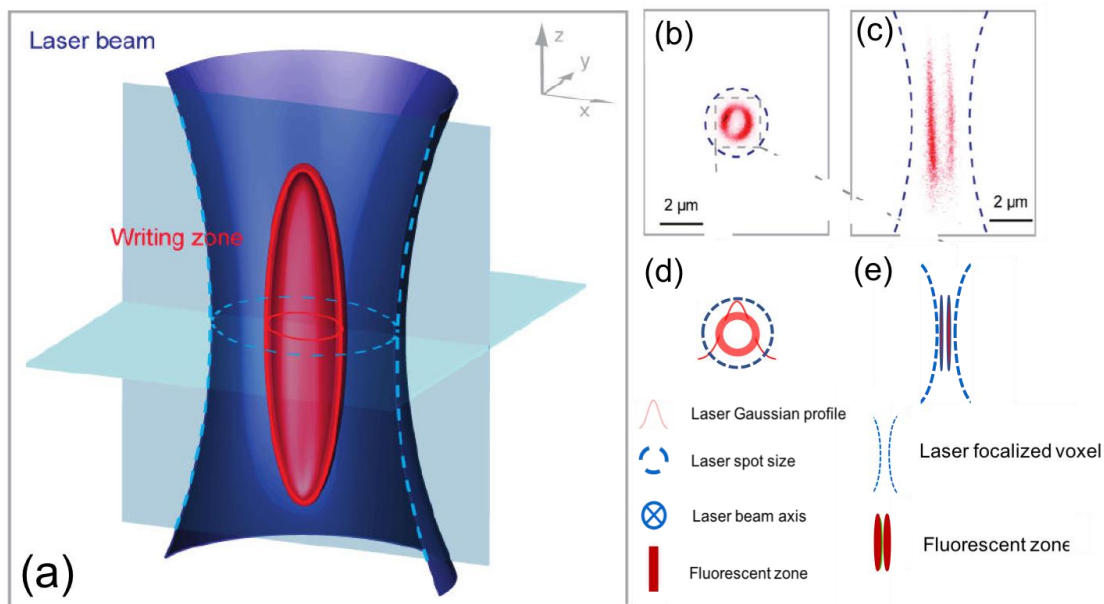


Figure II.25: (a) Sketch of the morphology of the structures following static direct laser writing (DLW) (b) confocal fluorescence images under UV excitation ($\lambda_{exc}=405\text{nm}$) of top view (xy) plane, ring shape (c) side view (xz) plane, two fluorescent lines in a pipe shape [136]. Schematic presentation of the writing process for (d) top view (xy) plane, photodissociation of the clusters in the middle (e) side view (xz) plane.

II.4.2.a. Physical processes associated to the formation of silver clusters

To better understand the laser-glass interaction and the spatial distribution morphology of the silver clusters, a theoretical model [140] was presented by our group (with the collaboration of other colleagues in CELIA and IMS) explaining the different physical mechanisms involved in the formation of silver clusters. The model takes into account the different non-linear photoionization processes, laser energy deposition followed by laser heating of the sample, diffusion ions, kinetic reactions and photo dissociation of metallic species [140]. The different physical mechanisms responsible for the formation of silver clusters (taken from [140]) are presented briefly herein. However for more details, the reader is referred to reference [140]. One should note that all the physical parameters for the modelling have been previously measured by our group and some data were taken from handbooks. All parameters could be found in reference [140]. First, a reservoir of free electrons is generated during the laser pulse: yellow circle that corresponds to the radial distribution of the free electrons as shown in Figure II.26. In the green region in Figure II.26.a, the formation of silver atoms Ag^0 starts to take place ($\text{Ag}^+ + e^- \rightarrow \text{Ag}^0$) where the concentration of free electrons is at its peak. During the formation of Ag^0 , holes are trapped by silver ions Ag^+ : $h^+ + \text{Ag}^+ \rightarrow \text{Ag}^{2+}$ and the product is assumed not to be mobile. In fact, Ag^{2+} should be considered as a hole trapped in proximity of a silver ion Ag^+ instead of a doubly ionized silver ion. Thus, the mobility of such pair is negligible compared to the mobility of silver ions Ag^+ , due to its delocalization around the phosphate chains that form the glass network. The reaction $e^- + \text{Ag}^+ \rightarrow \text{Ag}^0$ ends when the concentration of electrons vanishes. At that moment, the spatial distribution of Ag^0 corresponds to the slightly diffused distribution of pre-existing free electrons (green circle, Figure II.26.b). The absorption of the laser pulse induces and increases the temperature in the region resulting in thermal diffusion (Blue arrows, Figure II.26.b). The diffusion of Ag^0 (green arrows, Figure II.26.b) is highly activated by the temperature which allows these species to meet with Ag^+ ions and take a part in the following kinetic reaction: $\text{Ag}^0 + \text{Ag}^+ \rightarrow \text{Ag}_2^+$. The red circle (Figure II.26.b) reproduces the beginning of the reaction in the area of maximal concentration of Ag^0 . The reaction of the first stage of silver cluster formation $\text{Ag}^0 + \text{Ag}^+ \rightarrow \text{Ag}_2^+$ ends when the concentration of silver atoms Ag^0 wears off. So, the spatial distribution of Ag_2^+ corresponds slightly to the spatial distribution of pre-existing Ag^0 (red circle, Figure II.26.c). The trapping process and reactions are so fast that the concentration of free electrons, holes and Ag^0 wears off before the next laser pulse. The following laser pulse destroys the silver clusters in the center by photo-dissociations where

the laser pulse is so intense (Figure II.25). The next laser pulse again creates a reservoir of free electrons which triggers kinetic reactions responsible for the formation of silver clusters. The previously mentioned cycle repeats itself from one pulse to another and the non-dissociated silver clusters gathers on the periphery of the laser beam forming a ring shaped structure [33, 44, 136, 140, 141] following a train of pulses (Figure II.26.d). Thus, the fast diffusing of free electrons destroys the initial spatial charge neutrality of the electron-hole plasma inside the focal spot and creates an ambipolar electric field. It accelerates the diffusion of ions by a factor of two. Therefore, the electron-hole trapping process provides the formation of frozen charge redistribution in space and corresponding radial static electric field \vec{E}_{dc} (black arrows, Figure II.26.d) [140].

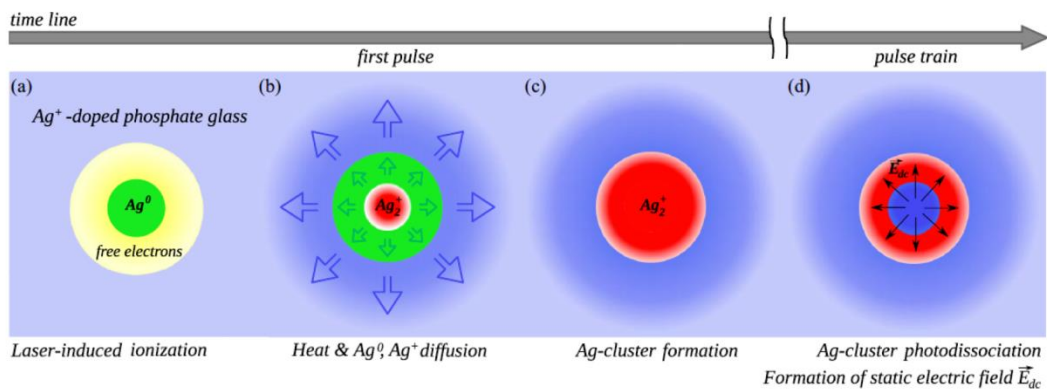


Figure II.26: Scheme of the formation of silver clusters during laser-glass interaction in silver containing glasses. Taken from [140].

Normally, glass as a centrosymmetric material exhibits no second harmonic generation response. However, based on the electric field \vec{E}_{dc} generated by the movement on the charged species a second harmonic generation response has been observed [142]. The process of creation of silver clusters inside silver containing glasses gives rise to a static electric field induced second harmonic generation (EFISHG). Following DLW of linear structures and under 1030 nm excitation, EFISHG patterns were observed as shown in Figure II.27.b. Figure II.27.a shows the typical cluster distribution under UV excitation while Figure II.27.c shows the superposition of the fluorescence and EFISHG patterns showing correlated but distinct spatial distributions [143]. Those results exhibit an advantage for the silver containing glasses representing a second harmonic response following DLW which is not common in other glasses. In case the reader is interested, the following readings [142, 144] are recommended.

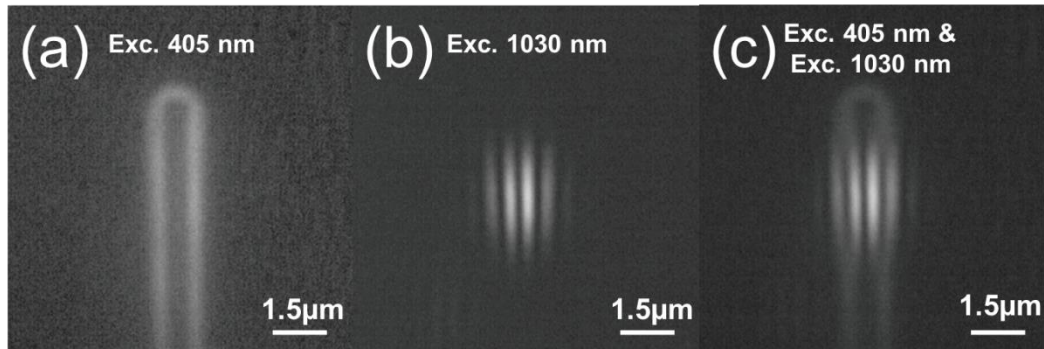


Figure II.27: (a) Fluorescence pattern of a written line under 405 nm excitation; (b) four-line of electric field induced second harmonic generation (EFISHG) under 1030 nm femtosecond laser excitation (c) superposition of the fluorescence and EFISHG correlated patterns under 405 nm and 1030 nm excitation. Taken from [143].

II.4.3. Writing window in silver containing glasses

Earlier, it was mentioned that the laser irradiation process in silver containing glasses occurs with a femtosecond laser, high repetition rate and at a wavelength of 1030 nm. A study was performed during the past years by previous colleagues about the evolution of the fluorescence intensity i.e. the creation of silver clusters as a function of the laser irradiance, number of deposited pulses and the repetition rate [11]. The laser irradiance is given by (I-23) in Chapter I and is related to the pulse energy. The study consisted in irradiating the glass with different laser irradiances for different laser repetition rates and monitoring the fluorescence intensity emitted by the structures under 405 nm excitation while collecting emitted fluorescence in a spectral range between 450 and 750 nm [11]. The results are presented in Figure II.28 in color scale: the lowest fluorescence intensity is represented in white, the highest in black and the intermediate intensities are exhibited in gradient red. The highest fluorescence intensity was observed at the highest irradiance possible at $11\text{TW}\cdot\text{cm}^{-2}$ below the explosion threshold and for a number of pulses of 10^7 .

Two conclusions could be derived from this study. In order to create silver clusters, a huge number of pulses is required as well as the right laser irradiance. The fluorescence intensity depends linearly on the irradiance while depending logarithmically on the number of pulses [44]. The second conclusion implies that a high repetition rate laser is required in order to activate and create the silver clusters. When using a low repetition rate laser, the creation of silver clusters is

possible but requires a longer time of exposure which limits the writing process. A minimum number of pulses is required in order to trigger the thermal process for silver cluster creation.

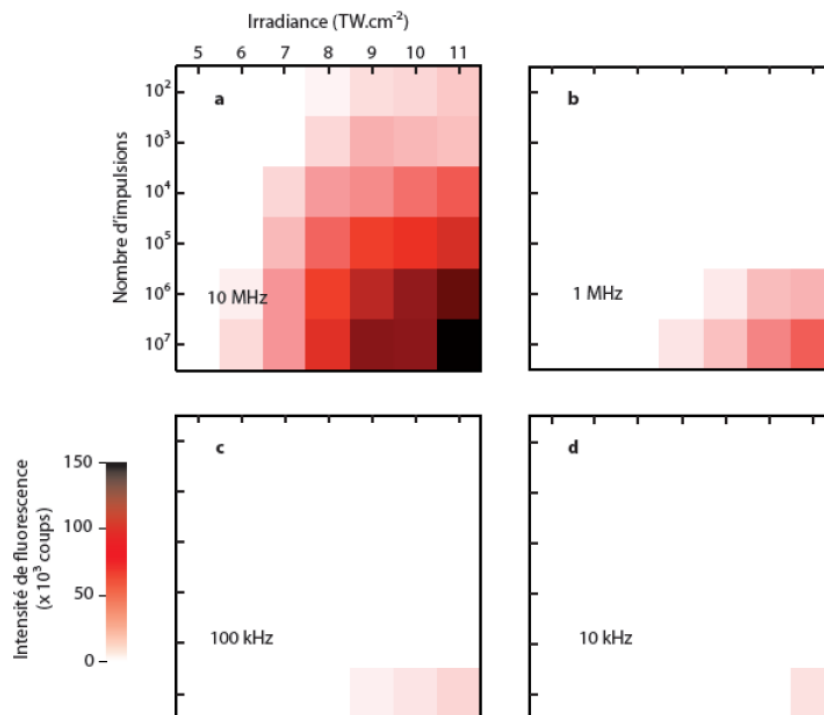


Figure II.28: Fluorescence intensity as a function of the laser irradiance and number of pulses for different laser repetition rates (a) 10MHz (b) 1MHz (c) 100kHz (d) 10kHz. Taken from [11].

II.4.4. Review of previous works on silver containing glasses

Few works were reported on direct laser writing inside silver containing zinc phosphate glasses. This is because the glass has been developed by the Institute of Chemistry of Condensed Matter of Bordeaux (ICMCB) since 2009, even though some research groups have reported some works on similar glasses. One should mention that silver doped glass is different from silver containing glasses. When talking about doping a material, the highest quantity is 2% mol of the main composition, once this limit is exceeded one can start talking about "silver containing" glasses.

In 2013 a Chinese group reported the creation of silver nanoparticles (NPs) following DLW using a 250 kHz repetition rate laser emitting at a wavelength of 800 nm using a writing speed of 150 $\mu\text{m/s}$. The glass was silver doped phosphate

with the following composition: $12\text{Al}_2\text{O}_3 - 10\text{Na}_2\text{O} - 70\text{P}_2\text{O}_5 - 0.5\text{Ag}_2\text{O}$ [145]. In 2015, a Russian research group reported the creation of color centres and luminescent silver NPs inside $0.55\text{Ag}_2\text{O} - 0.45\text{P}_2\text{O}_5$ and $0.5\text{Ag}_2\text{O} - 0.1\text{Nb}_2\text{O}_5 - 0.4\text{P}_2\text{O}_5$ using a 250 kHz repetition laser emitting at 800 nm using a writing speed of $2.5 \mu\text{m/s}$ [146]. In 2016, P. Kazansky in collaboration with a Russian research group using a glass ($40\text{P}_2\text{O}_5 - 55\text{ZnO} - 4\text{Ag}_2\text{O} - 1\text{Ga}_2\text{O}_3$) similar to the one used in this project reported the creation of luminescent silver NPs and birefringent micro-regions paving the way towards 6D information encoding following DLW [147]. The laser used was a 100kHz repetition rate emitting at a wavelength of 1030 nm [147]. In 2017, the same Russian research group reported the creation of ring shaped fluorescent silver clusters and silver NPs simultaneously in silver containing glasses in a single process for the first time [148]. The glass used was a $55\text{ZnO} - 41\text{P}_2\text{O}_5 - 4\text{Ag}_2\text{O}$ while the laser was the same as in the previous reported work [147]. Herein, we report that silver clusters and NPs were created inside silver containing zinc phosphate glasses with one process during this project as shown in Figure II.29. However, those results were not interesting for this framework given that the aim is towards the creation of optical components. Therefore no results or investigations were conducted concerning this matter.

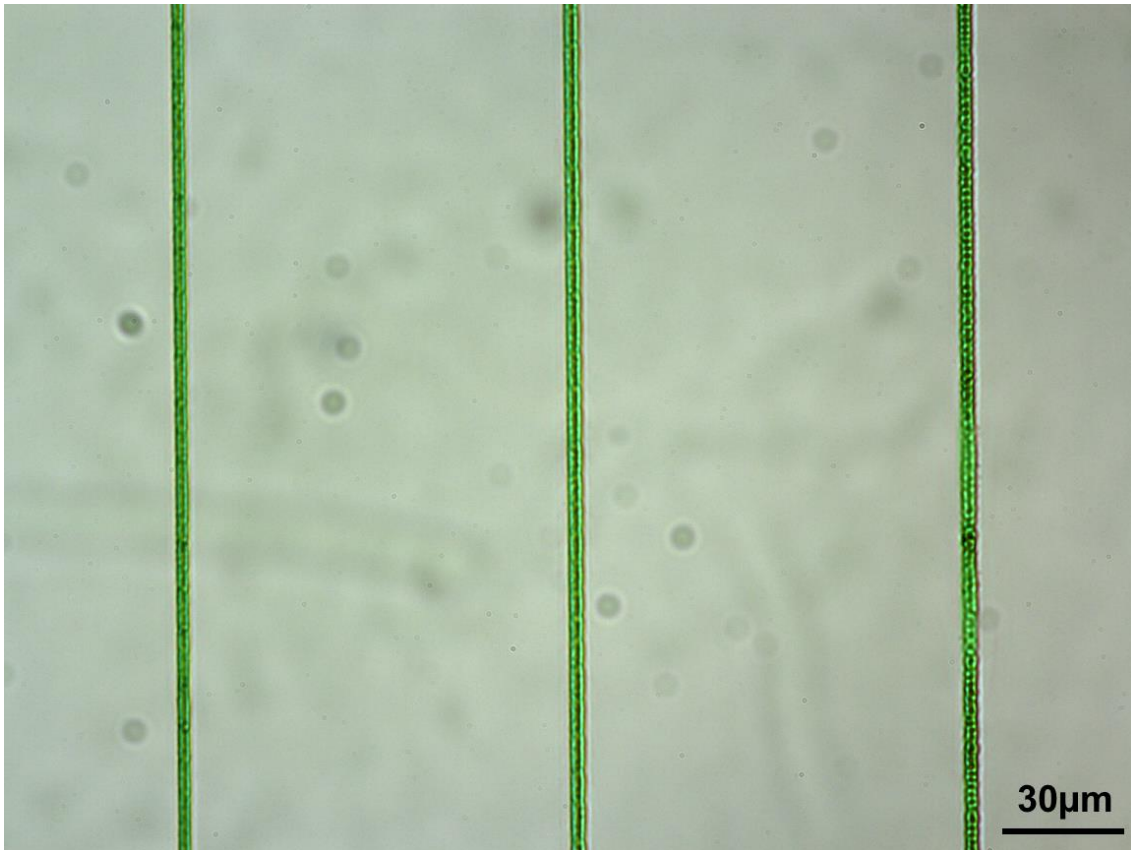


Figure II.29: Top view under white light illumination for different lines written using a 250 kHz laser emitting at 1030 nm with a fixed pulse energy of 0.26 μJ for three different speeds from the left to the right: 10 mm/s-5 mm/s-1 mm/s. To be compared with figure 4 in [148].

II.5. Experimental setup: Glass and laser used

II.5.1. Glass synthesis and fiber drawing

As mentioned before, three different silver containing glasses were used during this project. The silver concentration change for the glasses were provided by ICMCB while *Argolight* provided a slightly different glass composition. During the upcoming work two silver containing zinc phosphate bulk glasses PZnAg1 and PZnAg2 provided by ICMCB were used (Table II-1). The glasses were elaborated from a mix of powders $\text{Zn}(\text{PO}_3)_2$, ZnO , Ga_2O_3 and $\text{Ag}(\text{NO}_3)$. Both of the previously mentioned glasses were made by the same technique. A glass sample was made using a melt-quenching technique, as mentioned in section I.2.4.a. A platinum crucible containing the powders was heated at 1200°C during 12h. The sample was quenched, ground and melted twice with the intention of improving the chemical homogeneity of the glass and limiting the local refractive index variations in order

to get the best optical quality. Afterwards the samples were annealed at 40°C below the glass transition ($\sim T_g=380^\circ\text{C}$) for 4h to relax the accumulated mechanical constraints. Then the sample was cut in a parallel-piped shape and polished to allow DLW. Furthermore, following DLW, the side facets were cut and polished again in order to reveal the waveguides at the surface, to allow the laser injection and the visualization of the guided mode profile. A non-silver containing zinc phosphate glass (PZn) was also synthesized by the same method where the silver was replaced by Ga_2O_3 .

As mentioned before, silver containing zinc phosphate glasses exhibit a good transparency window from the visible up to around $2.7\ \mu\text{m}$ (Figure II.22). The change in silver concentrations does not highly affect the transparency window for this glass in the visible and NIR ranges. So, one could consider that the three glasses exhibit more or less the same optical properties.

II.5.2. Silver containing zinc phosphate glass fibers

In addition to that, silver containing zinc phosphate glasses were shaped into fibers by our colleague S.Danto at ICMCB [149]. It is a joint project with Professor Smektala at ICB in Dijon, France. Aiming towards sensing applications and integrated optical components, shaping glasses into fibers is an important point. Several sensors nowadays are fiber-optic based. In order to shape the glass into fibers, it all starts by making a preform that will be shaped into fibers. The glass preform in this case is a few centimetres thick and around 10 cm long, which is enough to create roughly 10 meters of optical fiber. The critical point while shaping glasses into fibers is to preserve the same characteristics of the bulk glass, trying to avoid any aggregation and crystallization of the glass during the fiber drawing process. In order to draw fibers, the preform composition used was $40\text{P}_2\text{O}_5\text{-}55\text{ZnO-}1\text{Ga}_2\text{O}_3\text{-}2\text{Na}_2\text{O-}2\text{Ag}_2\text{O}$. The introduction of sodium (Na) in the glass composition was for poling purposes that are not addressed in this manuscript. The glass was synthesized the same way as the previously mentioned bulk glass. However, to shape the preform, the glass was casted in a specifically designed brass mold, pre-heated at $\sim T_g\text{-}10\ ^\circ\text{C}$ and annealed at $T_g\text{-}40\ ^\circ\text{C}$ for 12 hours. As first demonstrated, two glasses were drawn where one of them did not exhibit any silver integration. The idea aims to highlight the luminescence properties of the silver containing glass. Both preforms are shown in Figure II.30.a. The preform with no silver shows no luminescence under UV excitation at $\lambda=260\text{nm}$ [149]. The silver containing zinc phosphate glasses exhibit an absorption band at $\lambda=245\text{nm}$ due to the presence of

silver ions Ag^+ resulting in fluorescence mainly around $\lambda=368\text{nm}$. This fluorescence emission has been attributed to the $d^{10}\leftrightarrow d^9s^1$ transition of Ag^+ ions homogeneously dispersed throughout the glass matrix [150]. Thermal drawing was performed using a dedicated 3-meter-high optical fiber draw tower composed of an annular electrical furnace with a sharp temperature profile, a diameter monitor, a tension dancer and a collecting drum. The preform was slowly fed into the furnace and the temperature was gradually increased up to $\sim 700^\circ\text{C}$ under continuous oxygen gas flow ($3\text{l}\cdot\text{min}^{-1}$). The preform holder motion and capstan rotation velocity were controlled in real-time to produce the targeted fiber diameter.

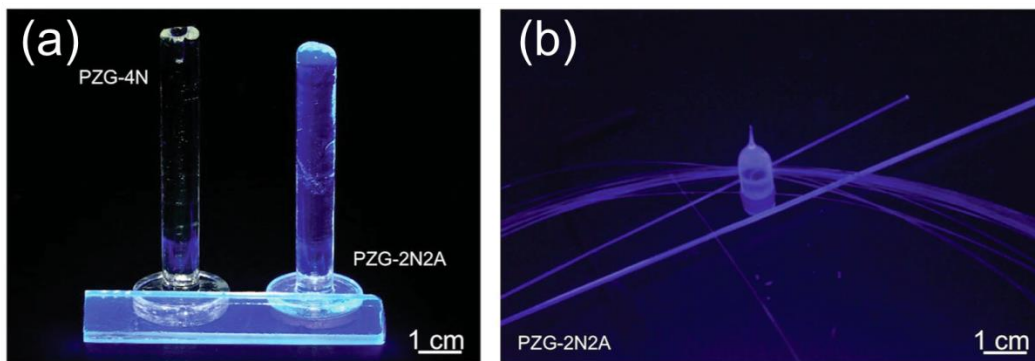


Figure II.30: Zinc phosphate glass under UV excitation (a) non-containing (PZG-4N) and silver containing (PZG-2N2A) preforms. PZG-2N2A only exhibiting fluorescence emission; (b) fibers and a leftover of a preform. Taken from [149].

Figure II.30.b shows the rest of the drawn preform, capillaries and fiber under UV excitation. At first impression, the homogenous macroscopic luminescence under UV excitation is correlated to the homogeneous distribution of silver ions Ag^+ in the preform, capillaries and fiber. The comparison of the fluorescence properties of the fiber and the bulk glass implies that the fluorescence emission is fully preserved at the microscopic level also as shown in Figure II.31. This refers to the successful drawing process where neither clustering nor reduction of the Ag^+ occurred.

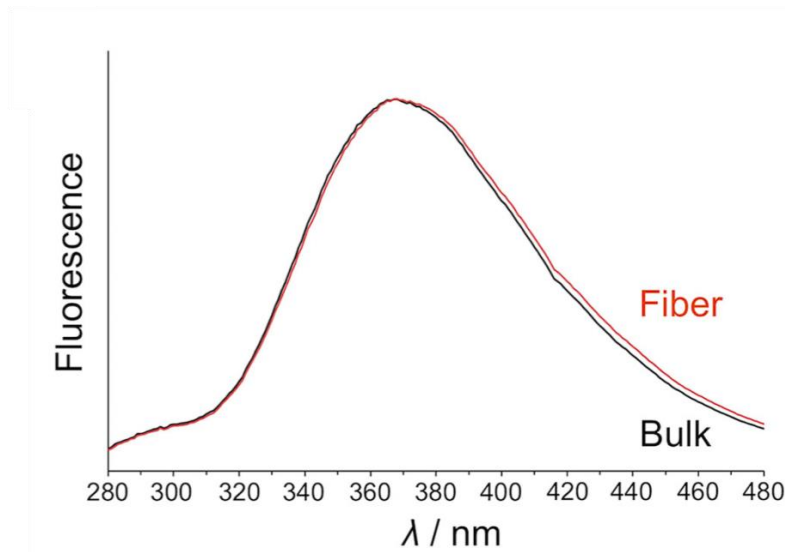


Figure II.31: Comparison between bulk glass and fiber fluorescence emission properties ($\lambda_{exc}=245\text{nm}$). A good match is found indicating that the drawing process preserved the glass properties. Taken from [149].

Focusing a laser beam on the cylindrical geometry of the fiber generates strong astigmatism and spherical aberrations, which complicates the process of femtosecond laser writing. To avoid such problems, usually an oil immersion objective is used as previously reported [151]. In order to bypass such complications, the new fibers were shaped into flat fibers or alternatively called “ribbon” fibers. Having a flat surface facilitates the manipulation and eases the direct laser writing process.

In this case, the preform is a rectangular one instead of a cylindrical one. To accomplish this, a glass slab is grinded and optically polished to proper dimensions then drawn into rectangular fibers as shown in Figure II.32 [149]. If the reader is interested in further details, the work of *Danto et al* [149] is recommended. Ribbon/flat fibers were drawn with diameters ranging from 250 μm down to 75 μm with a rectangular cross section as shown in Figure II.32.b. One can imagine the flat fiber as a cladding, and using DLW, many cores or optical components could be written in such fibers.

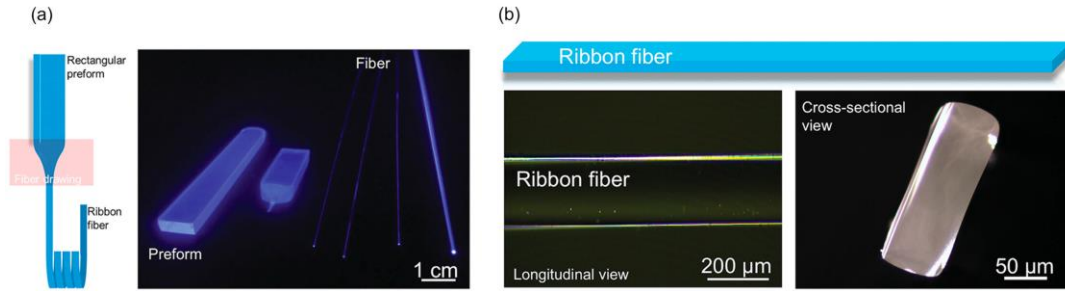


Figure II.32: (a) Thermal drawing of ribbon fibers. Preform, bottom-neck preform and drawn fibers under UV excitation ($\lambda_{exc}=245\text{nm}$). (b) Sketch, longitudinal and side view of the drawn ribbon fiber. A flat surface with a rectangular side view is obtained. Taken from [149].

DLW of many structures including cartography of inscription were performed inside the flat fiber as shown in Figure II.33. Under UV excitation, significant fluorescence was observed that could be compared to the fluorescence emitted by silver clusters induced in bulk samples (Figure II.33.b). Moreover, differential micro-transmission measurements on the structured zones with the pristine glass were performed for the written cartography (Figure II.33.c).

The cartography was written while changing the laser irradiance from 5.1 TW/cm^2 to 6.7 TW/cm^2 passing by 6.1 TW/cm^2 while the writing speeds were $10\mu\text{m/s}$ and $100\mu\text{m/s}$ corresponding to 1.6×10^6 and 1.6×10^5 of deposited pulses respectively. The results show a significant absorption band at $\lambda=324 \text{ nm}$ and another weaker one at around $\lambda=290 \text{ nm}$ for all structures as shown in Figure II.33.c. The amplitude of the absorption band varies as a function of the irradiance, which is expected. Using lower irradiance results in generating less silver clusters, therefore less absorption. Those two absorption bands are typical of the silver clusters Ag_m^{x+} as mentioned before and were reported in previous works of our group [44, 136, 141, 152]. Therefore, we confirm that the properties of the bulk glass were preserved after the drawing process and the successful creation of flat silver containing zinc phosphate fibers was achieved.

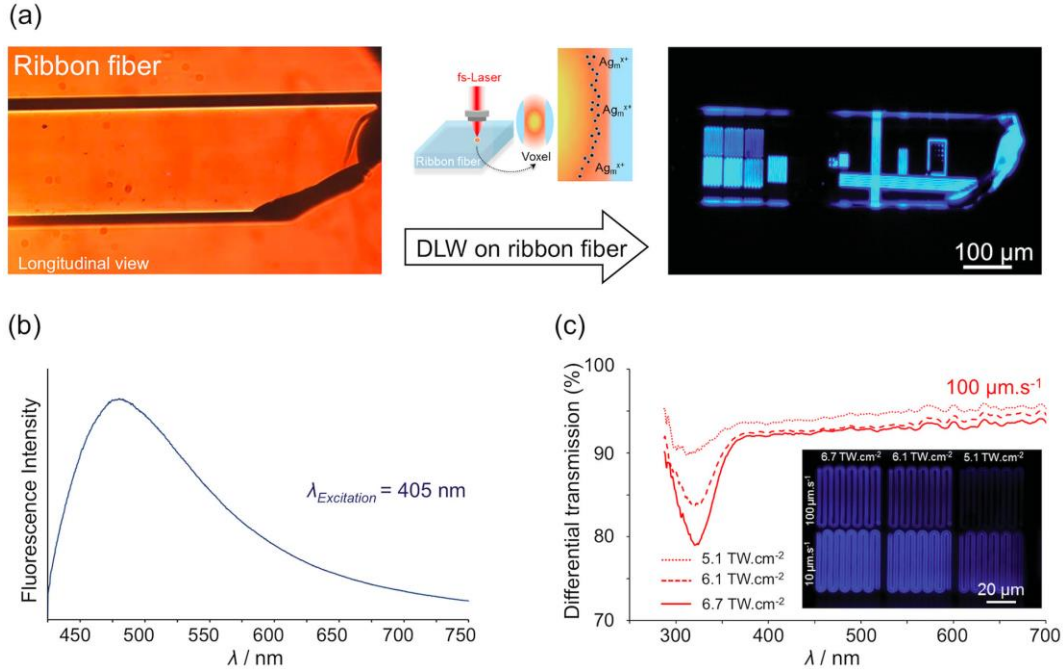


Figure II.33: Top view of the ribbon fiber (a) under white illumination before DLW (b) under UV excitation ($\lambda_{\text{exc}}=405 \text{ nm}$) following DLW. The fluorescence of the written structures could be observed. (b) Fluorescence intensity broad band emission of the structures under UV excitation ($\lambda_{\text{exc}}=405 \text{ nm}$). (c) Fluorescence of the written cartography and the corresponding differential transmission spectra. A higher absorption band is observed for a higher laser irradiance. Taken from [149].

II.5.3. Laser setup:

The laser used for performing DLW in this chapter is a Yb:KGW femtosecond oscillator (T-pulse 200 by Amplitude systems). A schematic of the setup is presented in Figure II.34. It operates at a wavelength of 1030 nm, pulse duration of 390 fs, a repetition rate of 9.8 MHz and an average power of 2.6 W. The laser irradiance deposited in the glass sample was controlled using an acousto-optic modulator enabling the accumulation of $N=10^5-10^6$ pulses with energies between 20 nJ and 120 nJ. A reflection type SLM is placed after the AOM in order to spatially shape the beam if needed before irradiating the glass sample. In this project, the SLM is used only as a convergence lens in order to compensate for the different focal planes and to compensate the spherical aberrations that occur when using high NA objectives [153] (the most dominant aberrations in this case given that they are proportional to NA^4) that occur when focusing the laser beam using a microscope objective. Generally, the microscope objective used in this case is adapted for laser focalisation under a microscope cover slide of $\sim 170 \mu\text{m}$ with a

refractive index (RI) of ~ 1.5 . Given that our glass exhibits an $RI \sim 1.6$, aberrations occur due to the refractive index mismatch. In the following work, two microscope objectives were used: 20x-0.4NA Mitutoyo, APO PLAN NIR and 20x-0.75NA Carl Zeiss. At the top, a CCD camera is placed in order to visualize the glass surface and the writing process. Bottom white and blue illuminations at 405 nm are applied. White light is used to visualize and find the surface of the glass while the blue illumination serves to monitor and visualize the fluorescence of the silver cluster created during DLW. A 405 nm high pass filter is placed before the CCD in order to cut the blue diode at 405 nm allowing the observation of the fluorescence of silver clusters.

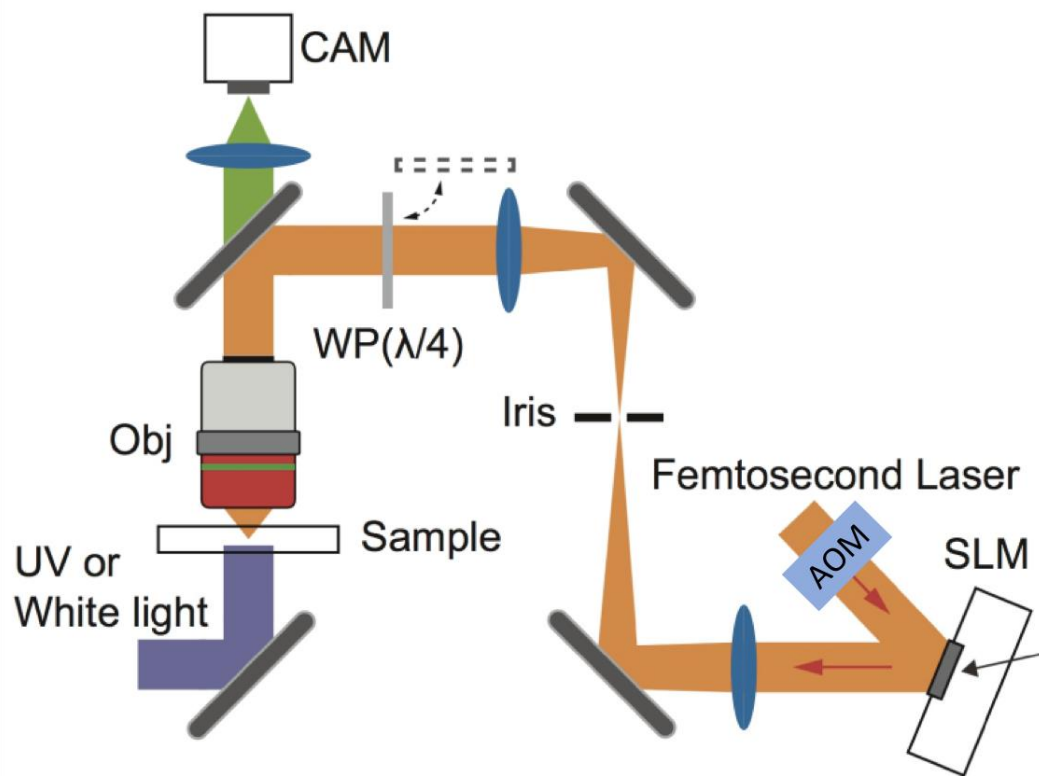


Figure II.34: Schematic of the laser setup used for direct laser writing.

II.5.4. Mode profile setup:

After performing DLW of waveguides, the sample was placed on the mode profile setup in order to characterize the waveguides. The mode profile setup consisted of a red diode operating at 630 nm that could be injected inside the waveguides using optical fibers. In this case a single mode HP460 fiber (core diameter 2.5 μm -

NA=0.13) at 630 nm was used to inject light inside the guiding structures (waveguides, beam splitter). Then, a 100x-0,55NA Mitutoyo objective was used on the output facet to visualize the guide mode profile and conjugate it on a CCD camera. Moreover, when needed, the CCD camera was replaced by a power meter to measure the transmission losses of our waveguides. The injection fiber, the sample as well as the collecting objective were placed on separated 3 axis stages.

II.5.5. Confocal Microscope:

The photo-induced structures in silver containing glasses are sub-diffraction limited structures, therefore, imaging them using a conventional microscope is not convenient. Because they exhibit significant fluorescence intensity under UV-Blue range excitation, they are visualized using a fluorescence confocal microscope to be able to resolve them. Confocal microscopes exhibit many advantages compared to standard ones, higher resolution (up to 300 nm), imaging planes separately and the possibility of reconstructing a 3D image/video of the structures. If the reader is interested, further details can be found in reference [154].

The fluorescent images were obtained using an Olympus FLUOVIEW FV1200 confocal microscope. An oil immersion objective of 60x – 1.3 NA was used to resolve the structures. Excitation wavelength was at 480 nm while the emission wavelength ranged between 500 nm and 600 nm.

II.5.6. Measuring Δn : SID4Bio Phasics

To better characterize the written waveguides and optical components in glasses, the Δn is a crucial parameter to especially know with respect to its sign and amplitude. During this project, the SID4Bio wave front sensor by PHASICS was used to measure and characterize the Δn of the written structures. It provides quantitative phase imaging of the waveguides. The sensor could be placed on any microscope operating in transmission mode. The sample where the structures are written inside is placed on the microscope and is imaged using incoherent light i.e. white light. The sensor is based on a CCD camera with a modified Hartmann Mask placed in front. The incident incoherent light beam is diffracted by the mask into four replicas to create an interferogram on the CCD as shown in Figure II.35.

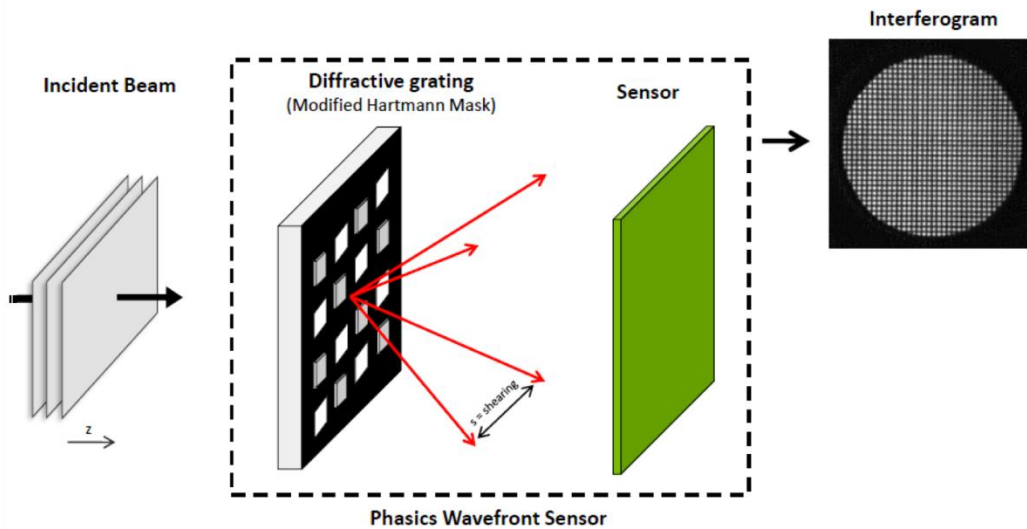


Figure II.35: Sketch of the SID4Bio wavefront sensor working principle. The incident beam is diffracted by the modified Hartmann Mask into four replicas making an interferogram on the sensor (CCD Camera) [155].

The phase is encoded in the interference fringe deformation. Following that, Fourier transforms allow the extraction of the intensity and phase image [156, 157]. In an easier way, the light passing through an object with different refractive index change is delayed and creates a difference in the optical path as shown in Figure II.36.

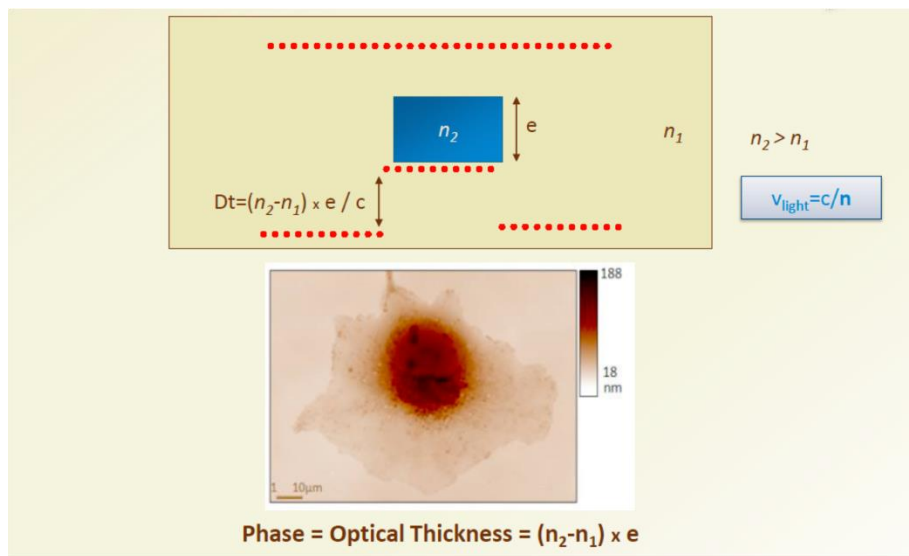


Figure II.36: Sketch of the light delayed by a refractive index object (n_2) with a specific thickness "e" different than the surrounding medium (n_1) leading to the construction of the phase image. The optical thickness i.e. optical path difference could be obtained [155].

The final output of the wave front sensor is an intensity image and a phase image showing the optical path difference (OPD) created by the light after passing by the sample as shown in Figure II.37. Given the OPD, the real value of Δn could be extracted by dividing the OPD by the thickness "e" of the object ($\Delta n = OPD/e$) i.e. the written structure Figure II.36. The wave front sensor exhibits a spatial resolution of $29.6 \mu\text{m}$ when no magnification is used and a dynamic range $>500 \mu\text{m}$ [155].

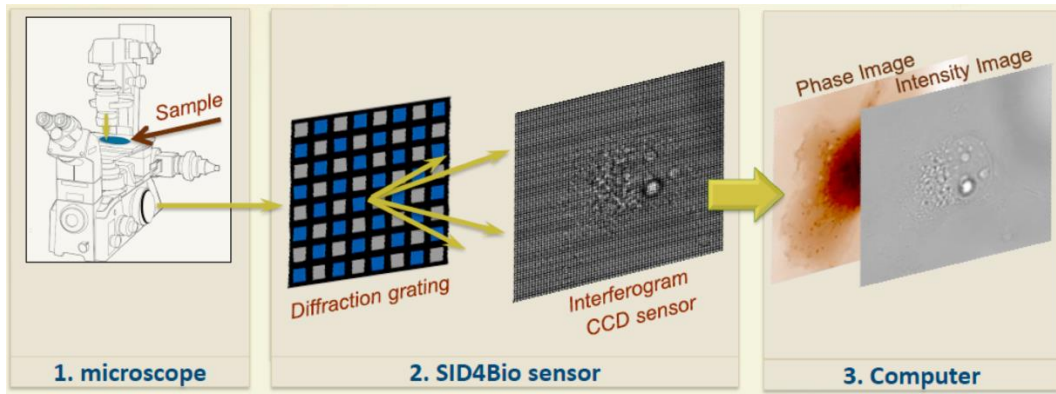


Figure II.37: The SID4Bio installed on a transmission microscope. The light is diffracted by the grating creating the interferogram on the CCD camera giving an output of an intensity and phase image [155].

Many methods nowadays exist to measure the photo-induced Δn in glasses following DLW. They could be classified in two: methods where the Δn could be calculated and methods where the Δn could be measured directly.

Some groups calculate the photo-induced Δn of the waveguides based on measuring the numerical aperture (NA) using the far-field intensity profile [131, 158]. Given the refractive index of the glass and the NA, one can compute the value of the refractive index change of the written waveguide from (II-4). The measurement of the output mode profile in the far field allows to determine the divergence of the mode as a function of the distance, therefore to measure the acceptance cone, i.e. the numerical aperture, therefore to calculate the Δn .

The previously mentioned methods are optical methods to measure the photo-induced Δn following DLW. However, recently a mechanical method was suggested by the group of Professor Yves Bellouard in Switzerland. It is a mechanical method based on the stress induced by laser irradiation inside glass. It consists of irradiating a glass cantilever which is deformed due to the stress induced by the laser [159, 160]. The Δn is calculated based on the Lorentz-Lorenz equation shown in (II-11).

$$\Delta n_{\lambda} = \frac{(n_{\lambda}^2 - 1)(n_{\lambda}^2 + 2)}{6n_{\lambda}} \left(\frac{\Delta \rho}{\rho} \right) (1 + \Omega) \quad (\text{II-11})$$

with: $\Omega = \left(\frac{\Delta \alpha}{\alpha} \right) \left(\frac{\Delta \rho}{\rho} \right)$

where n_{λ} is the refractive index at wavelength λ , α is the polarizability and ρ is the density. The Δn equation consists of two parts, volume changes in the glass $\left(\frac{\Delta \rho}{\rho} \right)$ and the change in polarizability $\left(\frac{\Delta \alpha}{\alpha} \right)$. The volume changes could be obtained from the cantilever based on the strain. The strain is measured by the deflection of the cantilever following laser irradiation. Furthermore, the change in polarizability was studied earlier by *Hiroshi et al* for fused silica and the range of values is well known [161]. So, based on the volume and the polarizability changes, the Δn could be calculated using (II-11) [159]. It was found that the calculated values are lower than the values expected so eventually, this mechanical method is still to be calibrated and compared to an optical one [160].

During my PhD, I was somehow involved in a comparative study between different quantitative phase imaging techniques. Those techniques allow to directly measure the Δn . More details are presented in the Appendix part A.3

II.6. Results

II.6.1. Structures' morphology

Previous results in the group were based mostly on static DLW in silver containing glasses trying to understand the basics of the laser-glass interaction. This project aims towards functionalizing those silver clusters, creating waveguides and optical components. In order to make waveguides, two crucial points are necessary: characterizing the morphology of the photo-induced structures and measuring the refractive index change (Δn).

In order to do so, many linear photo-induced structures were written inside silver containing zinc phosphate bulk PZnAg1 glass typically 160 μ m below the surface (to minimize the spherical aberrations and optimize the confocal fluorescence characterization). The glass sample was translated perpendicularly to the laser beam to form linear structures as shown in Figure II.38.a. Silver clusters were created based on the non-linear absorption effect as explained earlier. These

clusters are characterized by two main absorption bands, 290 nm and 345 nm resulting in a broad band fluorescence emission in the visible range as mentioned before (Figure II.24) and reported by [44, 136, 141, 152]. Therefore, the fluorescence refers to the presence of silver clusters.

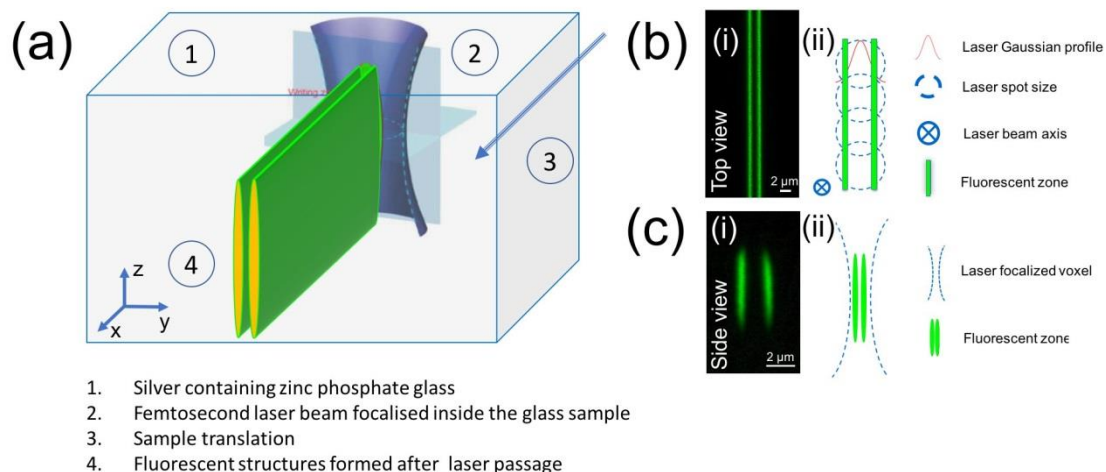


Figure II.38: (a) Schematic of the morphology of the structures following perpendicular translation to the laser beam propagation inside silver containing zinc phosphate glasses. Fluorescence confocal images of the (b.i) top view (xy) plane, and (c.i) side view (xz) plane. Schematic presentation of the writing process with (b.ii) top view and (c.ii) side view.

First, the morphology of the written structures had to be investigated. In order to do so, confocal fluorescence images of the top and side view of the structures were taken ($\lambda_{\text{ex}}=480\text{nm}$, $\lambda_{\text{em}}=550\text{nm}$). From the top view, two parallel fluorescent lines were observed (Figure II.38.b) while the cross section (side view) exhibited silver clusters distributed in two parallel planes (Figure II.38.c.i). These morphologies are typical for Ag_m^{x+} features being photo-induced by a Gaussian profile laser beam [44, 136, 141]. In fact, the inscription process could be illustrated as a laser quill leaving only fluorescence i.e. silver clusters on the edges (Figure II.38.b.ii). The absence of fluorescence in the middle of the structures is associated to the photo-dissociation of silver clusters [44, 136, 140, 141] as mentioned earlier. The clusters left on the edges were not exposed to high irradiance which prevents their photo-dissociation allowing their accumulation and aggregation [136, 141, 152]. The results from the side view are similar to the static writing in section II.4.2. (Figure II.25). However double lines were observed in the top view instead of a ring shape, which is expected. The reason for having two lines is that during a static focus, a fluorescence ring is formed. Thus, during the displacement of the sample, the silver clusters formed at the front of the laser beam along the path are progressively illuminated by the center of the laser Gaussian profile where the maximum laser

energy is located which dissociates the silver clusters already formed as shown in Figure II.38.b.ii. Furthermore, the side view (zy plane, as shown in Figure II.38.1.c) of the fluorescent structures reveals that the depth in the z plane is typically proportional to the nonlinear Rayleigh range associated to the multi-photon absorption [44], as shown in Figure II.38.c.ii. This indicates that the depth of the structures can be controlled based on the microscope objective used for DLW, i.e. controlling the dimensions of the written waveguides. Such depth can also be ideally controlled by preparing the laser pulse profile to pre-compensate its phase profile in a way to further minimize the resulting spherical aberrations at the voxel, due to the refractive index mismatch between the zinc phosphate glass ($n \sim 1.6$) used here and the glass slides from which microscope objectives are designed.

II.6.2. Δn vs laser parameters

To investigate the Δn created inside the glass following laser-glass interaction, a cartography of square linear structures of $100 \mu\text{m} \times 100 \mu\text{m}$ with an interline spacing of $10 \mu\text{m}$ were written inside the glass typically $160 \mu\text{m}$ below the surface (to minimize the spherical aberrations and optimize the confocal fluorescence characterization) as shown in Figure II.39.a. The irradiance as well as the writing speed were changed during the writing, from $6 \text{TW}/\text{cm}^2$ to $10 \text{TW}/\text{cm}^2$ (from 280 mW to 470 mW average power measured after the microscope objective) while the writing speed was varied between $10 \mu\text{m}/\text{s}$ and $50 \mu\text{m}/\text{s}$ corresponding to 1.7×10^6 deposited pulses and 3.3×10^5 deposited pulses respectively as shown in Figure II.39.a. Top view fluorescent images under 480 nm excitation reveals the written structures as shown in Figure II.39.a. The fluorescence intensity of the written structures exhibits a variation as a function of the laser parameters which was also previously reported by our group [44]: the higher the laser irradiance and/or the number of pulses, the greater the resulting fluorescence intensity.

Furthermore, top view phase images were conducted using the wave front sensor SID4bio. A pop-up of the written structure B2 of Figure II.39.a reveals a positive optical path difference (OPD) i.e. positive Δn correlated to the spatial distribution of the silver cluster as shown in Figure II.39.b (to be compared with Figure II.39.a). Based on the phase contrast images and given the depth of the structures, the qualitative value of Δn of the written structures could be ascertained. Figure II.39.c shows the Δn profile determined from the phase image in Figure II.39.b. One can observe that every laser passage results in two positive Δn peaks correlated to the

spatial distribution of the silver clusters. This is one of the first proofs that the photo-induced silver clusters are responsible for the positive Δn following DLW.

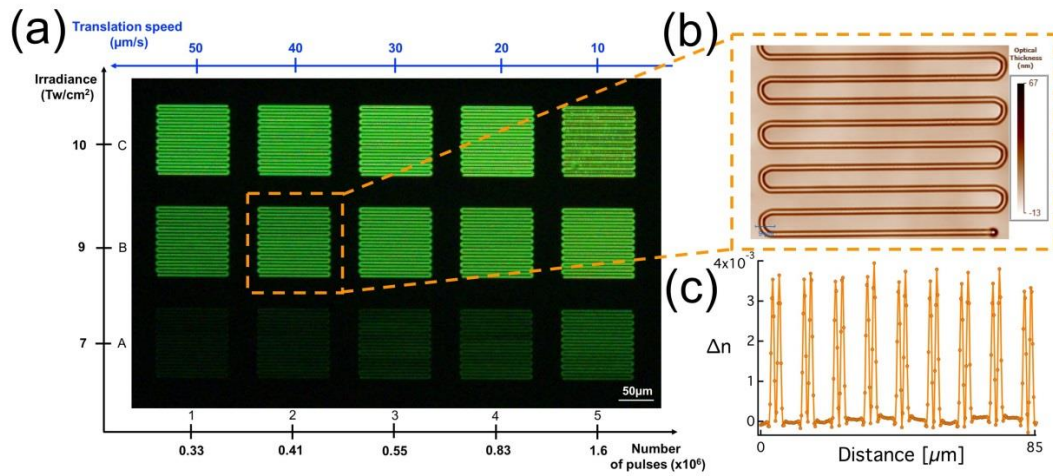


Figure II.39: (a) Fluorescence image ($\lambda_{ex}=480\text{nm}$, $\lambda_{em}=550\text{nm}$) of the written cartography. Writing irradiances are presented along the vertical axis while the number of pulses appears along the horizontal axis (b) Blowup of the phase image under white light illumination of the B2 structure (c) positive refractive index change (Δn) determined from the phase image of B2.

In the square written at $6\text{TW}/\text{cm}^2$ with a writing speed of $50\mu\text{m}/\text{s}$ the fluorescence was too low to be observed (not shown in Figure II.39). However, that square was visible while imaging the structures using the SID4Bio. It exhibited a single positive peak of Δn as shown Figure II.40.c. The depth of the structure could not be determined given that it was not possible to visualize the side view fluorescence of the structure. Nevertheless, one should mention that in this case minimum effort was put into visualizing the side view fluorescence of this structure. The single positive peak refers to a disk of fluorescence and not a ring shape. It is due to the fact that, when using a low irradiance, the silver clusters created in the middle are not photo-dissociated by the laser beam given that the intensity is not too high. This was also experimentally observed by Bellec et al. [44] and confirmed numerically based on the model of the creation of silver clusters in silver containing glasses [140] as shown in Figure II.40.c.viii. Unfortunately, the following structure exhibited such weak Δn that the waveguiding process was not possible in such structures. So no further effort was devoted in measuring the depth of such structure.

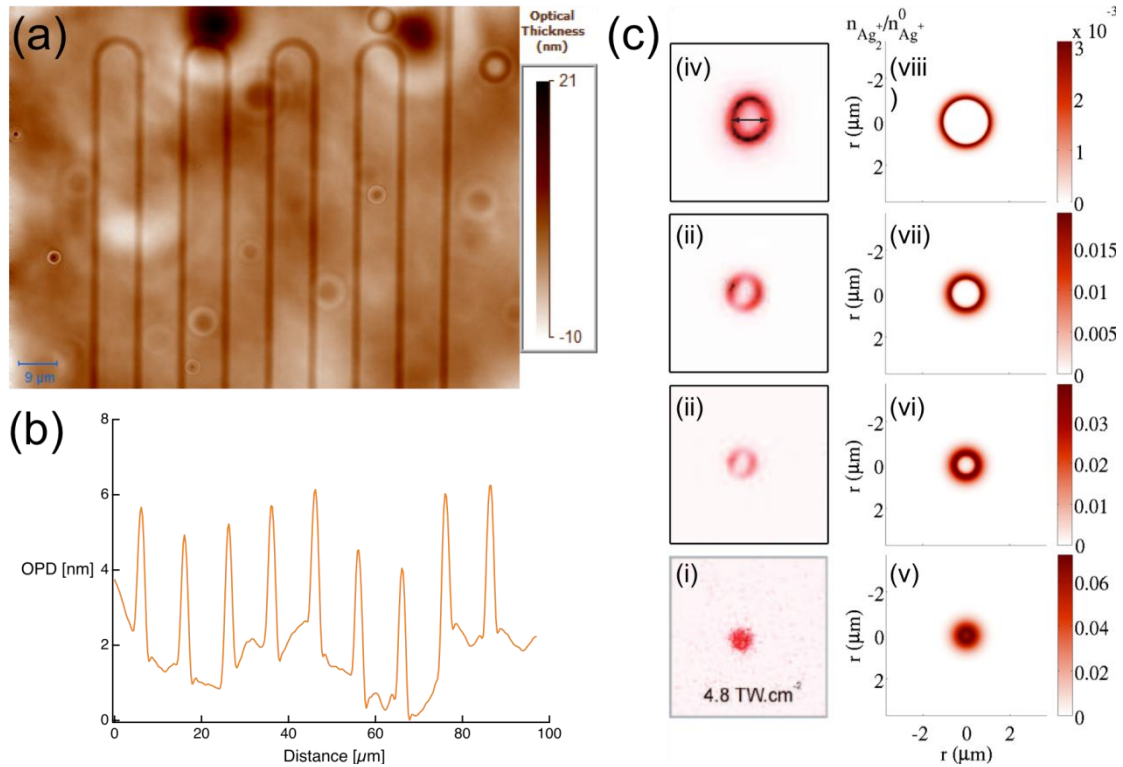


Figure II.40: (a) Phase image under white light illumination showing one line of phase shift; (b) Line profile obtained from the phase image revealing only one positive peak of optical path different in that case for the structures instead of two peaks; (c) left column: experimental silver cluster spatial distribution for a progressive scale of irradiances; right column: simulated distribution of the silver clusters. For (i) and (v) low laser irradiance is used and a full disk of fluorescence is observed, which is not the case for higher irradiances. Taken from [140]

Our study shows that Δn increases as a function of the number of deposited pulses as well as the laser irradiance Figure II.41. The result is expected, since a larger number of deposited pulses contributes to an increase in the local temperature (well below the glass transition temperature T_g). This moderate increase in temperature allows the thermal activation of the migration of silver ions as well as the chemical reactivity leading to the formation of a larger number of silver clusters [136], which results in a higher Δn . The same scenario applies for increasing the laser irradiance: the higher the irradiance, the greater the formation of silver clusters, as previously reported [44]. The Δn increases from 9×10^{-4} up to 8×10^{-3} in this case (Figure II.41), which is to be compared to the Δn values obtained in fused silica going from 1.3×10^{-3} up to 1.7×10^{-2} with type I modifications [53, 162]. In this study, the depth (length in the z plane (Figure II.38.a) of the structures) was averaged to $8 \mu\text{m}$ i.e. all the structures were considered having a depth of $8 \mu\text{m}$.

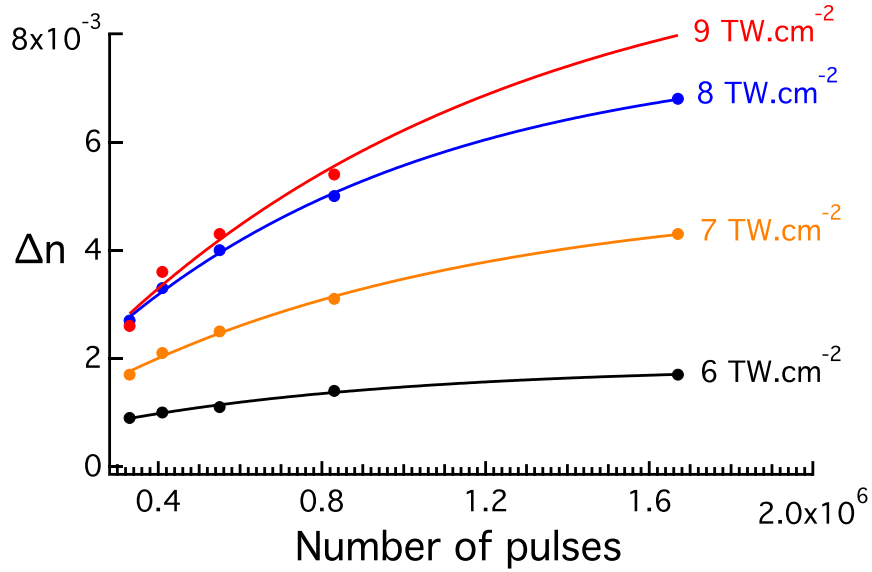


Figure II.41: Refractive index change variation (Δn) as a function of the number of pulses and laser irradiance. Δn increases as a function of the laser parameters. Laser repetition rate 9.8 MHz.

However, another study was performed to investigate the depth (length in z plane) of the structures as a function of the laser parameters. This study will lead probably to a more accurate measurement of Δn for all the written structures as a function of their depth given that Δn is determined based on the measured ODP and the length of the structures in z plane (Figure II.38.a). The study consisted also in cartographies of square structures of $100 \mu\text{m} \times 100 \mu\text{m}$ with an interline spacing of $10 \mu\text{m}$. The laser irradiance varied between $7 \text{ TW}/\text{cm}^2$ to $11.8 \text{ TW}/\text{cm}^2$ while the writing speed was changed from $10 \mu\text{m}/\text{s}$ up to $100 \mu\text{m}/\text{s}$ corresponding to 1.7×10^6 deposited pulses and 1.7×10^5 respectively using a $20\times$ -0.75NA objective. The results reveal that the writing speed i.e. the number of deposited pulses seems to not have a big effect on the length of the structure. However the laser irradiance plays a major role in that case, as shown in Figure II.42. The structure's depth in z varied from $5 \mu\text{m}$ to $\sim 13 \mu\text{m}$.

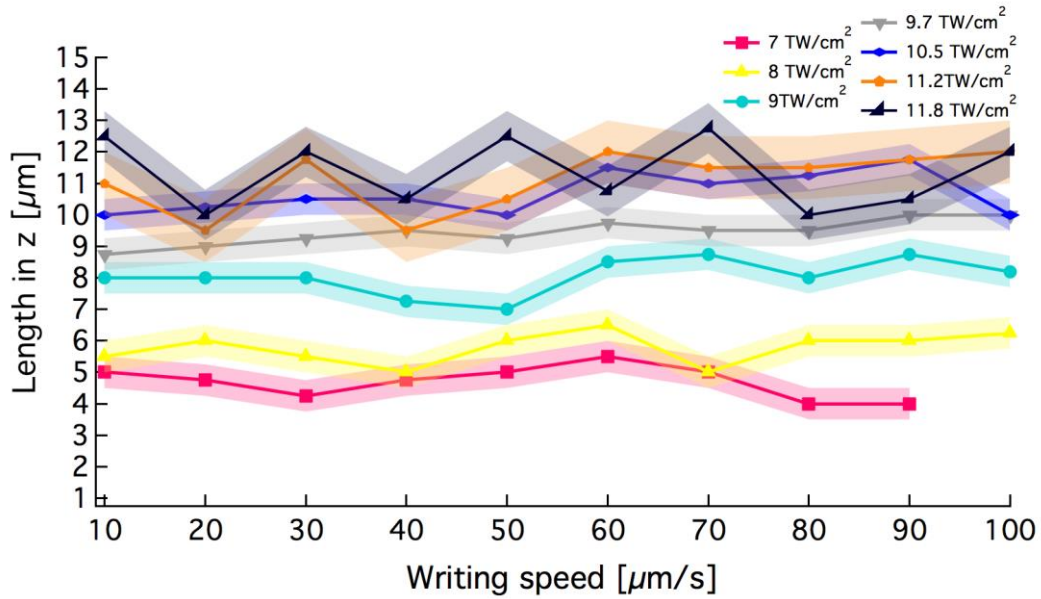


Figure II.42: Variation of the length of the structure along z as a function of the laser parameters, laser irradiance and writing speed. The dimensions increase as a function of the laser irradiance. Laser repetition rate 9.8 MHz. The shades correspond to the standard deviation of the values.

Based on those results, the Δn was properly calculated for the written structures. It was found that in that case the results do not converge with the previous results i.e. increasing the number of pulses or the laser irradiance does not lead to a higher Δn in all cases especially for high irradiances. This is due to the fact that high irradiances induce deeper structures in the z plane. It was found that the imaging system used SID4Bio + 100x-1.3NA oil objective is limited to a depth measurement of $\sim 6\mu\text{m}$. Several lines were written with the same laser conditions but spaced in the z plane by $1\mu\text{m}$ and were imaged using the SID4Bio and a 100x-1.3NA oil objective as shown in Figure II.43.

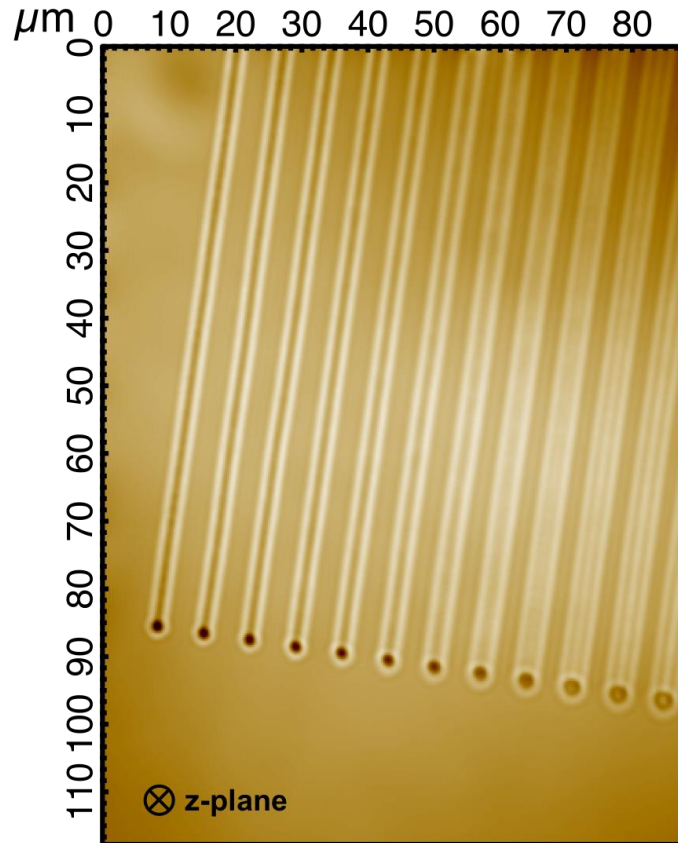


Figure II.43: Top view phase image of different lines separated by 1 μm in the z plane. The seventh line becomes blurry indicating that the optical system is limited to around 6 μm in depth.

The use of a 100x-1.3NA objective with the SID4Bio is necessary in order to spatially resolve our structures. Taking into account the length of coherence, the shape of our structure in the z plane, it was found that the depth of view is around $\sim 6 \mu\text{m}$ and after that the structures are blurry and the OPD is underestimated. Therefore, the measurement of our imaging system in this case is limited to around 6 μm . If the structure is deeper, the OPD is underestimated i.e. underestimating the Δn , which explains the divergence of the value of Δn when taking into consideration the real depth of the structure. Considering that and compensating for it ($\Delta n = OPD / e_{real} * C_{compensation}$), the Δn values were plotted again in Figure II.44, where e_{real} is the real thickness of the structures and $C_{compensation}$ the calculated compensation coefficient. The compensation method took into consideration the Fresnel number in that case. One can see that the results make more sense i.e. increasing the number of pulses and/or laser irradiance increases the Δn .

In the first study of the Δn as a function of the laser parameters (Figure II.41), all the structures' lengths were fixed to 8 μm . For this study, all the structures

exhibiting lengths more than 6 μm where considered as having a length of 6 μm (fixed method with $(\Delta n = OPD/6000)$) given that our system is limited to around 6 μm of depth of field (z plane Figure II.43). The results are plotted in Figure II.44 and compared to the compensation method. We used the compensation method and took into account that all the structures exhibiting 6 μm in length (in the z plane) converge and have more or less the same values. However, not compensating for the OPD value leads to an underestimating to the Δn value of our structures, which is not plotted in Figure II.44.

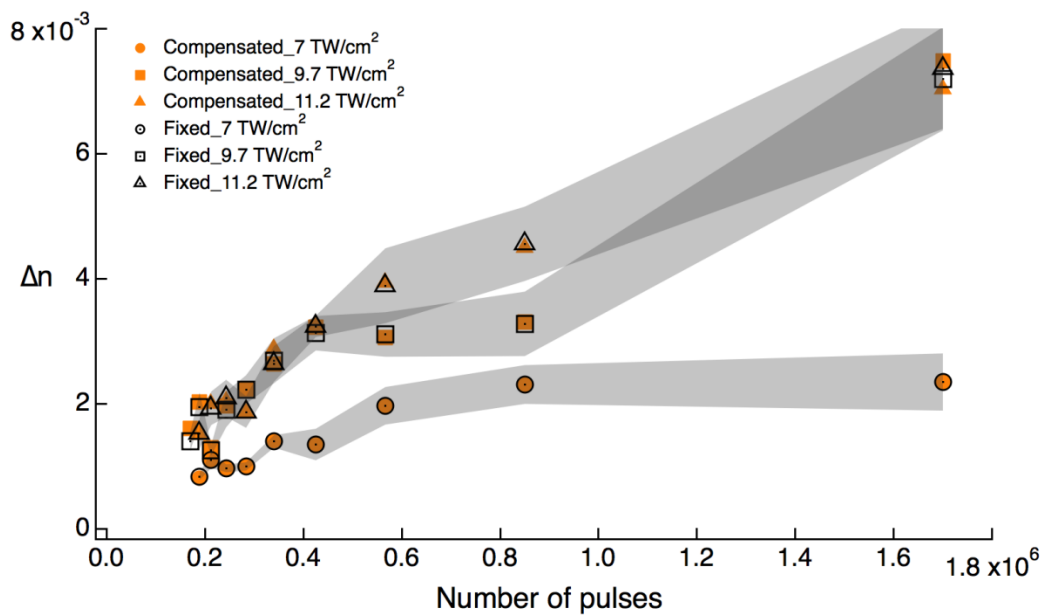


Figure II.44: Refractive index change (Δn) as a function of the number of pulses for two methods: (orange) using the compensation method (black) fixed method where the depth of the structure higher than 6 μm is considered as 6 μm . Both methods converge more or less to the same values. The black shades correspond to the standard deviation of the values.

To further support our hypothesis that the photo-induced Δn is related to the creation of silver clusters, a non-silver containing zinc phosphate (PZn) glass was irradiated using the same laser conditions and even higher irradiance. Neither fluorescence nor refractive index change were observed in this case, which indicated that the formation of silver clusters is the main and direct cause for the Δn in silver containing glasses, in the low pulse energy regime. Moreover, the photo-induced ring shape structure was investigated using High Resolution Scanning Electron Microscopy (HRSEM) photos and Atomic Force Microscopy (AFM) [136]. The glass sample was polished and etched using acid to reveal the structures to the surface. The HRSEM profile line exhibited a rise on the edges of

the photo-induced structures with 80 nm width indicating a change in the chemical composition or a topological bump (Figure II.45.b) [136].

In order to investigate these hypotheses, an AFM image proves that the topology on the edges of the photo-induced structure does not increase (Figure II.45.c). Therefore, we can attribute the enhanced contrast in the edge of the HRSEM image to a change in chemical composition i.e. the presence of silver clusters. However, in the middle of the structure a topological modification is observed that is due to the selective acid-etching performed [136].

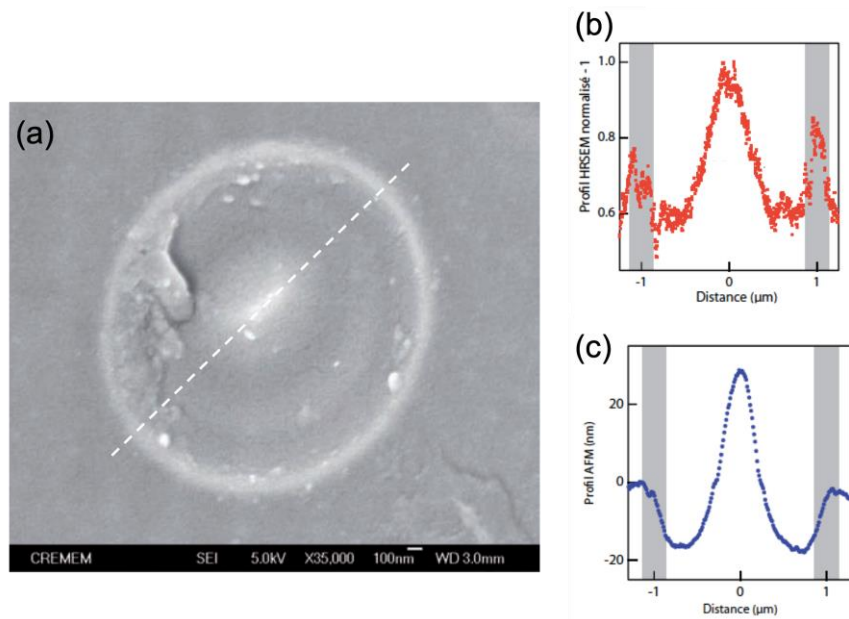


Figure II.45: (a) High Resolution Scanning Electron Microscopy (HRSEM) image of the top view of a ring shape structure formed by silver clusters; (b) Line profile extracted from the HRSEM photo indicating a bump on the edges; (c) Atomic Force Microscopy (AFM) profile indicating no bumps on the sides. The bumps observed in the HRSEM are due to a change in the chemical composition and not to topological changes. Taken from [136].

In addition to that, the typical spatial fluorescence distribution was correlated to the HRSEM image confirming once more that the silver clusters are responsible for the fluorescence (Figure II.46), for the change in chemical composition [136] and therefore the new type of refractive index change.

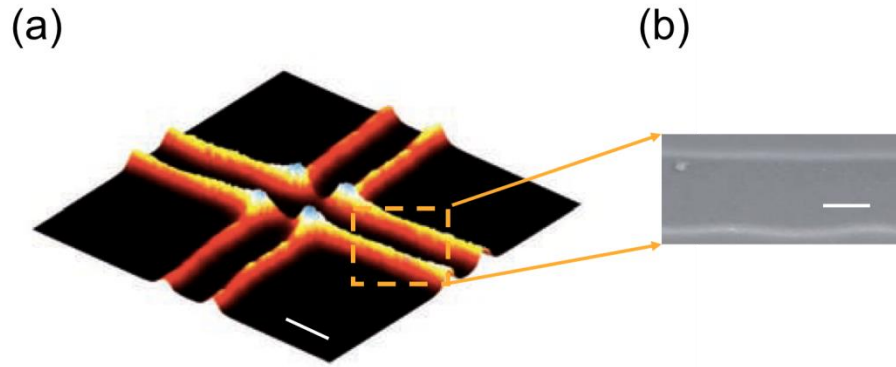


Figure II.46: (a) fluorescence; (b) HRSEM, top view of the photo-induced structures. The fluorescence spatial distribution is correlated to the HRSEM indicating that the silver clusters are responsible for the change in the chemical composition. The scale bar is 1 μm . Taken from [136].

Moreover, a large area of 2 x 2 mm² was irradiated by the laser. Silver cluster absorption spectrum could be inferred from differential transmission measurements between the 2 x 2 mm² irradiated area and a pristine one, taking into consideration the filling factor of the silver clusters' spatial distribution. Results are depicted in Figure II.47. Two typical absorption bands were observed in the visible range that corresponds to the absorption of the silver clusters as previously reported by *Marquestaut et al.* [139]. Based on the differential silver cluster absorption, one notes that the silver clusters exhibit a large cross section absorbance in the visible range. To further support our hypothesis that the silver clusters are responsible for the Δn in our glasses, a Kramers-Kronig (K-K) analysis was conducted on the differential absorption spectrum of the silver clusters to determine the Δn (Fig 4.b). A positive Δn was observed over the whole visible (VIS)-near infrared (NIR) ranges exhibiting a maximum value, in this case of 2.5×10^{-3} at $\lambda=365$ nm.

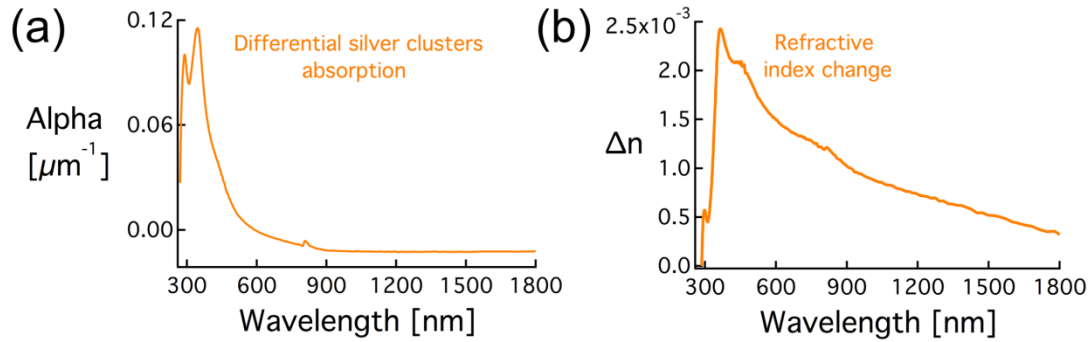


Figure II.47:(a) Silver clusters differential absorption spectrum as a function of the wavelength showing two main absorption bands near 290 nm and 350 nm; (b) Refractive index change (Δn) determined from the spectrum shown in (a) based on a Kramers-Kronig analysis, considering the filling factor of the silver clusters' spatial distribution. DLW parameters: $7\text{TW}/\text{cm}^2 - 40 \mu\text{m}/\text{s}$.

Indeed, we claim that our Δn is not based on a standard index modification of the glass matrix itself due to the laser-induced modifications of the local density as it is the case for *type I* modification. Here, we report that the Δn produced is based on the localized laser-induced creation of a new chemical silver species with enlarged molecular electric polarizability, locally leading to an increase in the electric susceptibility and associated refraction index change.

II.6.3. Waveguiding

II.6.3.a. Multimode waveguiding

In order to illustrate the potential of this new DLW process for practical applications, a first approach took place by writing two 7 mm long waveguides typically 160 μm below the surface in a PZnAg2 glass provided by ICMCB. The DLW process of two waveguides took place using the 1030 nm laser setup as mentioned in the experimental part (section II.5.3) while using a 20x-0.4 NA Mitutoyo microscope objective. The laser irradiance used was $8 \text{ TW}/\text{cm}^2$ while two writing speeds were used, $10 \mu\text{m}/\text{s}$ (WG1) and $20 \mu\text{m}/\text{s}$ (WG2). Then the sample was rotated 90° for top laser injection and bottom collection of the guided light as shown in Figure II.48.a. A micrograph of the bulk sample and the fluorescence of one of the written waveguides under broad field UV illumination at 405 nm are depicted in Figure II.48.b. A blue diode operating at 405 nm illuminated the top surface while imaging the induced fluorescence from the bottom as shown in Figure II.48.c. Based on that photo, the first waveguide dimensions were estimated to be $\sim 15 \mu\text{m}$ by $4 \mu\text{m}$ exhibiting the double-line shape features which were shown

earlier in the manuscript. The depth of the waveguide in z plane is higher than what was measured earlier and this is because in this case another microscope objective is used for the DLW. The objective exhibited lower NA, 0.4 compared to 0.75 NA. Therefore the photo-induced structures are larger given that the Rayleigh range is larger. Following that, the blue diode was turned off, and a CW low power 1030 nm laser (to avoid any fluorescence excitation or glass structuration) was injected inside the waveguide. Upon laser injection, a transmitted light was observed localized on the double-line shape structures (Figure II.48.d), which was the first observation of the waveguiding properties of the photo-induced silver clusters in silver containing glasses [149].

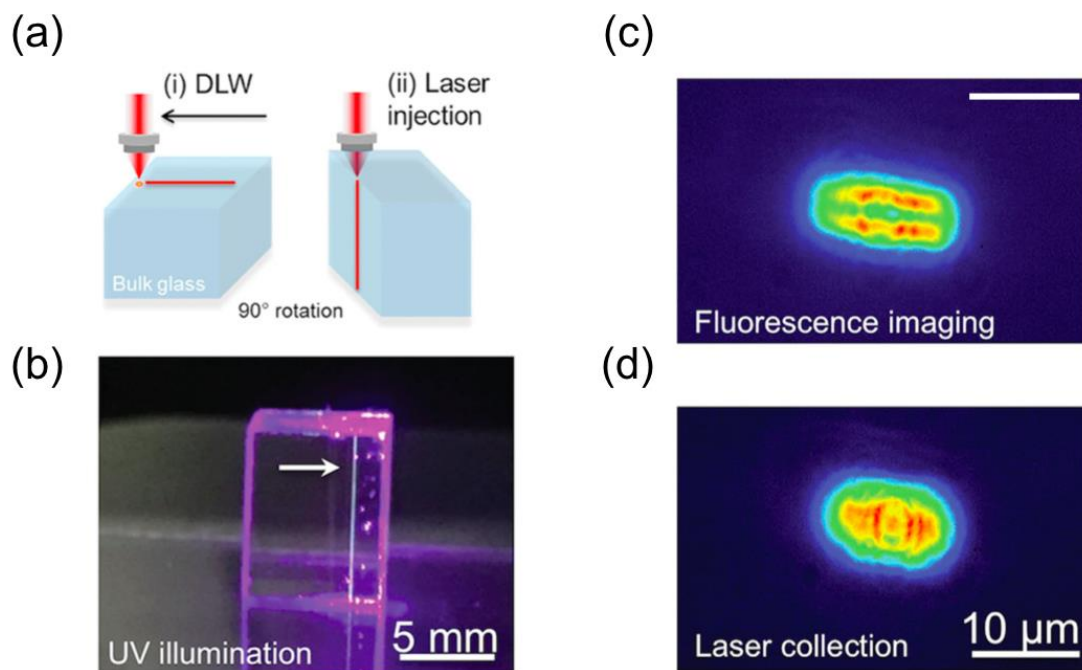


Figure II.48: (a) Schematic of the direct laser writing process and the laser injection; (b) Picture of the bulk sample under UV excitation ($\lambda_{ex}=405\text{nm}$) highlighting the fluorescence of the waveguide (indicated by the white arrow); (c) fluorescence image of the side view of the waveguide under UV excitation ($\lambda_{ex}=405\text{nm}$); (d) near-field guided mode profile following laser injection [149].

Further investigations were required to better characterize the written waveguide. One of the advantages of writing *type A* waveguides is that injection of light could be possible without the need to cut and polish the side facets if they are already polished. During the writing process and while exiting the glass facet, no ablation nor damage were noticed to the glass for *type A* waveguides, which makes the injection of light possible. It is not the case when writing *type I* waveguides where when reaching the glass facet, the glass explodes and is damaged. Therefore, the polishing process is a must in order to inject light inside such waveguides. Still, to

optimize the injection and characterization process of type A waveguides, the samples were always cut and polished prior to DLW.

The sample was placed on the mode profile setup and a red laser beam at 660 nm was injected inside the waveguides. The sample was excited from the side using a 405 nm before laser injection in order to visualize the structures. Figure II.49.a and Figure II.49.e shows the fluorescent side view of WG1 and WG2 respectively. Then, the laser was injected inside the waveguides. Both waveguides exhibited a multimode aspect. Figure II.49.b and Figure II.49.f show one of the higher order guided mode profiles following laser injection. The UV light was filtered using a 450 HP filter. One can observe that the guided mode profile is supported by the two fluorescent planes i.e. the two planes of silver clusters, therefore providing another proof that the silver clusters are responsible for the Δn in silver containing glasses. The 405 nm diode was turned off in order to better visualize the guided mode profile, as shown in Figure II.49.c and Figure II.49.g respectively for WG1 and WG2. Moreover, simulations were conducted using LUMERICAL software to simulate the propagation of light in such structures. The details of the simulations were presented earlier in the manuscript. Figure II.49.d and Figure II.49.h show the simulated modes. A significant match is noticed between the experimental and the simulated modes confirming once again our hypothesis. WG1 exhibited a Δn of 4.5×10^{-3} while WG2 a Δn of 3×10^{-3} . The Δn was measured using the SID4Bio wave front sensor. Many modes were supported by those waveguides given that they exhibit relatively large dimensions of 15 μm with a relatively high Δn .

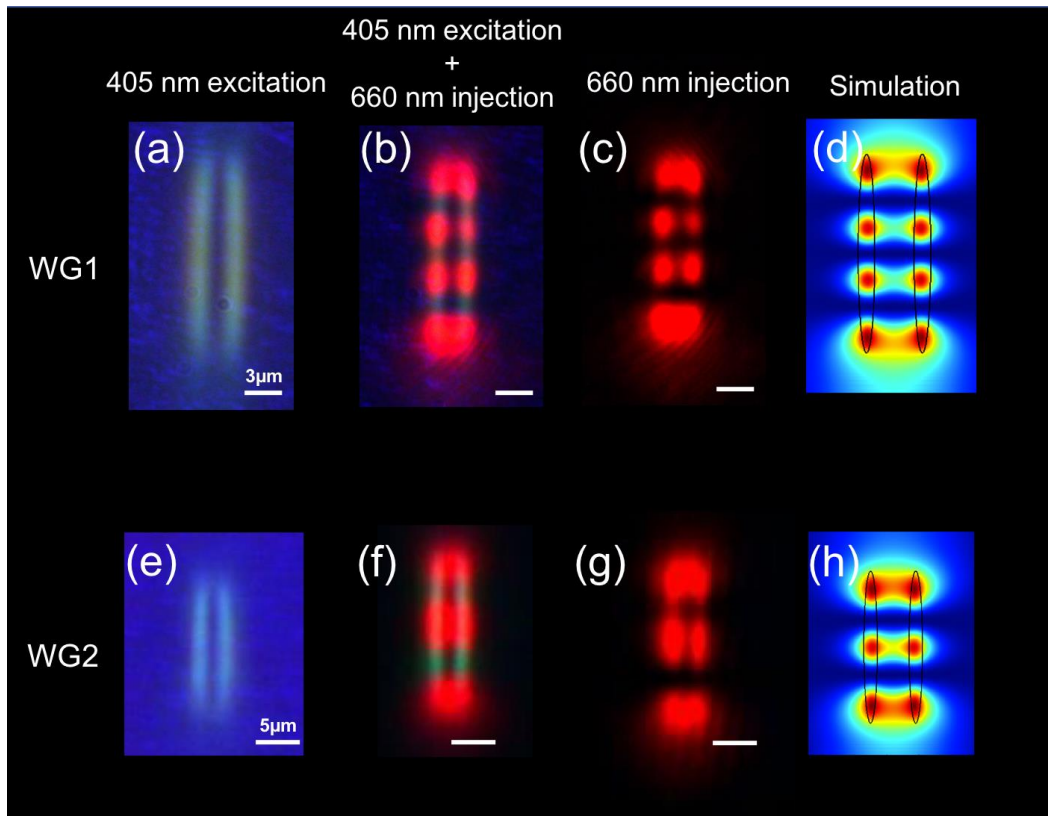


Figure II.49: Cross section view of fluorescence under UV side-excitation ($\lambda_{exc}=405\text{nm}$) of (a) WG1, (e) WG2. Superimposed near field mode profile and fluorescence features for (b) WG1, (f) WG2. Near field mode profile for a high order propagating mode of (c) WG1, (g) WG2. Simulated mode profile using LUMERICAL for (d) WG1, (h) WG2. DLW parameters for WG1: $8\text{ TW/cm}^2 - 10\mu\text{m/s}$. For WG2: $8\text{ TW/cm}^2 - 20\mu\text{m/s}$.

Furthermore, a $1.55\ \mu\text{m}$ laser was injected in WG1 to verify the capacity of such waveguides to guide light at wavelengths in the NIR. The guided mode profiles are presented in Figure II.50. Even at $1.55\ \mu\text{m}$, the waveguide supported two propagating modes i.e. a multimode waveguide. This is due to the large dimensions and the relatively high Δn of the waveguide.

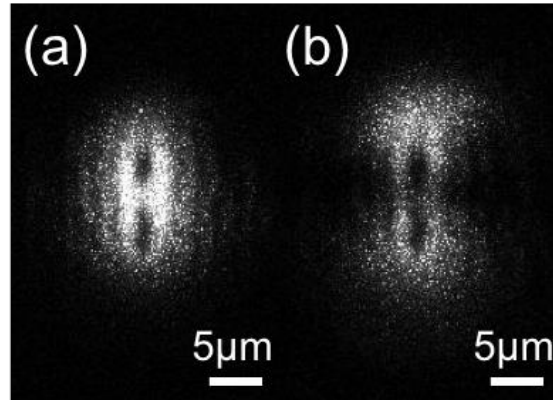


Figure II.50: Near field mode profile following laser injection at 1.55 μm (a) fundamental mode, (b) higher order mode. The waveguide presented a multimode aspect. DLW parameters: $8\text{TW}/\text{cm}^2 - 10 \mu\text{m}/\text{s}$.

II.6.3.b. Single mode waveguide

The first approach to write waveguides resulted in multimode waveguides in the visible and NIR range. For optical circuits and optical components, multimode waveguides are a disadvantage due to the various numbers of modes supported by the waveguide and the complexity of characterizing such waveguides. Therefore, single mode (SM) waveguides needed to be written. In order to do so, a series of waveguides were written in PZnAg1 silver containing zinc phosphate glass. The waveguides were written typically 160 μm below the surface. The DLW was performed using a 20x-0.75NA objective aiming to produce smaller waveguides. The target was to reduce the dimensions of the waveguides as well as the Δn . Eventually the number of modes supported by a waveguide is linked to the dimensions and Δn of the waveguide (II-5). To get a single mode waveguide, the laser irradiance as well as the number of pulses were optimized to get the appropriate size and Δn . Many waveguides were written, some were multimode, some single mode. For the sake of simplicity and given that the multimode aspect was presented earlier, only one single mode will be presented.

Following DLW, the sample was cut and polished. The structures were imaged using a confocal fluorescence microscope (Figure II.51.a), which provides a better resolution of silver cluster spatial distribution. As expected, the photo-induced structures consisted of two parallel planes exhibiting a full width half maximum (FWHM) of 0.55 μm (limited by confocal microscope resolution) and spaced by 1.85 μm along the y direction (Figure II.51.b). The corresponding length of the twin structure along z was measured to be around 6 μm (Figure II.51.c). However, the spacing between the two parallel fluorescent planes as well as their extent along z

could both be varied from 1.8 μm to 3 μm and 4 μm to 15 μm respectively, depending on the microscope objective used as well as the laser parameters. The study of the extent along z was shown earlier as a function of the laser parameters (Figure II.42).

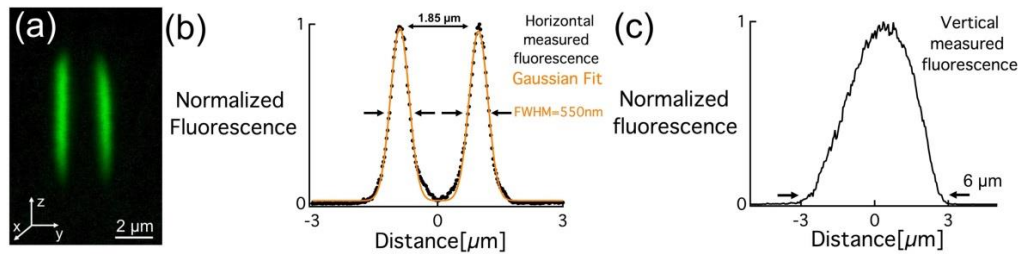


Figure II.51: (a) Fluorescence confocal image of the side view of the waveguide. (b) Normalized horizontal fluorescence profile averaged along the y axis. (c) Normalized vertical fluorescence profile averaged along the z axis.

Given the right dimensions of the photo-written waveguide, the Δn was characterized using the wave front sensor SID4bio from PHASICS. The Δn exhibits a smooth and homogenous aspect as well as a sharp spatial distribution as shown in Figure II.52.a. The transverse profile shows two peaks of positive Δn of 2.5×10^{-3} spaced by $\sim 1.8 \mu\text{m}$ with a FWHM approximately $0.8 \mu\text{m}$ (Figure II.52.b). Note that the measured FWHM of $0.8 \mu\text{m}$ is limited by the instrument's spatial resolution. The good match between the top view spatial distribution of the silver clusters (Figure II.38.b) and the Δn profile (Figure II.52) confirms that the Δn is once again correlated to the creation of the silver clusters.

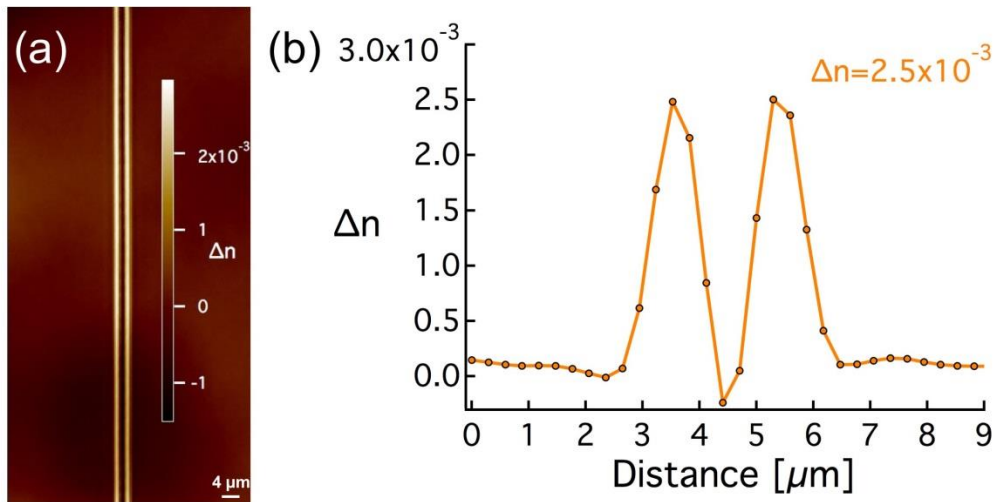


Figure II.52: (a) Phase image of the top view of the waveguide under white illumination (b) Refractive index change (Δn) profile obtained from the phase image. DLW parameters: $9\text{TW}/\text{cm}^2 - 60 \mu\text{m}/\text{s}$.

A small negative Δn dip was observed between the two sharp positive peaks (Figure II.52.b). It is the case when using relatively high irradiance and/or low writing speed (high number of pulses) or following many laser passages as shown in Figure II.53. For instance, for the same laser irradiance, the negative dip starts to appear for lower writing speeds (Figure II.53). Furthermore, for a moderate laser irradiance and writing speed, no negative dip was observed. However, the negative Δn dip starts to appear and grows as a function of the number of laser passages as shown in Figure II.53.a. For a relatively low speed of writing, the dip is present, yet it grows as the number of laser passages grows (Figure II.53.b-c).

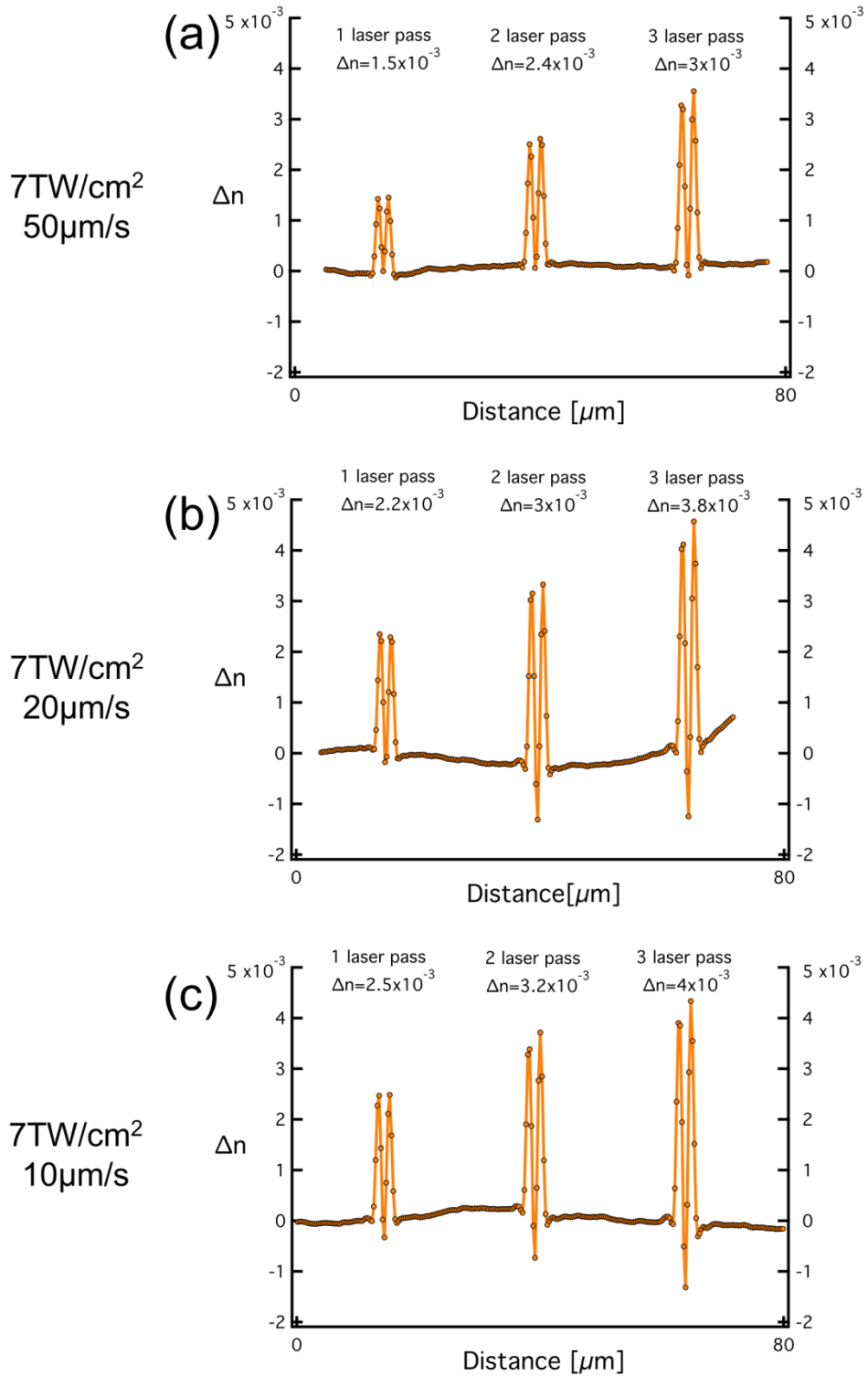


Figure II.53: Refractive index change (Δn) profile for different laser passages for an irradiance of $7 \text{ TW}/\text{cm}^2$ and a speed of writing of (a) $50 \mu\text{m}/\text{s}$, (b) $30 \mu\text{m}/\text{s}$, (c) $20 \mu\text{m}/\text{s}$. A negative Δn dip appears for lower writing speeds and for many laser passages.

This negative Δn dip could be correlated to the diffusion of silver ions to the edges. In 2015, a topological and silver concentration distribution study was performed by *Desmoulin et al* [141]. The fluorescence distribution, the topology following chemical etching and the silver concentration distribution were plotted together for the same spatial distribution of silver clusters (Figure II.54). One can observe that the concentration of silver ions exhibits a dip in the middle referring to fewer quantities of silver ions. It could be due to the diffusion of such ions but no increase was observed on the edges. However, this increase on the edges could be very small and probably could not be detected by the microprobe used. The dip in the middle refers to the lack of silver ions. Therefore it could be also correlated to the small negative Δn dip observed in phase image.

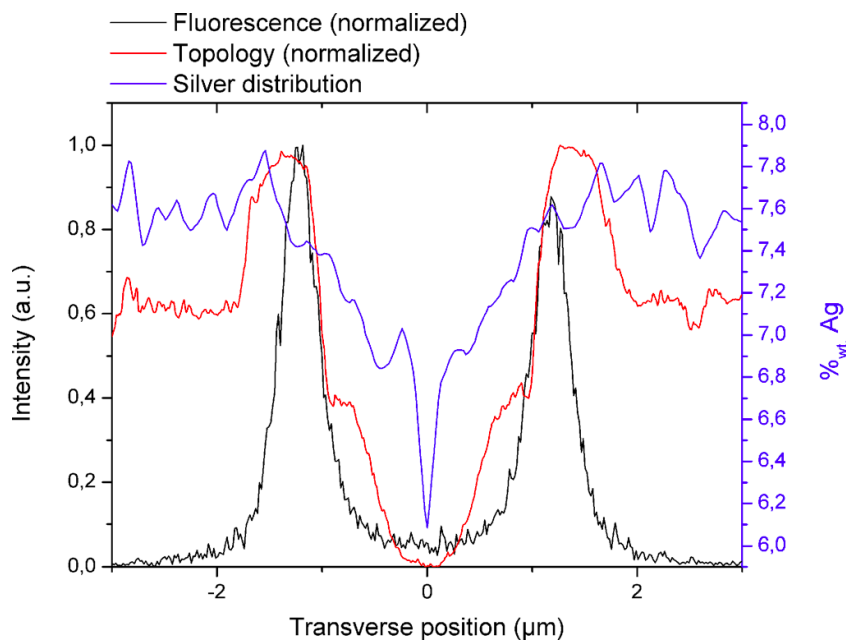


Figure II.54: Superposition of the silver cluster fluorescence spatial distribution (black), normalized topology after chemical etching (red) and silver ions concentration distribution (blue). Taken from [141].

During the development of silver containing glasses, it was observed that incorporating silver ions in the glass matrix tended to increase the refractive index of the glass, as shown in Figure II.55 [135]. Therefore, the absence of silver ions in the middle could be responsible for the negative Δn dip observed in the middle. Furthermore, many laser passages imply more consumption of the silver ions reservoir i.e. the silver ions are no longer present in the middle, probably diffused leaving a small negative Δn dip.

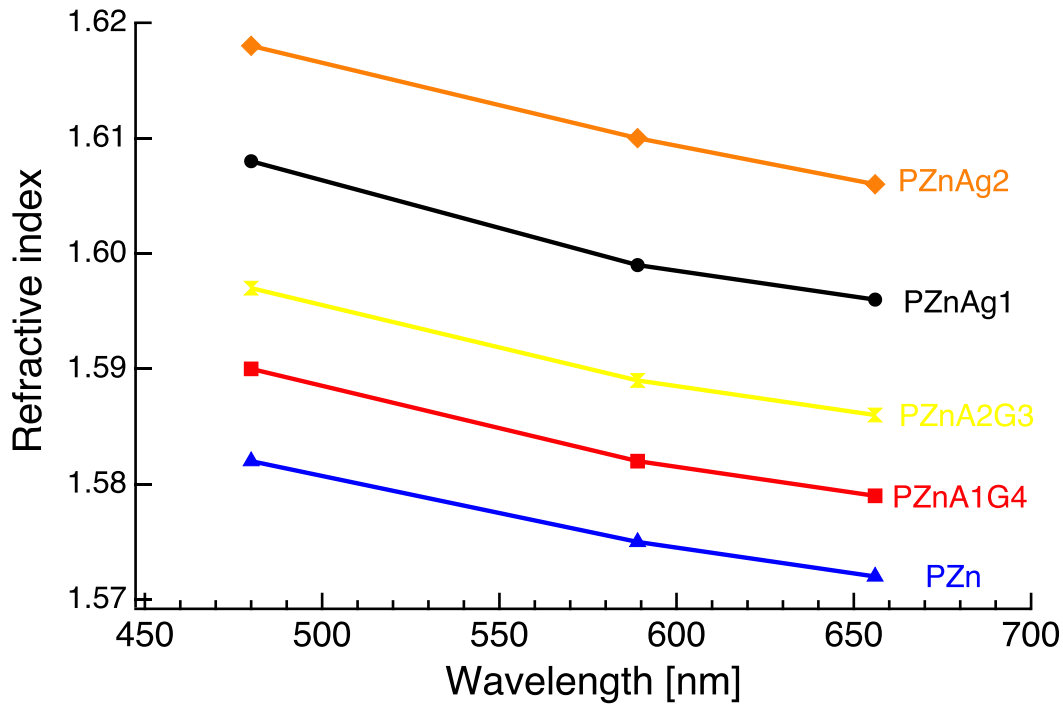


Figure II.55: The variation of the refractive index of the non-containing and silver containing zinc phosphate glasses as function of the silver concentration incorporated in the glass matrix. The higher the concentration of silver the higher the refractive index of the glass is (from bottom to top). Data from [135].

After characterizing the morphology of the waveguide as well as the Δn value, we moved to testing the waveguiding properties. A 630 nm light was injected inside the structure while the near field intensity profile was imaged using a CCD camera and a microscope objective as mentioned in the experimental part section II.5.4. The horizontal intensity mode profile depicted in Figure II.56.a.ii is a non-standard single mode profile that can be fitted by the superposition of two Gaussian distributions (total FWHM $\sim 3 \mu\text{m}$) while the vertical intensity mode profile shows a good match with a Gaussian fit as expected (FWHM $\sim 5.2 \mu\text{m}$) (Figure II.56.a.iii). Based on numerical simulations, each single laser-induced trace of silver cluster Ag_m^{x+} is expected to support waveguiding by itself. In the case of experimental structures, the Ag_m^{x+} traces are separated by a relatively small separation distance ($\sim 1.5 \mu\text{m}$) and a relatively low Δn ($\sim 2.5 \times 10^{-3}$). The horizontal mode profile (Figure II.56.a.i) was observed to remain the same whatever the injection condition. Indeed, the spatial overlap of the injecting fiber with the guiding structure only influence the transmitted intensity of the guided mode, without affecting the guided mode profile. Therefore, this allows us to conclude that the following waveguide is a single mode waveguide operating at 630 nm and supporting one single mode despite its original profile. This was not the case for the previously mentioned

waveguides where the spatial overlap of the injecting fiber with the waveguide affected the guided mode profile and resulted in exciting higher order modes, as shown in Figure II.49. Such original double trace structure supported by the laser-induced silver clusters thus seems to behave similarly to two close and highly interacting waveguides [163, 164], globally corresponding to a structure that sustains a single super mode. Although for single-mode, one can still note that such a waveguide is elliptical ($\epsilon=1.7$).

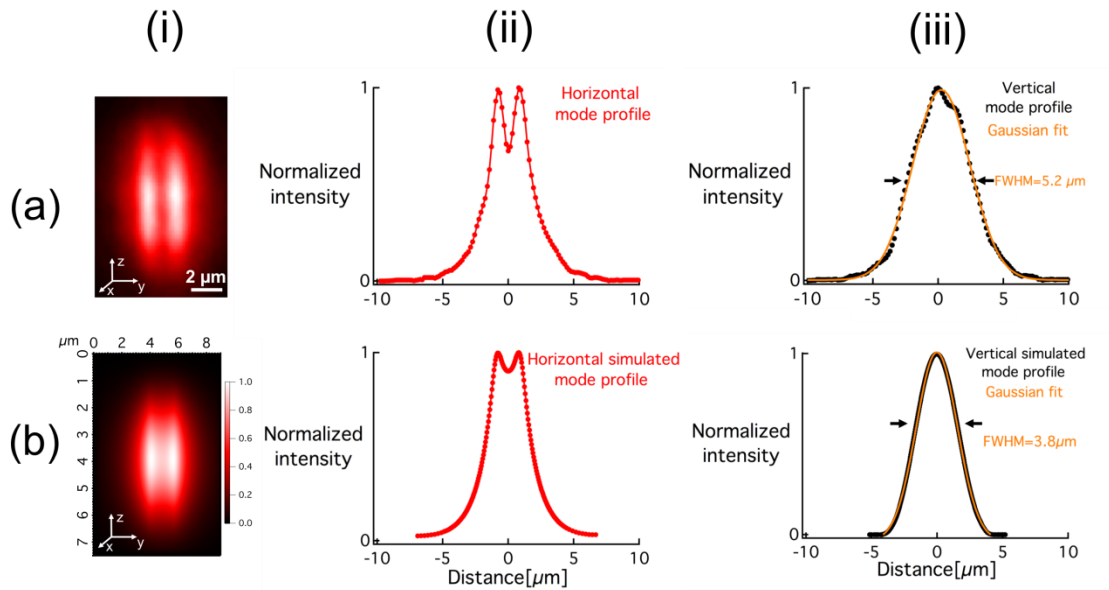


Figure II.56: (a) Experimental: (a.i) Near field mode profile after injecting a 630 nm laser, (a.ii) normalized horizontal mode profile intensity averaged along the z axis, and (a.iii) normalized vertical mode profile intensity averaged along the y axis. (b) Simulations: (b.i) simulated mode profile (to compare with Figure II.56.a.i), (b.ii) normalized horizontal intensity mode profile averaged along the z axis (to compare with Figure II.56.a.ii), and (b.iii) normalized vertical mode profile intensity averaged along the y axis.

Furthermore, simulations were conducted to correlate the experimental and simulated near-field mode profiles. All the waveguides were simulated as two parallel ellipsoids with a specific thickness "e", spaced by the measured distance "d" with the measured depth "z" in the z axis and a step index Δn corresponding to the values measured for each waveguide, as shown in Figure II.57.

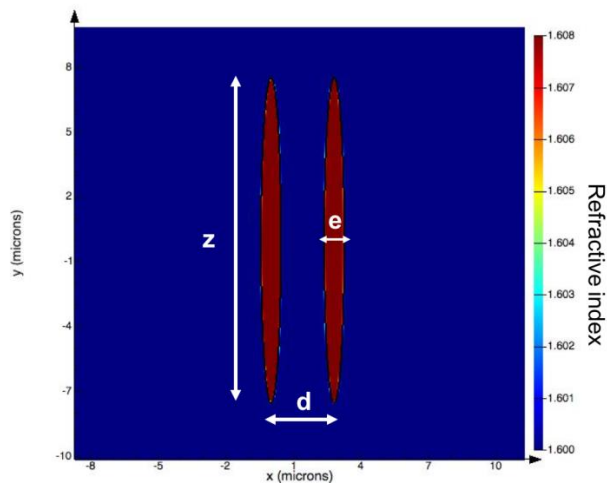


Figure II.57: Schematic model of the simulated waveguides using Lumerical Mode solutions software. The waveguides are simulated as two parallel ellipsoids with thickness “e”, with a length “z” and separated by a distance “d”. The color scale corresponds to the refractive index change. In this case, the glass refractive index change is 1.6 while the waveguide is 1.608 corresponding to a refractive index change (Δn) of 8×10^{-3} .

The single mode waveguide was simulated as two parallel ellipsoids with 550 nm thickness, separated by $1.85 \mu\text{m}$ with a depth of $6 \mu\text{m}$ in the z axis and a step index Δn of 2.5×10^{-3} . The simulated mode in Figure II.56.i.b shows a significant match with the experimental mode, which supported our claim concerning the new type of refractive index change based on silver cluster formation. Furthermore, it confirms the correlation between the fluorescence i.e. silver cluster spatial distribution and the Δn . However, we noticed a difference between the dimensions in the experimental and simulation modes (Figure II.56). This is most likely due to the step index Δn used during simulation instead of a smooth distribution of Δn in the structured glass and the fact that the waveguide is simulated as two ellipsoids with positive Δn , which slightly differs from the real gradient of the index change and forms the real shape of the waveguide. Therefore, the simulated mode profile is more confined in the structures than the experimental one. Moreover, the Δn profile as well as the experimental and simulated mode profiles are presented on the same scale in Figure II.58. Once again, a significant match could be noticed between the Δn profile, experimental and simulated mode profiles. The guided mode is supported by the Δn variation indicating again that the silver clusters support the waveguiding process.

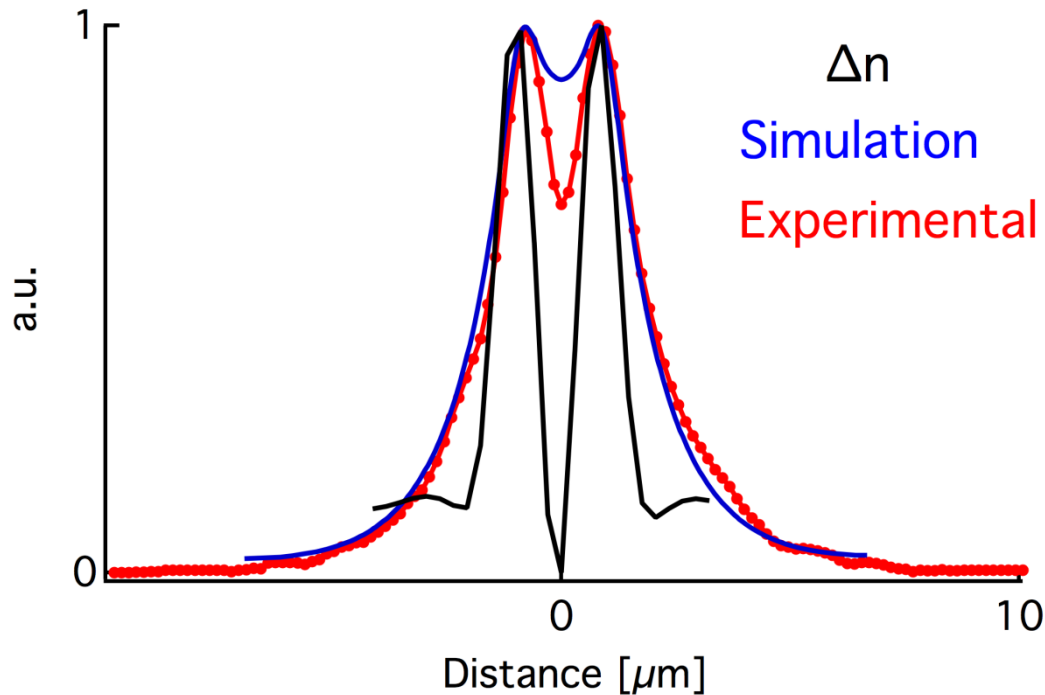


Figure II.58: Spatial superposition of the measured refractive index profile (Δn) (black), simulated near-field mode profile (blue) and experimental near-field mode profile (red). A good match is observed between the simulated and experimental modes and the Δn distribution.

The waveguide was simulated as two ellipsoids with a thickness of 550 nm and a Δn of 2.5×10^{-3} . The fluorescence confocal microscope images reveal that the width of the structure is around ~ 550 nm and this is probably limited by the resolution of the confocal microscope. Earlier work in the group performed by Marquestaut et al., revealed that the structure's thickness is ~ 100 nm using HRSEM images [139] using another microscope objective but still the results are interesting. Therefore, we assume that in this case we are probably over estimating the thickness of our structures. Unfortunately, no HRSEM measurements were performed on those structures to confirm our hypothesis. But, on the other hand, using simulations, when decreasing the thickness of structures, a higher Δn is required to support waveguiding and a higher Δn is required to trigger the multimode aspect, as shown in Figure II.59. This is expected, since decreasing the dimensions of a waveguide decreases the V parameter i.e. the number of guided modes. Therefore, if we are underestimating the thickness of our structures, it implies that we are underestimating the value of the photo-induced Δn . For instance, if we estimate the structure's thickness to be 500 nm, the Δn required to trigger the multimode aspect is 4×10^{-3} , while if the thickness is 200 nm a Δn of 2×10^{-2} is required to trigger the multimode aspect.

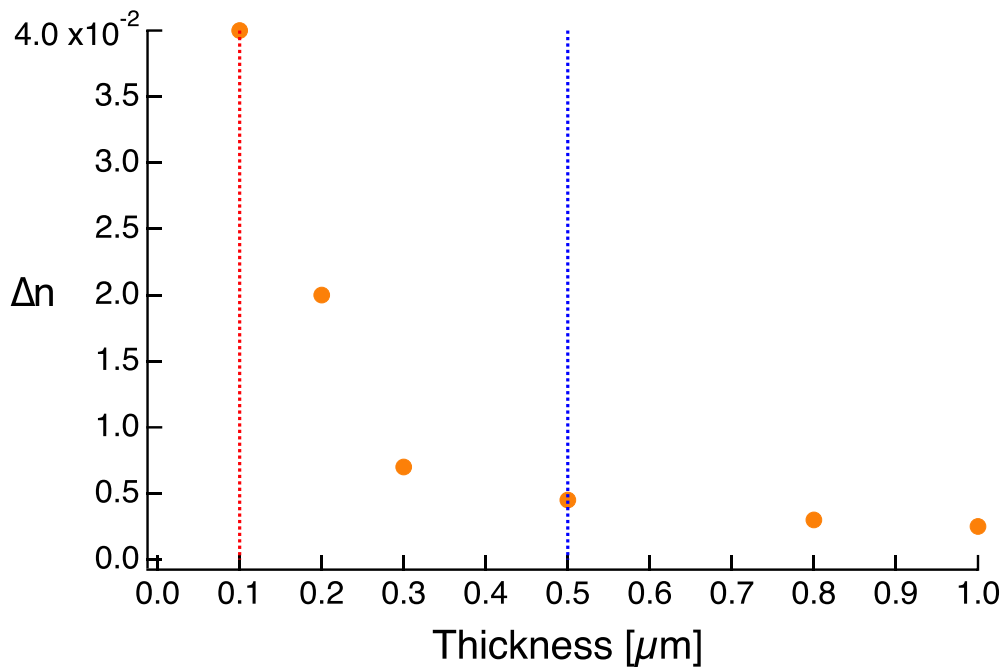


Figure II.59: Variation of the minimum Δn required to trigger the multimode aspect as a function of the thickness of the structures. Blue vertical line indicates the thickness measured by confocal microscope and used during simulations ($\sim 500\text{nm}$) while the red line indicates the HRSEM measurement ($\sim 100\text{nm}$) performed earlier in our group [139].

Finally, a large mismatch between the injected mode profile and the geometry of the waveguide results in injection losses estimated to be at its best at 5.22 dB as estimated by numerical simulations. The losses could be higher depending on the glass surface condition during injection (for example dust, not well polished). That is also related to the fact the waveguide is not a circular one but can be illustrated as two ellipsoids with positive Δn spaced by $\sim 1.85 \mu\text{m}$. The upper bound of the overall losses is 1.2 dB/cm, estimated considering the simulated mismatch (5.22 dB), Fresnel losses of (0.43 dB) ($n=1.59$) and the measured insertion losses of the 7-mm waveguide. One should mention that the traditional methods for characterizing propagation losses is not highly efficient due the large mismatch between the fiber and the waveguide geometry, and the short length of the waveguide. One of the best methods to identify the propagation losses is the cut-back method. It is normally used to characterize the losses in fibers. Light is injected inside a fiber roll of many meters or centimetres. The transmission is monitored while a specific length of the fiber is cut while the light injection is fixed. The transmission increases every time a part of the fiber is cut which leads to the propagation losses per unit of length (dB/Km, dB/m, dB/cm). Unfortunately, during

the project, it was not possible to have long samples up to 10 cm in order to perform the study. Therefore we limited the estimation of losses to the previously mentioned method. Further efforts are required in the future to get a more accurate evaluation of the propagation losses of such waveguides. Compared to the type I waveguides in phosphate glasses, the lowest losses were ~ 0.54 dB/cm at a wavelength of 660 nm [132]. While at 1530 nm-1565 nm, wavelengths losses were lower than 0.4 dB/cm [134]. Both were reported in Er:Yb doped zinc phosphate glasses. However, one should mention that the coupling losses in both cases were not as high as in our case given that the waveguides exhibited a more circular shape. The most critical point in estimating the losses of silver-based waveguides is the power coupling/overlap between the injected mode and the elliptical waveguide shape. Numerical simulations estimate the losses to be 5.22 dB but those losses could be underestimated which makes the estimation of the propagation losses harder.

II.6.3.c. Multimode - Single mode aspect

Multimode waveguides and single mode waveguides were presented during this work. As mentioned before, a single mode (SM) waveguide is defined by the fact that the spatial movement of the injecting fiber does not excite a higher order mode. Therefore only one mode can propagate in the waveguide no matter how the injection occurs. However, for the multimode (MM) waveguides, it is not the case. Changing the injection affects the guided mode and excites higher order modes. The number of higher modes that could be excited in a multimode waveguide could be defined by the dimensions and the Δn of the waveguide (V parameter in (II-5)). Some multimode waveguides exhibit two guided modes only and others exhibit four to five guided modes for instance. However, even for a multimode waveguide, the fundamental mode could be excited. Figure II.60.a shows the fundamental mode of a multimode waveguide while Figure II.60.b shows the fundamental mode of a single mode waveguide. The MM waveguide is 13 μm long while the SM waveguide is 6 μm . The transverse profiles of both modes are presented in Figure II.60.c. One can see that for the MM waveguide, the global mode is more confined. The two silver planes better confine light compared to the SM waveguide. The light intensity drops in the middle to 0.3 compared to 0.65 for the SM waveguide. This is probably due to the higher Δn for the MM waveguide that results in more confining of the light inside each silver cluster plane compared to SM, where the Δn is relatively lower and the light is less confined. This was observed for all MM and SM waveguides. As mentioned before, the waveguides behave as two highly interacting

waveguides coupling light between each other, exhibiting a super mode profile as an output. In the case of a higher Δn , the light is more confined in one plane and the interaction between them is lower. Nevertheless, all waveguides studied during this project guided light supported by both silver planes acting as one waveguide.

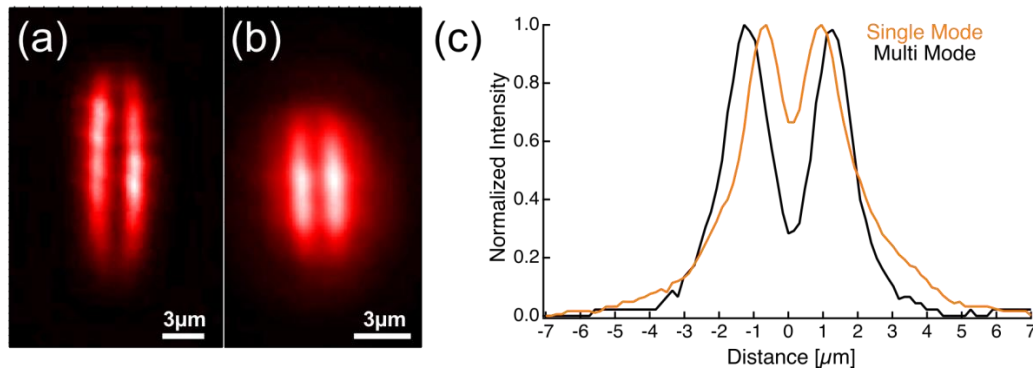


Figure II.60: Fundamental near-field mode profile of a (a) multimode (MM) waveguide, (b) single mode (SM) waveguide. (c) Near-field mode profiles of the MM and SM waveguides. DLW parameters for SM: $9\text{TW}/\text{cm}^2 - 60\mu\text{m}/\text{s}$, for MM: $10.5\text{TW}/\text{cm}^2 - 20\mu\text{m}/\text{s}$.

Moreover, for the multimode modes presented in Figure II.49.c-g one can see that the interaction between the modes in the middle of the waveguide is less significant compared to the modes on the top and bottom. The modes on the top and bottom are observed as one mode combined instead of two modes interacting with each other, as it is the case for middle ones. This is probably because on the top and bottom, the waveguides have thinner planes and probably lower Δn than the middle. So, the light is less confined in those areas and the coupling effect is more significant on the top and bottom of the waveguides, as also observed in simulation Figure II.49.d-h.

II.6.4. Optical components

II.6.4.a. Y-beam splitter

Once the waveguiding properties were investigated, confirmed and characterized, the control of Δn and multimode and single mode aspects is mastered, we moved to the creation of optical components taking a step forward towards applications such as 3D integrated circuits. The first approach was the inscription a 50-50 Y-beam splitter typically $160\mu\text{m}$ below the surface of PZnAg1 glass. It consisted of two partially overlapping S-bended waveguides as shown in Figure II.61.a. The S-bend waveguides were written using an irradiance of $9\text{TW}/\text{cm}^2$ with a writing speed

of $60\mu\text{m/s}$. The curvature radius R_c was fixed to 25 mm while the distance between the input and output waveguides Δh was $20\mu\text{m}$. This led to two outputs separated by $40\mu\text{m}$, which is normally sufficient to avoid any coupling effect based on the evanescent wave. The optical component divides the input light power equally through each of the two output branches (Figure II.61.a). Fluorescence image of the written beam splitter is shown in Figure II.61.b. Following laser injection in the beam splitter, the output facet of the sample was imaged and two spots indicated that the input beam was split into two output branches as shown in Figure II.61.c. Moreover, the mode profiles of both outputs are similar to the mode profile of a linear waveguide (Figure II.56.a), which indicates the beam splitter did not affect the guided mode profile. The near-field intensity profile shows that the transmitted power is indeed divided equally between the two branches with an uncertainty of 3.5% (Figure II.61.d) confirming the successful inscription of a 50-50 beam splitter based on a *type A* refractive index change.

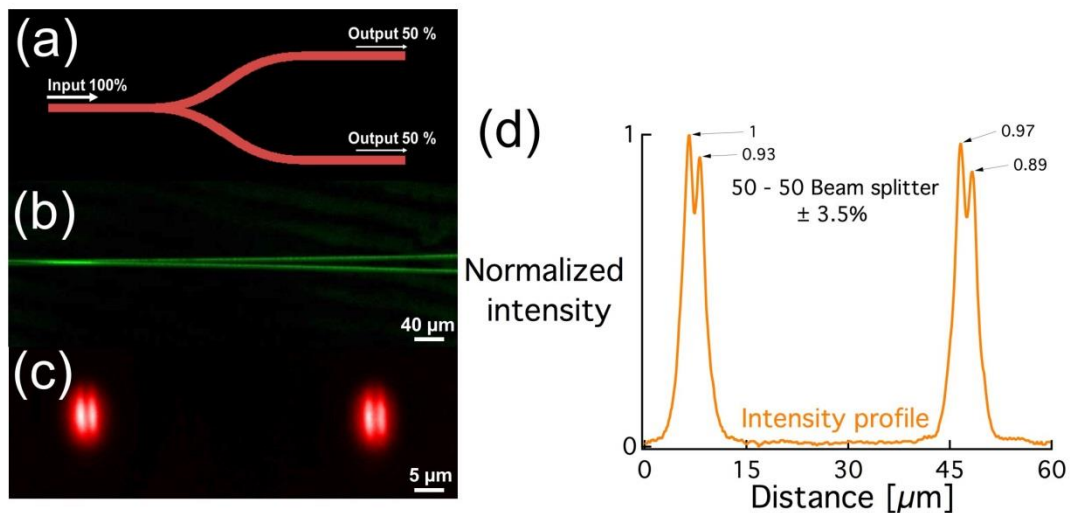


Figure II.61: (a) Sketch of the Y-beam splitter dividing the input light into two equal outputs (top view), (b) top view fluorescence image of the Y-junction ($\lambda_{\text{ex}}=480\text{nm}$, $\lambda_{\text{em}}=550\text{nm}$), (c) output modes of the beam splitter (d) normalized intensity profile of the output modes indicating an almost equal splitting of light between both outputs. DLW parameters: $9\text{TW/cm}^2 - 60\mu\text{m/s}$.

II.6.4.b. Directional couplers

The second demonstration was inscribing directional couplers. First a preliminary study was conducted to design and to monitor the corresponding losses for different S-bend waveguide configurations. The S-bend waveguides written with the same laser conditions consisted first of a straight part, then a curvature radius R_c

based on a radius circle then another identical one but with a reversed curvature, then a straight part, as shown in Figure II.62. The input and the output of the S-bend waveguide were separated by Δh (Figure II.62).

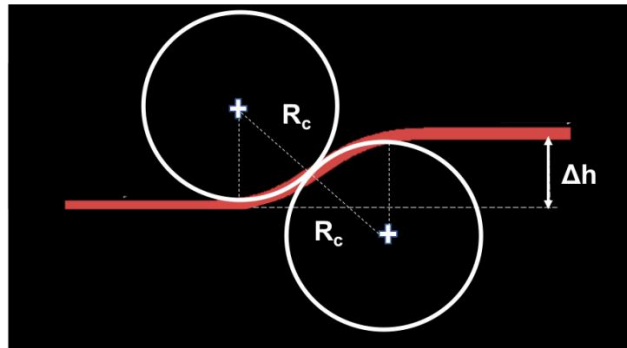


Figure II.62: Sketch of the S-bend

A series of S-bend single mode waveguides were written using a laser irradiance of $9.3\text{TW}/\text{cm}^2$ and a writing speed of $40\ \mu\text{m}/\text{s}$ using a $20\times -0.75\text{NA}$ obj. The chosen R_c were 25 mm, 50 mm and 100 mm while the Δh values were $10\ \mu\text{m}$, $25\ \mu\text{m}$, $50\ \mu\text{m}$, $100\ \mu\text{m}$ and $150\ \mu\text{m}$. The results are shown in Figure II.63. The transmission of the S-bend was normalized compared to a straight waveguide written in the same laser conditions. The lowest losses were observed for an $R_c=100\ \text{mm}$ and a Δh between $10\ \mu\text{m}$ and $25\ \mu\text{m}$. For an R_c of 25 mm even for a small Δh of $10\ \mu\text{m}$, the losses were high. Acceptable losses of around 20% (0.96 dB) were observed for $R_c=50\ \text{mm}$ and $\Delta h=10\ \mu\text{m}$. However, for a Δh of $25\ \mu\text{m}$ losses were significant and equivalent to losses at a Δh of $50\ \mu\text{m}$. We believe that in that case the waveguide exhibited some defects implying higher losses.

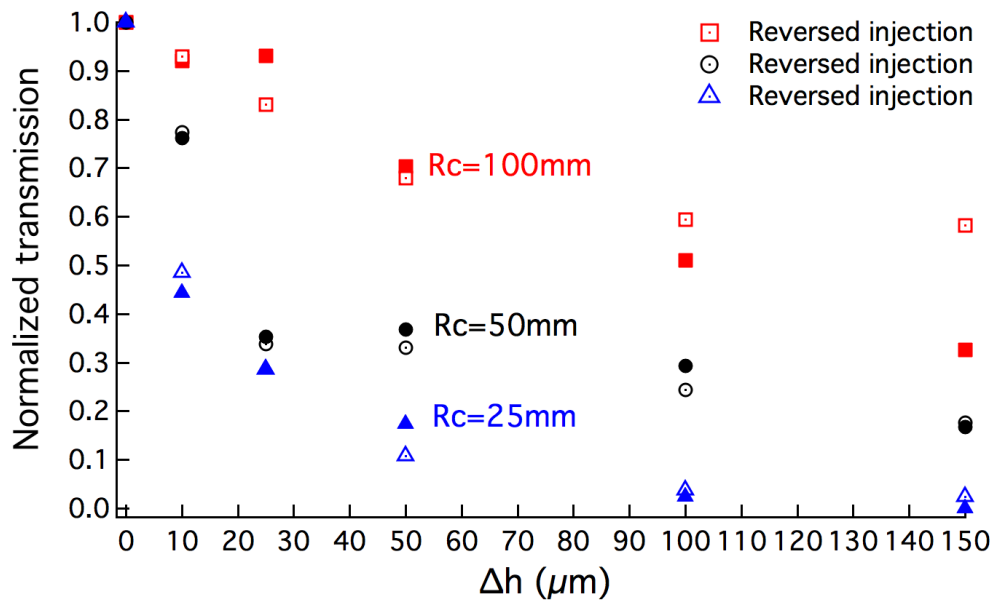


Figure II.63: Normalized transmission of the S-bend waveguides as a function of the radius curvature R_c and the separation distance Δh . Reversed injection data corresponds to backward injection in the S-bend waveguides. DLW parameters: $9.3\text{TW}/\text{cm}^2 - 40\mu\text{m}/\text{s}$.

A series of couplers were written in order to optimize the coupling parameters i.e. the interaction length "L" and the separation distance. The couplers consisted of 8 mm straight waveguides written typically $160\mu\text{m}$ below the surface. Then 2 mm away from the input facet, a S-bend waveguide is written spaced by a distance "d" with an interaction length "L" providing the coupling zone as shown in Figure II.64.

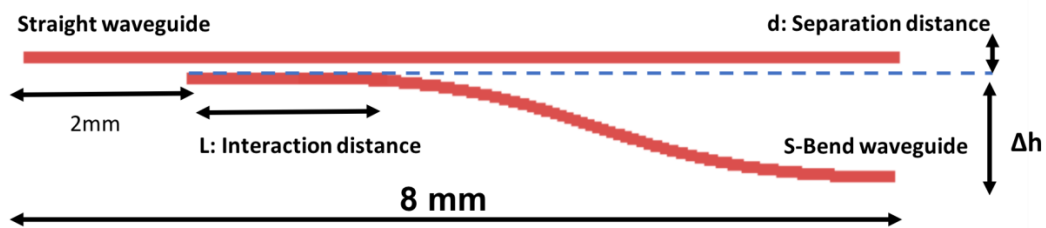


Figure II.64: Sketch of the coupler consisting of straight and S-bend waveguides.

Given that the glass samples were limited in dimension to $\sim 8\text{ mm}$, the choice of R_c and Δh were 50 mm and $40\mu\text{m}$ respectively in order to spatially fit the component inside the 8 mm glass sample. The following parameters exhibited losses of course, but these were acceptable losses in order to demonstrate the coupling effect between *type A* waveguides. Following primary tests, it was found that for $L=1\text{ mm}$

the coupling is not high enough while the 2 mm length was sufficient to observe coupling effects from one waveguide to another. Therefore, the interaction length was fixed to 2 mm and the separation distance d between two waveguides was varied from 5 to 20 μm by steps of 2.5 μm . The power transmitted by the straight waveguide P_s was normalized by dividing it by the overall sum of the guided power $P_s + P_c$. Consequently, one can have a better idea of the coupling ratio. The experimental and the simulated power coupling ratios are shown in Figure II.65. The simulations were based on plotting the coupled power from (II-8). One can see the oscillation of the coupling ratio between 5 μm and 7.5 μm , which is typical of the coupler's behaviour. However, that was not observed in the experimental data owing to the fact that the distance step was 2.5 μm , which is too large compared to a step of 0.1 μm in simulations. Moreover, an acceptable match between the simulated and the experimental data was found. The small differences could be related to the fact that the waveguide is elliptical ($\epsilon=1.3$) and not a circular one given that the simulations are based on LP_{01} circular modes interacting together.

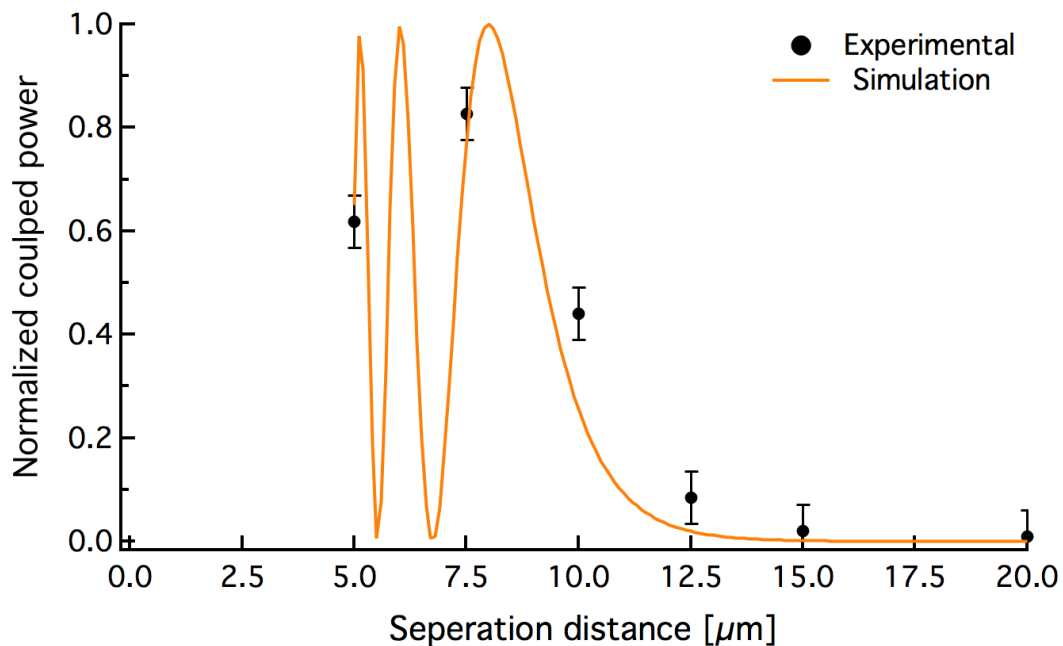


Figure II.65: Simulated and experimental normalized coupled power as a function of the separation distance between the two waveguides. DLW parameters: $9.3\text{TW}/\text{cm}^2 - 40\mu\text{m}/\text{s}$

A 50-50 coupler at a wavelength of 630 nm was written later using a laser irradiance of $10.8\text{ TW}/\text{cm}^2$ and a writing speed of $40\mu\text{m}/\text{s}$ in an 8 mm bulk glass sample. The straight waveguide and the S-bend were separated by $d=7\mu\text{m}$, the interaction length set at $L=2\text{mm}$, $R_c=50\text{mm}$ and $\Delta h=40\mu\text{m}$. The near-field mode intensity profiles of the two outputs show equivalent power for each output as

indicated in Figure II.66.b. The double line features of the silver clusters are not visible in this image. This could be due to the beam profiler used for imaging the guided near-field mode profile and not a high definition CCD camera like the previous cases.

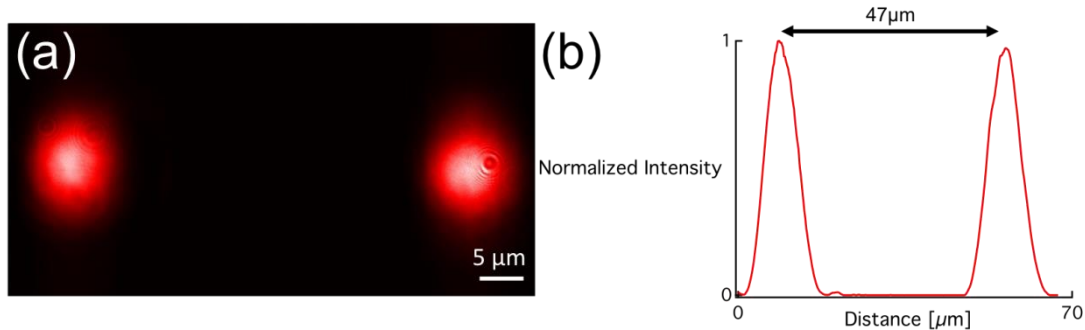


Figure II.66: (a) Near-field mode profiles of the output of the coupler; (b) normalized intensity of the mode profiles indicating the creation of a 50-50 coupler. DLW parameters: 10.8 TW/cm² – 40µm/s.

II.6.5. Waveguides in Ribbon Fibers

Finally, DLW of waveguides was conducted in silver containing ribbon fibers. As mentioned before in section II.5.2, DLW of small schemes like a Mach-Zenhdner and resonator was successfully performed on ribbon fibers but the waveguiding process was never tested [149]. Therefore, a 1.4 cm waveguide was written inside a 500 µm x 200 µm ribbon fiber typically 50 µm below the surface. A laser irradiance of 10TW/cm² was used while the writing speed was 25 µm/s. After the writing process, the end facets of the fiber were polished manually to optical quality to reveal the structures to the surface, to allow laser injection and profile imaging. The fluorescent structures exhibited the same morphology as the one in the bulk which also demonstrated the equivalence of the index modification profiles in bulk and fiber-shaped samples. A 630 nm laser was injected inside the 1.4 cm waveguide and the near field image was taken. Light was guided all over the full length of the waveguide, as shown in Figure II.67.a. The near field mode profile (Figure II.67.b) was similar to that of a single mode waveguide in bulk glasses, as shown previously in Figure II.56.

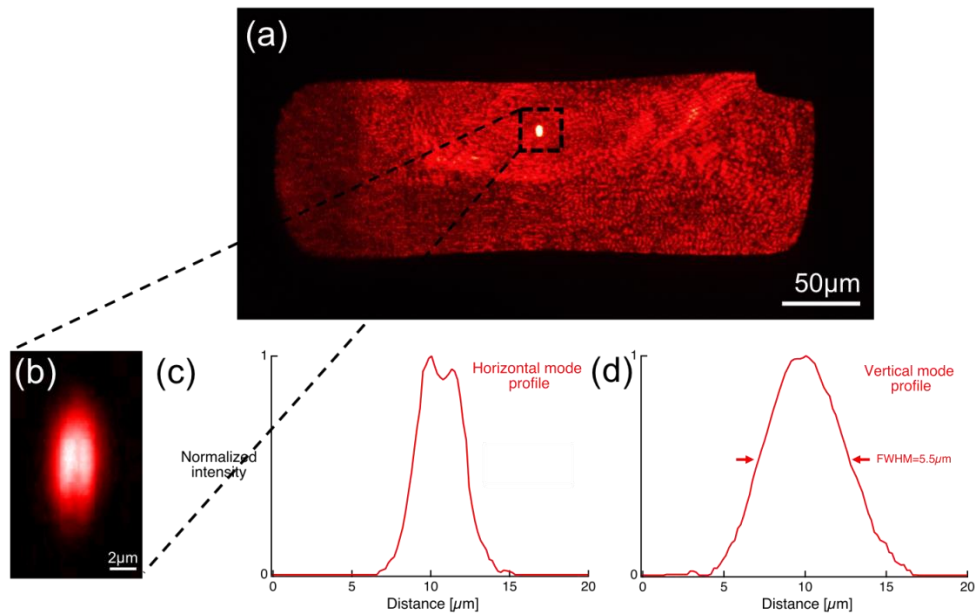


Figure II.67: (a) Cross-section view of the ribbon fiber with the guided mode in the middle; (b) blowup of the near-field mode profile; (c) horizontal mode profile; (d) vertical mode profile. The mode profile is similar to the mode profile in bulk glasses as shown in Figure II.56. DLW parameters: $10\text{TW}/\text{cm}^2$ – $25\mu\text{m}/\text{s}$.

Therefore, we demonstrate the capability of creating waveguides in ribbon fibers, thus paving the way for fiber applications in spectroscopy sensing, filtering and/or fully integrated photonics. DLW in silver-containing zinc phosphate bulk glasses and ribbon fibers allows the formation of a perennial new type of waveguides which take advantage of the thermal stability and bleaching-free fluorescence of the photo-induced silver clusters up to the glass transition temperature (typically $380\text{--}400\text{ }^\circ\text{C}$ here) [152, 165]. Furthermore, as mentioned before such laser-induced modifications had already led to original second-order effective nonlinearities by means of direct laser poling (EFISHG), allowing for a localized second-harmonic generation that showed a significant efficiency with an effective coefficient close to the pm/V level [142, 143]. In addition, a post laser irradiation thermal treatment ($T_g + 20\text{ }^\circ\text{C}$) in silver-containing zinc phosphate glass had allowed the growth of silver metallic nanoparticles exhibiting an effective dielectric/metal medium bearing a plasmonic resonance response in the structured glass matrix [139]. To the best of our knowledge, combining optical and plasmonic waveguiding in the same glass sample is not achievable otherwise, which highlights the novelty and tremendous potential of these new type waveguides. Finally, one must emphasize that the creation of silver clusters is not only limited to the silver-containing zinc phosphate glasses but can also be generated in other silver containing glass matrices such as sodocalcic and borosilicate glasses, as previously reported by our group [140]. This proves the universality in terms of processes when considering tailored materials as

silver-containing photosensitive glasses [33], and the novelty of this technique in making hybrid integrated circuits

II.7. Conclusion

Direct laser writing (DLW) in silver containing glasses induces the creation of fluorescent silver clusters Ag_m^{x+} around the interaction voxel. Their spatial distribution is dictated by the laser Gaussian beam. Those Ag_m^{x+} are responsible for a new type of refractive index change (Δn) that is compatible for waveguiding applications. This new type of Δn totally differs from the well-known *type I* as it originates from the creation of the photo-induced silver clusters around the interaction voxel involving such new chemical bonds with more polarizable electron clouds than those of initial silver ions Ag^+ leading to a local refractive index change independent of any modification of the glass matrix itself. The photo-induced Δn increases as a function of the laser parameters reaching a maximum value of around 8×10^{-3} . Multimode (MM) and single mode (SM) waveguides were created inside silver containing glasses. MM waveguides in the visible and IR wavelengths exhibited dimensions of $4 \times 15 \mu\text{m}^2$ with a $\Delta n = 4.5 \times 10^{-3}$ while a SM waveguide operating at $\lambda = 630 \text{ nm}$ exhibited dimensions of $\sim 3 \times 6 \mu\text{m}^2$, $\Delta n = 2.5 \times 10^{-3}$ and propagation losses estimated to be 1.2 dB/cm. The SM waveguide mode profile consists of one mode supported by each of the two silver cluster planes acting as one supermode. The simulation of mode profiles exhibited a significant match with the experimental modes confirming that the Δn is based on the creation of silver clusters. Following that, a 50-50 Y-beam splitter and a 50-50 coupler were written paving the way for 3D integrated optical components. Finally, the waveguiding process was demonstrated in silver containing ribbon shaped fibers by writing a 1.4 cm waveguide. These results provide unique opportunities for applications such as spectroscopy fiber sensing, filtering and/or fully integrated photonics.

Table of contents:

III. Comparative study between type A and the type I refractive index changes.....	122
III.1 Introduction	122
III.3 Type I modification in phosphate – zinc phosphate glasses	124
III.3 Experimental methods.....	124
III.3.1 Glasses	124
III.3.2 Laser setup.....	125
III.3.2.a Introduction	125
III.3.2.b Ti:Sapphire REGA-Coherent	125
III.4 Results	126
III.4.1 Type I modification in silver containing and non-containing zinc phosphate glasses	126
III.4.2 Structure morphology.....	133
III.4.3 Refractive index and mode profiles	135
III.4.4 Flipping Δn	138
III.4.5 Advantages of type A	144
III.5 Conclusion	146

Chapter III

Comparative study between the type A and the type I refractive index changes

III.1. Introduction

Direct Laser Writing (DLW) in glasses generally induced three types of refractive index changes classified as a progressive scale of the laser irradiance/fluence: *type I*, *type II* and *type III* [64, 65] as previously mentioned in Chapter II. *Type I* is a smooth refractive index change caused by a variation of the glass density induced at low fluence [61, 75, 166] which is due to the local heating and melting followed by a cooling process after laser passage [46], and/or the formation of color centers [60, 75, 76] (see section II.2.1). It consists of an intrinsic modification of the glass matrix itself leading to a refractive index change. Increasing the fluence of the laser, induces the creation of a *type II* refractive index modification which is birefringent and associated with formation of nanogratings [72-74]. Further increase of the fluence leads to the creation of *type III* modifications resulting in formation of voids or chaotic damage formation in the glass matrix.

Type I refractive index change is the most communally used for the creation of optical components such as waveguides [62, 63, 66-71], integrated optical components [114, 167-169] and recently quantum photonic circuits in glasses [170, 171]. However, a *type I* modification has been reported to exhibit a decrease in the refractive index change in some glasses such as BK7 borosilicate, ZBLAN and phosphate glasses [49, 76, 89, 100, 172, 173], which complicates the creation of optical waveguides. It depends on the glass composition as well as the inscription parameters.

In silver containing glasses, silver ions embedded inside the glass matrix act as a photosensitive support for DLW. In such silver containing glasses, DLW allows the formation of fluorescent silver clusters Ag_m^{x+} in the vicinity of the laser-glass interaction voxel [44, 136, 141]. Those silver clusters are at the origin of a novel type of refractive index modification that we call *type A* (based on the Latin name of silver, Argentum), acting as an extrinsic modification from the glass matrix in

silver containing glasses. It allows the creation of optical waveguides as well as photonic components as was demonstrated previously in Chapter II [149, 174].

In this chapter, a comparative study between the novel *type A* and the *type I* refractive index change is presented. We demonstrate that in the same glass substrate, which is a silver containing zinc phosphate glass, *type A* and *type I* refractive index changes can be induced by wisely adjusting the laser writing parameters. First, we start by investigating the *type I* modification in a silver containing and a non-containing silver glass. Then, in silver containing glass, we perform direct laser writing of single mode waveguides of both *type A* and *type I*. A morphology comparison between both waveguides then the refractive index mode profile, near field mode profile and losses are exploited. Finally, the advantages of the *type A* modifications are highlighted.

III.2. Type I modification in phosphate – zinc phosphate glasses

More specifically, phosphate glasses exhibit some challenges in the understanding of the laser-glass interaction and its control. This is due to the presence of several components in the glass composition that could affect the laser-glass interaction. As mentioned before in section II.3.8, network modifiers are added to the glass composition to stabilize the glass matrix and/or to dope the glass with high concentrations of rare earth metals. Two writing regimes exist, athermal and thermal (section I.3.4). While writing in the athermal regime i.e. generally low repetition rate and pulse energy in the microjoule (μJ) scale, it was reported that several laser passages switch the Δn from positive to negative in a phosphate Kigre QX glass [175]. In the thermal regime, positive and negative Δn were observed for the same photo-induced structures where in the latter case no waveguiding could occur [49]. Generally for the thermal regime, most of the Δn observed were negative ones making the writing of optical waveguides complicated [49]. Moreover, a self-organizing feature and ripple structures were observed by many research groups [49, 176] in phosphate glasses following DLW, which makes the writing of low loss waveguides nearly impossible. This indicates that the writing window of *type I* smooth waveguides in the thermal regime is really narrow in phosphate glasses. Moreover, it has been reported that the photo-induced Δn in phosphate and zinc phosphate glasses highly depends on the glass composition as well as the laser parameters [49, 62, 132, 173]. *Fletcher et al.* investigated the effect of the ratio O/P in zinc phosphate glasses and found that a ratio O/P=3.25 is the ideal one for having positive Δn and writing smooth waveguides [62, 132]. To sum up, creating smooth *type I* modifications exhibiting positive Δn in phosphate – zinc phosphate glasses is complicated due to the multicomponent nature of the glass and requires a fine optimisation of the laser parameters and/or the glass composition.

III.3. Experimental methods

III.3.1. Glasses

The glasses used in this work are PZnAg₂ with an O/P~3.37 and PZn with an O/P~3.58 (see Table II-1). In fact, PZn glass is the same glass as PZnAg₂ in which the silver is replaced by Gallium. Therefore it is a non-containing-silver zinc

phosphate glass. For more information about the glass synthesis process, please refer to section II.5.1.

III.3.2. Laser setup

For this work, two lasers were used: the T-pulse 200 with a high repetition rate (9.8 MHz) for the DLW of *type A* waveguides; and a second laser, a Ti:Sapphire amplified laser with low repetition rate (250 kHz, compared to T-pulse) for the DLW of *type I* waveguides. The different laser parameters are summarized in Table III-1.

III.3.2.a. T-pulse 200

Direct laser writing of *type A* waveguides was performed using the T-pulse 200 laser which is a 9.8MHz repetition laser emitting at a 1030 nm wavelength with pulse duration ~ 400 fs and energies in the range of 20 nJ to 120 nJ. For more detail, the setup was already presented in section II.5.3

III.3.2.b. Ti:Sapphire REGA-Coherent

Direct laser writing of *type I* waveguides was performed using a chirped pulse amplification system (Coherent RegA) operating at a low repetition rate of 250 kHz (compared to the 9.8 MHz laser) emitting at a wavelength of 800 nm with 100 fs pulse duration using a 50x-0.55NA Nikon microscope objective. Pulse energies from 0.5 to 2.5 μ J could be obtained using this setup. A quarter-wave plate was inserted in the beam path and adjusted to obtain circularly polarized light. The glass sample was mounted on a mechanical stage (Newport XML210 and GTS30V). In order to have a circular waveguide, a cylindrical lens telescope was used (ellipticity of $a/b=1/8$).

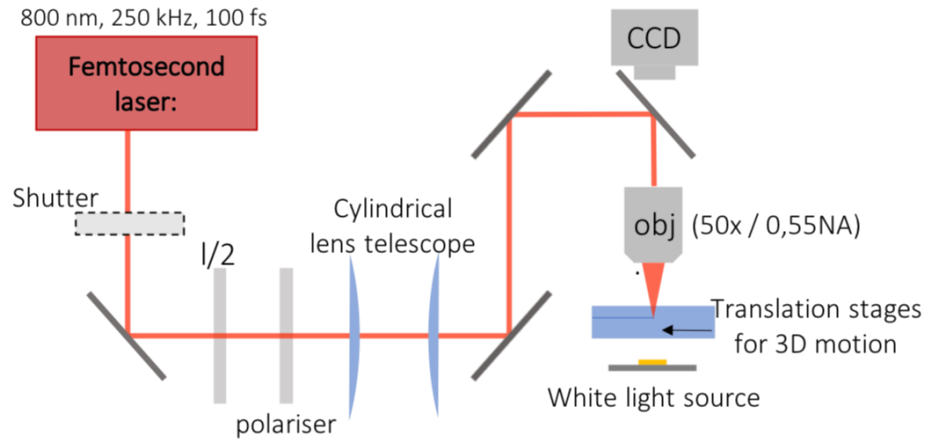


Figure III.1: Schematic presentation of the laser setup used for writing *type I* waveguides.

Table III-1: Table summarizing the different laser parameters for both lasers used in this chapter.

	T-pulse 200	REGA
Repetition rate	9.8 MHz	250 kHz
Wavelength	1030 nm	800 nm
Pulse duration	400 fs	100 fs
Pulse energy	0.2 nJ→120 nJ	0.5 μJ→2.5 μJ
Fluence	0.8 J/cm ² →4.75 J/cm ²	33 J/cm ² →140 J/cm ²

III.4. Results

III.4.1. Type I modification in silver containing and non-containing zinc phosphate glasses

Type I refractive index changes were created in both silver containing zinc phosphate glass (PZnAg₂) and non-containing-silver zinc phosphate glass (PZn), each glass exhibiting a different O/P ratio of 3.37 and 3.58 respectively. The laser used to perform the DLW is the Ti:Sapphire laser operating at 250 kHz while Δn was measured using the SID4Bio wave front sensor using a 50x-0.55NA objective (for more detail, see section II.5.6). For certain parameters, a negative Δn could be observed for the PZnAg₂ glass exhibiting an O/P ratio of 3.37 while a positive Δn is always observed for the PZn glass where the O/P ratio is 3.58 as shown in Figure

III.2. The following results are similar to the ones reported by *Fletcher et al.* indicating that changing the O/P ratio directly affects the sign of the photo-induced Δn in zinc phosphate glasses [62, 132]. In Figure III.2, the optical path difference (OPD) for both waveguides may not be the same magnitude, but this depends on the structures depth/thickness “e”. In all cases, we are not interested in the Δn values in this particular case ($\Delta n = OPD/e$) but rather in the profile and the sign of the Δn . One should note that in that case, the silver ions embedded in the glass matrix (in the case of PZnAg2) do not play any role in the photo-induced modification. It is a purely *type I* modification (this part will be further detailed in section III.4.2).

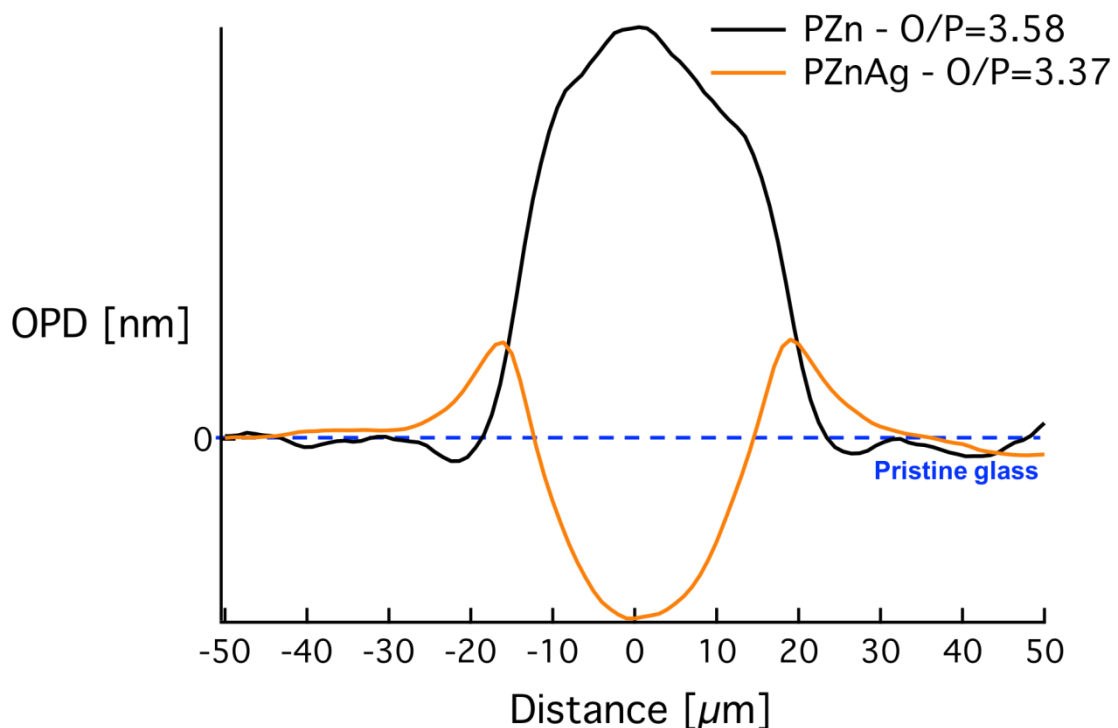
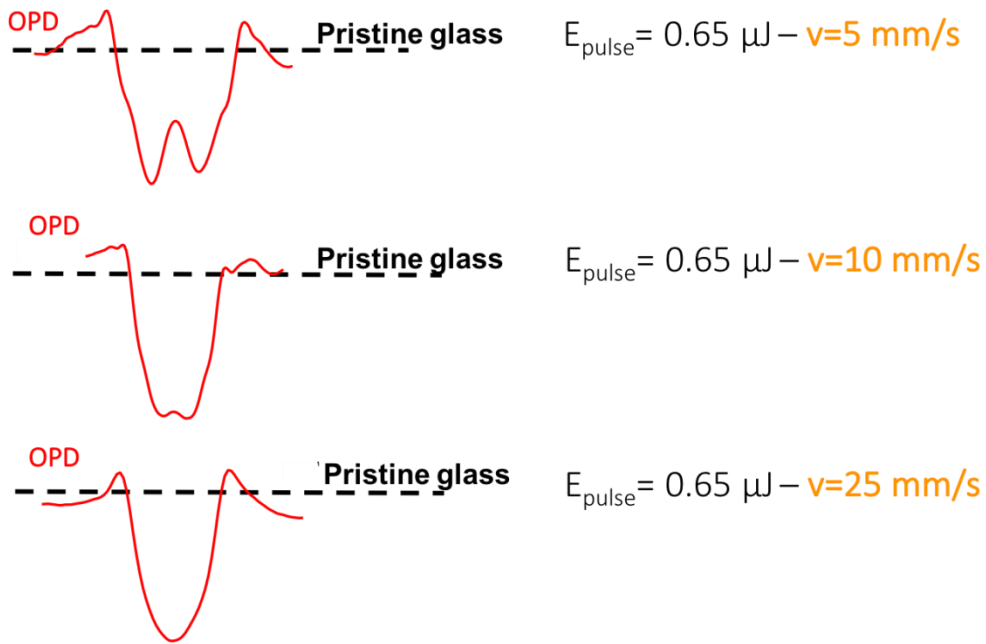


Figure III.2: Optical Path Difference (OPD) of the waveguide written in (orange) silver containing zinc phosphate glass (PZnAg2) and (black) non-containing silver zinc phosphate glass (PZn).

Many *type I* waveguides were written inside silver containing zinc phosphate bulk glass (PZnAg2) using different laser parameters and all the Δn were characterized using Sid4Bio. It was found that increasing the laser energy and/or decreasing the speed of writing in the PZnAg2 glass could trigger a positive refractive index change as shown in Figure III.3. It is a single positive peak that arises from the center of the negative Δn (Figure III.3). When changing the laser parameters of DLW i.e. the pulse energy and the writing speed, the sign of Δn flips, which was also observed

before by many research groups [49, 76, 89, 100, 172, 173]. Using a higher speed of writing, i.e. lower number of pulses, tends to switch the Δn from positive to negative and vice versa. The Δn flipping sign was also observed in borosilicate glasses [172], fluoride glasses [89] and phosphate glasses [175] as a function of the laser conditions used for DLW.

(a)



(b)

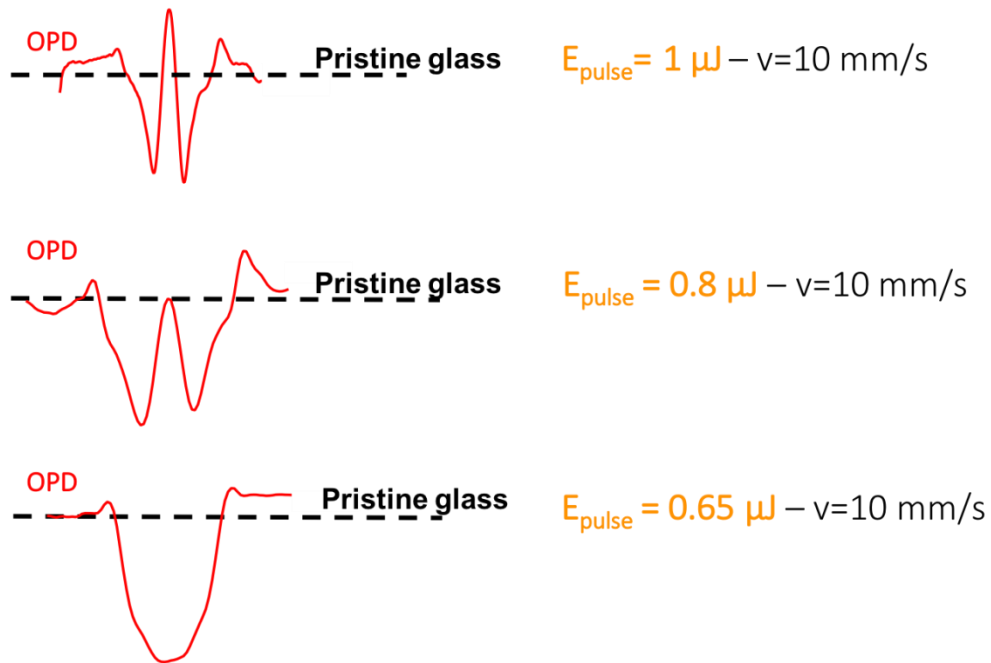


Figure III.3: Various optical path difference (OPD) profiles as a function of (a) writing speed (b) pulse energy. The Δn flips from negative to positive when increasing the pulse energy or decreasing the writing speed.

However, that was not the case for the non-containing silver zinc phosphate glass (PZn). For laser doses, i.e. pulse energy and writing speed, that are higher than the *type I* modification threshold, all the observed Δn were positive. However, the Δn profiles were not similar for all writing conditions. Figure III.4 shows the different Δn profiles measured for different laser conditions. The profiles shown are the only three possible profiles observed for different conditions. When writing with relatively high pulse energy and low writing speed, the Δn profile consists of three positive peaks where the side peaks are related to the heat affected zone and the middle peak dominates (Figure III.4.a). Writing using relatively medium pulse energy and/or writing speed results in a single positive peak of Δn (Figure III.4.b). When using low pulse energy even with low speed, very weak single positive Δn peak is observed (Figure III.4.c). After that, no more modifications were observed indicating that the laser conditions are lower than the *type I* modification threshold.

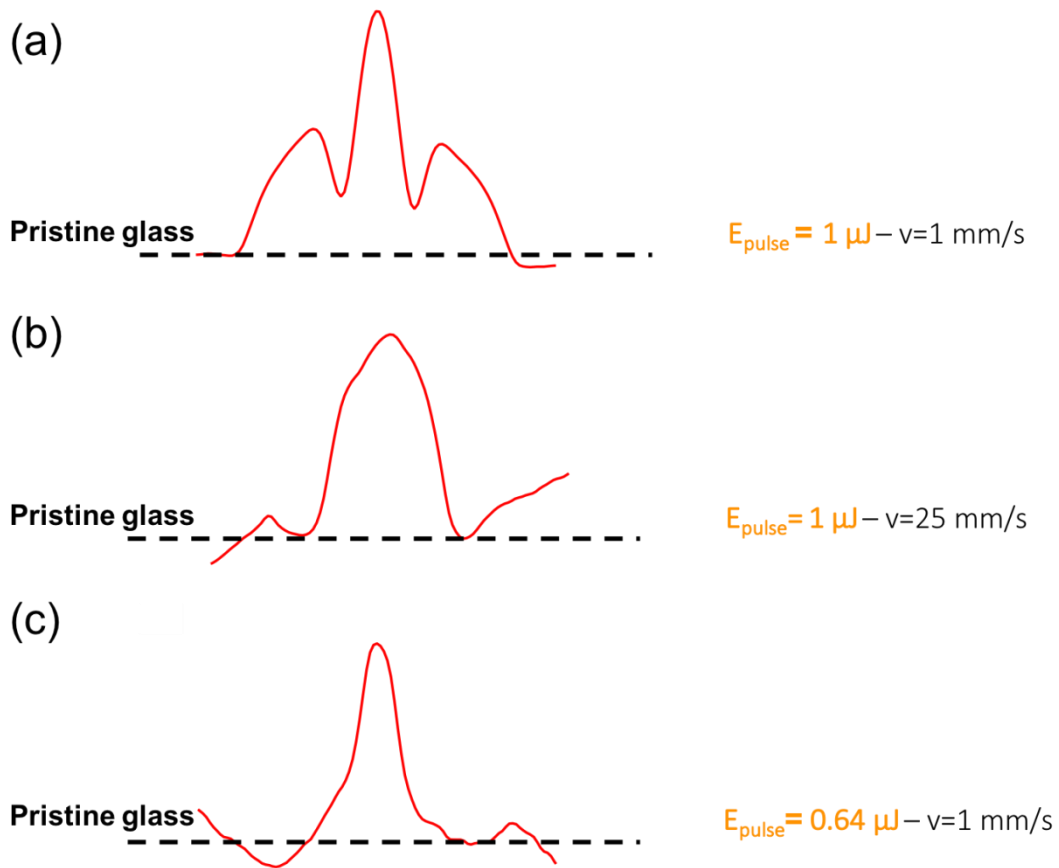


Figure III.4: Optical path difference (OPD) profiles of *type I* modification in non-containing silver zinc phosphate glass as a function of the laser parameters. The Δn is always positive.

To better understand the different Δn behaviours for the non-containing silver glass, a comparison between Δn profiles for both glasses using the same laser conditions ($E_p=1\mu J$ - $v=1\text{mm/s}$) is shown in Figure III.5. For the PZnAg2 glass, the Δn is a single positive peak that is surrounded by two negative Δn peaks that are below the pristine glass. However, for PZn glass, the Δn profile exhibits one dominating single positive Δn peak surrounded by two small positive Δn peaks that are above the pristine glass level. So over all, for PZn the Δn is always positive, which is not the case for PZnAg2. The two negative peaks in PZnAg2 glass are more or less in the same spatial position of the two small positive peaks for PZn. Comparing the behaviour of Δn for both glasses, we see they both exhibit one main single peak that decays as the applied laser dose decreases. But, for the PZnAg2, the positive peak was surrounded by two negative ones. So when the positive peak disappears, only the negative Δn remains. However for PZn glass, when the single

positive peak disappears no more modification is observed. It could be related to the Gallium effect given that more gallium is incorporated in the PZn glass matrix or simply the difference in the O/P ratio.

Moreover, same DLW conditions were applied in an Argoglass (AG01) exhibiting an O/P ratio of 2.95 different from the glasses PZnAg2 & PZn provided by ICMCB. No positive Δn was observed in Argoglass using the same conditions used for other glasses. The following results match with what was reported earlier, that Δn is highly dependent of the glass composition as well as the laser irradiations in zinc phosphate glasses.

As it turns out, zinc phosphate glasses are already multicomponent glasses before the incorporation of silver ions and the Δn highly depends on the glass composition as well as the laser parameters, which makes it complicated to confirm the response. This project does not aim at understanding and perfecting the creation of *type I* waveguides. Therefore our investigation stopped at this point.

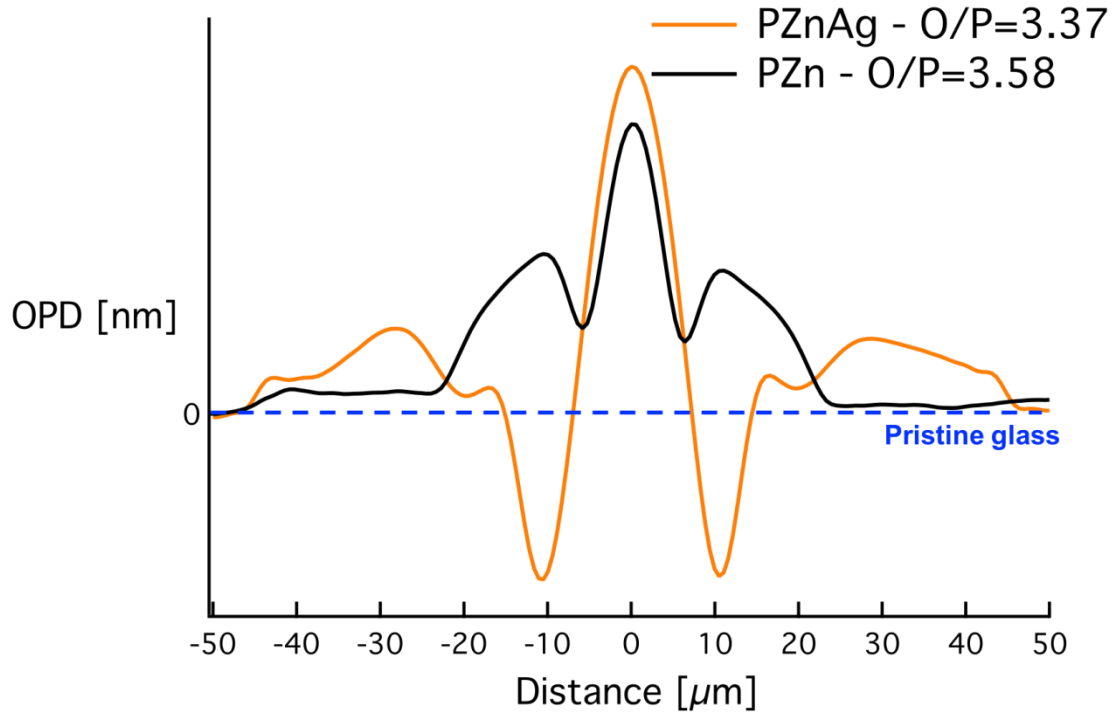


Figure III.5: Optical Path Difference (OPD) of the waveguide written in the same conditions ($E_p=1\mu\text{J}$ - $v=1\text{mm/s}$) in (orange) silver containing zinc phosphate glass (PZnAg₂) and (black) non-containing silver zinc phosphate glass (PZn).

A more interesting study occurred, where the *type I* and *type A* waveguides were written in the same silver containing zinc phosphate glass (PZnAg₂) by using two different lasers i.e. two different writing regimes. The comparison was based on the morphology structures, Δn and mode profiles for single mode waveguides operating at 660 nm wavelength.

III.4.2. Structure morphology

A series of *Type I* waveguides were written typically $\sim 160\ \mu\text{m}$ below the surface of a silver containing (PZnAg₂) glass (for details see section II.4) while changing the laser parameters. The pulse energy was changed from $\sim 0.65\ \mu\text{J}$ to $\sim 1\ \mu\text{J}$ while the writing speeds varied between 1 mm/s, 5 mm/s, 10 mm/s and 25 mm/s. Some waveguides were multimode and few were single mode but all exhibited more or less the same morphology. In the following work, only the single mode (SM) waveguide is fully characterized and compared to the *type A* single mode waveguide. Under white light illumination, the top view reveals a single smooth line modification that is typical of *type I* modification (Figure III.6.a.i). From the side view, a white colored roughly triangular shape waveguide was observed that is

surrounded by a dark circle as shown in Figure III.6.a.iii. The white color corresponds to a positive Δn while the dark one corresponds to a negative Δn acting as a cladding. The same shape of structures i.e. waveguide with a surrounding cladding was also observed by many research groups in the thermal regime in Eagle 2000 glasses [85, 177, 178]. More details are presented in section III.4.3. Under UV-blue excitation, a very weak fluorescence (compared to *type A* structures) was observed to be surrounding the waveguide as shown in Figure III.6.a.iv. The weak fluorescence indicates the formation of very few silver clusters following DLW. Given that the DLW is performed using a low repetition laser (compared to 9.8MHz) and high speeds, the conditions for the creation and aggregation of silver clusters were not met. The presence of few silver clusters on the edges indicates that the high temperature in the middle as well as the high laser intensity did not allow the formation of the silver clusters i.e. photo-dissociation. Therefore few were only formed on the edges. And so, we can assume that the overall modification is purely based on *type I* modification.

Figure III.6, shows a comparison between the morphology and fluorescence aspects between *type A* and *type I* waveguides. One can observe that the *type A* waveguide exhibits smaller structures compared to the *type I*. A noticeable heat affected zone is present in the case of *type I* waveguides when compared to the non-existing one in *type A* modification. This indicates that the writing regime in that case is a thermal one given that the modified zone is larger than the laser focal spot size. The *type I* waveguide exhibited structures of $\sim 24 \mu\text{m} \times 38 \mu\text{m}$ compared to $3 \mu\text{m} \times 6 \mu\text{m}$ for the *type A* waveguide. However, the *type I* waveguide exhibited a more circular waveguide (which is due to the cylindrical lens telescope used) compared to an elliptical *type A* waveguide.

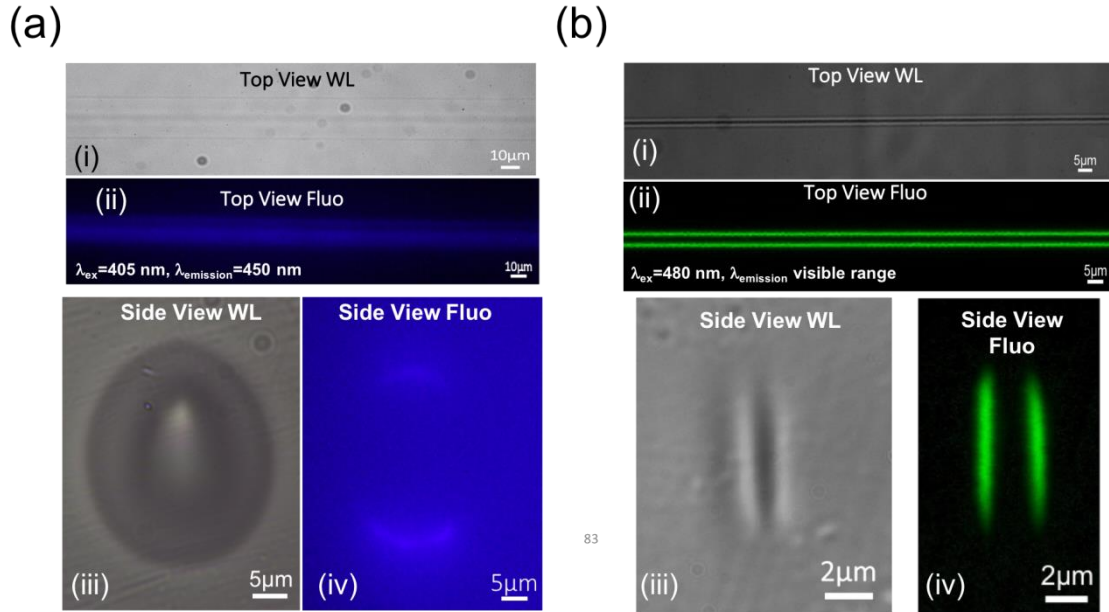


Figure III.6: Top view white light illumination (a.i) for *type I* waveguide, (b.i) for typical *type A* waveguide. Top view fluorescence (a.ii) for *type I* waveguide, (b.ii) for typical *type A* waveguide. Side view white light illumination (a.iii) for *type I* waveguide, (b.iii) for typical *type A* waveguide. Side view fluorescence image of (a.iv) for *type I* waveguide, (b.iv) for typical *type A* waveguide.

III.4.3. Refractive index and mode profiles

The refractive index change (Δn) was measured using SID4bio (see section II.5.6 for more details) for the SM *type I* waveguide, as shown in Figure III.7.a. A smooth single line was observed from the top view, which is typical of *type I* modification (Figure III.7a.i). The Δn profile extracted from the phase image showed a single positive Δn peak of $\sim 2 \times 10^{-3}$. This value was measured from the highest peak to the lowest level of the positive Δn peak located inside the Δn negative region, as shown in Figure III.7.a.ii. The surrounding negative Δn region acts as a waveguide cladding. Going back to the bright field side view photo of the waveguide that is shown in the inset of Figure III.7.b.ii. and based on the measured Δn profile, the dark region corresponds to a negative Δn while the white one corresponds to a positive one. Compared to the glass pristine refractive index, the positive peak exists below it. The DLW process induces a strong negative Δn on the borders of the interaction voxel but a positive peak in the center (Figure III.7b.ii). Moreover, Figure III.7 shows the top view phase image as well as the Δn profile for a *type A* waveguide to be compared with Figure III.7.b. For *type A* modification, one laser passage induces the creation of double lines exhibiting two positive Δn peaks compared to one single positive Δn peak for the *type I*.

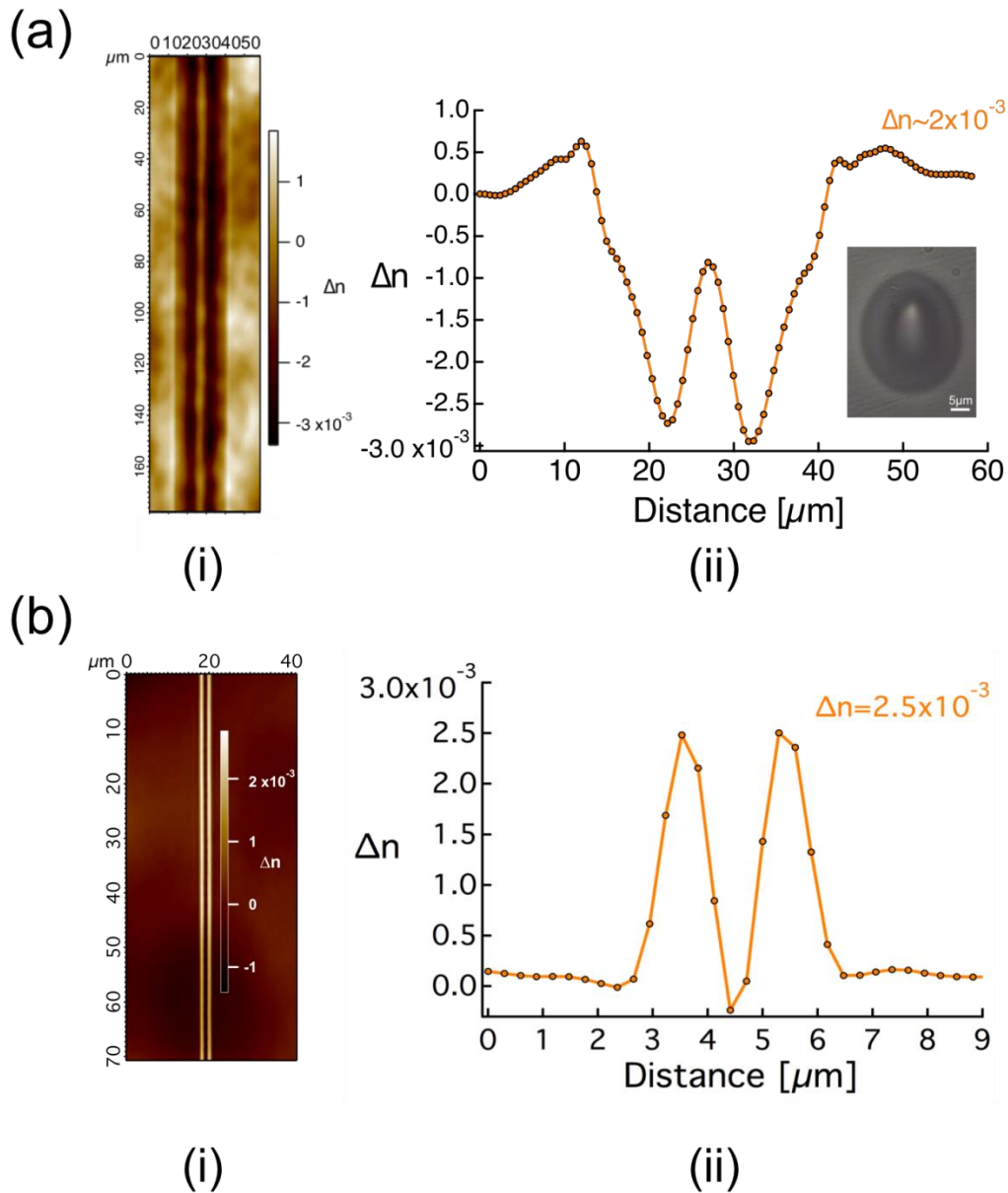


Figure III.7 Top view phase image of (a.i) *type I* waveguide, (b.i) *type A* waveguide. Refractive index profile of (a.ii) *type I* waveguide exhibiting one single positive Δn peak. Inset: side view of the *type I* waveguide under white light illumination. (b.ii) *Type A* waveguide exhibiting two positive Δn peaks. DLW conditions for *type I*: ($E_p=0.65\mu\text{J}$ - $v=5\text{mm/s}$ - $\tau_{rep}=250\text{ kHz}$ - $\text{NA}=0.55$ - $160\mu\text{m}$ below the surface), *type A* ($E_p=43\text{nJ}$ - $v=60\mu\text{m/s}$ - $\tau_{rep}=9.8\text{MHz}$ - $\text{NA}=0.75$ - $160\mu\text{m}$ below the surface).

Following Δn characterization, the sample was installed on the transmission setup and a 630 nm laser was injected inside the waveguides. As mentioned before, only one SM waveguide is fully characterized in this work. The near-field mode profile following laser injection is shown in Figure III.8.a. A circular mode was observed

that is the fundamental mode LP_{01} . Horizontal and vertical line profiles indicate that the mode is a Gaussian one $\sim 4.5\mu\text{m} \times 5.2\mu\text{m}$, almost a round mode. Even though the waveguide exhibited large dimensions of $\sim 24\mu\text{m} \times 38\mu\text{m}$, yet the guiding region is only around $\sim 5\mu\text{m} \times 5\mu\text{m}$. The guiding region is where the Δn is positive and is the white region in the side view bright field image (Figure III.6.b.iii). The large dimensions of the waveguide are due to the heat affected zone that is generated following DLW and does not support waveguiding.

Compared to the *type A* fundamental mode (Figure III.8.b), one can see the difference. The *type A* near-field mode is an elliptical supermode that tends to be an LP_{01} supported by two highly interacting waveguide modes. However the *type I* near-field mode is a circular LP_{01} mode. One should not forget that the in the case of writing *type I* waveguides, the beam was shaped using a cylindrical lens telescope in order to obtain circular waveguides, which was not the case for *type A* waveguides. In terms of dimensions, they are comparable. The *type A* guided mode is $\sim 3\mu\text{m} \times 5.5\mu\text{m}$ compared to $\sim 4.5\mu\text{m} \times 5.2\mu\text{m}$ for the *type I* waveguide. For the guiding losses, *type I* losses were estimated to be $\sim 4.5\text{ dB/cm}$ (same method used for estimating the propagation losses for *type A*, section II.6.3) which is quite high, especially compared to *type A* waveguides exhibiting upper losses of 1.2 dB/cm . The high losses in *type I* waveguides could be explained by the inhomogeneity of the glass sample as well as the defects during DLW. In addition to that, self-periodic ripples were sometimes observed for the waveguides, which is also one of the reasons for the high losses. Anyway, no further efforts were put into creating low loss *type I* waveguides given that this was not the aim of this project. Yet, waveguides exhibiting low losses, lower than 0.4 dB/cm were reported by many research groups in phosphate/zinc phosphate glasses [63, 134].

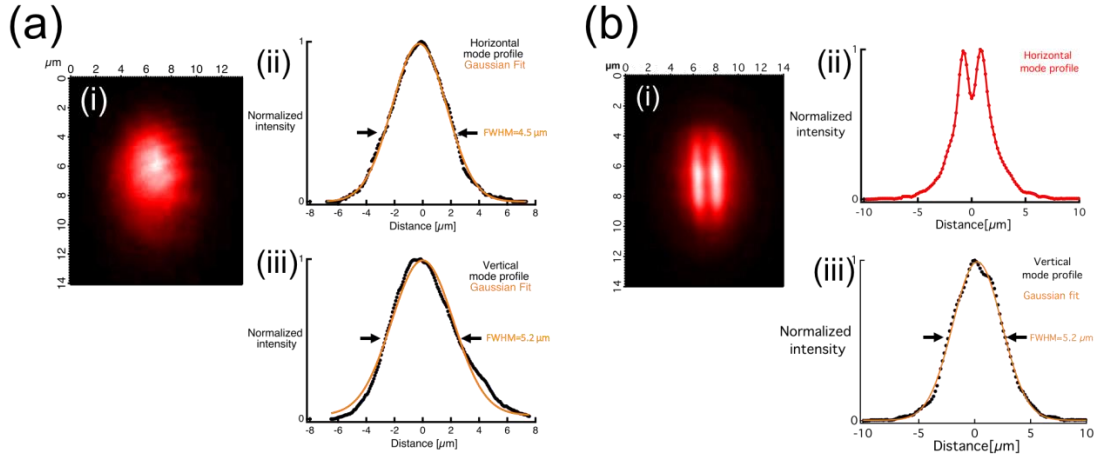


Figure III.8: Near-field mode profile following the injection of a 630nm laser for (a.i) *Type I* waveguide (b.i) *Type A* waveguide. Normalized horizontal intensity of (a.ii) *type I* waveguide (b.ii) *type A* waveguide. Normalized vertical intensity of (a.iii) *type I* waveguide (b.iii) *type A* waveguide. DLW conditions for *type I*: ($E_p=0.65\mu\text{J}$ - $v=5\text{mm/s}$ - $\tau_{rep}=250\text{ kHz}$ - $NA=0.55$ - $160\mu\text{m}$ below the surface), *Type A* ($E_p=43\text{nJ}$ - $v=60\mu\text{m/s}$ - $\tau_{rep}=9.8\text{MHz}$ - $NA=0.75$ - $160\mu\text{m}$ below the surface).

Finally, *type I* waveguides exhibited a heat affected zone referring to a thermal regime while the *type A* waveguides exhibited no heat affected zone referring to an athermal regime. Generally, thermal regimes are related to higher repetition rates compared to athermal regimes but not in this case. In fact, it depends not only on the repetition rate but also on the pulse energy. In the case of *type I*, the pulse energy is in the order of μJ compared to nJ in the *type A*. The *type A* modification is based on the photo-chemistry in the glass matrix whereas the *type I* modification is based on the melting and reconstruction of the glass matrix itself. The *type A* modification occurs in an extrinsic way to the glass matrix acting only on the silver ions and forming silver clusters compared to *type I* which is an intrinsic modification, heating the glass above the T_g , melting, reconstructing and changing the initial properties of the glass itself.

III.4.4. Flipping Δn

As reported in section III.4.1, the *type I* Δn flips as a function of the laser parameter (Figure III.3), which makes the DLW of waveguides more complicated in this case. However, *type A* modifications are always positive, exhibiting two positive peaks as long as the laser irradiance used is higher than the *type A* modification threshold. Figure III.9 shows that the *type A* OPD is constantly positive for all the laser parameters which is not the case for *type I* modification reducing the

complication of writing waveguides. In Figure III.9, all the OPD's presented may exhibit the same amplitude for different laser parameters but one should not forget that the Δn is calculated from the OPD using the following equation $\Delta n = \text{OPD}/e$. Moreover, as mentioned before, the thickness of the structures changes as a function of the laser parameters (see Figure II.42). Therefore the Δn is surely not the same for the different laser parameters. The purpose of Figure III.9 is to show that for all laser parameters, the photo-induced *type A* Δn is a positive one.

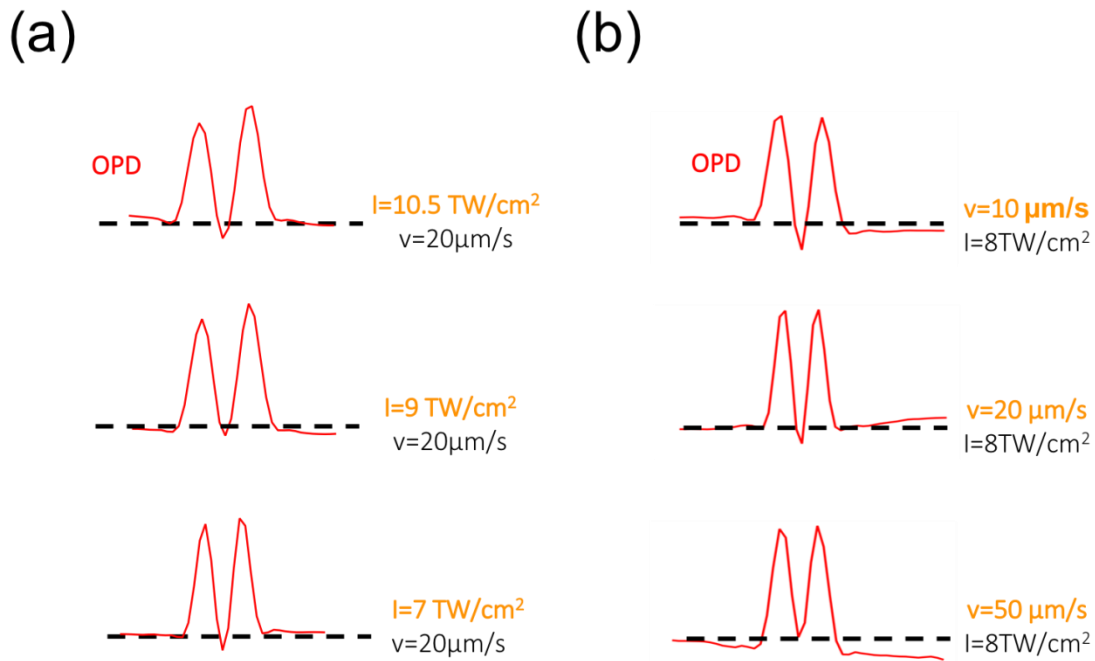


Figure III.9: Optical path difference (OPD) profiles as a function of (a) laser irradiance (b) writing speed. The *type A* Δn is always positive no matter what the laser conditions are. Pulse energies: 30 nJ \rightarrow 50 nJ.

Some *type I* waveguides exhibited negative Δn with different morphology compared to the *type I* waveguide with positive Δn . The bright field images under white light illumination reveals a single circular waveguide shape Figure III.10.a and the fluorescence surrounded the whole waveguide as shown in Figure III.10.b, which was not the case in positive Δn waveguides (Figure III.6). The circular shape is dark under WL illumination referring to a negative Δn . Furthermore, the intensity fluorescence was more intense compared to positive Δn waveguides, which refers to the creation of more silver clusters in this case. Writing in higher speed or lower pulse energies result in depositing lower laser doses in the glass. The latter conditions were more conducive to the creation of silver clusters in the periphery of the waveguide. The waveguides exhibiting negative Δn did not support waveguiding

of course, however, on the periphery, where the silver clusters are present, a weak guiding was observed as shown in Figure III.10.c. As mentioned in Chapter II the photo-induced silver clusters are responsible for a positive Δn in silver containing glasses. Therefore, the presence of these clusters around the waveguide even in small quantities (compared to the ideal conditions as shown in Chapter II) exhibited weak guiding properties. To have a better idea, the top view phase image using SID4Bio wave front were achieved on the waveguides exhibiting negative Δn . A smooth single negative peak was observed with two small positive Δn bumps on the periphery of the waveguide as shown in Figure III.10.d. The two small positive Δn bumps on the periphery are directly correlated to the presence of silver clusters around the waveguide as shown in Figure III.10.b. Therefore, once again, the silver clusters even in small quantities are responsible for a positive Δn in silver containing glasses. In the following conditions, negative *type I* modification was created in the glass as well as a weak positive *type A* on the periphery on the interaction voxel. However, the writing conditions were conducive to the creation of *type I* instead of *type A* given that we are working in the low repetition rate regime. One should mention that the smaller amount of silver clusters formed in the case of positive Δn waveguides were not enough to support guiding.

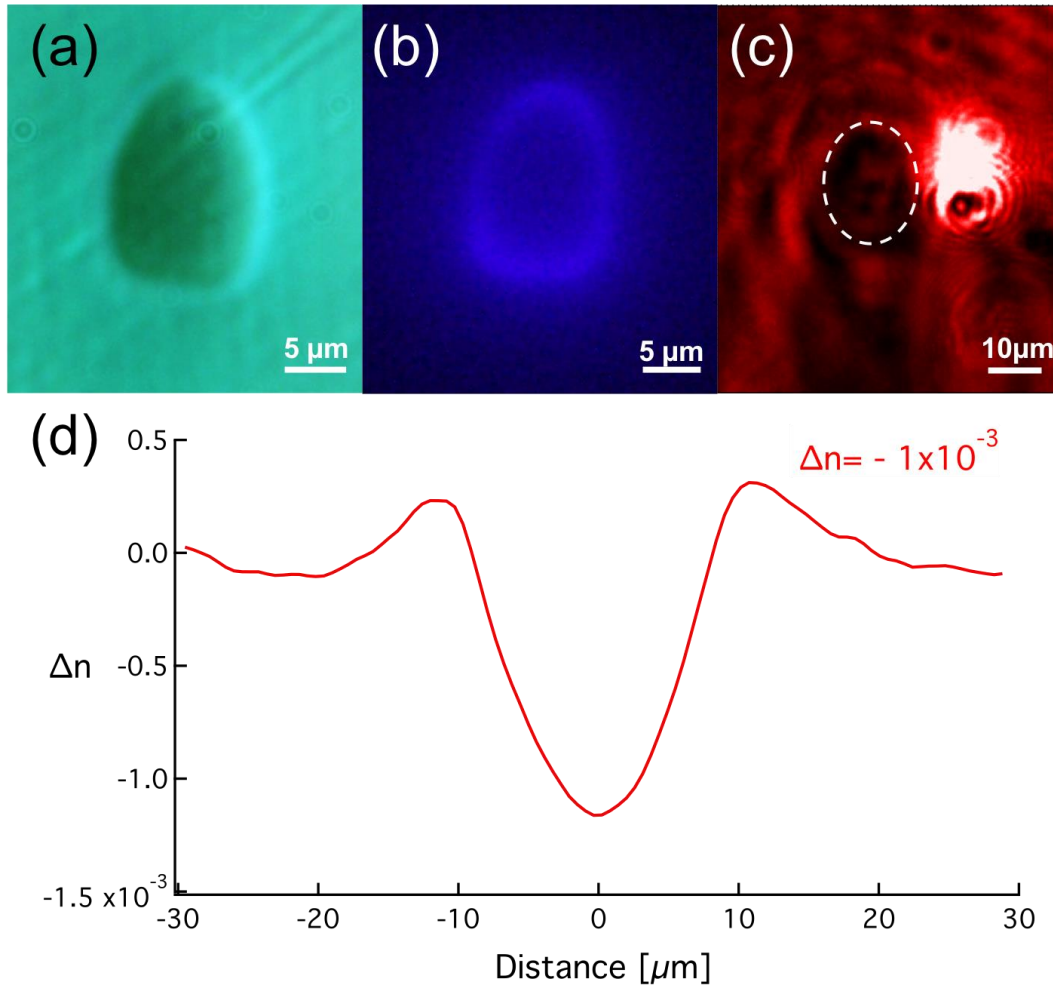


Figure III.10: Side view of a *type I* waveguide exhibiting negative Δn (a) under white light illumination; (b) fluorescence image under blue excitation and emission in the visible range; (c) guided mode profile following laser injection at 630 nm. The dashed lines indicates the location of the waveguide. A small portion of light is guided on the side of the waveguide. (d) Refractive index change profile of the waveguide exhibiting a negative one. DLW parameters: $0.65\mu\text{J}$ - 25mm/s .

Overall, the two lasers used in this work provided two totally different regimes each one responsible for the creation of a type of modification. Summarizing both laser parameters, one can see and understand the difference in the presence of two different regimes/modifications. Figure III.11 shows the ranges of the laser fluence, laser irradiance and the energy density deposited by voxel for both lasers. The T-pulse laser parameters used allowing the creation of *type A* modification presented very low laser fluence, laser irradiance as well as energy deposited by voxel compared to the Ti:Sapphire laser which presented much higher values, more than 3 orders of magnitude larger for instance in the case of the energy density deposited by voxel. The details of calculations of the values of the laser fluence, laser

irradiance as well as the energy density deposited by voxel are presented in the Appendix part A.4. As mentioned before, even though the T-pulse laser exhibits a high repetition rate of 9.8 MHz the writing regime is an athermal one in this case compared to a thermal regime for the Ti:Sapphire laser exhibiting a low repetition rate of 250 kHz. Generally, thermal regimes are linked to high repetition rate lasers compared to the athermal regimes where low repetition rate lasers are used, which is not the case in this experiment. Given that pulse energies used in the case of the T-pulse are in the few nanoJoule (nJ) range compared to microJoule (μJ) pulses for the Ti:Sapphire and comparing the density of energy deposited by voxel between both lasers, one can easily understand why. Furthermore, calculating ΔT , which is the highest temperature difference that occurs in one point induced by one laser pulse for both cases, confirms our claim. For the parameters used with the T-pulse 200, a maximum $\Delta T=10\text{K}$ was calculated compared to a very high value of ΔT in the case of the parameters used with the Ti:Sapphire laser. The calculation used for the T-pulse are not completely compatible for calculating high energies provided by the Ti:Sapphire laser. Therefore we limited our calculation to the maximum pulse energy used, which is $1 \mu\text{J}$ (see Appendix part A.4). Obviously, no heat affected zone was noticed for *type A* modification, which is well expected with a low ΔT while for *type I*, the glass heats and melts resulting in the creation of a heat affected zone i.e. the modification zone is larger than the laser spot.

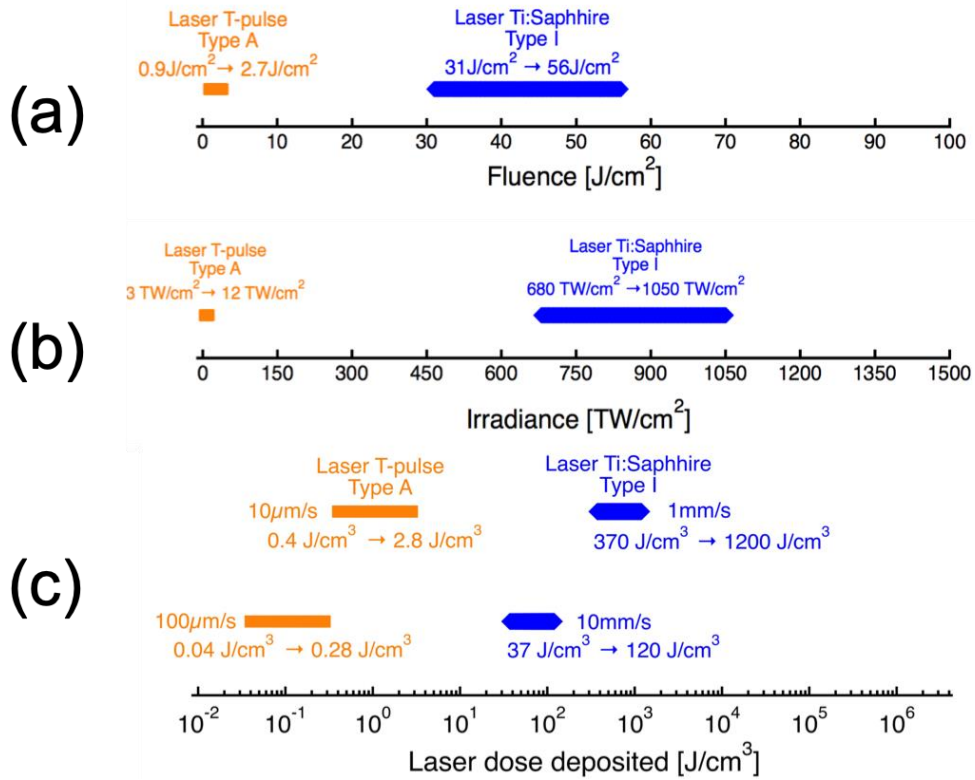


Figure III.11: Laser parameters for both lasers: (orange) T-pulse 200 which induces *type A* modification (blue) Ti:Sapphire which induces *type I* modification (a) laser fluence, (b) laser irradiance, (c) calculated laser dose deposited as a function of the writing speed.

In closing this discussion, one can say that wisely choosing the laser parameters and the laser regime, either *type A* or *type I* modification could be triggered in silver containing glasses. The *type A* modification is an extrinsic modification where the laser energy acts on the photo-chemistry inside the glass matrix by photo-exciting the pre-existing silver ions Ag^+ and developing the silver clusters Ag_m^{x+} responsible for the positive Δn in this case. *Type I* modification is an intrinsic modification acting on the glass matrix itself, where the laser energy heats (above T_g) and melts the glass and reconstructs it as a new glass exhibiting a Δn that could be positive or negative depending on the glass composition as well as the laser parameters. *Type A* modification clearly occurs in the low pulse energy regime compared to the *type I* modification. Therefore we can introduce to the community a new type of modification/refractive index called *type A* that exists well below the *type I* modification in the pulse energy regime and can be added to the Δn classifications as shown in Figure III.12.

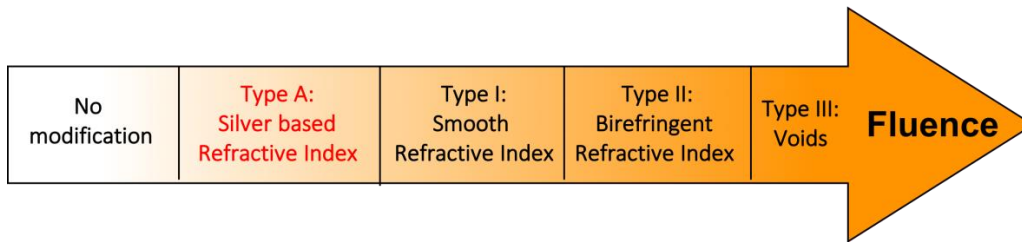


Figure III.12: Different types of modification classifications as a function of a progressive scale of the laser fluence. The introduction of the new *type A* modification sits below the standard well known *type I* modification.

III.4.5. Advantages of type A

Using different DLW conditions in silver containing glasses induces the creation of *type A* or *type I* modification. *Type A* modification is induced using a high repetition rate laser with pulse energies in the nJ range compared to a low repetition rate laser for *type I* modifications with pulse energies in the μJ . Low writing speeds (max 100 $\mu\text{m/s}$) are needed for the creation of *type A*, while *type I* modifications exhibiting positive Δn are achieved using high writing speeds (max 10 mm/s). *Type A* modification always exhibits a positive Δn (two positive peaks). However *type I* modification could be a positive Δn or a negative one (one single peak) based on the laser conditions which highlight the advantages of *type A* modification. The dimensions of the *type A* waveguides $3 \times 6 \mu\text{m}^2$ are smaller compared to the *type I* waveguides $\sim 24 \times 38 \mu\text{m}^2$, but the guided mode profile dimensions are comparable and almost the same. Yet, *type A* waveguides are elliptical waveguides with elliptical mode profiles compared to *type I* waveguides which exhibit a round mode profile. Of course, this is due to the beam shaping introduced in this case. Otherwise, *type I* modifications would also exhibit be elliptical if the beam was not shaped. Another advantage for the *type A* modification is the possibility to write near-waveguide surfaces with no need for additional processing. This is going to be presented in detail in Chapter IV. Finally, Table III-2 summarizes the comparison between *type I* & *type A* modifications in silver containing glasses.

Table III-2: Table summarizing the comparison between *type I* and *type A* modification

<i>Type I</i>	<i>Type A</i>
Low repetition rate 250 kHz, μJ pulses	High repetition rate 9.8 MHz, nJ pulses
High writing speed(mm/s)	Low writing speed ($\mu\text{m/s}$)
Round waveguide due to beam shaping	Elliptical waveguide shape
Large heat affected zone (Thermal regime)	No heat affected zone (Athermal regime)
One positive Δn peak	Two positive Δn peaks
Circular mode profile	Elliptical mode profile
Flipping Δn as a function of DLW parameters	Δn always positive
Additional processing for near surface waveguides	Near surface waveguides with no additional processing

III.5. Conclusion

Direct laser writing of *type I* modification/refractive index change was performed in both silver-containing and non-silver-containing zinc phosphate glass exhibiting different O/P ratio. Negative Δn could be observed for the silver-containing glass compared to an always positive Δn in non-silver-containing glass which is probably related to the difference in the O/P ratio which was also reported by other research groups.

On the other hand, in silver containing glasses, wisely choosing the laser parameters and regime, either *type A* or *type I* modifications could be triggered. The *type I* modification occurs in the thermal regime with high laser fluence using a low repetition laser (250 kHz) compared to an athermal regime for *type A* modification using with a low laser fluence using a high repetition rate laser (9.8 MHz). A morphology comparison between two single mode waveguides of each type shows a large heat affected zone for *type I* modification compared to a non-existing one for *type A*. The overall waveguide dimensions are $\sim 24 \mu\text{m} \times 38 \mu\text{m}$ and $3 \mu\text{m} \times 6 \mu\text{m}$ respectively for *type I* and *type A* waveguides. However, the guided mode profile dimensions are comparable given that the guiding region in the case of *type I* is around $\sim 5 \mu\text{m}^2$ exhibiting a circular mode profile compared to an elliptical one for *type A* ($3 \mu\text{m} \times 5.5 \mu\text{m}$). Moreover, *type I* modification flips from positive to negative as a function of the laser parameters whereas the *type A* modification is always a positive one. Finally, we reported a new type of modification/refractive index change called *type A* (from the Latin name of silver, Argentum), based on the creation of the silver clusters that occur in the low pulse energy regime sitting well below the *type I* modification regime. This new type exhibits many advantages compared to *type I*: always positive Δn for different laser parameters, smaller dimensions and occurring in the low pulse energy regime that could be used for writing near surface waveguides, paving the way for sensing applications, as will be presented in Chapter IV.

Table of contents:

IV. Direct laser writing of rising near-surface waveguides in silver containing glasses with no additional processing	150
IV.I Introduction	150
IV.2 Evanescent wave theory.....	152
IV.3 Evanescent wave based sensors.....	154
IV.3.1 Refractive index sensors.....	155
IV.3.1.a RI sensors using DLW	159
IV.4 Experimental methods.....	166
IV.4.1 Glass.....	166
IV.4.2 Laser setup	166
IV.5 Results	167
IV.5.1 Writing near surface waveguides	167
IV.5.2 RI sensor	176
IV.6 Conclusion.....	182

Chapter IV

Direct laser writing of rising near-surface waveguides in silver containing glasses with no additional processing

IV.1. Introduction

In the past years, the use of fiber optics for sensing applications (gases, liquids) has attracted strong interest. Optical sensing provides in-situ, fast, selective, remote, real time and non-destructive sensing. It is generally based on the interaction of light with the outer medium. When light propagates in an optical fiber, a portion propagates in the cladding. It is called evanescent wave. Fiber sensors are based on the evanescent wave interaction with the outer medium. Many evanescent wave based fiber sensors were created in the past years for gas [179], chemical detection [180, 181] and refractive index sensing [182-184]. However, to manufacture those sensors, the fiber should be tapered or a part of the cladding should be removed to reveal the sensing medium. Generally gas and chemical sensors are rather based on the absorption of the evanescent wave by the outer medium (complex part of the refractive index). However this phenomenon plays a minor role in refractive index sensors. These rather rely on the mode confinement (positive part of the refractive index) between the inner and outer medium (glass-liquid).

The Direct Laser Writing (DLW) technique is a well-established technique allowing to directly address 3D structures inside materials. More specifically, waveguides [62, 71, 86, 89, 123, 162, 185] and optical components [124] were written embedded inside glasses using DLW. Yet just a few works were reported on written waveguides near the glass surface [91, 169]. This is due to the ablation that occurs when writing near the surface given that the modification threshold decreases when approaching the glass surface [186]. The need to write near-surface optical components is to make the light interact with the outer medium in order to create

miniaturized sensors in glasses. However, few works report the creation of sensors based on the DLW technique [187, 188].

In the first part of this chapter, DLW of rising near-surface waveguides in silver containing glasses are reported with no need for additional processing. For the second part, the waveguides written are used to create a refractive index sensor in a ~ 1 cm glass chip with no need for etching or any additional process.

IV.2. Evanescent wave theory

Light propagates inside an optical fiber/waveguide as a form of mode. As mentioned before the waveguide could exhibit single mode or multimode aspects. The propagating mode is normally confined inside the core. However, a small portion of light propagates in the cladding and decays exponentially; it is called the evanescent wave as shown in Figure IV.2. The field distribution of the evanescent wave is given by:

$$E = E_0 e^{-z d_p} \quad (\text{IV-1})$$

Where E_0 is the field distribution at the waveguide interface, z is the length and d_p the depth penetration of the evanescent wave given by:

$$d_p = \frac{\lambda}{2\pi n_{core} \left[\sin^2 \theta - \left(n_{core} / n_{cladding} \right)^2 \right]^{1/2}} \quad (\text{IV-2})$$

Where λ is the wavelength, θ is the angle between the incident beam and the interface (propagation beam), n_{core} the refractive index of the core and $n_{cladding}$ the refractive index of the cladding.

The less the mode is confined inside the core (lower Δn), the more significant the evanescent wave is. The confinement factor is given by:

$$\Gamma = \frac{P_{core}}{P_{total}} = 1 - \frac{u^2}{V^2} (1 - \psi_l(w)) \quad (\text{IV-3})$$

With

$$\psi_l(w) = \frac{K_l^2(w)}{K_{l+1}(w)K_{l-1}(w)} \quad (\text{IV-4})$$

Where P_{core} is the power inside the core, P_{total} the total power injected in the fiber, u and w the normalized transverse parameters in the core and in the cladding respectively, V fiber parameter given by (II-7) and $K_l(w)$ is the second order of Bessel function where l is the azimuthal parameter of the LP_{lm} propagating modes.

The confinement factor for the fundamental mode LP_{01} propagating in an optical fiber has been simulated as a function of V , the fiber parameter as depicted in Figure IV.1: the higher the V parameter the higher the confinement of the mode. Thus, V is proportional to the fiber radius a and to the numerical aperture NA of the waveguide, $V = 2\pi\frac{a}{\lambda}NA$ (II-5). So, in order to further extend the evanescent wave i.e. minimize the confinement of the propagating mode to increase the interaction with the outer medium, one can either reduce the fiber radius and/or the Δn between the core and the cladding (to reduce V). Given that the Δn in fiber optics are generally fixed values, researchers tend more to reduce the fiber dimensions by tapering it to enhance the sensitivity, as will be presented in section IV.3.

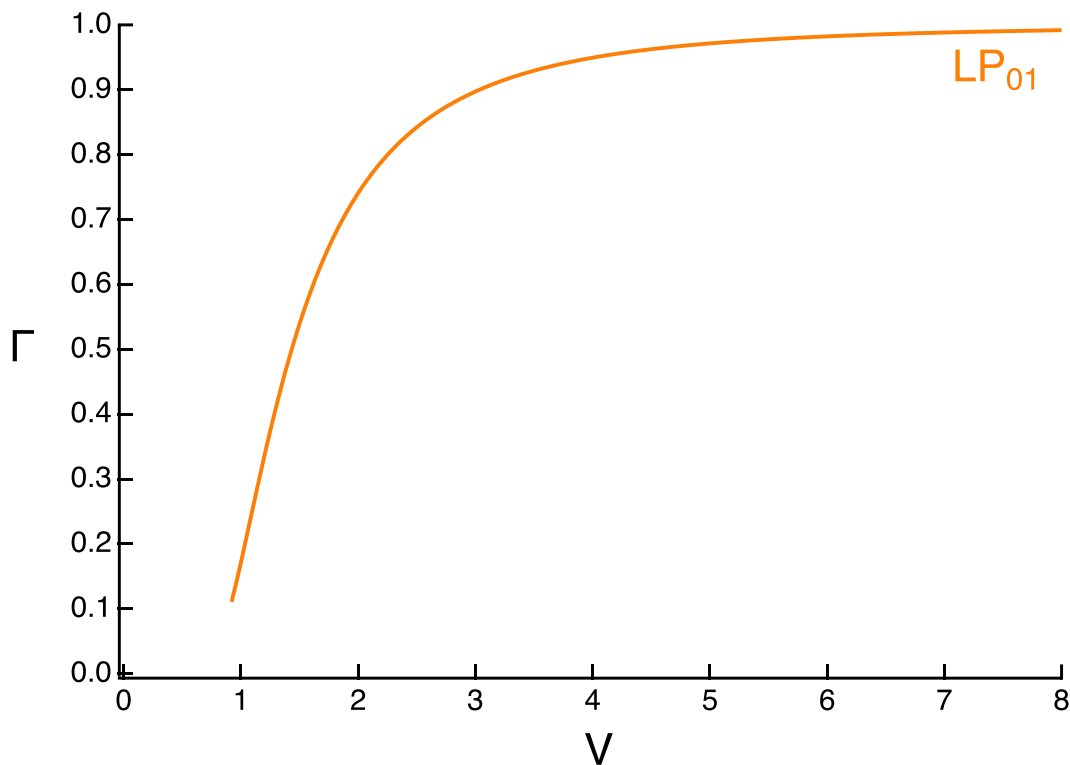


Figure IV.1: Simulations of the confinement factor Γ as a function of the V parameter of the fiber for an LP_{01} mode. The confinement of the mode increases as the V parameter increases.

IV.3. Evanescent wave based sensors

An evanescent wave is used to develop fiber based optical sensors. It is based on the interaction of the evanescent wave with the outer medium called sensing medium (gas, liquid), as shown in Figure IV.2. Optical sensing exhibits many advantages allowing fast, remote, selective and non-destructive sensing. Many sensors were developed in recent years based on this technique [179-181, 189-191]. Generally, evanescent wave based sensors are based on optical fibers where the cladding is removed or etched in order to make the evanescent wave interact with the sensing medium or by tapering the fiber. Fiber tapering consists in gently heating and stretching the optical fiber to reduce its size. In a tapered fiber, the optical field extends beyond the fiber with the evanescent wave carrying a significant part of the guided light [192] enhancing the interaction with the sensing medium.

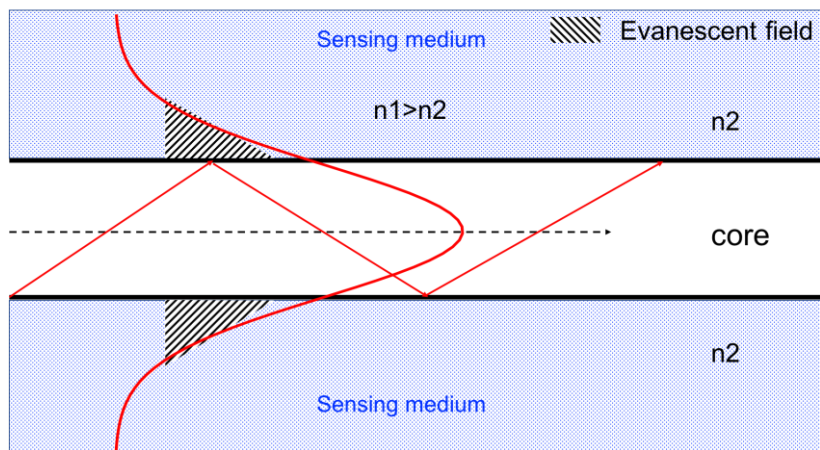


Figure IV.2: Schematic presentation of an evanescent wave based sensor.

In 1987, an optical fiber evanescent wave methane sensor was manufactured by heating and expanding (fiber tapering) a step-index multimode silica fiber [179]. A 1.8 μm fiberoptic sensor with a 10 mm diameter sensing length was reported to detect methane concentrations below the explosive limits [179]. Moreover, *Suresh Kumar et al.* reported an evanescent wave sensor capable of detecting trace nitrides in water using a multimode plastic clad silica fiber where a 12 cm length of the cladding had been chemically removed [181].

IV.3.1. Refractive index sensors

More specifically, refractive index (RI) sensors were manufactured by many research groups in fiberoptics [182-184, 191, 193, 194]. Given that Bragg gratings are so sensitive to the variation of the refractive index change, many RI sensors were based on the creation of Bragg gratings. *Chong et al.* developed a long period grating (LPG) in a B-Ge co-doped fiber where the resonant wavelengths shift as the refractive index changes [193]. *Chryssis et al.* developed an RI sensor based on Fiber Bragg Gratings (FBG) [191] where the cladding of a commercial fiber grating was etched to enhance the sensitivity of the sensors. The change in the refractive index in the sensing medium is detected by the shift of the Bragg wavelength.

However, RI sensors were also developed without relying on Bragg Gratings. Indeed, in 2005, *Polynkin et al.* reported a RI sensor based on a tapered SMF 28. The tapered fiber was placed in a polymer and a wide channel, 1 cm long by 3 mm wide (sensing medium), was manufactured as shown in Figure IV.3 [182].

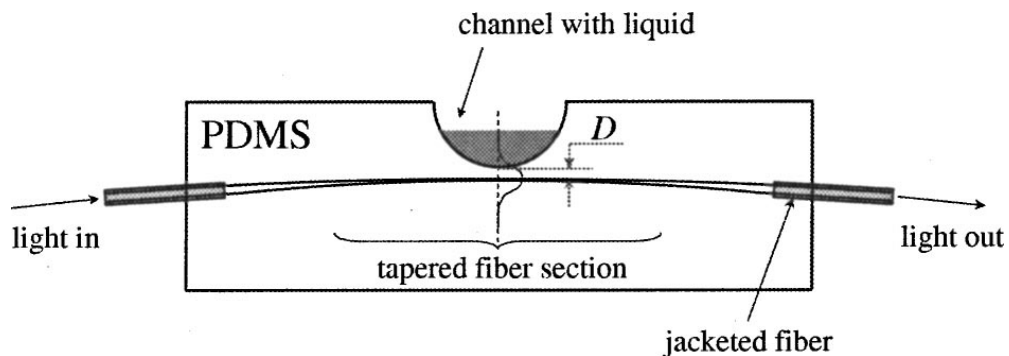


Figure IV.3: Schematic presentation of the sensor. Taken from [182].

Two tapered fibers were tested, one exhibiting a taper thickness at the waist of $\sim 1.6 \mu\text{m}$ and another of $\sim 700 \text{ nm}$. Several RI liquids were applied inside the channel to test the response of such sensors. The results are shown in Figure IV.4. It was found that for both fibres, the transmission is maximum when the liquid matches the RI of the surrounding polymer while the thinner taper exhibited a higher sensitivity to RI modifications.

They described the sensing mechanism as the following: the shape of the guided mode is affected by the surrounding medium i.e. the RI liquid used. If the RI of the liquid is higher than the cladding's RI (polymer in this case), the mode is ejected outside the polymer where it will be scattered by the channel and absorbed by the liquid. However, if the RI is lower, the mode propagates with no significant changes [182].

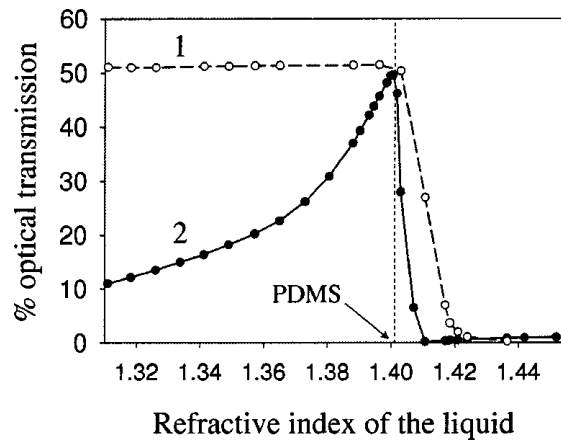


Figure IV.4: Variation of the optical transmission for different refractive index liquids for taper thickness of (1) $\sim 1.6 \mu\text{m}$ (2) $\sim 700 \text{ nm}$. Taken from [182].

Another similar work was reported in 2010 by *Bilro et al* [183] in a multimode plastic optical fiber. A part of the cladding was removed in order to create and reveal the sensing medium. It was an oval shape with a length of 19.35 mm and a diameter of 0.65 mm, as shown in Figure IV.5.

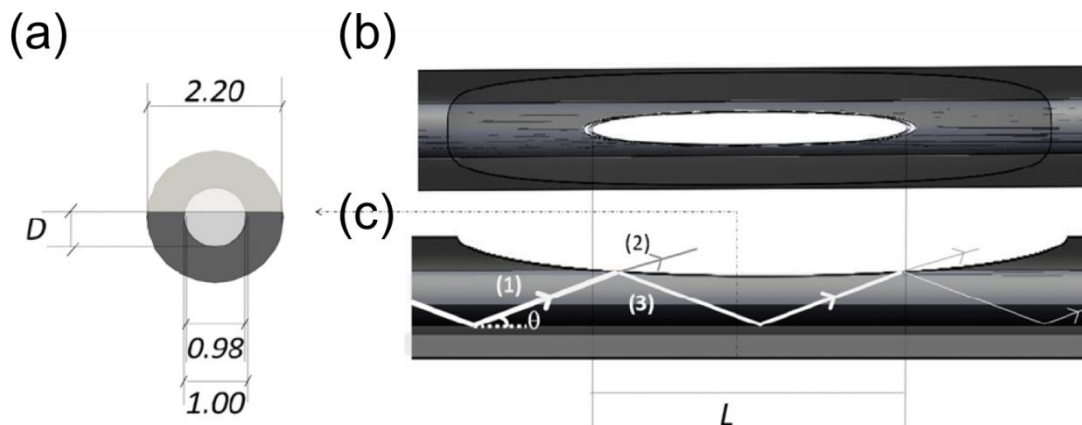


Figure IV.5: (a) Transverse cut of the plastic fiber. (b) Top view of the polished section. (c) Side view of the polished section. Due to the mismatch between the refractive index liquids and the fiber core, part of the beam is lost (2) by refraction in the sensing zone (3) guided by internal reflection. Taken from [183].

A theoretical model was suggested to be fitted with experimental results. The model is based on Fresnel's equation [98] of light bouncing inside a multimode optical fiber.

In the case of a dielectric medium, the equations could be reformulated in terms of the incident/propagation angle θ , the refractive index of the core n_{core} and the refractive index of the surrounding medium n_{ext} .

The amplitude reflection coefficients of perpendicular r_{\perp} and parallel r_{\parallel} polarization to the plane of incidence are given by:

$$r_{\perp} = \frac{\sin\theta - \sqrt{\left(\frac{n_{ext}}{n_{core}}\right)^2 - \cos^2\theta}}{\sin\theta + \sqrt{\left(\frac{n_{ext}}{n_{core}}\right)^2 - \cos^2\theta}} \quad (IV-5)$$

$$r_{\parallel} = \frac{\left(\frac{n_{ext}}{n_{core}}\right)^2 \sin\theta - \sqrt{\left(\frac{n_{ext}}{n_{core}}\right)^2 - \cos^2\theta}}{\left(\frac{n_{ext}}{n_{core}}\right)^2 \sin\theta + \sqrt{\left(\frac{n_{ext}}{n_{core}}\right)^2 - \cos^2\theta}} \quad (IV-6)$$

The intensity reflection coefficient of the unpolarised light can be calculated by:

$$R = \frac{|r_{\perp}|^2 + |r_{\parallel}|^2}{2} \quad (IV-7)$$

As mentioned in section II.3.1.a, the waveguiding process occurs if the incident beam is lower or equal to the critical angle θ_c . The injected light was approximated to a Lambertian source of light [195]; the input power of each ray is dependent of the angle θ of propagation inside the fiber and assumed proportional to $\cos\theta$. Another consideration is that the beam guided in the fiber undergoes multiple internal reflections (the case of a multimode fiber), which is related to the propagation angle θ , the dimension of the sensing medium i.e. the length L and the section D . Therefore, the number of reflections is given by:

$$N = \frac{L \tan\theta}{2D} \quad (IV-8)$$

After immersing the fiber in the liquids, the power remaining in the fiber after the sensing medium is:

$$P_{out} \propto \int_0^{\theta_c} R_{n_{ext}}^{N(\theta)} \cos\theta \sin\theta d\theta \quad (IV-9)$$

The power ratio between the immersed fiber and the non-immersed one is:

$$\eta_{RI} = \frac{P_{out}}{P_{air}} = \frac{\int_0^{\theta_c} R_{n_{ext}}^{N(\theta)} \cos\theta \sin\theta d\theta}{\int_0^{\theta_c} R_{n_{air}}^{N(\theta)} \cos\theta \sin\theta d\theta} \quad (IV-10)$$

Where $R_{n_{ext}}$ and $R_{n_{air}}$ are the intensity reflection coefficients for the interface fiber/surrounding medium and fiber/air respectively. So, the power output of the sensor is linked to the mismatch of RI between the liquids and the guided mode.

Several RI liquids were applied to the sensing medium with RIs ranging from 1.332 to 1.471. The experimental and simulated normalized transmissions as a function of the different RI liquids used are shown in Figure IV.6. A considerable match is observed between simulations and experimental data. The sharp decrease occurs when the liquid matches the RI of the cladding $n_{ext} = n_{cladding}$ (Figure IV.6). In this case, the new critical angle α_c is lower than θ_c ; all the rays with an incident angle $\theta < \alpha_c$ exhibit total reflection; however all the rays with an incident angle $\alpha_c < \theta < \theta_c$ will only be partially reflected and a part of the power will be ejected outside the fiber. A slight increase in the transmission was observed for RI values below $n_{cladding}$ which was not observed in simulations (Figure IV.6). This was explained by the scattering of light on the interface due to polishing irregularities [183].

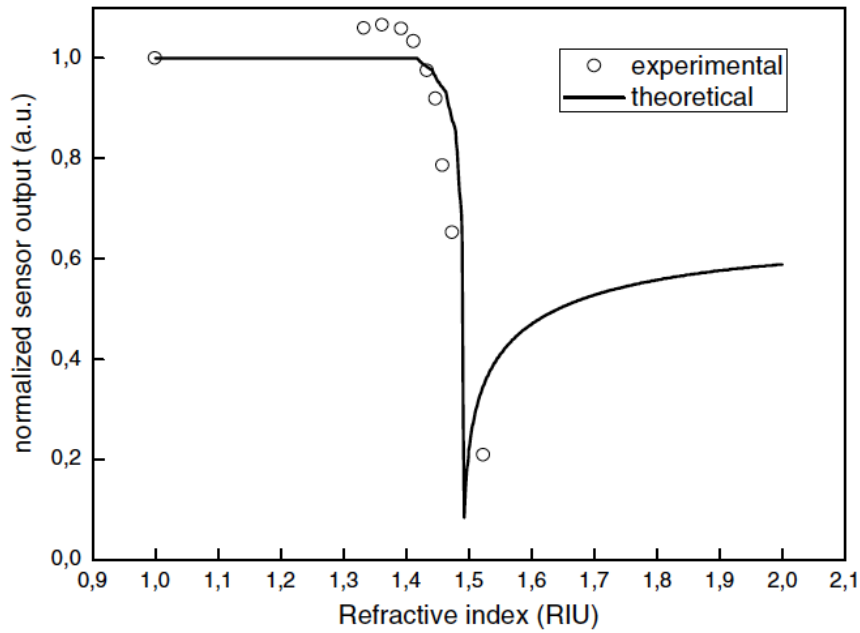


Figure IV.6: Experimental and theoretical normalized transmission output as a function of the refractive index liquids. Taken from [183].

IV.3.1.a. RI sensors using DLW

With the Direct Laser Writing (DLW) technique, RI sensors were also developed in fibers and glasses. Most of them are based on creating Bragg gratings and monitoring the Bragg wavelength shift. In 2006, *Grobnic et al.* manufactured an RI sensor in a tapered fiber where a fiber Bragg grating (FBG) was written using a Ti:Sapphire laser operating at 800 nm [196]. Then the fiber was inserted in RI liquids and the Bragg grating shift was monitored [196]. In 2007, *Zhou et al.* created an RI sensor also based on FBG [188]. A micro-slot was engraved inside the optical fiber and then FBGs were written using both the Direct Laser Writing technique followed by an etching process. The fiber tip immersed in the RI liquids and the Bragg wavelength shift were monitored as a function of the different RI liquids [188].

In 2009, the creation of an RI sensor in the range from 1 to 1.452 based on the creation of Waveguide Bragg Gratings (WBG), etching and microfluidics inside bulk fused silica glass was reported by *Maselli et al.* [187]. The reflected Bragg wavelength is highly affected by any change in the RI. The WBG and the microfluidic channels were written using the DLW technique. Then the micro-fluidic channels were etched (to reveal the channels) in order to fill them with different RI liquids. The sensor was based on filling the micro-channels with liquids and

monitoring the Bragg wavelength shift as the evanescent wave of the mode propagating in the WBG interacts with the nearby liquids in the channels [187]. The highest sensitivity and Bragg shift were obtained when the liquid matched the RI of the cladding i.e. the fused silica glass ($n=1.458$) [187].

Eventually, all the afore-mentioned Bragg grating based sensors developed by DLW monitor the shift of the Bragg wavelength as a function of the external RI liquid and are embedded inside the bulk glass or fiber. The etching process is a must in order to reveal the sensing medium or fiber tapering. However, *Lapointe et al.* in 2015 managed to create an RI sensor using the DLW technique with no need for etching or additional processing [169]. Their work was similar to the work reported by *Polynkin et al.* in 2005 [182] and *Bilro et al.* in 2010 [183] where both of them used the interaction of the evanescent wave in an optical fiber with the outer medium and the total internal reflection principle to create an RI sensor. Their sensor was based on a near-surface waveguide written using the DLW technique in a toughened Corning Gorilla bulk glass. The schematic representation of the sensor is depicted in Figure IV.7. A double S-bend waveguide is written at 5 cm near the surface and acts as the sensing medium. A 1550 nm light is injected using a single mode (SM) butt-coupled optical fiber. The light is guided and interacts with the outer medium and then collected using an optical fiber linked to a power meter.

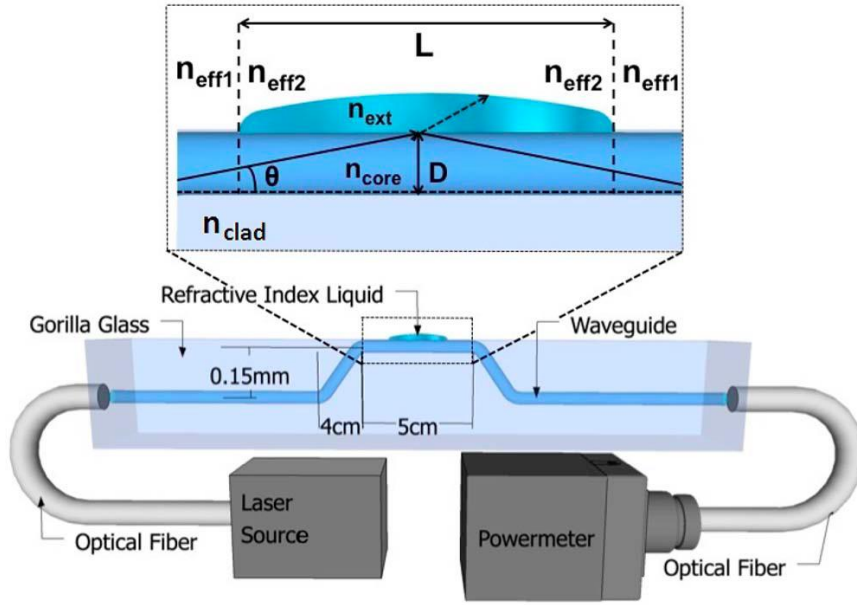


Figure IV.7: Schematic presentation of the refractive index (RI) sensor. Inset: Sketch of the optical rays in the sensing region. The refracted light represented in a dashed line only occurs when the RI of the liquid is higher than the RI of the cladding. Taken from [169].

An improvement in the theoretical model proposed by *Bilro et al.* [183] was introduced in *Lapointe's* work [169]. In fact, it is a hybrid approach where the model was adapted to single mode propagation (instead of multimode as introduced by Bilro et al.) and the variation of the effective RI (n_{eff}) as a function of the outer medium was taken into consideration. Given that the photo-written waveguides were circular, the propagating mode is assumed to be a Gaussian function i.e. proportional to $e^{-\theta^2/b}$ where b is related to the Gaussian distribution and characterized the mode field diameter. Therefore, (IV-9) and (IV-10) will now be given by:

$$P_{out} \propto \int_0^{\theta_c} R_{n_{ext}}^{N(\theta)} \sin\theta e^{-\theta^2/b} d\theta \quad (IV-11)$$

$$P_{norm} = \frac{P_{out}}{P_{air}} = \frac{\int_0^{\theta_c} R_{n_{ext}}^{N(\theta)} \sin\theta e^{-\theta^2/b} d\theta}{\int_0^{\theta_c} R_{n_{air}}^{N(\theta)} \sin\theta e^{-\theta^2/b} d\theta} \quad (IV-12)$$

The old model proposed by Bilro et al. [183] did not take into account the change in the effective RI (n_{eff}) of the guided mode as a function of the outer medium i.e. the RI liquids. The new model proposed by Lapointe took this into consideration (Figure

IV.7). Because calculating the effective RI is complicated, it was estimated using the following equations:

$$n_{eff_1} = (1 - x)n_{core} + xn_{air} \quad (IV-13)$$

$$n_{eff_2} = (1 - x)n_{core} + xn_{ext} \quad (IV-14)$$

where x characterizes the overlap of the mode with the different RI liquids applied on the glass and can take values between 0 and 1. It could be evaluated using the V parameter in (II-5). However V is unknown, so x was adjusted to fit the simulation and experimental data. Assuming that the Fresnel reflection coefficient is independent from θ (single mode waveguide, so θ very small), it is given by:

$$R_{Fr} = \left(\frac{n_{eff_1} - n_{eff_2}}{n_{eff_1} + n_{eff_2}} \right)^2 \quad (IV-15)$$

So, in that case (IV-11) and (IV-12) could be written as:

$$P_{out} \propto (1 - R_{Fr})^2 \int_0^{\theta_c} R_{n_{ext}}^{N(\theta)} \sin\theta e^{-\theta^2/b} d\theta \quad (IV-16)$$

$$P_{norm} = \eta_{RI} = \frac{P_{out}}{P_{air}} = \frac{(1 - R_{Fr})^2 \int_0^{\theta_c} R_{n_{ext}}^{N(\theta)} \sin\theta e^{-\theta^2/b} d\theta}{\int_0^{\theta_c} R_{n_{air}}^{N(\theta)} \sin\theta e^{-\theta^2/b} d\theta} \quad (IV-17)$$

Different RI oil drops were placed on the near surface portion of the waveguide and the output transmission was monitored for every RI oil. The transmission of the waveguide following the deposit of an oil drop is normalized with respect to the transmission of the waveguide where no oils were deposited. The experimental and the new model exhibit a significant match as shown in Figure IV.8. According to *Lapointe et al*, three different regimes were observed. The first one is when the RI is lower than the $n_{cladding}$ i.e. $RI=1 \rightarrow 1.5114$. Light is guided based on the total internal reflection (TIR) exhibiting some losses due to the mismatch of the effective RI with the deposited liquids. The second region is from 1.5514 to n_{core} (~ 1.5117) where the critical angle θ_c decreases drastically and all beams with a higher incident angle are ejected outside the waveguide, as also suggested by *Bilro et al* [183].

The third region is where the RI of the liquids is higher than the n_{core} where the light is guided by many internal Fresnel reflections and not TIR [169].

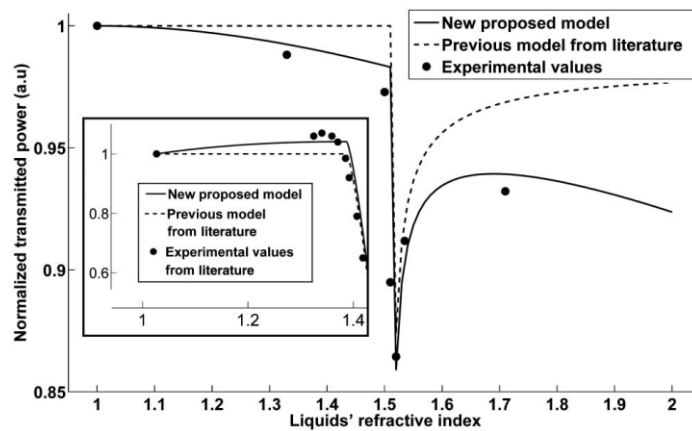


Figure IV.8: Experimental and simulated normalized transmitted powers as a function of the refractive index of the liquids. The previous model of Bilro et al [183] is represented with a dashed line. Inset: Comparison between Lapointe’s model [169] and Bilro’s model [183]. Taken from [169].

The difficulty in writing Bragg grating-based waveguides near the surface is one of the reasons why the majority of RI sensors are manufactured by DLW and not on the work reported by *Lapointe et al* [169]. Generally, DLW on the surface of the glass induces ablation which makes the writing process of waveguides on/near the surface almost impossible. Very few works have reported on this over the last few years.

Lapointe managed to write near-surface waveguides in reinforced Corning Gorilla glass with a relatively low $\Delta n \sim 5 \times 10^{-4}$ [71]. Figure IV.9 shows written waveguides at 25 μm below the surface and a waveguide near the surface as well as the guided mode profiles for each waveguide. The mode profile is shown to touch the glass-air interface, as illustrated in Figure IV.9.g-h. Those waveguides were used to create the RI sensor mentioned above. Attempts at writing near-surface waveguides inside standard soda-lime glass proved unsuccessful (Figure IV.9 a-b) as opposed to the case of Gorilla glass which protects the glass surface from ablation during the writing process [71].

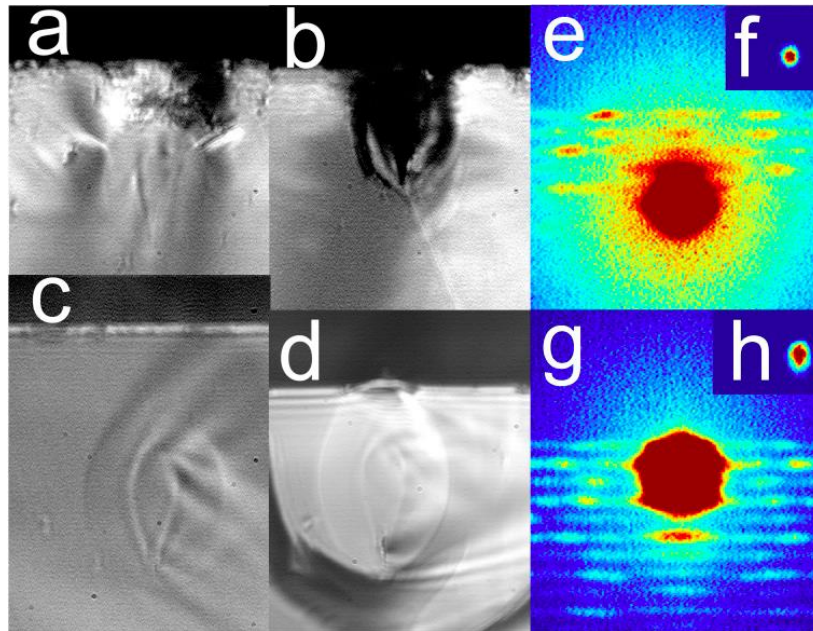


Figure IV.9: Side view of (a) (b) the near-surface waveguides written in soda lime glass. (d) Gorilla glass. (c) 25 μ m below the surface. Near field mode profiles of the waveguides in Gorilla glass. (e)(f) 25 μ m below the surface. (g)(h) Near-surface waveguide. Taken from [71]

Another interesting work was reported by *Bérubé et al.* where near surface waveguides were written inside Eagle 2000 and silica glasses using a compensation method [91]. He overcame the ablation problem by placing a glass slide cover in optical contact with the top surface of the glass. This suppresses the air-glass interface enabling the laser writing near the surface with a moderate Δn of $\sim 2.9 \times 10^{-3}$. After the DLW process is finished, the glass slide cover could be easily removed. The near-surface waveguides using the compensation method for Eagle 2000 and silica glass are shown in Figure IV.10. The near-surface waveguide morphology is comparable to waveguides typically written $\sim 150 \mu\text{m}$ below the surface while exhibiting a comparable Δn .

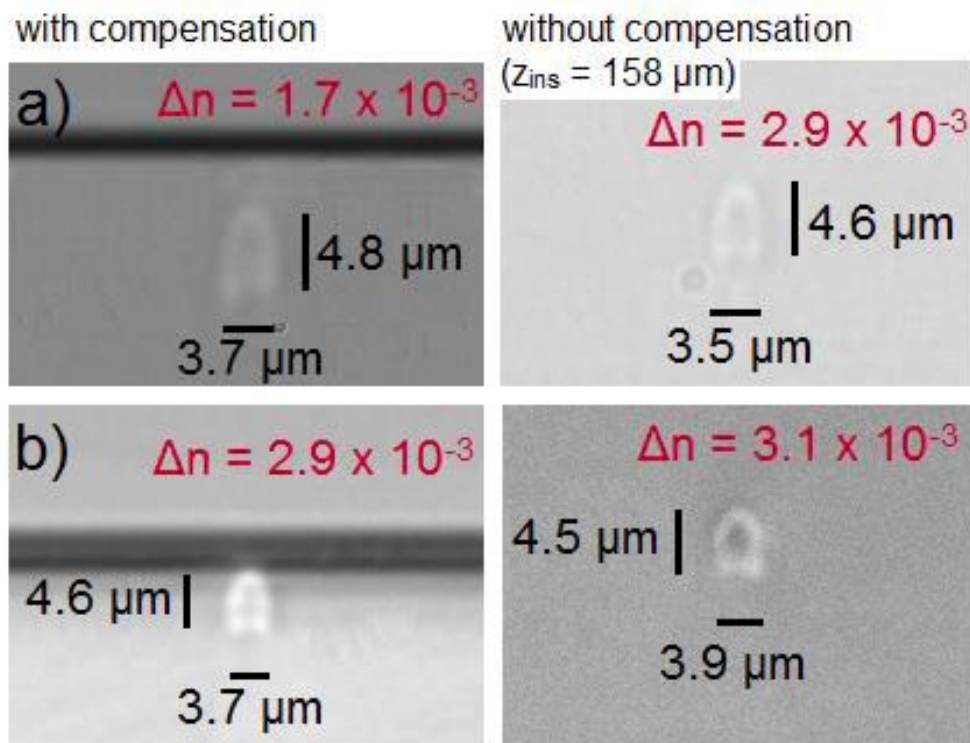


Figure IV.10: Side view of the near surface waveguides using the compensation method compared to waveguides written $\sim 150 \mu\text{m}$ below the surface without the glass cover in (a) fused silica (b) Eagle. Taken from [91].

The following written waveguides were used to photo-excite nanoparticles deposited on the glass surface of an Eagle 2000 based on the evanescent wave interaction with the outer medium [197]. The side view under white illumination of the near-surface waveguide is shown in Figure IV.11.a while the near-field mode profile (touching the air-glass interface) following the injection of 488 nm light is shown in Figure IV.11.a. Next, sensitive materials (Fluorescein isothiocyanate ($\lambda_{\text{ex}}=488\text{nm}$, $\lambda_{\text{em}}=515 \text{ nm}$) and Ag@SiO₂@FITC self-assembled periodic linear nanowires) were deposited on the glass surface near the portion of the waveguide. A strong green fluorescence emission is observed showing that the evanescent wave of the near-surface waveguide excited the sensitive materials as shown in Figure IV.11.b-c-d [197].

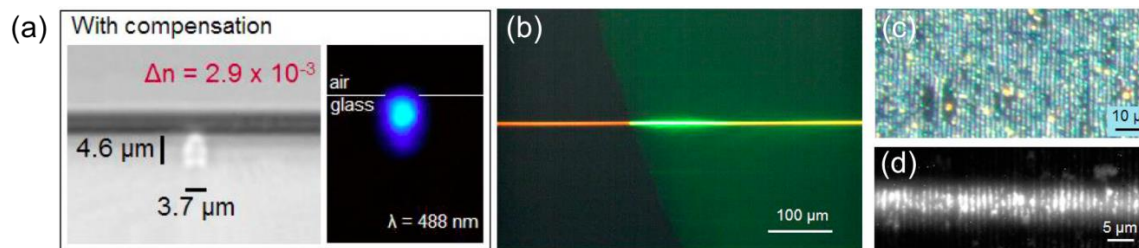


Figure IV.11: (a) Side view of near-surface waveguide using the compensation method and the guided mode profile following laser injection at $\lambda=488$ nm. (b) Fluorescence emission of an aqueous fluorescein solution excited by the evanescent wave of the light guided ($\lambda=488$ nm) in the near-surface waveguide observed through a band pass filter 528/38 (top view) (c) Dark field image of a linear periodic assembly of AG@SiO₂@FITC nanowires (top view) (d) Fluorescence emission of AG@SiO₂@FITC nanowires (top view). Taken from [197].

Another work on the interaction of the photo-inscribed waveguides in glasses with the outside medium was reported by Çirkinoglu et al. recently. It consisted of coupling whispering gallery modes in a silicon microsphere deposited on the glass surface [198].

IV.4. Experimental methods

IV.4.1. Glass

The glass used is an Argoglass AG01 provided by Argolight company. The glass samples were shaped and optically polished into a parallelepiped with the following dimensions 9.9 mm x 9.9 mm x 700 μm.

IV.4.2. Laser setup

DLW in this experiment was performed using a Clark - Impulse laser Yb-doped fiber oscillator/amplifier system operating at 1030 nm with an adjustable repetition rate from 0.2 MHz up to 25 MHz with an average output power of 15 W (at 25 MHz repetition rate). A 12.6 MHz repetition rate was used with a pulse duration of 360 fs in order to perform the DLW of *type A* waveguides using a Nikon 100x-0.8NA objective. The glass sample was mounted on Aerotech 3D stages.

IV.5. Results

IV.5.1. Writing near surface waveguides

Direct laser writing (DLW) in silver containing glasses as mentioned in Chapter II and Chapter III induces the creation of fluorescent silver clusters. Those silver clusters are responsible for a new type of refractive index change called *type A* that allows the fabrication of optical waveguides and components [174]. A series of 1 cm S-bend rising near surface waveguides (~ 5 mm from the surface) were written in silver containing glass based on *type A* refractive index change with no additional process. The conditions of DLW were optimized in order to avoid ablations of the glass when reaching the surface. First, the laser beam is focused on the surface or typically ~ 1 μm below the surface. The writing speed was fixed to 50 $\mu\text{m/s}$ while the laser pulse energy was changed. In this chapter, we are relying on the pulse energy as our power reference given that the window for writing is so narrow. Therefore if we express the writing conditions using laser irradiance, the slight difference would be exaggerated. The DLW writing process starts while reducing the pulse energy until we reach just below ablation conditions. This pulse energy is chosen to make waveguides as it sits just below the ablation threshold allowing the creation of *type A* waveguides hopefully with a moderate refractive index change (Δn). One should mention that the energy window is quite narrow while writing near the glass surface. A variation of 2 to 3 nJ in the pulse energy could cause ablations. A series of 1 cm near surface waveguides were written ~ 5 mm from the surface in a step process where the laser is focused deeper inside the glass with each pass starting at $1\mu\text{m}$ to $\sim 12\mu\text{m}$. The waveguides were written using a 12.6 MHz repetition rate Impulse laser by Clark-Mxr.Inc operating at 1030 nm with a pulse duration of 370 fs. The pulse energy was fixed to 28 nJ corresponding to 7.2TW/cm^2 and the writing speed to 50 $\mu\text{m/s}$. A 100 x -0.8NA Nikon microscope objective was used. The S-bend near surface waveguides exhibited an $R_c=80\text{mm}$ and a $\Delta h=32\mu\text{m}$ (Figure IV.12). Ideally, the waveguide is preferred to be a double S-bend waveguide with a portion rising to the surface and the input and the output on the same level. However, due to the small dimensions of the sample and to minimize the curve losses of our waveguides, it was based only on a single S-bend as shown in Figure IV.12.

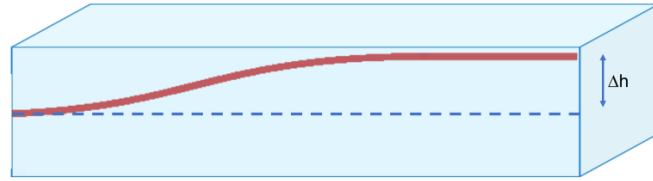


Figure IV.12: Sketch of the rising near-surface waveguide.

The near surface waveguides exhibited smooth writing with no ablation observed on the end facet of the glass nor from the top view indicating that the writing process is smooth and based on *type A* modification as shown in Figure IV.13. The side view under white light illumination of a straight waveguide written typically $\sim 32 \mu\text{m}$ below the surface and three near-surface rising waveguides that are neighbouring the surface are shown in Figure IV.13.a.b.c.d. One can see that the morphology of all the waveguides is conserved as well as the dimensions ($\sim 3 \times 5.25 \mu\text{m}^2$), except for Figure IV.13.b where the waveguide (NWG1) is smaller than the waveguide written at $32 \mu\text{m}$. This is due to the fact that the DLW process occurred exactly on the surface of the glass sample and a part of the waveguide is missing. It virtually exists outside the glass sample. Therefore it results in having a waveguide with smaller dimensions. All the other waveguides exhibited the same dimensions roughly $\sim 5.25 \mu\text{m}$ except this waveguide even though no ablations or cracks were observed on the side facets of the glass for all the written waveguides even in the case of writing on the surface. Furthermore, the morphology of the waveguide exhibiting two parallel planes is typical of the *type A* and silver clusters' spatial distribution [44, 174]. From the top view (Figure IV.13.d), a smooth modification was observed where no ablations or mini explosions were observed along the rising portion of the waveguide.

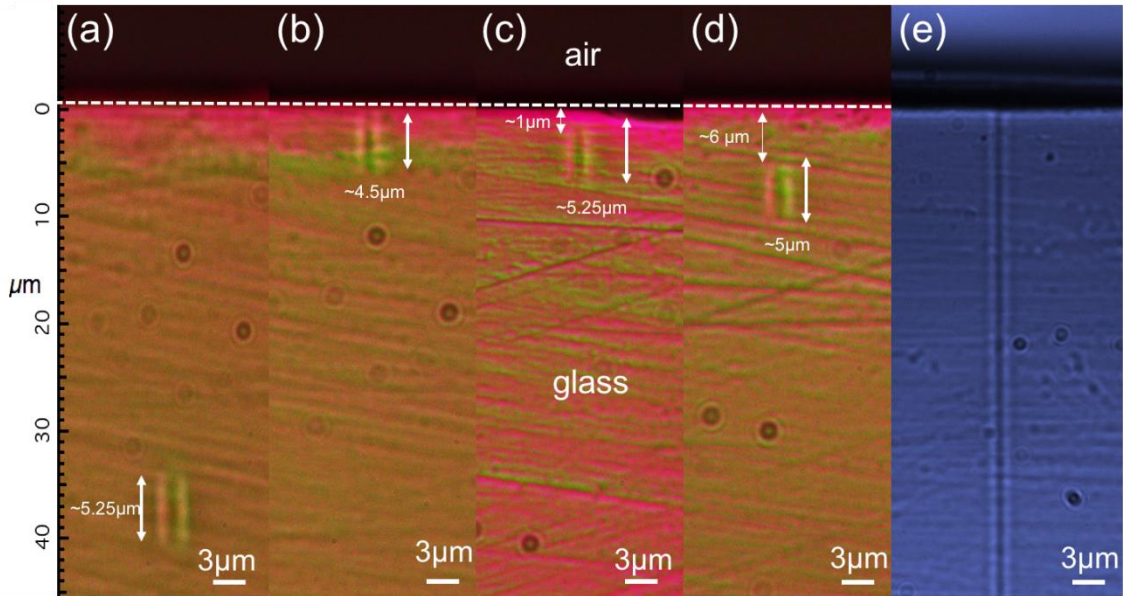


Figure IV.13: Side view under white light illumination of (a) 32 μm straight waveguide (b)(c)(d) rising near-surface waveguides. (e) Top view under white light illumination of a portion of a near-surface waveguide. Smooth modifications where no ablations or mini explosions were observed. DLW parameters: 28 nJ – 50 $\mu\text{m}/\text{s}$.

To test the waveguiding properties and sensing properties, a 660 nm laser was injected in all the near-surface waveguides. All the written waveguides exhibited a single mode aspect at a wavelength of 660 nm. Figure IV.14.b shows the mode profile for NWG1 following laser injection. One can see that the mode is slightly different from the mode observed in Figure II.56 where *type A* waveguide is written $\sim 160 \mu\text{m}$ below the surface. This is probably due to the air-glass interface and to the fact that a part of the waveguide exists virtually outside the surface. The large difference in refractive index between the air ($n=1$) and the glass ($n\sim 1.602$) confines the mode towards the glass as shown in Figure IV.14.b. Moreover, when writing the S-bend rising waveguide, we believe that in that case, when reaching the surface, the waveguide is cropped and exhibits smaller dimensions from the initial part of the waveguide. To support our hypothesis, numerical simulations were conducted where $\sim 1 \mu\text{m}$ of the dimensions of the waveguide virtually existed outside the glass as shown in Figure IV.14.c. The simulated mode profile (Figure IV.14.d) matches the experimental mode confirming our assumption that a part of the waveguide is missing which affects the shape of the mode. As mentioned before in section II.6.3.b, the simulated mode is more confined than the experimental mode due to the step index Δn used during simulations. Finally, this confirms the ability of writing *type A* waveguides on the surface of the glass sample which is not achievable yet in any other glass.

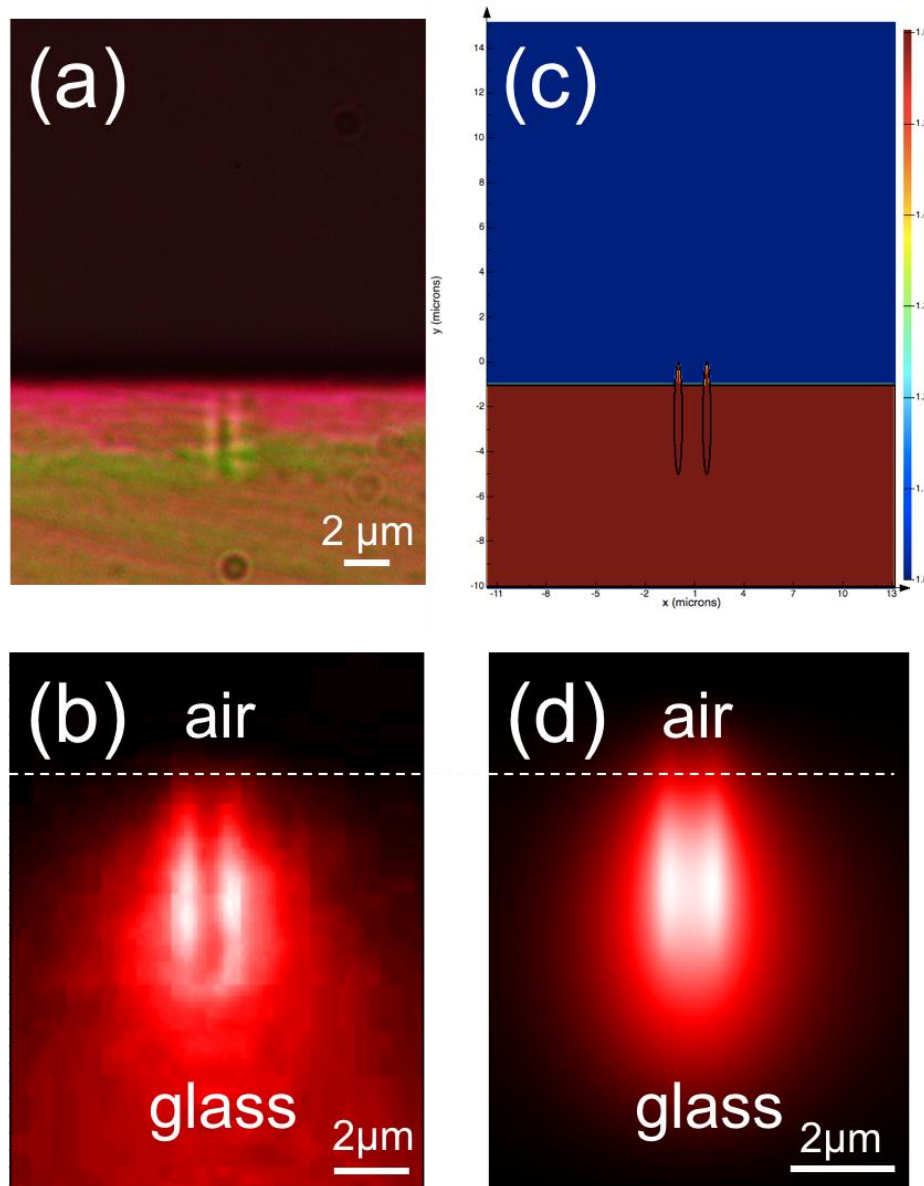


Figure IV.14: (a) Side view of the rising near-surface waveguide NWG1 under white light illumination. (b) Near-field mode profile following the injection of a 660 nm laser. (c) Sketch of the simulation of the waveguide where $\sim 1 \mu\text{m}$ of the waveguide is simulated outside the glass. (d) Simulated mode profile based on the simulations shown in (c). A good match between experimental and simulated modes showing that the mode is confined more towards the glass due to the glass-air interface.

Moreover, Figure IV.15 shows the side view, experimental near-field mode profile, simulation sketch and simulated near-field mode profile of a waveguide neighbouring the surface $2 \mu\text{m}$ away. The experimental near-field mode profile (Figure IV.15.b) exhibited the same shape of the mode reported in Figure II.56 for a waveguide written typically $\sim 160 \mu\text{m}$ below the surface. The simulated mode

profile (Figure IV.15.d) fits very well with the experimental one implying that, for this waveguide, the mode is generally well confined inside the glass and the glass-air interface does not significantly affect the shape of the propagating mode. This confirms our previous assumption that NWG1 exhibited a part of the mode outside the glass which highly affected the near-field mode profile.

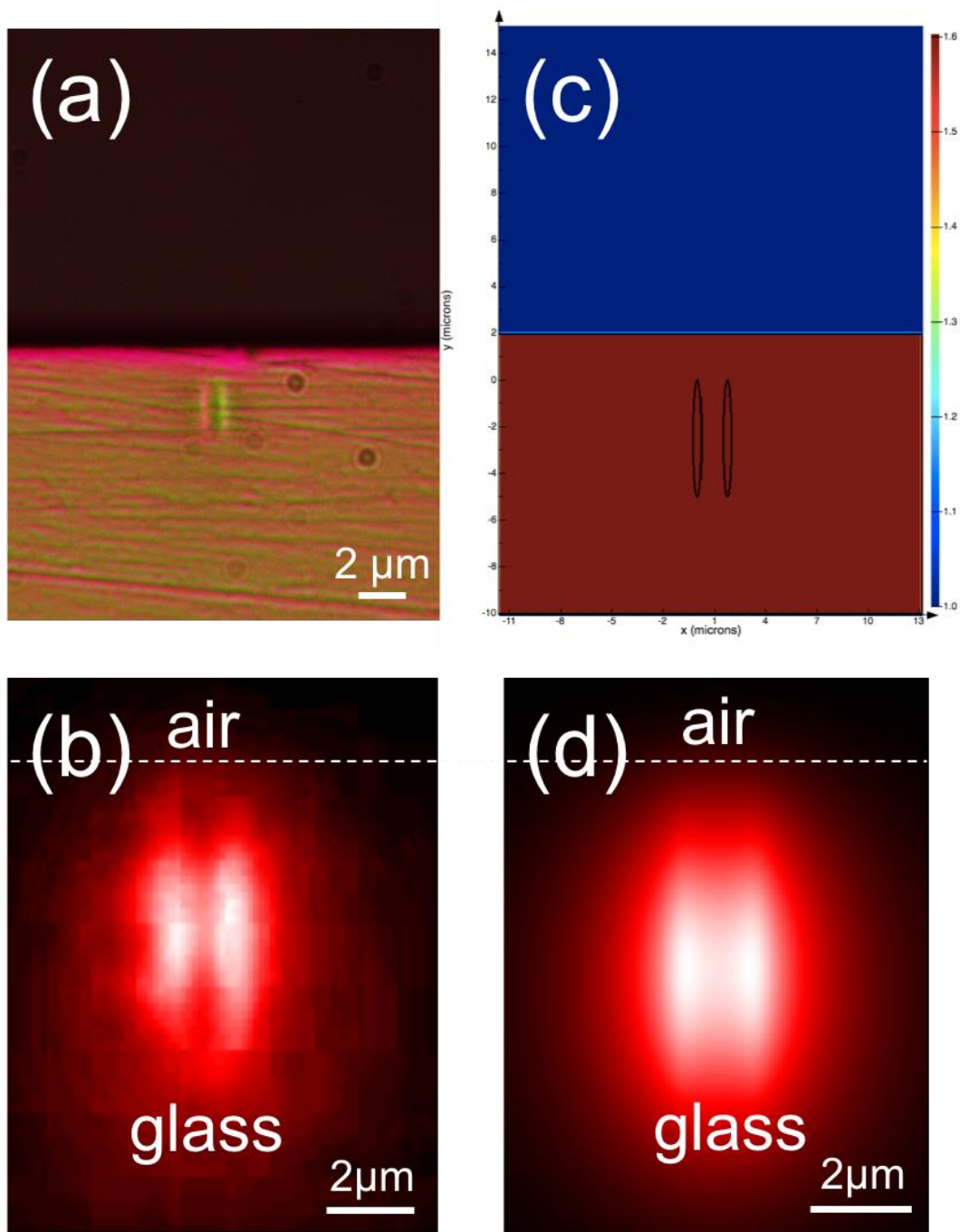


Figure IV.15: (a) Side view of a rising near-surface waveguide under white light illumination. (b) Near-field mode profile following the injection of a 660 nm laser. (c) Sketch of the simulation of the waveguide 2 μm away from the surface. (d) Simulated mode profile based on the simulations shown in (c). A good match between experimental and simulated modes showing that the mode is not affected.

The refractive index change (Δn) of the surface-rising waveguides was measured using SID4bio wave front sensor, as previously explained in section II.5.6. As expected, two sharp positive Δn peaks were observed correlated to the silver

clusters' spatial distribution which is typical for *type A* waveguides (Figure IV.16). A Δn of $\sim 2.4 \times 10^{-3}$ was measured (Figure IV.16.b) for all the near-surface waveguides measured on the portion neighbouring the surface that could be compared to the SM waveguide written at $\sim 160 \mu\text{m}$ below the surface ($\Delta n \sim 2.5 \times 10^{-3}$ in Figure II.40). Generally, it is a challenge to make near-surface waveguides. Moreover, it is a challenge to have a moderate Δn . The pulse energy threshold for glass modifications decreases as the beam approaches the glass surface [186], which makes it more complicated to make near-surface waveguides with a good value of Δn . Previous works on near-surface waveguides reported a relatively low $\Delta n \sim 5 \times 10^{-4}$ in the case of reinforced Gorilla glass [169] and a moderate $\Delta n \sim 2.9 \times 10^{-3}$ in Eagle glass, but using the compensation method [91]. For *type A* waveguides, there is no need for reinforced glass or compensation method to write near-surface waveguides while exhibiting a moderate Δn of $\sim 2.4 \times 10^{-3}$ (Figure IV.16). On one hand, one tends to reduce the Δn to extend the evanescent wave and enhance the sensitivity of the waveguides but on the other hand, one is interested in a moderate Δn in order to reduce the propagation losses due to the curvature of the rising near-surface waveguides (curvature losses).

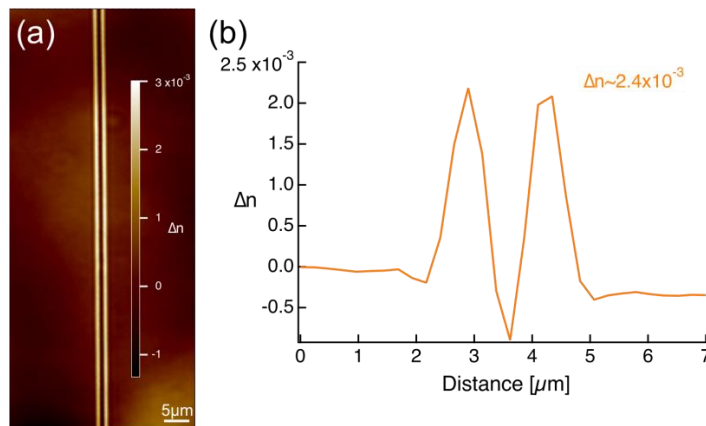


Figure IV.16: (a) Top view phase image of a portion of a waveguide neighboring the surface waveguides exhibiting smooth type A modification. (b) Δn profile extracted from the phase image showing two positive peaks of $\sim 2.4 \times 10^{-3}$. DLW parameters: 28 nJ – 50 $\mu\text{m/s}$.

All the written near-surface waveguides were tested by injecting a 660 nm laser and dropping a $\sim 4 \mu\text{m}$ droplet of Cargille oil with an RI of 1.604 on the rising portion of the waveguide. The choice of an RI of 1.604 came after testing several oils. Further details will be presented in section IV.5.2. The following study aims to monitor the sensitivity of the waveguides i.e. the transmission drop following the

deposition of the oil droplet on the glass surface as a function of their distance from the surface. The results are depicted in Figure IV.17. The transmission of each waveguide is normalized with respect to the transmission of the waveguide where no oil was deposited on the sample. The distance from the surface is from the glass-air interface to the upper part of the waveguide as shown in Figure IV.13. Even though the NGW1 is written on the surface, it does not exhibit the highest sensitivity between the written waveguides. This is because the mode is cropped at the interface, weakly guided and weakly confined. And it is hard to monitor the transmission decrease following the deposition of the oil droplet. The farther the waveguides are from the surface, the lesser the interaction is with the outer medium, which is expected. The interaction between the waveguides and the outer medium stops at a distance of $\sim 9 \mu\text{m}$ from the surface (Figure IV.17). The most sensitive waveguides are the ones which are $\sim 1 \mu\text{m}$ to $\sim 1.75 \mu\text{m}$ away from the surface exhibiting a transmission loss of $\sim 65\%$ ($\sim 4.8 \text{ dB}$) for a 4 mm oil droplet. The mode profile of one of the most sensitive waveguides is shown in the inset of Figure IV.17. The mode profile exhibits no distortion and is totally located inside the glass. Furthermore, even the last written waveguide interacting with the outside medium $\sim 6.5 \mu\text{m}$ away from the surface exhibits significant transmission losses of $\sim 33\%$ (1.73 dB) showing the high sensitivity of *type A* waveguides. Compared to the work of *Lapointe et al* where the maximum transmission drop is less than 15% (0.7 dB) for an oil droplet of $\sim 1 \text{ cm}$ [169], our waveguides seem to be much more sensitive, up to four times more sensitive. However, one should take into consideration the distance of the waveguides to the surface in the case of *Lapointe et al*. In a previous work [71], a side view picture of the near-surface waveguides was shown, and it seems that the waveguides are farther than ours to the surface, which could explain the lower sensitivity. Thus, we believe that it is impossible to write *type I* waveguides on the surface of the glass like it is the case for *type A*. This is explained by the fact that the *type A* occurs before the *type I* in the pulse energy scale. The DLW in silver containing glasses targets the chemicals inside the glass i.e. silver ions and produce silver clusters. The pulse energy needed to activate the chemical reactions is significantly lower than the pulse energy needed to create *type I* modification (melting the glass and/or creating color centers). Finally, *type A* waveguides are based on two sub-wavelength waveguides highly interacting together guiding one single supermode. It is well known that sub-wavelength waveguides exhibit a greater evanescent wave and sensitivity [182, 199] compared to normal waveguides. This could also be one of the reasons that *type A* waveguides exhibit a high sensitivity compared to *type I* waveguides.

Eventually, given that few works have been reported on this subject, one can only assume the hypothesis.

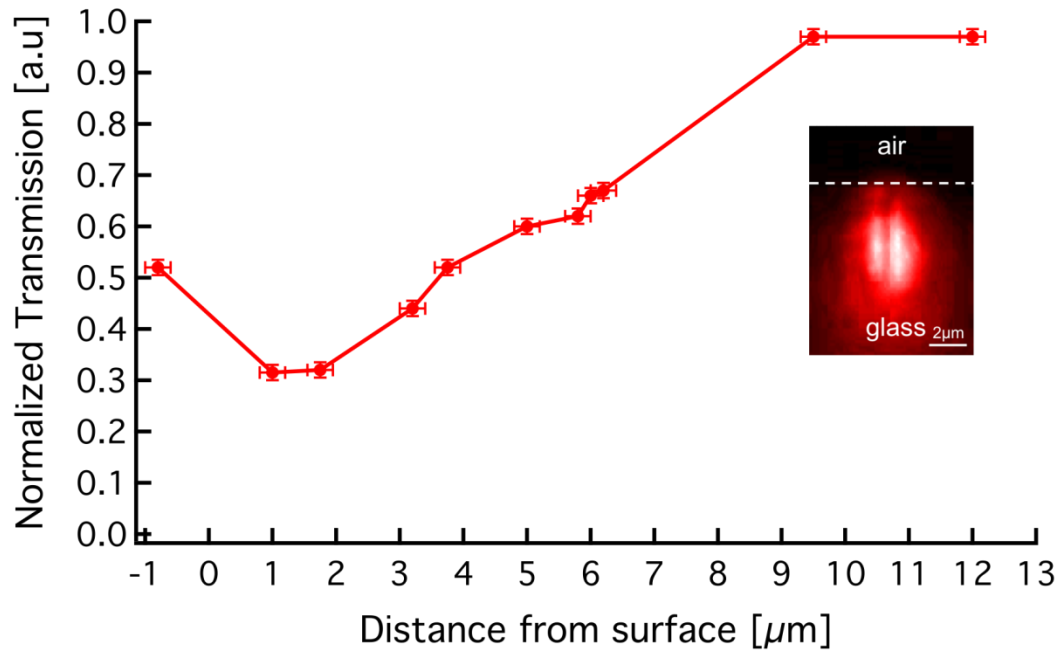


Figure IV.17: Normalized transmission for all written waveguides following the deposition of a $\sim 4 \mu\text{m}$ droplet of 1.604 Cargile oil. No interaction was observed after $7 \mu\text{m}$ spacing between the waveguide and the surface. Inset: Near-field mode profile of the most sensitive waveguide at $\sim 2 \mu\text{m}$ below the surface. DLW parameters: 28 nJ – 50 $\mu\text{m/s}$.

Finally, a test of the transmission decrease as a function of the dimensions of the oil droplet was performed. As expected, the larger the droplet of oil, the higher the transmission drop for an RI oil of 1.604, as shown in Figure IV.18. The larger the dimension of the droplet is, the higher the interaction length. Therefore more light rays are ejected outside the waveguide. After covering almost all the near-surface portion of the waveguide, the drop of transmission stops as expected. The highest transmission drop was observed to be around 80% ($\sim 7 \text{ dB}$) when covering the entire interaction length of $\sim 5 \text{ mm}$ for the most sensitive waveguide (Figure IV.18).

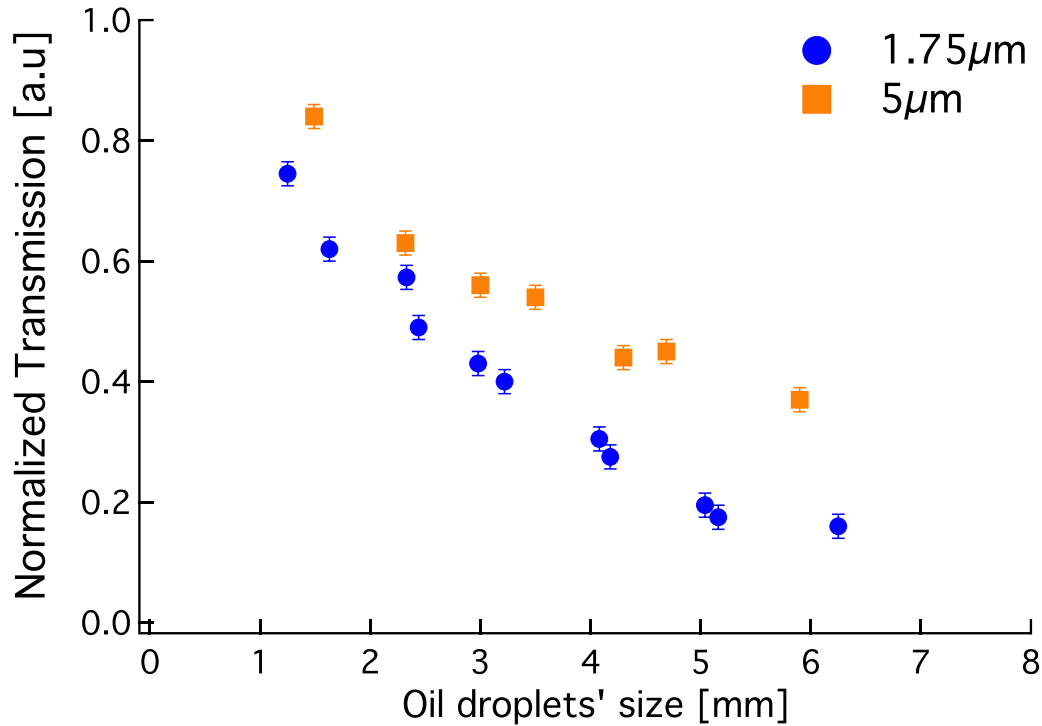


Figure IV.18: Normalized transmission as a function of the size of the droplet of a 1.604 Cargille oil for two waveguides with different distances from the glass surface. The larger the droplet the higher the losses in transmission.

Therefore, we demonstrated the writing of near-surface waveguides with high sensitivity, a moderate Δn value with no need for additional processing based on *type A* modification, highlighting the advantages of the new *type A* modification.

IV.5.2. RI sensor

A refractive index (RI) sensor was created based on the written near-surface waveguides. Four waveguides were taken into consideration for this experiment exhibiting different distances from the surface. First, the NWG1 waveguide mentioned before where $\sim 1\mu\text{m}$ of this waveguide exists virtually outside the glass and NWG2, NWG3, NWG4 which are $\sim 1\mu\text{m}$, $3.75\mu\text{m}$ and $6\mu\text{m}$ away from the glass surface respectively. Different RI Cargille oils were dropped on the glass surface using a micropipette in a way that the oil droplet exhibits the same dimensions ($\sim 4\text{mm}$) for every measurement. The oil droplets dimensions were visualized using a top view CCD camera. Then, the transmission was monitored for each waveguide, for different RI oils. The transmission was normalized with respect to the transmission where no oil was dropped on the glass surface. Following every droplet of oil, the sample was cleaned using Ethanol until the transmission power

returned to the initial value measured before dropping oil. This confirms the exactitude of the measurements. The results are shown in Figure IV.19 for the four different waveguides. NWG1 and NWG2 exhibited a non-standard behaviour exhibiting two resonances, one where the transmission is increased up to $\sim 50\%$ for an oil RI of 1.602 and the other one where the transmission is decreased for an oil RI of 1.604. The second resonance is an expected one and comparable to the one observed in the literature for similar works [169, 182, 183], as shown in Figure IV.4, Figure IV.6 and Figure IV.8. However, the first resonance was observed for the first time in such sensors created by the DLW technique. It was observed by Polynkin et al. when injecting a $1.5 \mu\text{m}$ light in a tapered fiber of $\sim 700 \text{ nm}$ thick and applying RI liquids with lower RI than the cladding. However, it was not explained and interpreted [182]. The taper exhibited around 40% more losses compared to the taper with a thickness of $1.6 \mu\text{m}$. When applying the RI liquids below the cladding's RI, the transmission increased and almost all the losses were compensated with RIs matching the cladding's (Figure IV.4) before decreasing when exceeding the cladding's RI [182], which is similar to our results. Also observed by *Bilro et al* [183] in Figure IV.6 but explained as scattering of the light on the surface due to irregularities and the polishing process.

In our case, this could be explained by the fact that these two waveguides are so close to the surface, even one of them has a part cropped by the glass interface. Compared to deeper waveguides, those waveguides exhibited losses up to 50% (3 dB), which is probably due to the mode evading the waveguide when reaching the surface (glass-air interface). Once we match the RI of the glass which is ~ 1.602 in this case, the glass-air interface disappears and the mode is re-confined and re-guided inside the waveguide as a normal waveguide embedded totally inside the glass (RTI reflections), thus the increase in the transmission and almost full compensation of the initial losses. Furthermore, this double resonance was not observed for the waveguides that are deeper in particular NWG3 & NWG4 which are $\sim 3.75 \mu\text{m}$ and $6 \mu\text{m}$ from the surface respectively. Only one resonance is observed as reported by all the previous works [169, 182, 183]. The sensing process could be described as three different regions (Figure IV.4, Figure IV.6 and Figure IV.8); the first region where the RI of the liquid is lower than the glass, $n_{ext} \leq n_{glass}$; the second region where the RI of the liquid is equal to the waveguide, $n_{ext} \sim n_{waveguide}$; and the third where the RI is higher than glass, $n_{ext} > n_{glass}$. The first region is where the light is guided by total internal reflection (TIR) inside the waveguide with a slight augmentation of the transmission ($\sim 2-4\%$) observed that could be correlated to the fact that the oil drops are lowering the Fresnel reflection coefficient between the propagating mode and the outer medium. This leads to the

fact that for deeper waveguides, the whole mode is confined/located inside the glass and no part of the mode is evading it. The second region is where $n_{ext} \sim n_{waveguide}$, a large portion of light is ejected outside the waveguide given that the critical angle θ_c is now much lower. The third is for $n_{ext} > n_{glass}$, where light is no longer guided by TIR but by many internal Fresnel reflections.

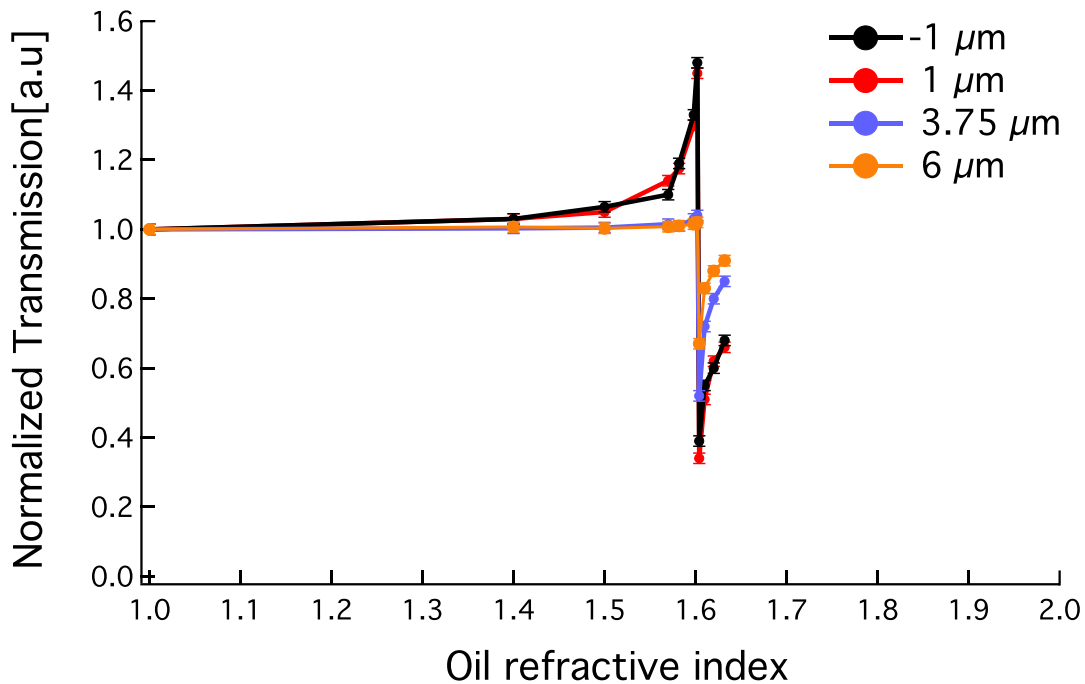


Figure IV.19: Normalized transmission as a function of different refractive index (RI) Cargille oils deposited on the glass surface for four different waveguides at different depths from the surface. DLW parameters: 28 nJ – 50 $\mu\text{m/s}$.

A theoretical model was suggested in this case in order to fit the experimental results. It consisted of three parts. The first part covering the first region where $n_{ext} \leq n_{glass}$, the second part for $n_{ext} \sim n_{glass}$ and the third part for $n_{ext} > n_{glass}$. For the first region $n_{ext} \leq n_{glass}$, the guided mode in the waveguide is affected by the glass-outer medium interface when the waveguide is close enough to the surface. Based on this hypothesis, the overlap coefficients between the normal mode embedded totally inside the glass and the mode near the surface were calculated as a function of the different exterior RIs (see Appendix part A.5). Using Lumerical Mode Solutions, we ran the simulations for our exotic waveguide and obtained the exotic mode profile for a normal waveguide well embedded inside the glass. Following that, the simulations of a near-surface waveguide took place for different exterior RIs, and the overlap coefficients between the two modes (the mode embedded in the glass and the near-surface mode) were calculated. The simulations were conducted for two waveguides, one which is $\sim 1 \mu\text{m}$ below the surface and another

one $\sim 3.75 \mu\text{m}$. Simulations and experimental results are shown in Figure IV.20. One can see that the simulations fit the experimental results. The first resonance i.e. the increase of the transmission for $n_{ext} \leq n_{glass}$ was also seen in simulations as well as the experiment, which was not observed by the previous suggested models. For the second region where $n_{ext} \sim n_{waveguide}$, when the RI of the oil matches the core's ($n_{ext} \sim n_{waveguide}$), the mode should be completely ejected outside the waveguide and the transmission should drop to 0% theoretically. Experimentally, it is not the case for our sensor. This could be explained by the following hypothesis. When the mode is propagating in the waveguide, it is well confined due to the Δn , and a small portion of the light travels outside as an evanescent wave. However, when immersing the waveguide totally in a liquid exhibiting the same RI as the core, the refractive index difference is almost null and the mode starts to get ejected outside the waveguide from both sides. But, in this case, the waveguide is immersed only from the top side, which means that only the upper part of the mode interacting with the oil will be ejected while a small part of light (lower part of the waveguide) will still be guided inside the waveguide. A certain distance is required in order to eject the totally mode from the waveguide, which we did not achieve in our case. This was supported by the fact that increasing the oil droplet's size caused the transmission to drop also (see Figure IV.18). In this case the total interaction distance was $\sim 5 \text{ mm}$ which was not enough to eject the entire mode outside the waveguide. Therefore, the transmission does not drop to zero in our case when the RI of the oil matches the RI of the waveguide (more specifically, the effective refractive index of the propagating mode). A rough calculation where we assumed that half of the mode is ejected outside the waveguide and that the interaction zone with the mode exhibits a square intensity distribution resulted in transmission dropping to 93.5% (compared to 70% for the experiment) for a 4 mm droplet of oil. In order to increase the exactitude of such calculations, one should consider the real shape of the mode and the real intensity distribution interaction with the liquid, which will not be taken into consideration in this case. For the third region where $n_{ext} > n_{glass}$ and based on Lumerical simulations, no waveguiding should occur. In fact, as mentioned before, the mode is no longer guided due to TIR but is guided due to several Fresnel reflections. Every time the light beam hits the upper part interacting with the oil ($n_{oil} > n_{glass}$), a part of light is ejected outside the waveguide and another part is reflected and guided. The third part was simulated and fitted to experimental results based on the Fresnel Reflection Coefficient and the RI of the oil (which is similar to the previous suggested models) as shown in Figure IV.20.

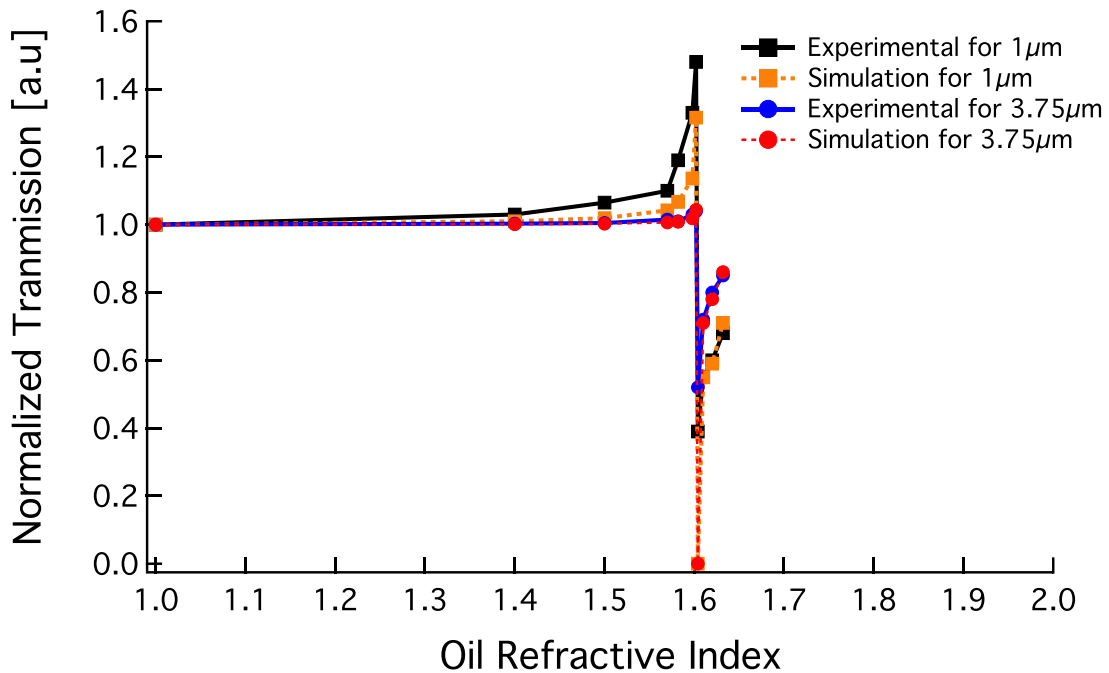


Figure IV.20: Experimental (full line) and simulations (dashed lines) for two different near surface waveguides at different distances from the surface. A good match between the experiment and the simulations.

In order to have a better idea, a sketch of the behaviour of the evanescent wave/mode profile as well as simulated mode profiles as a function of different RI liquids is depicted in Figure IV.21. For $n_{ext} < n_{glass}$ (Region I), one can see that the mode is confined towards the glass as shown in Figure IV.21.a. The simulated mode profile for a glass-air interface clearly shows it (Figure IV.21.a.i). It is due to the huge difference in RI between the glass and air. For $n_{ext} > n_{glass}$ (Region III), the mode tends to be guided in the higher RI medium which is the oil in this case (mode ejected). However a portion of light is still guided in the waveguide Figure IV.21.b. No guided mode could be simulated in this case given that the mode is no longer propagating based on TIR. Therefore no real solution was found by the software.

When matching the RI of the cladding i.e. glass $n_{ext} \sim n_{glass}$, the mode is guided normally with no aberrations as if the waveguide was embedded deep inside the glass Figure IV.21.c. This also confirms the significant increase in the transmission for NWG1 and NWG2 when the oil matches the RI of the glass (see Figure IV.19).

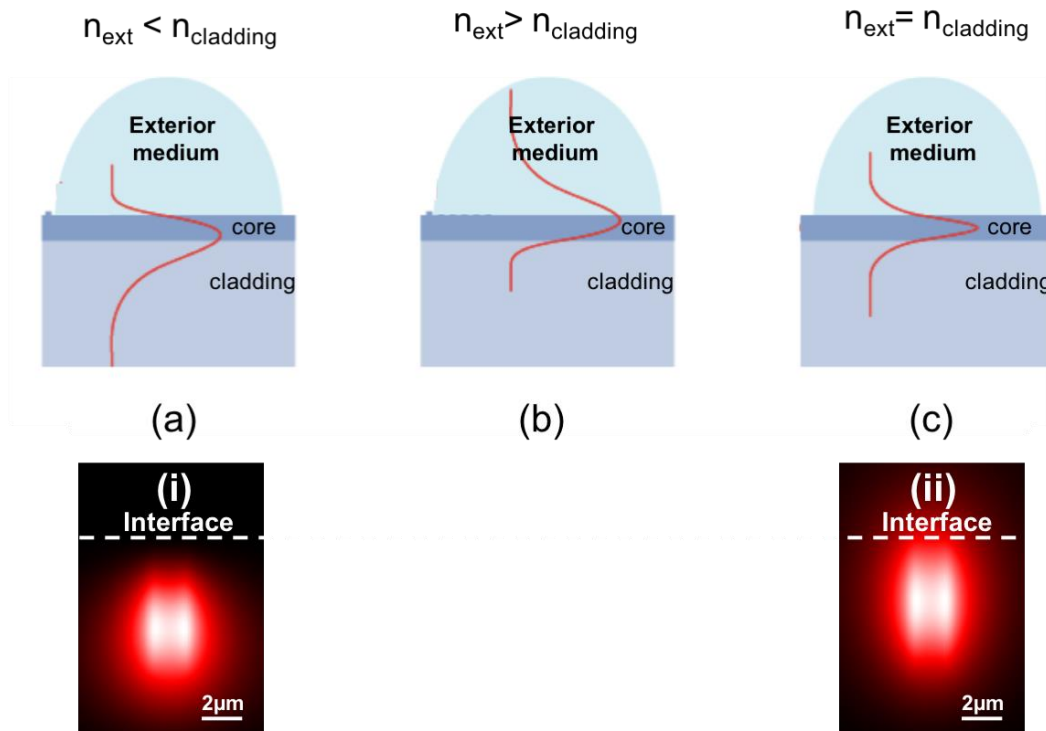


Figure IV.21: Sketch of the evanescent wave/mode profile inside a near-surface waveguide for a refractive index (RI). (a) Lower than the cladding/glass; (b) higher than the cladding/glass; (c) equal to the cladding/glass. Inspired from [200]. Simulated mode profile for a (a.i) glass-air interface; (c.ii) glass-oil interface with a refractive index of oil matching the glass $n_{ext} \sim n_{glass}$.

So, an RI sensor was created in a 1 cm glass chip based on *type A* waveguides that allow to show a double resonance enabling double sensing regions for lower and higher RIs of the waveguide. The sensor operates in a region between 1 and 1.632, which has not been reported before. The significance of this work exists in the fact that the RI sensor was created in a 1 cm glass chip with higher sensitivity and much more compact design compared to all previous models [169, 182, 183]. With an interaction length of ~ 5 mm, the transmission drops up to $\sim 80\%$ (7 dB) which is not achievable yet with the DLW technique. Finally, one should not forget that silver containing zinc phosphate glasses are shaped into ribbon fibers while preserving all the characteristics of bulk samples [149]. Therefore, the RI sensor could be transported and manufactured inside a ribbon fiber paving the way towards fiber based RI sensors.

IV.6. Conclusion

Taking advantage of the low pulse regime of *type A* compared to *type I*, rising near-surface waveguides were written in silver containing zinc phosphate glasses with no need for additional processing which is a first. No etching, nor reinforced glass, nor compensation method were required to achieve near-surface *type A* waveguides compatible with sensing applications. Not only are near-surface waveguides achievable with *type A* waveguides, but also direct writing on the glass surface. Based on the rising near-surface waveguides, an RI sensor was created in a 1 cm glass chip that makes it possible to show double resonances (when the waveguide is very close to the surface, $\sim 1\mu\text{m}$) allowing a double sensing region before and after the RI of the waveguide. An increase of $\sim 50\%$ in the transmission ($n_{\text{oil}}=1.602$) and a decrease of $\sim 66\%$ was observed for a 4 mm oil droplet ($n_{\text{oil}}=1.604$). For waveguides that are deeper inside the bulk, only one weaker resonance is observed, which is the transmission drop when the RI of the oil is equal to the RI of the waveguide. A new theoretical model is proposed taking into account the mode shape between the glass and the outer medium as well as the Fresnel reflection coefficient. The resulting new model is the first one to simulate the increase in the transmission before the RI of the waveguide. Finally, a very high sensitive RI sensor in the range of $1 \rightarrow 1.632$ refractive index, exhibiting a transmission drop up to 80% (7dB) for an interaction length of 5 mm was fabricated in a 1 cm silver containing glass chip,. This was a first using the DLW technique, paving the way towards more sensing applications in silver containing glasses.

General Conclusion

This project aimed at creating a new type of optical waveguides and components inside silver containing glasses introducing new advantages compared to the standard glasses.

Direct Laser Writing (DLW) in silver containing glasses induces the creation of fluorescent silver clusters Ag_m^{x+} in the vicinity of the interaction voxel due to the non-linear absorption (multi-photon) allowing the creation of sub-wavelength 3D structures. It was found that those Ag_m^{x+} are responsible for a new type of photo-induced modification/refractive index change (Δn), following DLW in silver containing glasses that we called *type A*. This new type of Δn , allows the creation of optical waveguides as well as optical components. Several single and multi-mode waveguides were created based on *type A* Δn in silver containing glasses in the visible and NIR ranges. More specifically, a $3 \times 6 \mu\text{m}^2$ single mode 7 mm waveguide at a wavelength of 660 nm was written inside silver containing glasses exhibiting a Δn of 2.5×10^{-3} , while showing upper bound propagation losses of 1.2 dB/cm at 660 nm. The photo-induced *type A* Δn could reach a maximum value of around 8×10^{-3} , which is fairly comparable to what is achieved with the *type I* modification. Based on *type A* modification, several optical components were written inside silver containing zinc phosphate glasses (exhibiting dimensions not longer than 1 cm): a 50-50 Y beam splitter dividing light equally into two output branches, optical couplers showing typical coupling behaviour, as well as a perfect 50-50 coupler operating at a wavelength of 660 nm.

In addition, it was found that wisely tuning the laser writing regime could trigger either *type A* or *type I* modifications in silver containing glasses. Writing using a 250 kHz laser with μJ pulses (thermal regime in this case) induces a thermal effect and a change in the glass matrix itself corresponding to an intrinsic type of modification compared to an athermal regime using a 9.8 MHz laser and nJ pulses where the type of modification is purely based on the aggregation of the silver ions Ag^+ pre-existing in the glass matrix. A comparison between the two types shows that the *type I* exhibits a noticeable thermal affected zone, exhibiting a positive region that is surrounded by a negative one acting as a cladding while the guiding process occurs in the positive region (circular mode profile $4.5 \times 5.2 \mu\text{m}^2$ due to the circular beam shaping). *Type A* modification showed smaller waveguides with no presence of an affected thermal zone with an elliptical mode profile of $3 \times 5.5 \mu\text{m}^2$. The photo-induced *type A* modification is always a positive one, which was not the

case for *type I* modification that flips its sign as a function of the laser parameters and the glass composition. This makes DLW of optical waveguides in zinc phosphate glasses more complicated. Furthermore, it was found that the *type A* modification occurs well before the *type I* modification on the pulse energy scale putting the *type A* modification in the region of the low pulse energy regime.

Taking advantage of the low pulse energy regime, near-surface and on surface waveguides were written in silver containing zinc phosphate glass for the first time with no special needs such as reinforced glass or any compensation methods. Based on near-surface waveguides, an RI sensor was created that could exhibit a double resonance presenting the opportunity to create two sensing regions when the waveguide is around 1 μm from the surface. A new improved theoretical method was also introduced that fits the experimental results and was able to simulate the behaviour of the double resonances for the first time. It is based on the mode shape confinement when it reaches the glass-outer medium interface as a function of the RI of the different oils, as well as the Fresnel reflection coefficients. Finally, a 1 cm highly sensitive RI sensor (80% - 7 dB transmission drop for a 5 mm oil droplet) operating in the region of $1 \rightarrow 1.632$ refractive index was created based on *type A*. It exhibited the highest reported sensitivity for a DLW RI sensor and possible double sensing regions, which paves the way towards more integrated sensors in silver containing glasses.

Finally, this project fulfilled expectations by producing the first waveguides that are based on the creation of silver clusters in silver containing glasses, paving the way towards a new type of optical circuits in bulks and fibers while exhibiting exotic properties not accessible using the standard *type I* modification, such as fluorescence, non-linearity, development of nanoparticles with plasmonic responses as well as writing near-surface waveguides with no need for any additional processing.

Perspectives

Many perspectives arise from such interesting work and a lot of work is required such as transposing the RI sensor into a ribbon shaped silver containing fiber. The only difficulty that one could face for this work is having a really flat top surface of the fiber (± 500 nm) in order to write a near-surface waveguide without problems. For instance, aviation companies demand a technology to detect the level of fuel in airplane fuel tanks. Writing such near-surface waveguides in silver containing ribbon shaped fibers could be one solution to be able to detect in real time the level of fuel in airplane fuel tanks.

Moreover, given that the *type A* modification exhibits a smooth quality and sub-wavelength spatial resolution, this could be used for the creation of WBGs in the visible range. It could be performed either by modulating the laser beam to create a modulation of the Δn , or by writing a waveguide and then overlapping gratings on top of it. This part was performed during the PhD project but not yet characterized.

One perspective that could be a very important and interesting one is studying the opto-optical effect.

- **Opto-Optical effect**

The photo-induced silver clusters exhibit two main absorption bands in the UV-visible range, as shown in Figure II.24 while emitting fluorescence in the visible range. An approach tested during the project was to monitor the behaviour of the refractive index change when exciting the silver clusters under UV light. A change in the refractive index could occur due to the populated excited states of the clusters. The term opto-optical is based on the principle of changing the behaviour of light using light like, for example, the electro-optical effect where light is modulated using electrical signals. Herein, we tried to modulate light using light itself, therefore the term opto-optical effect.

A 405 nm diode laser was added to the SID4Bio wave front sensor setup to excite the silver clusters from the bottom as shown in Figure A.b. In addition, a 405 nm notch filter was introduced in the microscope to eliminate the light coming from the blue diode into the CCD camera.

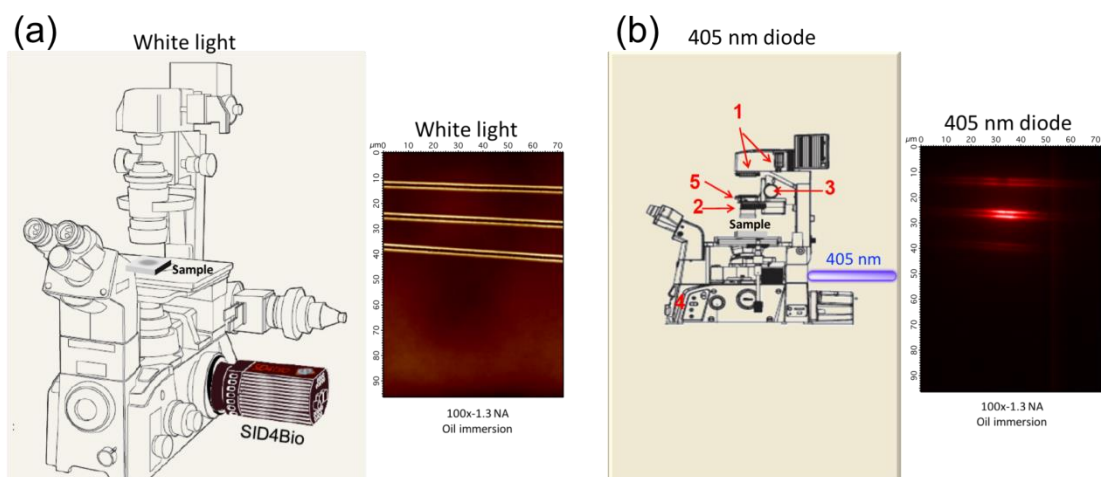


Figure A: The SiD4bio wavefront sensor mounted on a microscope operating (a) in white light illumination and providing top view phase image; (b) under blue (405 nm) illumination and providing top view local excited fluorescence image.

The experiment was conducted as follows. A normal phase image is acquired for the photo-induced structures, as shown in Figure B.a using white light illumination. Then the blue diode is turned on to excite a specific part of the structures simultaneously with the white light illumination, as shown in Figure B.b. Following that, the white light illumination is turned off and a picture of the fluorescence is acquired to precisely localize the excited zone Figure B.c. One notes that in that case, the CCD acquisition time was highly increased (10 times more) in order to acquire the fluorescence image.

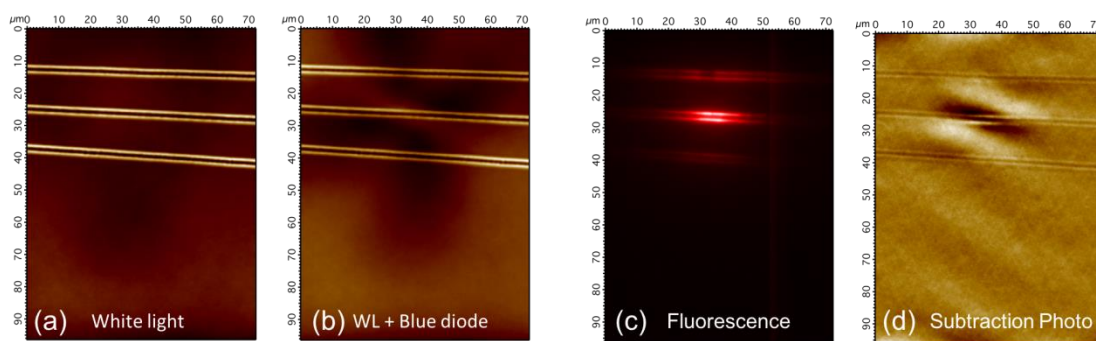


Figure B: Top view phase image under (a) white light illumination; (b) white light and blue light illumination simultaneously; (c) top view fluorescence image indicating the local excited zone by blue light illumination. (d) Subtraction phase image of "a" and "b" revealing a local change in the refractive index change

Then the two-phase images (under white illumination (WL) and under WL + blue light illuminations) were quantitatively subtracted (Figure B.d) in order to reveal if any difference in the optical path difference (OPD) had occurred following the excitation of the silver clusters at 405 nm. In fact, a change of the OPD i.e. the Δn was observed for the regions that were excited using the 405 nm diode. Figure C shows that the differential Δn increase is perfectly spatially correlated to the fluorescence of the excited zone. Those results indicate that, when exciting the silver clusters, a change in the Δn is observed. This paves the way towards very interesting applications such as the creation of dynamic components and optical switches based on the opto-optical effects in such *type A* waveguides, which is not accessible using the *type I* waveguides.

However, those measurements are not conclusive. Some doubts persist on the exactitude of such measurements. Indeed, we are not sure if the observed change in Δn is correlated to the fact that, when exciting the structures using the 405 nm diode, the fluorescence emission and the excited state population are affecting the intensity image on the SID4Bio, therefore affecting the phase image implying a false increase in the Δn or if it is a real change in the Δn . Further efforts are required in order to investigate and reveal the truth behind this feature.

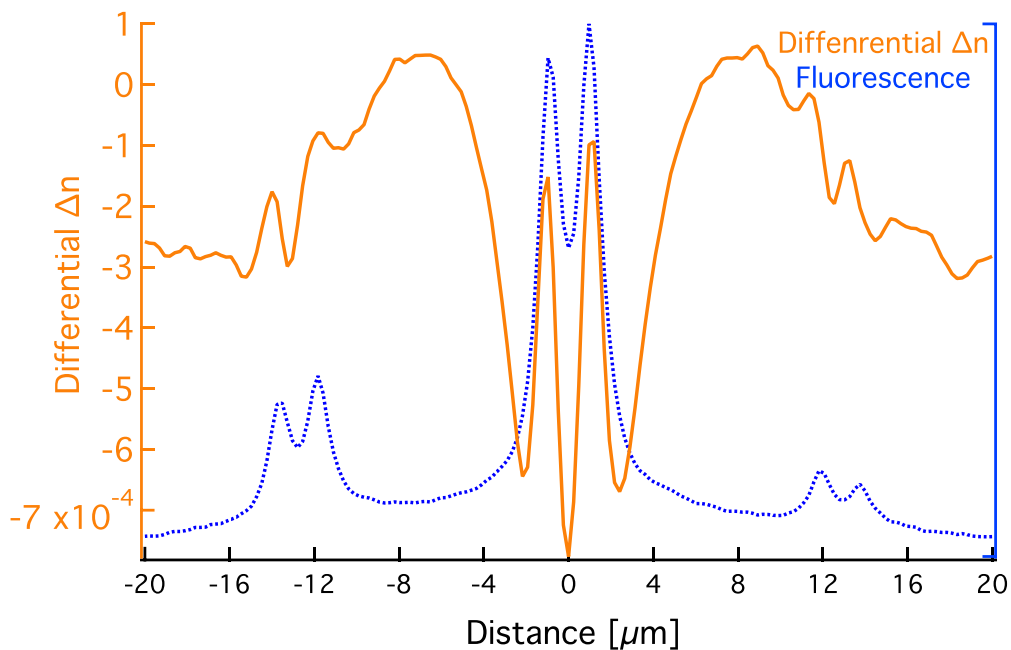


Figure C: Differential refractive index change (Δn) obtained from Figure B.d superposed with the fluorescence intensity line profile obtained from Figure B.c. The differential Δn peaks spatially overlap with the fluorescence peaks indicating that the differential Δn is caused by the excitation of silver clusters under blue light.

Nevertheless, one brilliant idea came to us about creating active Bragg Gratings. It consists in performing the DLW of a *type A* waveguide in silver containing glasses, then, from the top and using a periodic grating, diffracting a 405 nm laser diode with a very specific period and overlapping it with the waveguide to create Bragg gratings, as shown in figure D. When turning on the diode, the Bragg grating is active i.e. the Δn is modulated all along the waveguide based on the opto-optical effect and the waveguide reflects the Bragg wavelength (Figure D.b). However, when the blue diode is turned off, the Bragg gratings disappear (no more modulation of the Δn) and the waveguide acts as a standard waveguide with no specific reflection observed (Figure D.c). The opto-optical effect paves the way for the creation of dynamic optical components and light switches in silver containing glasses but further efforts are required to fully confirm this phenomenon.

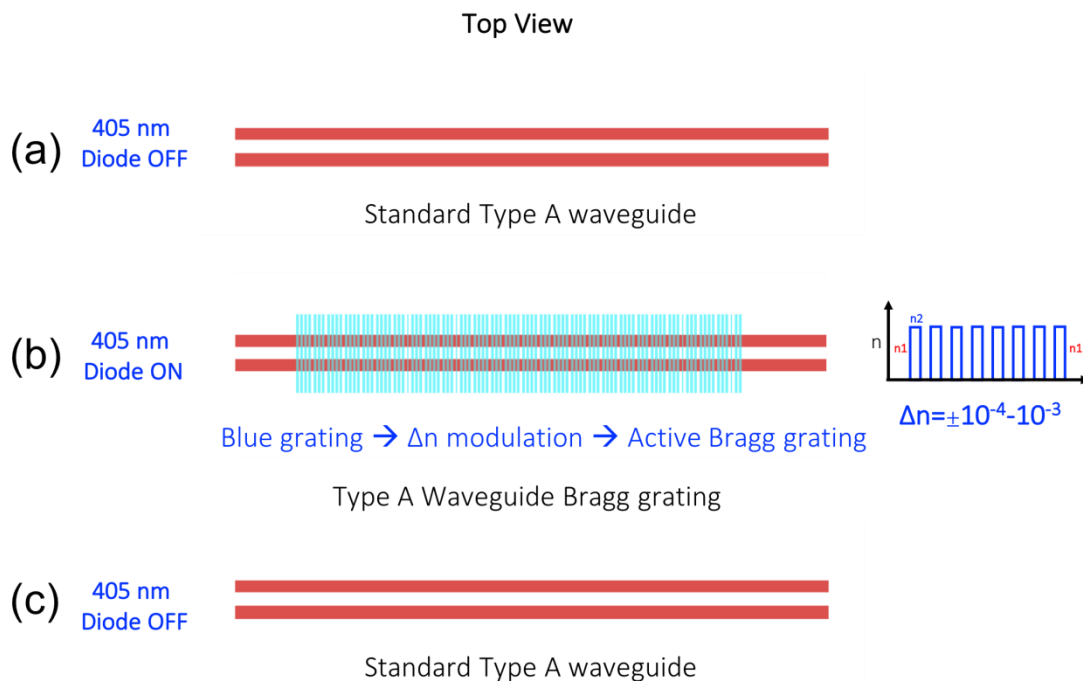


Figure D: (a) Top view of a standard *type A* waveguide exhibiting two lines; (b) using a blue diode and overlapping the grating with the *type A* waveguide to modulate the Δn based on the opto-optical effect and creating a waveguide Bragg grating; (c) turning off the diode induces the disappearance of the grating; therefore, a standard *type A* waveguide.

■ Waveguide laser

Given that under UV-Blue excitation a significant fluorescence intensity in the visible range is emitted by the silver clusters, we tried to create a waveguide laser (WGL) based on the fluorescent emission. A *type A* waveguide was written using DLW in silver containing glasses and was mounted on the transmission setup. A 532 nm laser was injected inside the waveguide simultaneously with a 394 nm laser diode inside the waveguide using a microscope objective (instead of an optical fiber). Given that the fluorescence emission peak is mainly centred in the green region (~ 532 nm), one would expect an amplification of the green laser following excitation of the silver clusters. However, unfortunately this was not the case. Following the injection of a 394 nm laser diode and exciting the silver clusters, a sudden 33% decrease of transmission was observed, as shown in Figure E.a. Moreover, shutting down the blue diode resulted in a slow increase of 33% of the power, going back to the initial transmission (Figure E.b). The fast drop and the slow increase in transmission could be explained by the creation of the triplet excited state of the silver clusters. Once excited to a higher level, they probably exhibit an absorption band at ~ 532 nm which explains the sudden decrease and the slow increase of the waveguide transmission at 532 nm after turning off the diode. As a first approach, the following results may kill the idea of making a WGL in silver containing zinc phosphate glasses.

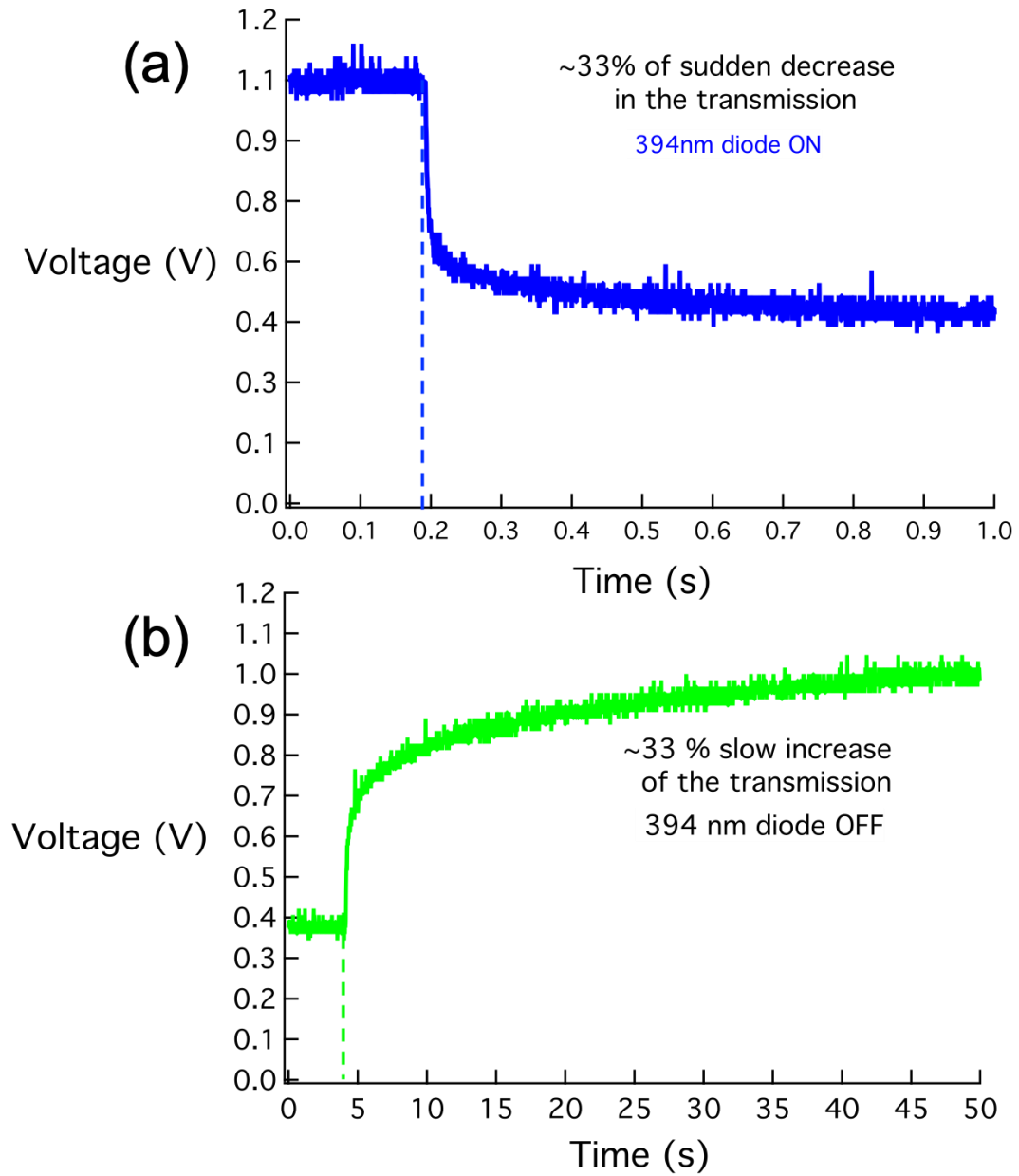


Figure E: (a) Sudden decrease of 33% in the waveguide transmission following the simultaneous injection of 394 nm with the 532 nm laser. The dashed line indicates the moment the blue diode was turned on. (b) Slow increase of the waveguide transmission when the 394 nm laser is turned off once it reaches its initial value. The dashed line indicates the moment the blue diode was turned off.

Appendix

A. List of communications

A.1. Scientific papers

- Photowritable Silver-Containing Phosphate Glass Ribbon Fibers
*S.Danto, F. Désévéday, Y. Petit, J.-C.Desmoulin, **A. Abou Khalil**, C. Strutyński, M. Dussauze, F. Smektala, T. Cardinal, L. Canioni*
Advanced Optical Materials, 2016. **4**(1): p. 162-168
- Direct Laser writing of new type of waveguides in silver containing glasses
***A. Abou Khalil**, J.P Bérubé, J.C Desmoulin, S.Danto, T. Cardinal, Y. Petit, R. Vallée and Lionel Canioni.*
Scientific Reports, 2017. **7**(1): p. 11124
- [Review] On the femtosecond laser-induced photochemistry in silver-containing oxide glasses: mechanisms, related optical and physico-chemical properties, and technological applications
*Y. Petit, S. Danto, T. Guérineau, **A. Abou Khalil**, A. Le Camus, E. Fargin,¹ G. Duchateau, J.-P. Bérubé, R. Vallée, Y. Messaddeq, T. Cardinal and L. Canioni*
Advanced Optical technologies
- Comparative study between the Type A and the type I photo-induced modification in silver containing glasses
Ongoing process
- Direct laser writing of near surface waveguides with no additional processing
Ongoing process

A.2. National and international conferences

- Direct laser writing of waveguides in photosensitive zinc phosphate glass
***A. Abou Khalil**, L. Canioni, Y. Petit and R. Vallée*
IONS QUEBEC 2016
*Québec city, Quebec, Canada, 20 - 22 May 2016 – **Oral***
- Inscription d'un guide d'onde dans des verres de phosphate de zinc à l'argent
***A. Abou Khalil**, J.-C. Desmoulin, S. Danto, T. Cardinal, Y. Petit, T. Cardinal, R.Vallée, L. Canioni*
Journée du COPL
*Québec city, Québec, Canada – May 2016 - **Poster***

- Inscription de guides d'onde par irradiation laser femtoseconde dans des verres de phosphate de zinc à l'argent
A. Abou Khalil, J.-P. Bérubé, J.-C. Desmoulin, T. Cardinal, Y. Petit, R. Vallée, L. Canioni
Optique Bordeaux – HORIZON 2016
Bordeaux, France, 04-07 July 2016 - **Poster**
- Fibres ruban de zinc-phosphate-argent photo-inscriptibles
S. Danto, F. Désévéday, Y. Petit, J.-C. Desmoulin, A. Abou Khalil, C. Strutynski, M. Dussauze, F. Smektala, T. Cardinal, L. Canioni
Optique Bordeaux – Journées Nationales de l'Optique Guidée (JNOG 2016)
Bordeaux, France, 04-07 July 2016 – **Oral**
- **[Invited]** Direct Laser Writing and microstructuring of silver-doped phosphate glasses for optical functionalities
T. Cardinal, J.C. Desmoulin, S. Danto, A. Abou-khalil, Y. Petit, Y. Ledemi, L. Canioni, Y. Messaddeq, M. Dussauze, V. Rodriguez, R. Vallée
BMIC Inorganic Chemistry and XVII Brazilian Meeting on Rare Earths) Sao Pedro, Brazil, 25-30 September 2016 - Oral
- Photo-writable Silver-containing Phosphate Glass Ribbon Fibers
S. Danto, F. Désévéday, Y. Petit, J.-C. Desmoulin, A. Abou Khalil, C. Strutynski, M. Dussauze, F. Smektala, T. Cardinal, L. Canioni
PHAROS Event, (Best Paper Award)
Bordeaux, France, 24-26 October 2016 – **Oral**
- Photo-writable Silver-containing Phosphate Glass Ribbon Fibers
S. Danto, F. Désévéday, Y. Petit, J.-C. Desmoulin, A. Abou Khalil, C. Strutynski, M. Dussauze, F. Smektala, T. Cardinal, L. Canioni
GDR Journées Verres
Bordeaux, France, 17-18 November 2016 – **Poster**
- New type of waveguides in silver containing zinc phosphate glasses by femtosecond laser writing
A. Abou Khalil, J.-P. Bérubé, S. Danto, J.-C. Desmoulin, T. Cardinal, Y. Petit, L. Canioni, and R. Vallée
SPIE – Photonics West
San Francisco, California, USA, 28 January – 02th February 2017-**Oral**

- Femtosecond laser writing of new type of waveguides in silver containing glasses
A. Abou Khalil, J.-P. Bérubé, S. Danto, J.-C. Desmoulin, T. Cardinal, Y. Petit, L. Canioni, and R. Vallée
 Symposium LIA-LUMAQ
 Bordeaux, France, 29-31 March 2017- **Oral**
- Intermediate-Tg-glasses for hybrid/composite fiber devices: recent advances and new prospects
 S. Danto, C. Strutynski, F. Désévéday, Y. Petit, J.-C. Desmoulin, **A. Abou Khalil**, M. Dussauze, J.-C. Jules, G. Gadret, F. Smektala, L. Canioni, T. Cardinal
 Material Research Society - MRS2017 (Spring meeting)
 Phoenix, Arizona, USA, 17-21 April 2017 - **Oral**
- Intermediate-Tg Phosphate and Tellurite Glasses For Multi-materials Fiber Devices
 S. Danto, C. Strutynski, F. Désévéday, Y. Petit, J.-C. Desmoulin, **A. Abou Khalil**, M. Dussauze, J.-C. Jules, G. Gadret, F. Smektala, L. Canioni, T. Cardinal
 Fibers Society
 Aachen, Germany, 17-19 May 2017 - **Oral**
- Direct laser writing of novel type of waveguides in silver containing zinc phosphate glasses
A. Abou Khalil, J.-P. Bérubé, S. Danto, J.-C. Desmoulin, T. Cardinal, Y. Petit, R. Vallée and L. Canioni
 International Conference for Professionals & Young Scientists - Low Temperature Physics (ICPYS-LTP2017)
 Kharkiv, Ukraine, 29 May - 2 June 2017 - **Oral**
- Nouveau type de variation d'indice de réfraction par inscription laser femto dans les verres à l'argent
A. Abou Khalil, J.-P. Bérubé, S. Danto, J.-C. Desmoulin, T. Cardinal, Y. Petit, R. Vallée et Lionel Canioni
 Journées Nationales d'Optique Guidée (JNOG2017)
 Limoges, France, 4-6 July 2017 - **Poster**
- Comparative study between the novel type A and the standard type I photo-induced refractive index change in silver containing zinc phosphate glasses
A. Abou Khalil, J.-P. Bérubé, S. Danto, T. Cardinal, Y. Petit, L. Canioni, and R. Vallée
 SPIE - Photonics West
 San Francisco, California, USA- 27 January - 1 February 2018 - **Oral**
- Intermediate-Tg glasses for multimaterial fibers

*Sylvain Danto, C. Strutynski, F. Désévéday, Y. Petit, J-C. Desmoulin, **A. Abou Khalil**, M. Dussauze, J-C. Jules, G. Gadret, F. Smektala, L. Canioni, T. Cardinal*
SPIE Photonics Europe
Strasbourg, France, 22-26 April 2018 – **Oral**

- Progress in femtosecond laser structuring of silver containing glasses: a review
*L. Canioni, Y. Petit, **A. Abou Khalil**, A. Le Camus, S. Danto and T. Cardinal, R. Vallée*
Progress in Ultrafast Laser Modifications of Materials (PULMM – 3rd edition)
*Telluride, Colorado, USA, June 13th – 16th, 2018- **Oral***
- **[Invited]** Multi-scaled architected materials: from vortex-induced to dual color laser structuring in silver-containing (non-)oxide glasses
*Y. Petit, **A. Abou Khalil**, A. Le Camus, S. Danto, T. Skopak, J.-C. Desmoulin, E.-J. Lee, K. Mischik, T. Cardinal, L. Canioni, J.-P. Bérubé, S.H. Messaddeq, Y. Messaddeq, R. Vallée*
ISNOG
Québec city, Canada, 17-21 June 2018
- Intermediate-Tg glasses for multi-materials fibers
*S. Danto, C. Strutynski, F. Désévéday, Y. Petit, **A. Abou Khalil**, M. Dussauze, J-C. Jules, G. Gadret, F. Smektala, L. Canioni, T. Cardinal*
ISNOG
Québec city, Canada, 17-21 June 2018
- DLW of silver containing phosphate glass and fiber
*Thierry Cardinal, Theo Guerineau, **Alain Abou Khalil**, Sylvain Danto; Jean Philippe Bérubé, Yannick Petit, Clement Strutynski, Marc Dussauze, Lionel Canioni, Real Vallee*
Advanced Photonics 2018 Congress
*ETH Zurich Swiss, 2-5 July 2018 – **Oral***
- Development of silver and rare-earth doped phosphate glasses for fiber Laser applications
*C. Strutynski, S. Danto, **A. Abou Khalil**, Y. Petit, L. Canioni, T. Cardinal*
PNCS-ESG
*Saint-Malo, France, 9-13 July 2018 - **Oral***
- The impact of the silver-containing phosphate glass composition on femtosecond laser induced optical properties
*T. Guérineau, C. Strutynski, S. Danto, M. Dussauze, L. Canioni, R. Vallée, **A. Abou Khalil**, Y. Petit, T. Cardinal*
PNCS-ESG

*Saint-Malo, France, 9-13 July 2018 - **Oral***

- Intermediate-Tg glasses for multi-materials fibers
*S. Danto, C. Strutynski, F. Désévéday, Y. Petit, **A. Abou Khalil**, M. Dussauze, J-C. Jules, G. Gadret, F. Smektala, L. Canioni, T. Cardinal*
PNCS-ESG

*Saint-Malo, France, 9-13 July 2018 - **Oral***

- Highly luminescent microstructures tailored by direct laser writing (DLW) technique in silver containing fluorophosphate glass: application in 3D waveguide and second harmonic generation (SHG)

*T. de Castro, **A. Abou Khalil**, H. Fares, J.-C. Desmoulin, S. Rouzet, C. Strutynski, Y. Petit, S. Danto, V. Jubera, L. Canioni, M. Nalin, S. J. L. Ribeiro, & T. Cardinal*

8th International Conference on Optical, Optoelectronic and Photonic Materials and Applications (ICOOPMA 2018)

*Maresias-SP, Brazil, 26-28 August 2018 - **Oral***

- Direct Laser writing of near-surface waveguides in silver containing glasses with no additional processing

A. Abou Khalil, J.P Bérubé, S. Danto, T. Cardinal, Y. Petit, R. Vallée and Lionel Canioni

SPIE – Photonics West

*San Francisco, California, USA- 2 January – 7 February 2019 - **Oral** (Upcoming)*

- Photonic functionalities with a new type of waveguides sustained by femtosecond laser inscribed fluorescent silver clusters in prepared glasses: From directional couplers to waveguide Bragg gratings

*Y. Petit, **A. Abou Khalil**, J.P Bérubé, S. Danto, T. Cardinal, R. Vallée and Lionel Canoni*

SPIE – Photonics West

*San Francisco, California, USA- 2 January – 7 February 2019 - **Oral** (Upcoming)*

A.3. Comparative study of different commercial techniques for Δn measurement.

This study compares three different commercially available techniques that could be used to measure the Δn photo-induced in glasses following DLW. The work compared the Quadri-wave lateral shearing interferometry (QWLSI), which refers to the SID4bio wavefront sensor used during my PhD, the digital holographic microscopy (DHM), and the last technique, which is the transport intensity equation (TIE). The DHM technique is based on a Mach-Zehnder interferometer. It is a fully integrated system in a microscope where a built-in 666 nm laser beam is divided

into two paths, one forming the object wave and the other forming the reference wave. The object wave diffracted from the sample interferes with the reference wave forming a hologram recorded by a digital camera [156]. After signal processing and reconstruction, the output of the system is somehow similar to the SID4bio: an intensity image and a phase image. More detail about the system can be found in the following reference [156]. The TIE method consisted in capturing the phase image based on several bright-field intensity images taken on both sides of the focus plane of the object [201]. Then, the phase image is obtained based on a Taylor series expansion from the bright-field intensity images [58]. The QWLSI and DHM methods are fast methods consisting in placing the sample on the microscope and imaging it in order to get the phase image. However, the TIE method consisted in taking many intensity images while defocusing in both positive and negative directions from the focus plane then feeding the images to the software in order to determine the OPD which consumes a huge amount of time compared to the first two techniques.

The comparison of those three methods was based on measuring a well-known optical fiber, which is an SMF28 fiber with a 125 μm cladding, 8.2 μm germanium doped core exhibiting a $\Delta n = 5.2 \times 10^{-3}$ [202]. The three methods managed more or less to converge to the same Δn value and profile, as shown in figure F. It was surprising to notice a small dip ~ 600 nm of Δn in the core that was not observed before. The following study proves that the three existing techniques are accurate, and reliable for measuring Δn modification in a fast non-destructive way [202]. For further details, the reader is referred to the following reference [202].

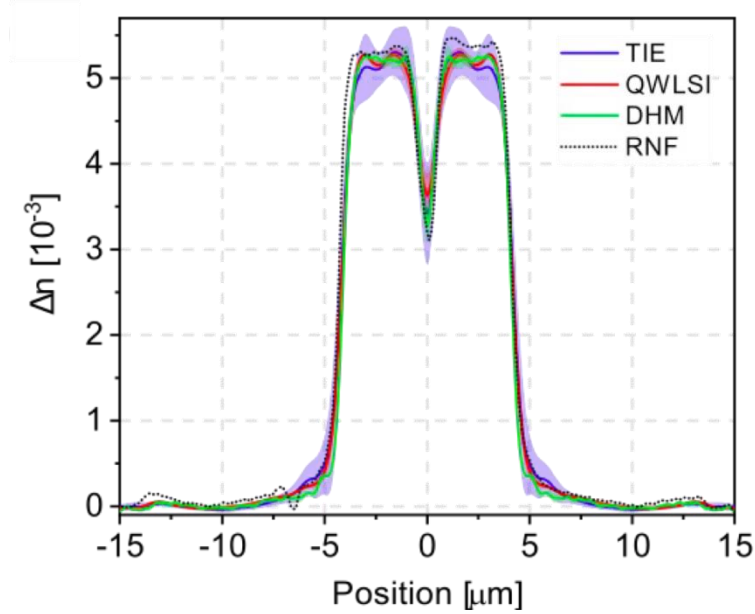


Figure F: The measured Δn profile using the four methods, (blue) TIE, (red) QWLSI/SID4Bio, (green) DHM and dashed lined RNF. All methods converge to the same Δn profile and value. Taken from [202].

A.4. Calculating the laser fluence, irradiance and energy deposited per voxel (Chapter III)

The average power, after the microscope objective was used, was measured for all parameters used for DLW for both lasers, the T-pulse and the Ti:Sapphire laser. Then, the pulse energy was extracted using the following equation:

$$E_p = \frac{P_{avg}}{T} \quad (A-1)$$

where P_{avg} is the averaged power measured after the microscope objective and T is the repetition rate of the laser used.

Then the laser fluence (J/cm^2) is calculated using the following equation:

$$F = \frac{E_p}{\pi w_0^2} \quad (A-2)$$

Where E_p is the pulse energy and w_0 is the waist calculated using (I-21) or (I-22) depending on the NA of the objective.

The laser irradiance in this case or laser intensity (TW/cm²) is calculated as a function of the spot size, the laser repetition rate and the pulse duration using (I-23).

The deposited energy was calculated using equations extracted from the PhD manuscript of Gautier Papon [203] where the deposited energy is given by:

$$E_D = \alpha^{(4)} 9 T \pi \left(\frac{w_{NL}}{3} \right)^2 I^4 \frac{3}{4} z_{NL} \quad (\text{A-3})$$

Where $\alpha^{(4)} = 14.6 \pm 1 \times 10^{-3} \text{ cm}^5 / \text{TW}^3$ is the coefficient absorption corresponding to the four photon process; T is the laser repetition rate with $w_{NL} = \frac{w_0}{\sqrt{N}}$ and $z_{NL} = \frac{z_r}{\sqrt{N}}$ the non-linear waist and Rayleigh length with $N=4$ corresponding to a four photon absorption effect, and I the laser irradiance.

The deposited energy calculated for parameters used for *type I* modification exceeded the energy of the pulse which is not normal. The formula used in that case is not fully compatible when using high pulse energies. Therefore the energy deposited was limited to 1 μJ . Finally, those calculations are only approximate to show the large difference between the two laser parameters used.

And the energy deposited by voxel/laser dose is obtained by dividing the last term (the deposited energy) by the volume of the voxel:

$$Q_0 = \frac{E_D}{\pi^{3/2} w_{NL}^2 z_{NL}} \quad (\text{A-4})$$

From the laser energy deposited by voxel, one can calculate the highest temperature difference that occurs in one point induced by one laser pulse as given by:

$$\Delta T = \frac{Q_0}{\rho C_p} \quad (\text{A-5})$$

Where ρ is the molar density of the glass and C_p the heat capacity.

A.5. Theoretical model of the refractive index sensor (chapter Chapter IV)

The new theoretical model proposed during this work is divided into two parts. The first part is where the refractive index (RI) of the oil is lower than the RI of the glass ($n_{oil} < n_{glass}$). For this first part, the model is based on the spatial distribution of the mode when reaching the glass-oil medium. With a big difference in the refractive index change between the glass and the outer medium, which could be the air or the deposited oil droplets, the spatial distribution of the mode could change drastically, as shown in Figure IV.21. Therefore, the first part was simulated using Lumerical Mode solutions. Waveguides neighbouring the surface to 1 μm and 3.5 μm were simulated while changing the RI of the outer medium from 1 to 1.602. Then, the mode spatial distribution was overlapped with the normal standard mode which is totally embedded inside the glass. It measures the fraction of electromagnetic fields that overlap between the distorted mode and the normal mode. It is also the fraction of power from the distorted mode that could propagate inside the normal mode. The power overlap was simulated using the following equation:

$$\eta = \frac{\left| \int_{-\infty}^{+\infty} E_{norm} E_{disto} \right|^2}{\left| \int_{-\infty}^{+\infty} E_{norm} \right|^2 \left| \int_{-\infty}^{+\infty} E_{disto} \right|^2} \quad (\text{A-6})$$

where E_{norm} is the electric field of the normal mode and E_{disto} the electric field of the distorted mode. In that case, only the electric field was taken into consideration without the magnetic fields.

In the second region where the RI of the oil matches the RI of the waveguide ($n_{oil} \sim n_{waveguide}$), (more specifically it tends to match the effective refractive index of the propagating mode in the fiber), a theoretical drop to 0% should occur. That is why in our model, the transmission drops to 0 at a RI of 1.604. The reason why the experimental transmission does not drop to 0% is explained above in Chapter IV.

The third region of the theoretical model is where the RI of the oil is higher than the RI of the glass ($n_{oil} > n_{glass}$). The simulations were based on the Fresnel Reflection coefficient for a TE mode and fitted to the experimental results using the following equations (similar to the previous suggested models):

$$R = \frac{n_{glass} \cos \theta_1 - n_2 \sqrt{1 - \left(\frac{n_{glass} \sin \theta_1}{n_{oil}}\right)^2}}{n_{glass} \cos \theta_1 + n_2 \sqrt{1 - \left(\frac{n_{glass} \sin \theta_1}{n_{oil}}\right)^2}} \quad (\text{A-7})$$

$$T = (1 - R^2)^n \quad (\text{A-8})$$

References:

1. Zarzycki, J., *Glasses and Amorphous Materials*. Vol. 9. 1991.
2. Elliot, S.R., *Physics of amorphous materials*. 1990: Harlow, Essex, England : Longman Scientific & Technical ; New York : J. Wiley, ©1990.
3. Varshneya, A., *Fundamentals of Inorganic Glasses*. 1994.
4. Schubert, U., *Introduction to glass science and technology*. Von J. E. Shelby. Royal Society of Chemistry, Cambridge, 1997. 244 S., Broschur, 18.95 £.—ISBN 0-85404-533-3. *Angewandte Chemie*, 1997. **109**(22): p. 2637-2637.
5. Zachariasen, W.H., *THE ATOMIC ARRANGEMENT IN GLASS*. *Journal of the American Chemical Society*, 1932. **54**(10): p. 3841-3851.
6. Grest, G.S. and M.H. Cohen, *Liquids, Glasses, and the Glass Transition: A Free-Volume Approach*, in *Advances in Chemical Physics*. 2007, John Wiley & Sons, Inc. p. 455-525.
7. Gibbs, J.H. and E.A. DiMarzio, *Nature of the Glass Transition and the Glassy State*. *The Journal of Chemical Physics*, 1958. **28**(3): p. 373-383.
8. Stillinger, F.H., *Supercooled liquids, glass transitions, and the Kauzmann paradox*. *The Journal of Chemical Physics*, 1988. **88**(12): p. 7818-7825.
9. Messaddeq, Y., *Le verre : principes théoriques et applications*, U. Laval, Editor.
10. Badrinarayanan, P., et al., *The glass transition temperature versus the fictive temperature*. *Journal of Non-Crystalline Solids*, 2007. **353**(26): p. 2603-2612.
11. Bourhis, K., *Photostructuration par laser infrarouge femtoseconde de verres photosensible de phosphate de zinc, d'argent et de gallium*. 2011, Université de Bordeaux.
12. Goldschmidt, V.M., *Die Gesetze der Krystallochemie*. *Naturwissenschaften*, 1926. **14**(21): p. 477-485.
13. Smekal, A. and W. Klemm, *Mechanische Messung chemischer Bindefestigkeiten*. *Monatshefte für Chemie und verwandte Teile anderer Wissenschaften*, 1951. **82**(3): p. 411-421.
14. Sun, K.H., *FUNDAMENTAL CONDITION OF GLASS FORMATION**. *Journal of the American Ceramic Society*, 1947. **30**(9): p. 277-281.
15. Shelby, J.E., *Introduction to Glass Science and Technology*. 2005: Royal Society of Chemistry.
16. Savage, J.A. and S. Nielsen, *Chalcogenide glasses transmitting in the infrared between 1 and 20 μ — a state of the art review*. *Infrared Physics*, 1965. **5**(4): p. 195-204.
17. Hooker, S. and C. Webb, *Laser Physics*. 2010

18. Abbott, B.P., et al., *Observation of Gravitational Waves from a Binary Black Hole Merger*. Phys Rev Lett, 2016. **116**(6): p. 061102.
19. Gordon, J.P., H.J. Zeiger, and C.H. Townes, *Molecular Microwave Oscillator and New Hyperfine Structure in the Microwave Spectrum of $N\{\mathrm{H}\}_3$* . Physical Review, 1954. **95**(1): p. 282-284.
20. Schawlow, A.L. and C.H. Townes, *Infrared and Optical Masers*. Physical Review, 1958. **112**(6): p. 1940-1949.
21. Maiman, T.H., *Stimulated Optical Emission in Fluorescent Solids. I. Theoretical Considerations*. Physical Review, 1961. **123**(4): p. 1145-1150.
22. Javan, A., W.R. Bennett, and D.R. Herriott, *Population Inversion and Continuous Optical Maser Oscillation in a Gas Discharge Containing a He-Ne Mixture*. Physical Review Letters, 1961. **6**(3): p. 106-110.
23. Littman, M.G. and H.J. Metcalf, *Spectrally narrow pulsed dye laser without beam expander*. Applied Optics, 1978. **17**(14): p. 2224-2227.
24. Hall, R.N., et al., *Coherent Light Emission From GaAs Junctions*. Physical Review Letters, 1962. **9**(9): p. 366-368.
25. Heard, H.G., *Ultra-violet Gas Laser at Room Temperature*. Nature, 1963. **200**: p. 667.
26. Fortin, V., et al., *Fluoride glass Raman fiber laser at 2185 nm*. Optics Letters, 2011. **36**(21): p. 4152-4154.
27. Emma, P., et al., *First lasing and operation of an ångstrom-wavelength free-electron laser*. Nature Photonics, 2010. **4**: p. 641.
28. Rocca, J.J., et al., *Demonstration of a Discharge Pumped Table-Top Soft-X-Ray Laser*. Physical Review Letters, 1994. **73**(16): p. 2192-2195.
29. Svelto, O., *Principles of Lasers*. fifth edition ed.: Springer, Boston, MA.
30. Bernier, M., et al., *3.77 μm fiber laser based on cascaded Raman gain in a chalcogenide glass fiber*. Opt Lett, 2014. **39**(7): p. 2052-5.
31. Sillfvast, W.T., *Laser Fundamentals*. Second ed. 2008.
32. Bhowmik, A. and A.E. Siegman, *Defining, measuring, and optimizing laser beam quality*. 1993. **1868**: p. 2-12.
33. Royon, A., et al., *Femtosecond laser induced photochemistry in materials tailored with photosensitive agents [Invited]*. Optical Materials Express, 2011. **1**(5): p. 866-882.
34. Chris, B.S., B. André, and M. Eric, *Laser-induced breakdown and damage in bulk transparent materials induced by tightly focused femtosecond laser pulses*. Measurement Science and Technology, 2001. **12**(11): p. 1784.
35. Bérubé, J.-P., *Étude des changements structuraux photo-induits dans le verre à l'aide des impulsions femtosecondes et application à l'inscription de composants photoniques*. 2014, Université Laval.

36. Stuart, B.C., et al., *Laser-induced damage in dielectrics with nanosecond to subpicosecond pulses*. Phys Rev Lett, 1995. **74**(12): p. 2248-2251.
37. Lenzner, M., et al., *Femtosecond Optical Breakdown in Dielectrics*. Physical Review Letters, 1998. **80**(18): p. 4076-4079.
38. V, K.L., *Concerning the theory impact ionization in semiconductors* Zh. Eksp. Teor. Fiz. 47 1945 (Engl. transl.Sov. Phys.–JETP 20 1307 (1965)), 1964.
39. Stuart, B.C., et al., *Nanosecond-to-femtosecond laser-induced breakdown in dielectrics*. Physical Review B, 1996. **53**(4): p. 1749-1761.
40. Gaier *, L.N., et al., *Hole-assisted energy deposition in dielectrics and clusters in the multiphoton regime*. Journal of Modern Optics, 2005. **52**(7): p. 1019-1030.
41. gamaly, E., *Femtosecond laser-matter interactions*. 2011.
42. Chichkov, B.N., et al., *Femtosecond, picosecond and nanosecond laser ablation of solids*. Applied Physics A, 1996. **63**(2): p. 109-115.
43. Couairon, A., et al., *Filamentation and damage in fused silica induced by tightly focused femtosecond laser pulses*. Physical Review B, 2005. **71**(12).
44. Bellec, M., et al., *3D Patterning at the Nanoscale of Fluorescent Emitters in Glass*. The Journal of Physical Chemistry C, 2010. **114**(37): p. 15584-15588.
45. Hernandez-Rueda, J., et al., *The influence of femtosecond laser wavelength on waveguide fabrication inside fused silica*. Applied Physics Letters, 2017. **110**(16): p. 161109.
46. Schaffer, C.B., J.F. García, and E. Mazur, *Bulk heating of transparent materials using a high-repetition-rate femtosecond laser*. Applied Physics A, 2003. **76**(3): p. 351-354.
47. Eaton, S.M., et al., *Heat accumulation effects in femtosecond laser-written waveguides with variable repetition rate*. Optics Express, 2005. **13**(12): p. 4708-4716.
48. Zhang, H., et al., *Heat accumulation during high repetition rate ultrafast laser interaction: Waveguide writing in borosilicate glass*. Journal of Physics: Conference Series, 2007. **59**: p. 682-686.
49. Gross, S., et al., *Ultrafast Laser Inscription in Soft Glasses: A Comparative Study of Athermal and Thermal Processing Regimes for Guided Wave Optics*. International Journal of Applied Glass Science, 2012. **3**(4): p. 332-348.
50. Stalmashonak, A., H. Graener, and G. Seifert, *Transformation of silver nanospheres embedded in glass to nanodisks using circularly polarized femtosecond pulses*. Applied Physics Letters, 2009. **94**(19): p. 193111.
51. Temnov, V.V., et al., *Multiphoton ionization in dielectrics: comparison of circular and linear polarization*. Phys Rev Lett, 2006. **97**(23): p. 237403.
52. Bhardwaj, V.R., et al., *Optically produced arrays of planar nanostructures inside fused silica*. Phys Rev Lett, 2006. **96**(5): p. 057404.

53. Ams, M., G.D. Marshall, and M.J. Withford, *Study of the influence of femtosecond laser polarisation on direct writing of waveguides*. Optics Express, 2006. **14**(26): p. 13158-13163.
54. Schaffer, C.B., et al., *Micromachining bulk glass by use of femtosecond laser pulses with nanojoule energy*. Optics Letters, 2001. **26**(2): p. 93-95.
55. Ashcom, J.B., et al., *Numerical aperture dependence of damage and supercontinuum generation from femtosecond laser pulses in bulk fused silica*. Journal of the Optical Society of America B, 2006. **23**(11): p. 2317-2322.
56. Davis, K.M., et al., *Writing waveguides in glass with a femtosecond laser*. Optics Letters, 1996. **21**(21): p. 1729-1731.
57. Hirao, K. and K. Miura, *Writing waveguides and gratings in silica and related materials by a femtosecond laser*. Journal of Non-Crystalline Solids, 1998. **239**(1): p. 91-95.
58. Barone - Nugent, E.D., A. Barty, and K.A. Nugent, *Quantitative phase - amplitude microscopy I: optical microscopy*. Journal of Microscopy, 2002. **206**(3): p. 194-203.
59. Osellame, R., et al., *Optical gain in Er-Yb doped waveguides fabricated by femtosecond laser pulses*. Electronics letters, 2002. **38**(17): p. 1.
60. Streltsov, A.M. and N.F. Borrelli, *Study of femtosecond-laser-written waveguides in glasses*. Journal of the Optical Society of America B, 2002. **19**(10): p. 2496-2504.
61. Chan, J.W., et al., *Waveguide fabrication in phosphate glasses using femtosecond laser pulses*. Applied Physics Letters, 2003. **82**(15): p. 2371.
62. Fletcher, L.B., et al., *Direct femtosecond laser waveguide writing inside zinc phosphate glass*. Optics Express, 2011. **19**(9): p. 7929-7936.
63. Ams, M., et al., *Slit beam shaping method for femtosecond laser direct-write fabrication of symmetric waveguides in bulk glasses*. Optics Express, 2005. **13**(15): p. 5676-5681.
64. Poumellec, B., et al., *Modification thresholds in femtosecond laser processing of pure silica: review of dependencies on laser parameters [Invited]*. Optical Materials Express, 2011. **1**(4): p. 766-782.
65. Hnatovsky, C., et al., *Pulse duration dependence of femtosecond-laser-fabricated nanogratings in fused silica*. Applied Physics Letters, 2005. **87**(1): p. 014104.
66. Will, M., et al., *Optical properties of waveguides fabricated in fused silica by femtosecond laser pulses*. Applied Optics, 2002. **41**(21): p. 4360-4364.
67. Osellame, R., et al., *Femtosecond writing of active optical waveguides with astigmatically shaped beams*. Journal of the Optical Society of America B, 2003. **20**(7): p. 1559-1567.
68. Shah, L., et al., *Waveguide writing in fused silica with a femtosecond fiber laser at 522 nm and 1 MHz repetition rate*. Optics Express, 2005. **13**(6): p. 1999-2006.

69. Salter, P.S., et al., *Adaptive slit beam shaping for direct laser written waveguides*. Optics Letters, 2012. **37**(4): p. 470-472.
70. Berube, J.P., et al., *Tailoring the refractive index of Ge-S based glass for 3D embedded waveguides operating in the mid-IR region*. Opt Express, 2014. **22**(21): p. 26103-16.
71. Lapointe, J., et al., *Making smart phones smarter with photonics*. Opt Express, 2014. **22**(13): p. 15473-83.
72. Shimotsuma, Y., et al., *Self-Organized Nanogratings in Glass Irradiated by Ultrashort Light Pulses*. Physical Review Letters, 2003. **91**(24): p. 247405.
73. Richter, S., et al., *Formation of femtosecond laser-induced nanogratings at high repetition rates*. Applied Physics A, 2011. **104**(2): p. 503-507.
74. Liang, F., R. Vallée, and S.L. Chin, *Mechanism of nanograting formation on the surface of fused silica*. Optics Express, 2012. **20**(4): p. 4389-4396.
75. Chan, J.W., et al., *Modification of the fused silica glass network associated with waveguide fabrication using femtosecond laser pulses*. Applied Physics A: Materials Science & Processing, 2003. **76**(3): p. 367-372.
76. Little, D.J., et al., *Mechanism of femtosecond-laser induced refractive index change in phosphate glass under a low repetition-rate regime*. Journal of Applied Physics, 2010. **108**(3): p. 033110.
77. Chan, J.W., et al., *Structural changes in fused silica after exposure to focused femtosecond laser pulses*. Optics Letters, 2001. **26**(21): p. 1726-1728.
78. Dekker, P., et al., *Annealing dynamics of waveguide Bragg gratings: evidence of femtosecond laser induced colour centres*. Optics Express, 2010. **18**(4): p. 3274-3283.
79. Zhao, Q.-Z., et al., *Temperature dependence of femtosecond laser induced refractive index change in Nd³⁺-doped phosphate glass*. Optical Materials, 2005. **27**(6): p. 1159-1162.
80. Little, D.J., et al., *Structural changes in BK7 glass upon exposure to femtosecond laser pulses*. Journal of Raman Spectroscopy, 2011. **42**(4): p. 715-718.
81. Abdel-Baki, M., et al., *Factors affecting optical dispersion in borate glass systems*. Journal of Physics and Chemistry of Solids, 2007. **68**(8): p. 1457-1470.
82. Messaddeq, S., et al., *Light-induced relief gratings and a mechanism of metastable light-induced expansion in chalcogenide glasses*. Physical Review B, 2001. **63**(22): p. 224203.
83. Messaddeq, S.H., et al., *Study of the photosensitivity of GeS binary glasses to 800nm femtosecond pulses*. Optics Express, 2012. **20**(3): p. 2824-2831.
84. Kanehira, S., K. Miura, and K. Hirao, *Ion exchange in glass using femtosecond laser irradiation*. Applied Physics Letters, 2008. **93**(2): p. 023112.
85. Arriola, A., et al., *Low bend loss waveguides enable compact, efficient 3D photonic chips*. Optics Express, 2013. **21**(3): p. 2978-2986.

86. Cerullo, G., et al., *Femtosecond micromachining of symmetric waveguides at 1.5 μm by astigmatic beam focusing*. Optics Letters, 2002. **27**(21): p. 1938-1940.
87. Bérubé, J.-P., et al., *Femtosecond laser direct inscription of mid-IR transmitting waveguides in BGG glasses*. Optical Materials Express, 2017. **7**(9): p. 3124-3135.
88. Mauclair, C., et al., *Ultrafast laser writing of homogeneous longitudinal waveguides in glasses using dynamic wavefront correction*. Optics Express, 2008. **16**(8): p. 5481-5492.
89. Bérubé, J.-P., M. Bernier, and R. Vallée, *Femtosecond laser-induced refractive index modifications in fluoride glass*. Optical Materials Express, 2013. **3**(5): p. 598-611.
90. McMillen, B., et al., *Ultrafast laser fabrication of low-loss waveguides in chalcogenide glass with 0.65 dB/cm loss*. Optics Letters, 2012. **37**(9): p. 1418-1420.
91. Bérubé, J.-P. and R. Vallée, *Femtosecond laser direct inscription of surface skimming waveguides in bulk glass*. Optics Letters, 2016. **41**(13): p. 3074-3077.
92. Nandi, P., et al., *Femtosecond laser written channel waveguides in tellurite glass*. Optics Express, 2006. **14**(25): p. 12145-12150.
93. Osellame, R., et al., *Waveguide lasers in the C-band fabricated by laser inscription with a compact femtosecond oscillator*. IEEE Journal of Selected Topics in Quantum Electronics, 2006. **12**(2): p. 277-285.
94. Ródenas, A., et al., *Three-dimensional mid-infrared photonic circuits in chalcogenide glass*. Optics Letters, 2012. **37**(3): p. 392-394.
95. Tong, L., et al., *Optical loss measurements in femtosecond laser written waveguides in glass*. Optics Communications, 2006. **259**(2): p. 626-630.
96. Lee, H., et al., *Ultra-low-loss optical delay line on a silicon chip*. Nature Communications, 2012. **3**: p. 867.
97. Li, G., et al., *Ultralow-loss, high-density SOI optical waveguide routing for macrochip interconnects*. Optics Express, 2012. **20**(11): p. 12035-12039.
98. Saleh, B.E.A. and M.C. Teich, *Fundamentals of photonics*. 1991: Wiley.
99. Saleh, B.E.A. and M.C. Teich, *Fundamentals of Photonics*. 2007: Wiley.
100. Fletcher, L.B., et al., *Femtosecond laser writing of waveguides in zinc phosphate glasses [Invited]*. Optical Materials Express, 2011. **1**(5): p. 845-855.
101. Bérubé, J.-P., *Étude des changements structuraux photo-induits dans le verre à l'aide des impulsions femtosecondes et application à l'inscription de composants photoniques*, in COPL. 2014, Université Laval.
102. Palmer, G., et al., *High slope efficiency and high refractive index change in direct-written Yb-doped waveguide lasers with depressed claddings*. Opt Express, 2013. **21**(14): p. 17413-20.

103. Lancaster, D.G., et al., *Versatile large-mode-area femtosecond laser-written Tm:ZBLAN glass chip lasers*. Optics Express, 2012. **20**(25): p. 27503-27509.
104. Yariv, A., *Optical Electronics*. 1990: Oxford University Press.
105. Vallée, R., *La fibre Optique*, U. Laval, Editor.
106. Snyder, A.W. and A. Ankiewicz, *Optical fiber couplers-optimum solution for unequal cores*. Journal of Lightwave Technology, 1988. **6**(3): p. 463-474.
107. Buck, J.A., *Fundamental of Optical fibers*. 2nd ed. 2004.
108. Crespi, A., et al., *Integrated photonic quantum gates for polarization qubits*. Nat Commun, 2011. **2**: p. 566.
109. Streltsov, A.M. and N.F. Borrelli, *Fabrication and analysis of a directional coupler written in glass by nanojoule femtosecond laser pulses*. Optics Letters, 2001. **26**(1): p. 42-43.
110. Eaton, S.M., et al., *Telecom-Band Directional Coupler Written With Femtosecond Fiber Laser*. IEEE Photonics Technology Letters, 2006. **18**(20): p. 2174-2176.
111. Kowalevicz, A.M., et al., *Three-dimensional photonic devices fabricated in glass by use of a femtosecond laser oscillator*. Optics Letters, 2005. **30**(9): p. 1060-1062.
112. Homoelle, D., et al., *Infrared photosensitivity in silica glasses exposed to femtosecond laser pulses*. Optics Letters, 1999. **24**(18): p. 1311-1313.
113. Liu, J., et al., *Directly writing of 1-to-N optical waveguide power splitters in fused silica glass using a femtosecond laser*. Optics Communications, 2005. **253**(4): p. 315-319.
114. Nolte, S., et al., *Femtosecond waveguide writing: a new avenue to three-dimensional integrated optics*. Applied Physics A: Materials Science & Processing, 2003. **77**(1): p. 109-111.
115. Marshall, G.D., M. Ams, and M.J. Withford, *Direct laser written waveguide-Bragg gratings in bulk fused silica*. Optics Letters, 2006. **31**(18): p. 2690-2691.
116. Zhang, H., et al., *Type II femtosecond laser writing of Bragg grating waveguides in bulk glass*. Electronics Letters, 2006. **42**(21): p. 1223.
117. Marshall, G.D., et al., *Three-dimensional imaging of direct-written photonic structures*. Optics Letters, 2011. **36**(5): p. 695-697.
118. Ams, M., et al., *Fabricating waveguide Bragg gratings (WBGs) in bulk materials using ultrashort laser pulses*. Nanophotonics, 2017. **6**(5): p. 743-763.
119. Taccheo, S., et al., *Er:Yb-doped waveguide laser fabricated by femtosecond laser pulses*. Optics Letters, 2004. **29**(22): p. 2626-2628.
120. Marshall, G.D., et al., *Directly written monolithic waveguide laser incorporating a distributed feedback waveguide-Bragg grating*. Optics Letters, 2008. **33**(9): p. 956-958.

121. Psaila, N.D., et al., *Er:Yb-Doped Oxyfluoride Silicate Glass Waveguide Laser Fabricated Using Ultrafast Laser Inscription*. IEEE Photonics Technology Letters, 2008. **20**(2): p. 126-128.
122. Sabapathy, T., et al., *Direct ultrafast laser written C-band waveguide amplifier in Er-doped chalcogenide glass*. Optical Materials Express, 2012. **2**(11): p. 1556-1561.
123. Lancaster, D.G., et al., *Fifty percent internal slope efficiency femtosecond direct-written Tm³⁺:ZBLAN waveguide laser*. Optics Letters, 2011. **36**(9): p. 1587-1589.
124. Della Valle, G., R. Osellame, and P. Laporta, *Micromachining of photonic devices by femtosecond laser pulses*. Journal of Optics A: Pure and Applied Optics, 2009. **11**(1): p. 013001.
125. Thomson, R.R., et al., *Ultrafast laser inscription of an integrated photonic lantern*. Optics Express, 2011. **19**(6): p. 5698-5705.
126. Spaleniak, I., et al., *Integrated photonic building blocks for next-generation astronomical instrumentation II: the multimode to single mode transition*. Opt Express, 2013. **21**(22): p. 27197-208.
127. Photonics, M.; Available from: <http://www.modularphotonics.com/>.
128. MESNAOUI, M., et al., *Spectroscopic properties of Ag⁺ ions in phosphate glasses of NaPO₃-AgPO₃ system*. European journal of solid state and inorganic chemistry, 1992. **29**(6): p. 1001-1013.
129. Montagne, L., G. Palavit, and R. Delaval, *Effect of ZnO on the properties of (100-x)(NaPO₃)₃-xZnO glasses*. Journal of non-crystalline solids, 1998. **223**(1): p. 43-47.
130. Inc, C., *Zinc containing phosphate glasses*. 1990: US.
131. Heisterkamp, A., et al., *All-optical characterization of fs-laser induced refractive index changes in bulk and at the surface of zinc phosphate glasses*. 2015. **9355**: p. 935518.
132. Fletcher, L.B., et al., *Effects of rare-earth doping on femtosecond laser waveguide writing in zinc polyphosphate glass*. Journal of Applied Physics, 2012. **112**(2): p. 023109.
133. Ferrer, A., et al., *Deep subsurface optical waveguides produced by direct writing with femtosecond laser pulses in fused silica and phosphate glass*. Applied Surface Science, 2007. **254**(4): p. 1121-1125.
134. Osellame, R., et al., *Lasing in femtosecond laser written optical waveguides*. Applied Physics A, 2008. **93**(1): p. 17-26.
135. Desmoulin, J.-C., *Synthèse et caractérisation de verres d'oxyde d'argent : évolution sous rayonnements ionisants et structuration multi-échelle par laser femtoseconde*. 2016, Université de Bordeaux.
136. Bellec, M., et al., *Beat the diffraction limit in 3D direct laser writing in photosensitive glass*. Optics Express, 2009. **17**(12): p. 10304-10318.

137. Peyser, L.A., et al., *Photoactivated fluorescence from individual silver nanoclusters*. *Science*, 2001. **291**(5501): p. 103-106.
138. Maurel, C., et al., *Luminescence properties of silver zinc phosphate glasses following different irradiations*. *Journal of Luminescence*, 2009. **129**(12): p. 1514-1518.
139. Marquestaut, N., et al., *Three-Dimensional Silver Nanoparticle Formation Using Femtosecond Laser Irradiation in Phosphate Glasses: Analogy with Photography*. *Advanced Functional Materials*, 2014. **24**(37): p. 5824-5832.
140. Smetanina, E., et al., *Modeling of cluster organization in metal-doped oxide glasses irradiated by a train of femtosecond laser pulses*. *Physical Review A*, 2016. **93**(1).
141. Desmoulin, J.-C., et al., *Femtosecond laser structuring of silver-containing glass: Silver redistribution, selective etching, and surface topology engineering*. *Journal of Applied Physics*, 2015. **118**(21): p. 213104.
142. Choi, J., et al., *Three-dimensional direct femtosecond laser writing of second-order nonlinearities in glass*. *Optics Letters*, 2012. **37**(6): p. 1029-1031.
143. Papon, G., et al., *Fluorescence and second-harmonic generation correlative microscopy to probe space charge separation and silver cluster stabilization during direct laser writing in a tailored silver-containing glass*. *Optical Materials Express*, 2013. **3**(11): p. 1855.
144. Papon, G., et al., *Femtosecond single-beam direct laser poling of stable and efficient second-order nonlinear optical properties in glass*. *Journal of Applied Physics*, 2014. **115**(11): p. 113103.
145. Tu, Z., et al., *Micro-modification of luminescence property in Ag⁺-doped phosphate glass using femtosecond laser irradiation*. *Journal of Non-Crystalline Solids*, 2014. **383**: p. 161-164.
146. Vasileva, A.A., et al., *Structural features of silver-doped phosphate glasses in zone of femtosecond laser-induced modification*. *Journal of Solid State Chemistry*, 2015. **230**: p. 56-60.
147. Lipat'ev, A.S., et al., *Formation of Luminescent and Birefringent Microregions in Phosphate Glass Containing Silver*. *Glass and Ceramics*, 2016. **73**(7-8): p. 277-282.
148. Shakhgildyan, G.Y., et al., *One-step micro-modification of optical properties in silver-doped zinc phosphate glasses by femtosecond direct laser writing*. *Journal of Non-Crystalline Solids*, 2018. **481**: p. 634-642.
149. Danto, S., et al., *Photowritable Silver-Containing Phosphate Glass Ribbon Fibers*. *Advanced Optical Materials*, 2016. **4**(1): p. 162-168.
150. Bourhis, K., et al., *Femtosecond laser structuring and optical properties of a silver and zinc phosphate glass*. *Journal of Non-Crystalline Solids*, 2010. **356**(44-49): p. 2658-2665.

151. Grenier, J.R., et al. *Optical Circuits in Fiber Cladding: Femtosecond laser-written Bragg Grating Waveguides*. in *CLEO:2011 - Laser Applications to Photonic Applications*. 2011. Baltimore, Maryland: Optical Society of America.
152. Royon, A., et al., *Silver clusters embedded in glass as a perennial high capacity optical recording medium*. *Adv Mater*, 2010. **22**(46): p. 5282-6.
153. Escobar, I., et al., *Reduction of the spherical aberration effect in high-numerical-aperture optical scanning instruments*. *Journal of the Optical Society of America A*, 2006. **23**(12): p. 3150-3155.
154. Robinson, J.P., *Chapter 4 Principles of confocal microscopy*, in *Methods in Cell Biology*. 2001, Academic Press. p. 89-106.
155. <http://phasicscorp.com/>. Available from: <http://phasicscorp.com/>.
156. Bon, P., et al., *Quadriwave lateral shearing interferometry for quantitative phase microscopy of living cells*. *Optics Express*, 2009. **17**(15): p. 13080-13094.
157. Rivet, S., *Caractérisation complète d'un faisceau laser impulsif femtoseconde : mise en évidence et analyse du couplage spatio-temporel dans la propagation linéaire et non linéaire*. 2001, Université Bordeaux 1.
158. !!! INVALID CITATION !!! {Homoelle, 1999 #314;Heisterkamp, 2015 #12;Heisterkamp, 2015 #12}.
159. Bellouard, Y., et al., *Stress-state manipulation in fused silica via femtosecond laser irradiation*. *Optica*, 2016. **3**(12): p. 1285.
160. Block, E.K., et al. *Non-ablative femtosecond laser exposure of fused silica in the sub-50 fs regime (Conference Presentation)*. in *SPIE LASE*. 2017. SPIE.
161. Hiroshi, K., S. Kazuya, and J.I. Akira, *Refractive Index, Density and Polarizability of Silica Glass with Various Fictive Temperatures*. *Japanese Journal of Applied Physics*, 2004. **43**(6A): p. L743.
162. Eaton, S.M., et al., *High refractive index contrast in fused silica waveguides by tightly focused, high-repetition rate femtosecond laser*. *Journal of Non-Crystalline Solids*, 2011. **357**(11-13): p. 2387-2391.
163. Marom, E., O. Ramer, and S. Ruschin, *Relation between normal-mode and coupled-mode analyses of parallel waveguides*. *IEEE journal of quantum electronics*, 1984. **20**(12): p. 1311-1319.
164. Lacroix, S., F. Gonthier, and J. Bures, *Modeling of symmetric 2x 2 fused-fiber couplers*. *Applied optics*, 1994. **33**(36): p. 8361-8369.
165. Royon, A., et al., *Durability study of a fluorescent optical memory in glass studied by luminescence spectroscopy*. *Microelectronics Reliability*, 2013. **53**(9-11): p. 1514-1518.
166. Fletcher, L.B., et al., *Changes to the network structure of Er-Yb doped phosphate glass induced by femtosecond laser pulses*. *Journal of Applied Physics*, 2009. **106**(8): p. 083107.

167. Chen, W.-J., et al., *Broadband directional couplers fabricated in bulk glass with high repetition rate femtosecond laser pulses*. Optics Express, 2008. **16**(15): p. 11470.
168. Minoshima, K., et al., *Fabrication of coupled mode photonic devices in glass by nonlinear femtosecond laser materials processing*. Optics Express, 2002. **10**(15): p. 645-652.
169. Lapointe, J., et al., *Toward the integration of optical sensors in smartphone screens using femtosecond laser writing*. Opt Lett, 2015. **40**(23): p. 5654-7.
170. Marshall, G.D., et al., *Laser written waveguide photonic quantum circuits*. Optics Express, 2009. **17**(15): p. 12546-12554.
171. Flamini, F., et al., *Thermally reconfigurable quantum photonic circuits at telecom wavelength by femtosecond laser micromachining*. Light: Science & Applications, 2015. **4**(11): p. e354.
172. Mermillod-Blondin, A., et al., *Flipping the sign of refractive index changes in ultrafast and temporally shaped laser-irradiated borosilicate crown optical glass at high repetition rates*. Physical Review B, 2008. **77**(10).
173. Ehrt, D., et al., *Femtosecond-laser-writing in various glasses*. Journal of Non-Crystalline Solids, 2004. **345-346**: p. 332-337.
174. Abou Khalil, A., et al., *Direct laser writing of a new type of waveguides in silver containing glasses*. Scientific Reports, 2017. **7**(1): p. 11124.
175. Ams, M., et al., *Investigation of Ultrafast Laser--Photonic Material Interactions: Challenges for Directly Written Glass Photonics*. IEEE Journal of Selected Topics in Quantum Electronics, 2008. **14**(5): p. 1370-1381.
176. Osellame, R., et al., *Optical properties of waveguides written by a 26 MHz stretched cavity Ti:sapphire femtosecond oscillator*. Optics Express, 2005. **13**(2): p. 612-620.
177. Eaton, S.M., et al., *Transition from thermal diffusion to heat accumulation in high repetition rate femtosecond laser writing of buried optical waveguides*. Optics Express, 2008. **16**(13): p. 9443-9458.
178. Jovanovic, N., et al. *Direct Laser Written Multimode Waveguides for Astronomical Applications*. in *Advanced Photonics & Renewable Energy*. 2010. Karlsruhe: Optical Society of America.
179. Tai, H., H. Tanaka, and T. Yoshino, *Fiber-optic evanescent-wave methane-gas sensor using optical absorption for the 3.392- μ m line of a He-Ne laser*. Optics Letters, 1987. **12**(6): p. 437-439.
180. Heo, J., et al., *Remote fiber-optic chemical sensing using evanescent-wave interactions in chalcogenide glass fibers*. Applied Optics, 1991. **30**(27): p. 3944-3951.
181. Kumar, P.S., et al., *A fibre optic evanescent wave sensor used for the detection of trace nitrites in water*. Journal of Optics A: Pure and Applied Optics, 2002. **4**(3): p. 247.

182. Polynkin, P., et al., *Evanescent field-based optical fiber sensing device for measuring the refractive index of liquids in microfluidic channels*. Optics Letters, 2005. **30**(11): p. 1273-1275.
183. Bilro, L., et al., *A simple and low-cost cure monitoring system based on a side-polished plastic optical fibre*. Measurement Science and Technology, 2010. **21**(11): p. 117001.
184. Ribeiro, R.M., et al., *An evanescent-coupling plastic optical fibre refractometer and absorptionmeter based on surface light scattering*. Sensors and Actuators A: Physical, 2002. **101**(1): p. 69-76.
185. Vazquez, R.M., et al., *Integration of femtosecond laser written optical waveguides in a lab-on-chip*. Lab Chip, 2009. **9**(1): p. 91-6.
186. Liu, D., et al., *Influence of focusing depth on the microfabrication of waveguides inside silica glass by femtosecond laser direct writing*. Applied Physics A, 2006. **84**(3): p. 257-260.
187. Maselli, V., et al., *Femtosecond laser written optofluidic sensor: Bragg grating waveguide evanescent probing of microfluidic channel*. Optics Express, 2009. **17**(14): p. 11719-11729.
188. Zhou, K., et al., *A refractometer based on a micro-slot in a fiber Bragg grating formed by chemically assisted femtosecond laser processing*. Optics Express, 2007. **15**(24): p. 15848-15853.
189. Liu, X. and W. Tan, *A Fiber-Optic Evanescent Wave DNA Biosensor Based on Novel Molecular Beacons*. Analytical Chemistry, 1999. **71**(22): p. 5054-5059.
190. Stewart, G., F.A. Muhammad, and B. Culshaw, *Sensitivity improvement for evanescent-wave gas sensors*. Sensors and Actuators B: Chemical, 1993. **11**(1): p. 521-524.
191. Chryssis, A.N., et al., *High sensitivity evanescent field fiber Bragg grating sensor*. IEEE Photonics Technology Letters, 2005. **17**(6): p. 1253-1255.
192. Bures, J. and R. Ghosh, *Power density of the evanescent field in the vicinity of a tapered fiber*. Journal of the Optical Society of America A, 1999. **16**(8): p. 1992-1996.
193. Chong, J.H., et al., *Measurements of refractive index sensitivity using long-period grating refractometer*. Optics Communications, 2004. **229**(1-6): p. 65-69.
194. Banerjee, A., et al., *Fiber optic sensing of liquid refractive index*. Sensors and Actuators B: Chemical, 2007. **123**(1): p. 594-605.
195. Bass, M., et al., *Handbook of Optics, Third Edition Volume I: Geometrical and Physical Optics, Polarized Light, Components and Instruments(set)*. 2010: McGraw-Hill, Inc. 1248.
196. Grobnic, D., et al., *Bragg grating evanescent field sensor made in biconical tapered fiber with femtosecond IR radiation*. IEEE Photonics Technology Letters, 2006. **18**(1): p. 160-162.

197. Bérubé, J.P., et al. *Direct inscription of waveguides in bulk glass for the photoexcitation of on-surface nanoparticles*. in *2017 Conference on Lasers and Electro-Optics (CLEO)*. 2017.
198. Çirkinoğlu, H.O., et al., *Silicon microsphere whispering gallery modes excited by femtosecond-laser-inscribed glass waveguides*. *Applied Optics*, 2018. **57**(14): p. 3687-3692.
199. Tong, L. and M. Sumetsky, *Subwavelength and Nanometer Diameter Optical Fibers*, in *Subwavelength and Nanometer Diameter Optical Fibers*. 2010, Springer Berlin Heidelberg: Berlin, Heidelberg. p. 1-14.
200. Agnarsson, B., et al., *Evanescent-wave fluorescence microscopy using symmetric planar waveguides*. *Optics Express*, 2009. **17**(7): p. 5075-5082.
201. Barty, A., et al., *Quantitative optical phase microscopy*. *Optics Letters*, 1998. **23**(11): p. 817-819.
202. Cheben, P., et al., *Comparative study of quantitative phase imaging techniques for refractometry of optical fibers*. 2018: p. 39.
203. Papon, G., *NANOSTRUCTURATION DES PROPRIÉTÉS OPTIQUES LINÉAIRES ET NON-LINÉAIRES D'UN VERRE PHOTOSENSIBLE PAR LASER FEMTOSECONDE*. 2012, Université de Bordeaux.

Titre : L'inscription laser directe d'un nouveau type de guides d'ondes et composants optiques dans des verres contenant de l'argent

Résumé : L'inscription laser directe est un domaine de recherche en croissance depuis ces deux dernières décennies, fournissant un moyen efficace et robuste pour inscrire directement des structures en trois dimensions (3D) dans des matériaux transparents tels que des verres en utilisant des impulsions laser femtosecondes. Cette technique présente de nombreux avantages par rapport à la technique de lithographie, qui se limite à la structuration en deux dimensions (2D) et implique de nombreuses étapes de fabrication. Cela rend la technique d'inscription laser directe bien adaptée aux nouveaux procédés de fabrication. Généralement, l'inscription laser dans les verres induit des changements physiques tels qu'un changement permanent de l'indice de réfraction localisé. Ces modifications ont été classées en trois types distincts: (*type I*, *type II* et *type III*). Dans ce travail, nous présentons un nouveau type de changement d'indice de réfraction, appelé *type A* qui est basé sur la création d'agrégats d'argent photo-induits. En effet, dans des verres dans lesquels sont incorporés des ions argent Ag^+ , lors de leur synthèse, l'inscription laser directe induit la création d'agrégats d'argent fluorescents Ag_m^{x+} au voisinage du voxel d'interaction. Ces agrégats modifient localement les propriétés optiques comme la fluorescence, la non-linéarité et la réponse plasmonique du verre. Ainsi, différents guides d'ondes, un séparateur de faisceau 50-50, ainsi que des coupleurs optiques ont été inscrits en se basant sur ce nouveau *type A* et complètement caractérisés. D'autre part, une étude comparative entre les deux types de guides d'ondes (*type A* et *type I*) est présentée, tout en montrant qu'en ajustant les paramètres laser, il est possible de déclencher soit le *type I* soit le *type A*. Enfin, en se basant sur des guides d'ondes de *type A* inscrits proche de la surface du verre, un capteur d'indice de réfraction hautement sensible a été inscrit dans une lame de verre de 1 cm de long. Ce capteur miniaturisé peut présenter deux fenêtres de détection d'indice, ce qui constitue une première mondiale. Les propriétés des guides d'ondes inscrits dans ces verres massifs ont été transposées à des fibres en forme de ruban, du même matériau contenant de l'argent. Les résultats obtenus dans ce travail de thèse ouvrent la voie à la fabrication de circuits intégrés en 3D et de capteurs à fibre basés sur des propriétés optiques originales inaccessibles avec des guides d'onde de *type I* standard.

Mot clés : Inscription laser directe, laser femtoseconde, verre, agrégats d'argent, guide d'ondes, nouveau type de changement d'indice.

Title: Direct Laser Writing of a new type of optical waveguides and components in silver containing glasses

Abstract: Direct Laser Writing (DLW) has been an exponentially growing research field over the last two decades, by providing an efficient and robust way to directly address three dimensional (3D) structures in transparent materials such as glasses using femtosecond laser pulses. It exhibits many advantages over the lithography technique which is mostly limited to two dimensional (2D) structuring and involves many fabrication steps. This competitive aspect makes the DLW technique suitable for future technological transfer to advanced industrial manufacturing. Generally, DLW in glasses induces physical changes such as permanent local refractive index modifications that have been classified under three distinct types: (*Type I*, *Type II* & *Type III*). In silver containing glasses with embedded silver ions Ag^+ , DLW induces the creation of fluorescent silver clusters Ag_m^{x+} at the vicinity of the interaction voxel. In this work, we present a new type of refractive index change, called *type A* that is based on the creation of the photo-induced silver clusters allowing the creation of new linear and nonlinear optical waveguides in silver containing glasses. Various waveguides, a 50-50 Y beam splitter, as well as optical couplers, were written based on *type A* modification inside bulk glasses and further characterized. In addition, a comparative study between *type A* and *type I* waveguides is presented, showing that finely tuning the laser parameters allows the creation of either *type A* or *type I* modification inside silver containing glasses. Finally, based on *type A* near-surface waveguides, a highly sensitive refractive index sensor is created in a 1 cm glass chip, which could exhibit a pioneer demonstration of double sensing refractive ranges. The waveguiding properties observed and reported in the bulk of such silver containing glasses were transposed to ribbon shaped fibers of the same material. Those results pave the way towards the fabrication of 3D integrated circuits and fiber sensors with original fluorescent, nonlinear and plasmonic properties that are not accessible using the standard *type I* modification.

Keywords: Direct laser writing, femtosecond laser, silver containing glasses, silver clusters, waveguides, new type of refractive index.